

Modeling and simulation of the plasma discharge in an electron cyclotron resonance thruster

by

Alvaro Sánchez Villar

*Thesis deposited in partial fulfillment of the requirements for the
degree of Doctor in*

Mecánica de Fluidos Programa Interuniversitario

Universidad Carlos III de Madrid

Advisors:

Mario Merino Martínez

Eduardo Ahedo Galilea

Tutor:

Mario Merino Martínez

December 2021

This thesis is distributed under license “Creative Commons **Atribution** - **Non Commercial** - **Non Derivatives**”.



Acknowledgements

First and foremost, I would like to make a special mention to my thesis advisors Mario Merino and Eduardo Ahedo, for their supervision and advice during the development of this thesis and whose contributions have improved its results considerably. I am very thankful to both of them for the opportunities they have given me. I want to thank Mario for his availability, patience, and perseverance during these years of guiding me through this road. My heartfelt gratitude to him for all the things he taught me both as a researcher and as a lecturer. I want to express my gratitude as well to Eduardo, for his bright advice and intelligent supervision which disentangled many of the difficult knots I found along the path.

I would like to thank also Ruben Otín for the very valuable and insightful discussions regarding the simulation of electromagnetic waves in plasmas. Thanks to Prof. Luis Emilio García-Castillo, and Adrián Amor for their advice in the development and verification of the finite element wave code; also to Syun'ichi Shiraiwa, for his crucial guidance in the details regarding the utilization of MFEM discretization library for electromagnetic wave applications.

Many thanks also to Denis Packan for giving me the opportunity to make a research stay with his group and for embracing and welcoming me. This experience was both very challenging and inspiring to me. Also, to my friends Victor Désangles, Amelie Jarnac from ONERA for all the moments we shared both in and out of the office/lab. To my good friend and colleague Federico Boni, with whom I shared many conversations and discussions about work and also life. You know it has been a pleasure to work side by side with you.

I am very grateful to my parents for their unconditional support and affection as well as for the values that they transmitted to me, which really helped me thrive in the completion of this challenge. I want to also thank the most special person of my life, Lorena, who arrived to it as light and never stops surprising me. Your support, love and dedication have helped me enormously, and this work would not be the same without you.

Naturally, I have to mention my great friends and colleagues Filippo and Adrián. Filippo, even having been my professor during my master studies, you always showed yourself available and affable from the beginning of this journey, willing to help and share your knowledge, teaching me advanced plasma concepts and others, even more advanced, as “keep calm and play beach volley”. Now we forged a friendship that I will cherish through the years. I could never forget my great friend Adrián who I appreciate tremendously, and with whom I laughed a lot, or, as he says, “pechá” during these years. Thank you for helping me with HYPHEN and for your support, and for making us run after you when going for our breakfasts. I expect to see you more than often in the future. Also, to Jaume, who always transmitted me a lot of peace and who I appreciate enormously. Thank you for the countless talks and coffees we shared. I hope there will be many more to come. Also, thanks to my friend Jiewei, who helped me with HYPHEN details at work and also instructed me in the chinese culinary arts and soccer style. You have always been a source of joy along this journey.

I do not want to forget my great friends Miguel and Pablo who have stayed with me through this road. Miguel, you know everything is said and all is there to live. Pablo, you are an extra inner voice, that one which feels good to have. Also, to Daniel, who is an excellent researcher and friend, and who helped me to distress in many occasions along the way including piano and philosophical lessons.

I want to acknowledge my gratitude to all the other outstanding people I met at EP2 group. In particular, I want to mention those which interacted most with me, starting with Xin, who inspired me, and her determination always fascinated me. Many thanks to Sara, not only for our talks about the ECR thruster and our trip to ONERA but also for your good vibes in and out of the office. To Scherezade, for being a good and caring friend, and to Enrique, with whom I shared a lot of moments, specially in the pre-COVID era, both at the office and on our trip to Vienna. To Pedro for our nice discussions about particle wave interaction and electromagnetism. To Jesús, who is an excellent workmate and friend. I hold you all in great esteem.

Finally, I want to thank the international experts who reviewed and improved this thesis, Prof. Dr. Ralf Schneider (Group leader of Computational Sciences at Greifswald University) and Dr. Paul-Quentin Elias (Research Scientist at the French Aerospace Lab ONERA).

The research leading to the results of this thesis has been funded mainly by the European Union H2020 program under grant agreement 730028 (Project MINOTOR). Subsequent funding came from the ESPEOS project, funded by Agencia Estatal de Investigación (PID2019-108034RB-I00/AEI/10.13039/501100011033). Sánchez-Villar funding came from the spanish Ministry of Science, Innovation and Universities under FPU scholarship program with grant FPU17/06352. Additionally, the same program funded the research stay carried out by Sánchez-Villar at ONERA's center in Paris during spring 2021, under grant agreement EST21/00696.

Alvaro Sánchez-Villar
Universidad Carlos III de Madrid
December 15, 2021

List of publications

Refereed journals

- A. Sánchez-Villar, J. Zhou, E. Ahedo and M. Merino. *Coupled plasma transport and electromagnetic wave simulation of an ECR thruster*. *Plasma Science Sources & Technology*, 30(3):035003, mar 2021. DOI: [10.1088/1361-6595/abde20](https://doi.org/10.1088/1361-6595/abde20).

The novel electromagnetic wave finite element solver ATHAMES is coupled to HYPHEN, a plasma transport code. A coupling tool prepared by J. Zhou was adapted by A. Sánchez-Villar to the interface with ATHAMES. With the aid and guidance of his advisors, A. Sánchez-Villar is author of the whole paper tasks: implementation of the electromagnetic wave code, preparation of the simulation data and adaptation of the simulation to ECRT, production and analysis of the results, and writing of the paper except the electron fluid module part, written by J. Zhou. The contents of this article are adapted to the thesis format and are fully included in chapters 2, 4, and 5. Whenever material from this source is included in this thesis, it is singled out with typographic means and explicit reference.

Two other publications are being prepared for journal submission:

- A. Sánchez-Villar, F. Boni, V. Désangles, J. Jarrige, D. Packan, E. Ahedo, M. Merino. *Comparison of hybrid coaxial ECR thruster model to experimental measurements* (to be submitted).

The contents of this paper show the comparison of experimental measurements obtained with a version of the ECRT prototype built at ONERA, to numerical results obtained using the hybrid ECRT coupled electromagnetic and plasma transport model presented in this thesis. The comparison was carried out during the research stay period of A. Sánchez-Villar at ONERA facilities. The experimental measurements were obtained by F. Boni and V. Desangles, and supervised by J. Jarrige and D. Packan. The numerical simulations were obtained by A. Sánchez-Villar with the aid and advice of M. Merino and E. Ahedo. The activities related to the paper writing, cases and results selection were led by A. Sánchez-Villar and F. Boni, and supervised by their respective advisors of EP2 and ONERA. The contents of this article are presented in chapter 9. Whenever material from this source is included in this thesis, it is singled out with typographic means and explicit reference.

- A. Sánchez-Villar, A. Domínguez-Vázquez, E. Ahedo and M. Merino. *Numerical parametric investigation of the optimal operation and design of an ECRT*. *Plasma Science Sources & Technology*, (to be submitted).

This article details part of the parametric investigations carried out during this thesis by A. Sánchez-Villar in the context of MINOTOR H2020 project. The contents of the paper, simulations selected, and results presented, and writing are, with the aid and supervision of the thesis advisors, implemented by A. Sánchez-Villar. A. Domínguez-Vázquez helped A. Sánchez-Villar in the use and adaptation of HYPHEN to the ECRT. The contents of this article are contained in chapter 6. Whenever material from this source is included in this thesis, it is singled out with typographic means and explicit reference.

Conference proceedings

Contributions to international conferences and scientific communications include:

- M. Merino, A. Sánchez-Villar, E. Ahedo, Bonoli, P. Jungpyo, L., Ram, A. & Wright, J. *Wave Propagation and Absorption in ECR Plasma Thrusters*. In 35th International Electric Propulsion Conference, paper IEPC 2017-105, Atlanta, GA, USA, October 8-12, 2017.
- D. Packan, P.Q. Elias, J. Jarrige, M. Merino, **A. Sánchez-Villar**, E. Ahedo, G. Peyresoubes, K. Holste, P. Klar, M. Bekemans, T. Scalais, E. Bourguignon, S. Zurbac, M. Mares, A. Hoque and P. Favier. *The “MINOTOR” project for ECR thruster development*. In 35th International Electric Propulsion Conference, paper IEPC 2017-547, Atlanta, GA, USA, October 8-12, 2017.
- A. Sánchez Villar & M. Merino. *Advances in wave-plasma modelling in ECR thrusters*. In Space Propulsion Conference, paper SP2018-346, Seville, Spain, May 14-18, 2018. 3AF.
- A. Domínguez-Vázquez, J. Zhou, A. Sánchez-Villar, M. Merino, P. Fajardo & E. Ahedo. *HYPHEN: A simulation platform for space plasma thrusters*. In 8th European Conference for Aeronautics and Space Science, Madrid, Spain, July 1-4, 2019.
- M. Merino, A. Sánchez-Villar, A. Domínguez-Vázquez, E. Bello, P. Jiménez, M. Inchingolo, J. Navarro-Cavallé, F. Cichocki, P. Fajardo, E. Ahedo, C. Hidalgo, B. Van Milligen, F. Tabarés, I. Calvo, J.L. Velasco, A. Cappa, & E. De la Cal. *Synergies between space plasma propulsion and magnetic confinement for plasma fusion: PROMETEO project*. XXXVII Reunión Bienial de la RSEF, Zaragoza, España, Julio 15-19, 2019.
- E. Ahedo, P. Fajardo, M. Merino, J. Navarro-Cavallé, A. Sánchez-Villar, M. Wijnen & J. Zhou. *Helicon and ECR plasma sources for space propulsion: simulation and testing*. 21th International Conference on Electromagnetics in Advanced Applications (ICEAA 2019), paper 788, Granada, Spain, September 9-13 2019, La Société Savante de l’Aéronautique et de l’Espace. DOI: [10.1109/ICEAA.2019.8879300](https://doi.org/10.1109/ICEAA.2019.8879300).
- A. Sánchez-Villar, J. Zhou, M. Merino & E. Ahedo. *PIC/fluid/wave simulations of the plasma discharge in an ECR plasma thruster*. In 36th International Electric Propulsion Conference, paper IEPC 2019-633, Vienna, Austria, September 15-20, 2019.
- A. Sánchez-Villar, M. Merino & E. Ahedo. *A numerical parametric investigation on the optimal design and operation of coaxial ECR thrusters*. In Space Propulsion Conference, paper SP2021-396, March 17-19, 2021. 3AF.

Abstract

The interest in novel disruptive technologies as the electrodeless plasma thrusters (EPTs) is growing with the maturity of electric propulsion (EP). EPTs combine a magnetic nozzle (MN) with a radiofrequency waves as the Helicon plasma thruster (HPT) or microwaves as the electron cyclotron resonance thruster (ECRT), to generate the plasma and sustain the discharge, thus eliminating electrodes which are often considered lifetime-limiting components. The implementation of robust and reliable simulation codes capable of reproducing the phenomena occurring in EP thrusters and estimating performances is crucial not only to accelerate and optimize their design but also allows to bring deeper insight to the details governing their operation.

This thesis focuses on the numerical modeling and simulation of ECRTs. The thesis contents can be divided into: *(i)* literature review and exploration of a one-dimensional (1D) wave model, *(ii)* development of a two-dimensional (2D) electromagnetic (EM) wave code, *(iii)* coupled simulations of ECRTs, and *(iv)* comparison campaign with experimental results.

Part of the thesis is focused in the development of an EM code, in absence of one applicable to the description of EM wave propagation and absorption in ECRTs. First of all, a thorough literature review of existing methods and phenomena present in ECR plasmas, ECRTs and related technologies was carried out. Specifically, a 1D model of the right-hand polarized wave propagation and absorption was revisited, providing further insight on the role of collisionality and showing the response of individual electrons to the wavefields obtained, estimating the energy absorbed by electrons per resonance pass.

A 2D axisymmetric full-wave code, named ATHAMES, is implemented to solve Maxwell's inhomogeneous wave equation combined with a collisional cold plasma model using a variational formulation based on Galerkin's finite element method. The code uses an unstructured mesh which provides several benefits, being the most relevant the description of complex arbitrary geometries and the use of local refinement. The latter allows to perform a predictive mesh refinement strategy based on the local EM properties key to obtain computationally efficient solutions. Solutions of the EM wave fields and power absorbed by the plasma were obtained together with other outputs and these were related to the EM parametric regions found locally in the plasma.

ATHAMES was coupled to HYPHEN, a 2D axisymmetric hybrid code, and utilized to solve for the coupled plasma transport and EM wave solutions of ECRTs. Specifically, the low power prototype ECR30 developed by ONERA was investigated with a thorough analysis of a reference case, followed by several parametric investigations covering mass flow rate and power, resonance location, injector configuration and propellant species. Simulations of a 200 W ECRT prototype were analyzed and compared with the ECRT30.

Finally, a numerical and experimental campaign has been carried out in collaboration with FPA unit of ONERA-DPHY department at their research center. The comparison tested the simulation model highlighting its main limitations. Results show that the coupled model is capable of partially reproducing the experimental measurements taken along the plasma plume by the including a dominant cross-field diffusion in both particle and energy transport.

Resumen

El interés en tecnologías disruptivas como los propulsores de plasma sin electrodos (EPTs) está creciendo con la madurez de la propulsión eléctrica. Los EPTs combinan una tobera magnética (MN) con una fuente plasma por radiofrecuencia o microondas, que se usa para generar el plasma y mantener la descarga, eliminando así los electrodos que suelen ser considerados componentes que limitan la vida útil del sistema propulsivo. La implementación de códigos de simulación robustos y fiables capaces de reproducir los fenómenos que ocurren en los propulsores EP y estimar sus actuaciones es fundamental, no solo para acelerar y optimizar su diseño sino para también proporcionar un entendimiento más profundo de los detalles que dominan su correcto funcionamiento.

La tesis se centra en la modelización y simulación numérica de los propulsores por resonancia electrón-ciclotrón, y sus contenidos pueden ser clasificados en: *(i)* una revisión bibliográfica del estado del arte y exploración de un modelo unidimensional (1D), *(ii)* desarrollo de un código electromagnético (EM) de ondas bidimensional (2D), *(iii)* simulaciones acopladas para ECRTs, *(iv)* comparación con resultados experimentales.

Parte de la tesis se ha centrado en el desarrollo de un código EM, en ausencia de uno apto para describir la propagación y absorción de ondas electromagnéticas en ECRTs. El primer paso se basó en realizar una revisión bibliográfica de los modelos existentes usados para describir la fenomenología existente en los propulsores ECRT, así como en tecnologías similares. Un modelo EM 1D de ondas en plasmas ECR fue implementado analizado en detalle, incluyendo el papel de la colisionalidad. Se analizó también la respuesta individual de electrones a las soluciones de onda obtenidas, estimando la energía absorbida por cada pase por la resonancia.

Se ha implementado un código 2D axisimétrico de onda completa llamado ATHAMES, que resuelve mediante una formulación variacional basada en el método de elementos finitos de Galerkin, la ecuación de ondas inhomogénea de Maxwell junto con un tensor de plasma frío colisional. El código emplea mallas no estructuradas que proporcionan ventajas como la capacidad de describir geometrías complejas o el uso de refinamiento local. Este último permite hacer un refinado de malla predictivo en función de las propiedades electromagnéticas locales. Las soluciones electromagnéticas se han relacionado con las regiones de propagación EM halladas localmente en el plasma.

ATHAMES se ha acoplado con HYPHEN, un código bidimensional axisimétrico, y se ha utilizado para resolver el transporte acoplado con el problema electromagnético en ECRTs. El propulsor ECR30 desarrollado por ONERA es investigado en detalle para un caso de referencia y también realizando estudios paramétricos del punto de operación, localización de la resonancia, geometría del inyector, o el propulsante utilizado. Además un prototipo de alta potencia (200 W) es analizado y comparado frente al ECR30.

Finalmente, se ha realizado una campaña numérico-experimental en colaboración con la unidad FPA de ONERA-DPHY en sus instalaciones. La campaña puso a prueba el modelo implementado detallando sus limitaciones. Los resultados demostraron que el modelo acoplado es capaz de reproducir parcialmente las mediciones experimentales mediante la introducción de un transporte anómalo perpendicular dominante en la difusión perpendicular de partículas y energía.

Contents

Acknowledgements	i
List of Publications	iii
Abstract	v
List of Figures	xvi
List of Tables	xvii
Glossary	xix
1 Introduction	1
1.1 Background	1
1.2 Objectives	3
1.3 Thesis structure	4
2 Electromagnetic waves in cold plasmas	7
2.1 Maxwell's Equations	7
2.2 The cold plasma approximation	8
2.3 Susceptibility and the cold plasma dielectric tensor	8
2.3.1 Cold plasma dielectric tensor including collisions	9
2.3.1.1 Cold-plasma collisionless dielectric tensor	10
2.3.2 Diagonalization of the dielectric tensor	11
2.3.3 Hermitian and antihermitian parts of the dielectric tensor	12
2.4 The wave equation	13
2.5 The infinite homogeneous plasma dispersion relation	14
2.6 Parallel and perpendicular propagation	15
2.6.1 Parallel propagation	15
2.6.2 Perpendicular propagation	17
2.7 Cutoffs and resonances	17
2.7.1 Cutoffs	17
2.7.2 Resonances	18
2.8 Clemmow-Mullaly-Allis diagram for a two-component plasma	18
2.9 Poynting's theorem for harmonic fields in cold plasmas	20
2.9.1 Electromagnetic power absorption: the antihermitian part of the dielectric tensor	21

3	One-dimensional ECR model	23
3.1	1D RHP wave model	23
3.1.1	RHP wave equation	24
3.1.2	Asymptotic solutions in the collisionless limit	25
3.1.2.1	Case (i): wave propagating in the direction of increasing magnetic field	25
3.1.2.2	Case (ii): wave propagating in the direction of decreasing magnetic field	26
3.1.2.3	Behavior of the energy close to an infinite refractive index	27
3.1.3	Numerical solutions including damping	28
3.1.3.1	Case (i): a single wave propagating towards $s \rightarrow \infty$ at boundary b . Propagation with increasing magnetic field.	29
3.1.3.2	Case (ii): a single wave propagating towards $s \rightarrow -\infty$ at boundary a . Propagation with decreasing magnetic field.	31
3.1.4	Parametric study	31
3.1.4.1	Transmission factor for case (ii)	33
3.1.4.2	Transmission and reflection factors for case (i)	34
3.1.5	Concluding remarks	35
3.2	Electron particle response	35
3.2.1	Analytical solution	35
3.2.2	Numerical solution	38
3.2.3	Concluding remarks	39
4	ATHAMES: A finite element electromagnetic wave code	41
4.1	Objectives and capabilities	41
4.2	The full wave model	42
4.2.1	Physical model	43
4.2.2	Mathematical model	44
4.2.2.1	Variational formulation	44
4.2.2.2	Mixed finite element discretization	45
4.2.2.3	Planar problem	47
4.2.2.4	Axisymmetric problem	48
4.2.3	Coaxial transmission line model	50
4.3	Numerical implementation	51
4.3.1	Code architecture	51
4.3.2	Integration with HYPHEN	54
4.3.2.1	Wrapper structure overview	54
4.3.2.2	HYPHEN-ATHAMES intercommunication subroutines	55
4.3.3	Meshing	55
4.3.3.1	Predictive mesh refinement	56
4.4	Verification	58
4.4.1	Method of manufactured solutions	59
4.4.1.1	THAMES verification	59
4.4.1.2	ATHAMES verification	62
4.4.1.3	Annular geometry tests	63
4.4.1.4	Cylindrical geometry tests	65
4.4.2	Mesh refinement sensitivity analysis	66
4.5	Sensitivity analysis on the electron collisionality	70
4.6	Concluding remarks	73

5	Coupled simulation of the plasma discharge of an ECRT	75
5.1	Introduction	75
5.2	Simulation model	77
5.2.1	The I-module	78
5.2.2	The E-module	78
5.2.3	The W-module	80
5.2.3.1	W-module mesh refinement strategy	80
5.2.4	Simulation setup	81
5.3	Results and discussion	83
5.3.1	Quasi-steady plasma transport properties	83
5.3.2	Fast electromagnetic fields and power absorption	86
5.3.3	Particle and energy wall fluxes	89
5.3.4	Propulsive performance	90
5.4	Concluding remarks	94
6	Parametric investigation of ECR30 operation and design	95
6.1	Reduced-domain simulation	95
6.2	Parametric investigation on the operating point	97
6.2.1	Neutral density	97
6.2.2	Electron dynamics	98
6.2.3	Ionization and ion-wall recombination	101
6.2.4	Acceleration	103
6.2.5	Propagation and absorption of electromagnetic waves	105
6.2.6	Thruster performances	108
6.3	Effects of ECR location	110
6.3.1	Propagation and absorption of electromagnetic waves	111
6.3.1.1	CMA regions	112
6.3.1.2	Poynting flux vector	112
6.3.1.3	Power absorption density	113
6.3.1.4	EM wave electric fields	113
6.3.2	Neutral and plasma transport	115
6.3.2.1	Neutral and plasma density	115
6.3.2.2	Electron temperature and plasma potential	116
6.3.2.3	Ion velocity	118
6.3.2.4	Ionization rate	119
6.3.3	Thruster performances and energy usage	120
6.4	Effects of variations on the injector geometry	120
6.4.1	Neutral and electron density	121
6.4.2	Electron pressure	122
6.4.3	Electron temperature and plasma potential	123
6.4.4	Ion acceleration	124
6.4.5	Propagation and absorption of electromagnetic waves	124
6.4.5.1	CMA regions	124
6.4.5.2	EM wave radial electric fields and Poynting vector	124
6.4.5.3	Power absorption	126
6.4.6	Thruster performances and energy usage	126
6.5	Sensitivity analysis on the anomalous transport	127
6.6	Concluding remarks	128

7	Alternative propellants	131
7.1	Alternative propellant properties	131
7.1.1	Collisions and interaction rates	132
7.2	Simulations results	134
7.2.1	Simulation setup	134
7.2.1.1	Geometry, applied magnetic field and operating parameters	134
7.2.2	Results	134
7.2.2.1	Xenon	135
7.2.2.2	Krypton	136
7.2.2.3	Argon	137
7.2.3	Thruster performances	138
7.3	Discussion	138
7.3.1	Thruster modifications	142
7.4	Concluding remarks	142
8	ECRT Scale-up study	143
8.1	Thruster scale-up configurations	143
8.1.1	Simulation setup	143
8.1.2	Simulation results	145
8.1.2.1	Case 1: ECRT 30 W reference simulation	147
8.1.2.2	Case 2: ECRT 200 W simulation	148
8.1.2.3	Case 3: ECRT 200 W with larger coaxial cable outer radius	149
8.2	Discussion	150
8.2.1	Thruster optimization	153
8.3	Concluding remarks	153
9	Comparison of ECRT model to experimental measurements	155
9.1	Introduction	155
9.2	Methodology	156
9.2.1	Experimental setup	158
9.2.2	ECRT model	158
9.3	Results and discussion	160
9.3.1	Angular profiles	161
9.3.2	Cross-field diffusion	161
9.3.3	Thruster performances and ion energy	165
9.3.4	Electron cooling and other model limitations	167
9.4	Concluding remarks	169
10	Conclusions	171
10.1	Main thesis contributions	171
10.2	Future research lines	174
A	Simulation list	177

List of Figures

2.1	Sketch of (a) electron helical motion and (b) ECR heating.	16
2.2	CMA diagram for a two component plasma for a singly-charged ion to electron mass ratio of 2.5.	19
3.1	Refractive index squared for multiple values of γ	29
3.2	RHP wave solutions and Poynting's vector for wave propagation in the (a)-(b) increasing and (c)-(d) decreasing magnetic field direction.	30
3.3	RHP electric field complex amplitude for wave propagation in the (a) increasing and (b) decreasing magnetic field direction.	30
3.4	Effect of parameters η and γ on the RHP wave solutions.	32
3.5	Evolution of the transmission factor as a function of the plasma density.	33
3.6	Evolution of transmitted, reflected and absorbed coefficients of the RHP wave crossing an ECR region in the increasing magnetic field direction.	34
3.7	Evolution the complex magnitude of the velocity vector in a single resonance crossing for different phases.	37
3.8	Kinetic energy and perpendicular velocity of an electron during an ECR crossing.	38
3.9	Mean energy gained as a function of the RHP wave electric field amplitude.	39
4.1	Nédélec vector basis functions for a linear triangular element.	46
4.2	Degrees of freedom in a Lagrange triangular element for different p_L	46
4.3	Representation in a reference element of the magnitude of first order Nédélec and Lagrange functions.	47
4.4	Coaxial lossless transmission line terminated in a load [86].	50
4.5	ATHAMES overall architecture	52
4.6	Example of unstructured mesh obtained using GMSH using partitions, a curved internal boundary and local refinement.	56
4.7	(a) Target element size function and (b) resulting mesh after the application of predictive refinement.	57
4.8	Complex phase of the E_z fast electromagnetic field and number of mesh elements per local wavelength for a uniform mesh (left) and for a refined mesh (right).	57
4.9	Manufactured solution with parameters $k_1 = k_3 = 2\pi$, $k_2 = k_4 = 4\pi$	60
4.10	Convergence of THAMES verification.	62
4.11	Convergence of the L^2 -norm errors for test MMS-1 and MMS-2 with magnetic field.	64
4.12	Convergence of the L^2 -norm errors for test MMS-2 with electron collisionality.	64
4.13	Convergence of the L^2 -norm errors for test MMS-3 and MMS-4 with magnetic field.	65
4.14	ATHAMES inputs for the mesh refinement sensitivity analysis.	66
4.15	Mesh refinement study (a) meshes used and (b) CMA regions in the plasma.	67

4.16	Evolution of the radial electric field complex amplitude (a) magnitude and (b) phase for different consecutive refinements.	68
4.17	Evolution of error mean and standard deviation of each complex field component amplitude and phase with the number of refinements.	69
4.18	Absorbed power for different number of refinement steps.	70
4.19	Convergence of the absorbed power and power reflection ratio.	70
4.20	Evolution of the radial electric field complex amplitude (a) magnitude and (b) phase for different scaling factors on the electron collisionality.	71
4.21	Absorbed power for different electron collisionalities.	72
5.1	Sketch of the ECRT simulation domain.	77
5.2	Overall code structure, composed of an ion/neutral module, an electron module, and a wave module.	77
5.3	(a) PIC mesh, (b) MFAM and (c) representation of the W-module mesh with the applied magnetic field and ECR region.	80
5.4	Complex phase of the \tilde{E}_z fast electromagnetic field and number of mesh elements per local wavelength for a uniform mesh (left) and for a refined mesh (right).	81
5.5	Time evolution of the thrust contributions of the different plasma species.	82
5.6	Quasisteady plasma transport results.	84
5.7	Electron azimuthal current density.	86
5.8	(a) Electromagnetic parametric regions and (b) minimum principal wavelength.	87
5.9	Electromagnetic wave electric field.	88
5.10	Electromagnetic power density absorbed by the electron species.	89
5.11	(a) Particle flux, (b) net energy flux and (c) average impact energy, of the different plasma species to the thruster walls.	91
6.1	(a) PIC-mesh and (b) MFAM elements, with applied magnetic field and ECR location.	96
6.2	Comparison of key plasma transport results between reference and reduced domain simulations.	96
6.3	Neutral density axial evolution for different operating points.	98
6.4	Neutral density radial evolution for different operating points.	98
6.5	Electron temperature radial evolution for different operating points.	98
6.6	Electron pressure radial evolution for different operating points.	99
6.7	Electron density radial evolution for different operating points.	100
6.8	Radial evolution of the principal forces on the radial electron momentum balance, for different operating points.	100
6.9	Ionization rate 2D map for different operating points.	101
6.10	Singly-charged ion (a) impacting flux to the walls, (b) density, and (c) radial velocity, for different mass flow rates.	102
6.11	Singly-charged ion (a) impacting flux to the walls, (b) density, and (c) radial velocity, for different input powers.	103
6.12	Effect of the mass flow rate on the electrostatic potential.	103
6.14	Effect of mass flow rate on (a) the axial and (b) the radial evolution of electrostatic potential.	104
6.13	Effect of the input power on the electrostatic potential.	104
6.15	Effect of input power on (a) the axial and (b) the radial evolution of electrostatic potential.	105
6.16	Radial evolution of the local ion Mach number for different operating points.	105
6.17	Influence of mass flow rate on the (a)-(c) EM parametric regions (CMA), (d)-(f) the EM wave electric field norm, and (g)-(i) power absorption density maps.	106
6.18	Influence of input power on the (a)-(c) EM parametric regions (CMA), (d)-(f) the EM wave electric field norm, and (g)-(i) power absorption density maps.	107
6.19	Specific impulse against the square root of the energy deposited per propellant mass.	109

6.20	Efficiency map and energy use for different points of operation.	109
6.21	ECR region locations investigated.	110
6.22	Influence of ECR location on the (a)-(c) EM parametric regions (CMA), (d)-(f) the the time-averaged Poynting vector, and (g)-(i) power absorption density maps. . .	111
6.23	Influence of ECR location on the principal EM wave electric field components. . .	114
6.24	Effect of ECR location on the radial profiles of neutral and electron density. . . .	115
6.25	Influence of ECR location on electron density 2D maps.	116
6.26	Influence of the ECR location on 2D electron temperature maps.	116
6.27	Influence of the ECR location on 2D electron temperature maps.	117
6.28	Influence of the ECR location on the electrostatic potential and its corresponding electric field.	118
6.29	Influence of the ECR location on the singly-charged ion velocity.	118
6.30	Influence of the ECR location on the radial evolution of the local ion Mach number at the simulated plume end.	119
6.31	Influence of the ECR location on the ionization source rate 2D maps.	119
6.32	Influence of ECR location on the maps of specific impulse, efficiency, and energy use, compared to other operating points.	120
6.33	Effect of injector geometry on the neutral density 2D maps.	121
6.34	Effect of injector geometry on the radial (a) neutral and (b) electron density profiles within the thruster chamber, and on (c) the axial evolution of electron density. . .	121
6.35	Effect of injector geometry on the ionization source rate 2D maps.	122
6.36	Effect of injector geometry on the radial and axial profiles of the electron pressure. .	122
6.37	Effect of injector geometry on the radial profiles of the (a) electron temperature and (b) electrostatic potential within the thruster chamber; (c) shows the axial evolution of the electrostatic potential.	123
6.38	Effect of injector geometry on the radial evolution of the local Mach number at the end of the simulated plume.	124
6.39	Influence of injector geometry on the most relevant electromagnetic variables. . . .	125
6.40	Influence of injector geometry on the maps of specific impulse, efficiency, and energy use, compared to other operating points.	126
6.41	Effects of anomalous transport coefficient on the electron density and temperature. .	127
7.1	Collisional rates for xenon (solid), krypton (dashed-dotted) and argon (dashed). . .	133
7.2	Principal simulation results using xenon as propellant.	135
7.3	Principal simulation results using krypton as propellant.	136
7.4	Principal simulation results using argon as propellant.	137
8.1	Applied magnetic field geometry together with MFAMs of the 30 W and 200 W thruster simulations. Magnetic streamlines are shown in white and their perpendicular in black compose the MFAM.	144
8.2	Principal simulation results of the scale-up case 1: ECRT 30 W simulation.	147
8.3	Principal simulation results of the scale-up case 2: ECRT 200 W simulation.	148
8.4	Principal simulation results of the scale-up Case 3.	149
9.1	(a) ECRT prototype operating in the ONERA-B09 facility; (b) ECRT simulation domain and relevant elements.	157
9.2	Comparison between numerical estimations and experimental measurements of the angular profiles of the (a) ion current density and (b) electron density.	161
9.3	Repeatability of experiment A electron density measurements.	162
9.4	Comparison of the effective Hall parameter in the meridional plane for different anomalous diffusion coefficients at 2 SCCM - 30 W.	162
9.5	Axial evolution of the angular electron density profiles for different anomalous trans- port coefficients at 2 SCCM - 30 W.	163

9.6	Axial evolution of (a) the total ion current density and (b) the electron density at 2 SCCM - 30 W.	164
9.7	(a) Comparison of the IEDF of Xe^+ at the end of the simulated plume with measurements taken at the end of the vacuum chamber; (b) Evolution of both the ion energy and ionization rate along different streamlines.	166
9.8	Comparison of axial and angular Langmuir probe measurements of electron temperature and electrostatic potential with model results at 2 SCCM - 30 W.	168
A.1	Principal simulation results of case REF.	179
A.2	Principal simulation results of case I2.	180
A.3	Principal simulation results of case RED.	181
A.4	Principal simulation results of case M0.	182
A.5	Principal simulation results of case M2.	183
A.6	Principal simulation results of case P0.	184
A.7	Principal simulation results of case P2.	185
A.8	Principal simulation results of case ECR0.	186
A.9	Principal simulation results of case ECR2.	187
A.10	Principal simulation results of case INJZ0.	188
A.11	Principal simulation results of case INJR.	189

List of Tables

3.1	Reference case parameters.	28
3.2	Illustrative parameter values of the existing ECR thruster, based on or estimated from the references given.	31
4.1	Block matrix of bilinear integrators for the planar problem.	48
4.2	Block matrix of bilinear integrators for the axisymmetric problem.	49
4.3	MFEM integrators utilized for the purely axisymmetric system.	54
4.4	Major inputs and outputs of ATHAMES (see Fig. 5.2).	54
4.5	List of major ATHAMES tests.	58
4.6	Convergence of both L^2 -norm errors and computational time for THAMES.	61
4.7	Information on the number of elements, refinement steps and computational time for each mesh used in the convergence test. Workstation specifications: 16Gb RAM, Intel Core™i7-6700 CPU @ 3.40GHz x 8.	69
4.8	Influence of the electron collisionality used on the simulation computational time.	72
5.1	Geometrical, operational, simulation and mesh parameters.	82
5.2	Thruster performances.	90
6.1	Comparison of mesh sizes and computational performance.	96
6.2	Injector geometrical parameters.	120
6.3	Thruster performances and energy usage distribution for different values of both momentum and heat flux anomalous transport coefficients.	128
7.1	List of alternative propellants and their main characteristics.	132
7.2	Thruster performances for different propellant species.	138
8.1	Geometric parameters for the 30 W and 200 W thrusters.	144
8.2	Operational parameters for the 30 W and 200 W thrusters.	145
8.3	Thruster performance results of the cases considered in the scale-up study.	146
9.1	Comparison of thruster performances measured experimentally with simulations for different anomalous diffusion coefficients.	165
A.1	Outline of cases studied in the parametric investigation shown in chapter 6, including operational parameters, electromagnetic performances, thruster performances and losses conspectus.	178

Glossary

List of Symbols

α	Axial gradient of the normalized magnetic field near the resonance.
α_t	Anomalous transport coefficient.
β	Angle of the propagation vector with respect to the magnetic field direction.
\mathbf{B}	Magnetic field vector.
\mathbf{D}	Electric displacement field vector.
\mathbf{E}	Electric field vector.
\mathbf{F}	Force density vector.
\mathbf{j}	Electric current density vector.
\mathbf{k}	Wave vector.
\mathbf{q}	Heat flux vector.
\mathbf{S}	Poynting flux vector.
\mathbf{u}	Fluid velocity vector.
\mathbf{v}	Particle velocity.
$\mathbf{1}$	Unit vector.
χ	Hall parameter.
χ'	Corrected Hall parameter.
χ_{eff}	Effective Hall parameter.
dS	Surface differential.
dV	Volume differential.
δ_w	Macroscopic SEE yield.
$\ell_{th,s}$	Thermal Larmor radius of species s .
ϵ	Energy fraction.
η	Efficiency when used with a subscript; when alone it refers to the dimensionless density parameter used in Chapter 3.
η_d	Divergence efficiency.
η_e	Energy efficiency.
η_F	Thrust efficiency.

η_{prod}	Production efficiency.
η_p	Coupling efficiency.
η_u	Utilization efficiency.
γ	Normalized collisionality in Chapter 3. In the context of Chapter 9 is utilized for the polytropic coefficient.
\Im	Imaginary part.
λ	Wavelength.
λ_i	Baricentric coordinate of i^{th} edge.
\mathbf{v}	Wave phase velocity vector.
\mathcal{D}	Element of the dielectric tensor in the local magnetic basis associated to the <i>difference</i> between \mathcal{R} and \mathcal{L} .
\mathcal{L}	Element of the dielectric tensor in the rotating basis associated to the propagation of transverse left-hand polarized waves in the direction of the magnetic field.
\mathcal{M}	Mesh batch.
\mathcal{O}	Referring to the ordinary electromagnetic mode; when followed by a magnitude between parenthesis, it represents “of order”.
\mathcal{P}	Element of the dielectric tensor associated to the longitudinal waves propagating in the magnetic field direction.
\mathcal{R}	Element of the dielectric tensor in the rotating basis associated to the propagation of transverse right-hand polarized waves in the direction of the magnetic field.
\mathcal{S}	Element of the dielectric tensor in the local magnetic basis associated to the <i>sum</i> of \mathcal{R} and \mathcal{L} .
\mathcal{X}	Referring to the extraordinary electromagnetic mode.
\mathfrak{F}	Generic function.
μ	Magnetic permeability.
ν	Collision frequency / collisionality.
Ω	3D simulation domain.
ω	Angular frequency; without subscript it refers to the excitation frequency.
Ω_s	Signed cyclotron frequency of species s .
ω_{cs}	Cyclotron frequency of species s .
ω_{ps}	Plasma frequency of species s .
$\partial\Omega$	Simulation boundaries of domain Ω .
$\partial\Omega_D$	Dirichlet boundaries of simulation domain Ω .
$\partial\Omega_N$	Neumann boundaries of simulation domain Ω .
Φ	Phase difference between the right-hand polarized wave electric field and the perpendicular electron velocity.
ϕ	Electrostatic potential.
π	Pi number.
ψ	Angle between the symmetry axis and the position vector of the probes, defined with origin at the intersection of the symmetry axis with the backplate axial position; see chapter 9.
\Re	Imaginary part.

$\bar{\rho}$	Electric charge density. In chapter 9 is the radial distance to the probes from the backplate.
Σ	2D simulation domain.
σ	Collisional cross-section.
τ	Time related variable.
$\bar{\chi}$	Susceptibility tensor.
$\bar{\kappa}$	Dielectric tensor.
$\bar{\sigma}$	Electric conductivity tensor.
\tilde{L}	Lagrange nodal function.
\tilde{N}	Nédélec vector function.
ε	Electric permittivity.
$\varphi()$	Phase of the complex amplitude.
ξ, ζ	Auxiliary variables for the change of variable used in the expression of the asymptotic solutions of the model shown in Chapter 3.
ζ	Arc-length coordinate covering the thruster walls meridian section in chapter 5.
A	Area. In chapter 7 it represents a neutral species.
A^*	In chapter 7 it represents an excited species.
c	Light velocity in vacuum.
e	Electric charge unit.
e^-	Electron representation.
E_i	Ion energy.
E_s	Crossover energy of the material.
$e_{()}$	L ² -norm error.
F	Thrust.
f	Wave frequency.
F_m	Magnetic thrust.
F_p	Pressure thrust.
F_s	Thrust contribution of species s .
f_s	Distribution function of species s .
G	Derivative of the electric field with respect to s in Chapter 3.
g_0	Standard acceleration of gravity.
g_s	Particle flux of species s .
h	Characteristic element length.
i	Imaginary number.
I_b	Ion beam current.
I_i	Integrated ion current.
I_{sp}	Specific impulse.
K	Kinetic energy.
k	Wavenumber.

L	Length or scale in the axial direction; without subscript it refers to the thruster length.
l	Length.
m	Azimuthal mode number.
m_s	Mass of each particle of species s .
M_s	Mach number of species s .
N_λ	Number of elements per minimum wavelength.
n_s	Particle density of species s .
p	Convergence rate.
P_a	Power absorbed or deposited in the plasma.
P_s	Total power of plasma species s leaving the domain through open boundaries.
p_s	Pressure of species s .
P_f	Input power forwarded to the thruster.
P_r	Reflected power.
Q_a	Electromagnetic power absorption density.
q_s	Electric charge of species s .
R	Thruster radius.
r, θ, z	3D cylindrical coordinates.
$R_{()}$	Volume rate.
s	Dimensionless axial coordinate used in Chapter 3.
S_{ion}	Ionization source rate.
T	Time period.
t	Time.
T_s	Temperature of species s .
t_c	Computational time.
U	Wave's group velocity.
V	Voltage.
V	Volume.
W	Trial function used in the finite element method.
$W_{a,b}$	Whittaker function with parameters a and b ; solution of Whittakers equation.
W_{ecr}	Electron energy gain per pass through an ECR region.
x, y, z	3D Cartesian coordinates.
Z	Impedance.
Z_s	Charge number of species s .
S1, S2, S3	Streamline identifiers utilized in chapter 9.

Subscripts

LH	Referring to the lower-hybrid resonance.
----	--

UH	Referring to the upper-hybrid resonance.
+	Referring to the left hand polarized direction.
-	Referring to the right hand polarized direction.
0	Referring to vacuum or to a reference value.
∞	Referring to the variables at the open boundary.
\parallel	Referring to the B-parallel component.
\perp	Referring to the B-perpendicular component.
\pm	Referring to the rotating basis.
θ	Referring to the azimuthal component
<i>coax</i>	Referring to the coaxial shell.
<i>coll</i>	Referring to collisional processes.
<i>ex</i>	Referring to excitation collisions.
<i>e</i>	Referring to the electron population.
<i>i1, i2</i>	Referring to singly-charged and doubly-charged ions.
<i>inj</i>	Referring to the injection of macroparticles in the domain.
<i>ion</i>	Referring to ionization collisions.
<i>I</i>	Referring to the imaginary part.
<i>i</i>	Referring to ion species or populations.
<i>mat</i>	Referring to material walls (excluding injector walls).
<i>max, min</i>	Referring to maximum and minimum values, respectively.
<i>n</i>	Referring to the neutral species or populations.
<i>p</i>	Referring to the plume.
<i>R</i>	Referring to the real part.
<i>r</i>	Referring to the inner rod.
<i>r</i>	Referring to the radial component
<i>s</i>	Referring to the s^{th} heavy species.
<i>t</i>	Referring to tangential field (i.e. contained in the meridional plane).
<i>use</i>	Referring to the useful power.
<i>w</i>	Referring to a material wall boundary.
<i>x</i>	Referring to the Cartesian <i>x</i> -component
<i>y</i>	Referring to the Cartesian <i>y</i> -component
<i>z</i>	Referring to the axial component.

Superscripts

*	Complex conjugate / conjugate transpose.
INC	Referring to the incident part.
REF	Referring to the reflected part.
TR	Referring to the transmitted part.

A	Antihermitian part of.
H	Hermitian part of.
I	Imaginary part of.
R	Real part of.

Accents

\bar{A}	Generic tensor A .
$\tilde{\mathfrak{F}}$	Space harmonic Fourier complex amplitude field of \mathfrak{F} .
$\hat{\mathfrak{F}}$	Time harmonic Fourier complex amplitude of field \mathfrak{F} .
$\tilde{\mathfrak{F}}$	Harmonic Fourier complex amplitude field of \mathfrak{F} as a result of a expansion in time and one coordinate, z for the planar problem and θ for axisymmetric geometries.

Acronyms

ATHAMES	Axisymmetric time harmonic Maxwell's equations solver.
BDD	Behavior-driven development.
BN	Boron nitride.
CMA	Clemmow-Mullaly-Allis.
ECRH	Electron cyclotron resonance heating.
ECRIS	Electron cyclotron resonance ion sources.
ECRT	Electron-cyclotron-resonance thruster
EM	Electromagnetic.
EP	Electric propulsion.
EP2	Equipo de Propulsión espacial y Plasmas.
EPT	Electrodeless plasma thrusters.
FD	Finite differences.
FDM	Finite difference method.
FE	Finite elements.
FEM	Finite element method.
GIT	Gridded ion thruster.
GLVIS	OpenGL finite element visualization tool.
GMRES	Generalized minimal residual method.
H2020	Horizon 2020.
HET	Hall effect thruster.
HPT	Helicon plasma thruster.
HYPHEN	Hybrid plasma thruster holistic simulation environment.
ICR	Ion cyclotron resonance.
ICRH	Ion cyclotron resonance heating.

LHP	Left-hand polarized.
LHR	Lower hybrid resonance.
LHS	Left hand side.
LLNL	Lawrence Livermore National Laboratory.
MFEM	Modular finite element methods.
MINOTOR	Magnetic nozzle thruster with electron cyclotron resonance.
MINRES	Minimal residual method.
MMS	Method of manufactured solutions.
NWC	Near-wall conductivity.
ONERA	Office National d'Etudes et de Recherches Aéropatiales.
PCG	Preconditioned conjugate gradient.
PEC	Perfect electric conductor.
PMC	Perfect magnetic conductor.
PSFC	Plasma Science Fusion Centre.
RF	Radiofrequency.
RHP	Right-hand polarized.
RHS	Right hand side.
S/C	Spacecraft.
SOL	Scrap-off layer.
THAMES	Time harmonic Maxwell's equations solver.
TRL	Technology readiness level.
UC3M	Universidad Carlos III de Madrid.
UHR	Upper hybrid resonance.
UMFPACK	Unsymmetric multifrontal methods package.
VASIMR	Variable specific impulse magnetoplasma rocket.
WKB	Wentzel-Kramers-Brillouin.

Chapter 1

Introduction

1.1 Background

The utilization of plasma discharges as propulsive systems for in-space missions is generally known as electric propulsion (EP). The advent of EP is driven by several factors, being the most relevant their associated reduced cost in the generation of an specific impulse (I_{sp}). Compared to conventional chemical propulsion systems, the specific impulse of EP systems is not limited by temperature of the gas discharge, neither by the propellant specific heat capacity, nor by the thruster walls melting temperature. EP systems employ electric power to ionize the propellant, and to energize the generated plasma in order to exhaust its constituents at high velocities into space [1–3]. The electrical power is only limited by the power available on-board of the spacecraft (S/C). Moreover, the heat fluxes to the walls can be reduced in many cases with respect to the chemical alternatives.

Although the use of EP systems is limited to non-impulsive in-space applications given their characteristic low thrust density, their efficient use of propellant decreases the cost of space missions considerably and makes them a clear-cut alternative to other propulsion systems. EP applications not only cover attitude control systems (ACS) to maintain adequate in-orbit S/C orientation, specially popular amongst commercial missions with the new dawn of nanosatellite constellations, but also the development of deep space exploration missions with higher total impulse increment requirements, which would be otherwise unattainable. Other EP advantages are their associated long-term operation capabilities and the flexibility they provide to space missions due to the throttleability of their propulsive systems.

The complexity and diversity of EP technologies employed to move satellites and S/C in space requires substantial investment and research efforts in order to achieve a high Technology Readiness Level (TRL). Amongst these, mature EP technologies ordered in increasing I_{sp} and decreasing thrust to weight ratio are the resisto-jet, the arc-jet, the Hall-effect thruster (HET) and the gridded ion thruster (GIT). The first two belong to the category of electro-thermal thrusters as they heat the propellant up with electric energy and utilize the same principle of chemical propulsion systems to convert the thermal energy into kinetic directed energy through the use of a conventional Lavar nozzle. The GIT is considered an electro-static propulsion system as the ions are accelerated by the use of an electrostatic field generated by two biased grids to different potentials. The HET belongs to the category of electro-magnetic propulsion systems since its operation is based on the interaction between an internal plasma current \mathbf{j} and a magnetic field \mathbf{B} .

The abovementioned mature technologies make use of electrodes either for sustaining the electric discharge or as means of plume charge neutralization. For instance, the HET makes use of an

external cathode to perform these two tasks, while the GIT always uses an external cathode to neutralize the discharge, and the discharge is sustained either by the use of an emissive cathode or by radiofrequency (RF) generation [4]. Electrodes suffer from enhanced erosion driven by the strong plasma-wall interaction and the considerable particle and energy fluxes they are subjected to. As a result, these are often lifetime-limiting components. Electrodeless plasma thrusters (EPTs) use electromagnetic (EM) heating to generate and energize the plasma, and thus allow eliminating exposed electrodes from their design. The plasma is then accelerated through the use of a magnetic nozzle (MN), that reduces plasma-wall interaction guiding the plasma expansion downstream and contributing to generating thrust. EPT technologies are the electron cyclotron resonance plasma thruster (ECRT)[5–12], the Helicon plasma thruster (HPT) [13–17] and the VASIMR [18]. The fundamental difference between these technologies is the type of electromagnetic power absorption utilized by the concept. The HPT utilizes non-resonant heating to increase the electron temperature of the plasma discharge. The VASIMR, with a further complex design, adds to a helicon heating stage a second rocket stage where ion cyclotron resonance heating is employed to increase the ion energy with main objective of achieving higher thruster specific impulse. The ECRT utilizes an electron cyclotron resonance (ECR) region to heat the plasma. In this region, the right-hand polarized (RHP) electromagnetic fields resonate with the electron motion, increasing the kinetic energy of their cyclotron motion. The resulting electron distribution function (EDF) is highly anisotropic, featuring high perpendicular electron temperatures.

Electron cyclotron resonance has been successfully used to generate and heat up plasmas since the 1960's. In 1960, the energization of a magnetoplasma with microwave power by electron cyclotron resonance heating (ECRH) was first observed experimentally in the Oak Ridge energetic-ion trapping program. Afterwards, theoretical and experimental efforts were made to obtain a consistent unified theory of ECR phenomena. Amongst the main applications of ECR phenomenology, noteworthy are ECR emission and absorption for fusion plasmas[19] and the design of ECR ion sources (ECRIS)[20]. ECRIS have been found to be a useful technology for various applications such as atomic physics and plasma etching[21]. The combination of an ECR source with a magnetic nozzle (MN) has also been proposed as a plasma thruster for space propulsion[9, 22–26]. In this concept, microwaves of a few GHz are used to generate and energize a plasma that then expands in a divergent magnetic field to generate thrust contactlessly.

As could be expected, the plasma-wave interaction problem is central to ECR thrusters and any other ECR applications. The complexity of this problem is high, as it results from the interplay of multiple simultaneous phenomena, including wave propagation, absorption, cutoffs, reflections, resonances and mode conversions[27–30]. All these mechanisms depend on the plasma and magnetic parameters, in particular the plasma density and collisionality, the magnetic field strength and direction, and the geometry and boundary conditions of the domain. Moreover, to a large extent, especially near resonances, propagation and absorption are affected by plasma temperature, kinetic features, inhomogeneities, and bulk plasma velocity. Lastly, while the abovementioned phenomena are linear, non-linear interactions also exist in the case of high-amplitude waves. In order for an ECR source to operate successfully and heat the plasma, the wave must be able to propagate through the plasma and reach the resonance regions where it is absorbed without being reflected, a problem known as accessibility[31].

Substantial effort has been dedicated to understand and model the mechanisms that govern the propagation and absorption of electromagnetic waves in a plasma near the ECR [32–36]. On the one hand, ray and beam tracing algorithms [37–39] have been successfully employed to analyze the propagation and accessibility problems. These methods rely either on a cold plasma or on a kinetic dielectric tensor description, and are suitable for regions where the WKB condition is satisfied, i.e., wherever the wavelength is much smaller than the characteristic gradient lengths in the plasma or magnetic field. This, unfortunately, excludes the neighborhood of resonances and cutoffs. Given their small size, often comparable to the wavelength, ray and beam tracing schemes are not the best approach to model ECR thrusters. On the other hand, full-wave models solve Maxwell's equations simultaneously for all propagating modes in all propagating directions in the simulation domain, either in the time[40, 41] or frequency domain[42–45], and either in 1D,

2D or 3D geometries. The majority of full-wave numerical models can be broadly classified into finite difference, finite volumes, and finite element methods. By large and far, since the advent of computers, the most extended and successful of these techniques for electromagnetic problems have been finite differences[46] (FD) and finite elements[47, 48] (FE):

1. In FD, the differential operators of the wave equations are discretized on a structured grid. These methods are typically simple to analyze and easy to set up and implement. The main drawbacks of FD stem from their reliance on a structured grid: it is difficult to deform the mesh to accommodate complex geometries, or to refine the resolution in a particular region.
2. On the other hand, FE are based on expressing the solution in a vector basis of a given function space. A weak formulation of the problem is used to find the best linear combination of the functions of this basis to represent the solution according to some criterion. The domain is decomposed into cells—elements—of arbitrary size and shape, and the basis functions are selected such that they have a compact support, with non-zero values only in a small number of these elements. FE methods do not rely on a structured grid and thus they can easily deal with complex geometries or regions with different resolutions. As a downside, the formulation and implementation of these methods is more complex than FD, and accuracy assessment is less straightforward.

In spite of these experimental and modeling efforts and the plethora of existing techniques, the understanding of the plasma-wave problem in ECR thrusters is still far from complete, and at present, a predictive model that can explain power deposition and be used to optimize the thruster design is still lacking.

In 2016, the 2020 Horizon project MINOTOR[49], prepared in joint efforts with other research groups and companies and led by ONERA-DPHY FPA's unit, was funded by the European commission (EC). The main goal of the project was to demonstrate the feasibility of a novel ECRT technology based on a coaxial waveguide design [11, 12, 26, 50–53] as a disruptive game-changer in EP, with an in-depth numerical and experimental investigation plan to bring the technology from TRL3 to TRL5.

In the context of this project, this Thesis focuses on the theoretical modeling efforts required to develop a complete coupled plasma transport and electromagnetic simulation code of the real prototypes and to assist in its development and optimization. Previous models available [54] for electromagnetic simulation resulted inapt and insufficient for the modeling required for this application, specifically to the case of resonant absorption plasmas using ECR. Thus, it was required to develop a novel electromagnetic wave simulation code for low temperature ECR plasmas. The transport modeling would be carried out applying HYPHEN simulation platform to the ECRT, and the development of an infrastructure to obtain coupled simulations of both the transport and electromagnetic problems.

1.2 Objectives

The main objectives of the thesis are:

1. The main goal of the Thesis is the development and implementation of a complete two-dimensional axisymmetric code that simulates the plasma production, its transport and acceleration in electron cyclotron resonance thrusters.
2. Among this development, the biggest contribution of the Thesis is to model the propagation and absorption of electromagnetic waves in magnetized inhomogeneous plasmas, capable of reproducing the ECR absorption, hybrid resonances and the different propagation cutoffs.
3. The third objective is based on simulating the ECRT-MINOTOR prototype and assisting the improvement and optimization of the prototype design based on the understanding of the thruster operation.

4. Additionally, in order to comprehend the operational principles of the thruster and its major inefficiencies, several parametric studies on both thruster operation and design are carried out.
5. A secondary goal of the Thesis is to analyze the performances and operation of the thruster with different propellants.
6. Furthermore, using the model, simple scaling laws of the thruster are obtained based on simulations using different powers and thruster size.

1.3 Thesis structure

The rest of the thesis is structured as follows:

- Chapter 2 details the fundamental concepts of electromagnetic wave in cold magnetized plasmas, highlighting the principal wave modes, cutoffs and resonances that serve as a theoretical baseline for the rest of the thesis.
- Chapter 3 revisits the one dimensional right-hand polarized wave propagation and absorption model of Williamson [34] and the asymptotic solutions obtained by Budden [55] for the collisionless limit. The model is analyzed in detailed exploring its main parameters. Additionally, the solutions obtained are applied to solve for the electron response in a ECR crossing event and the energy gain per electron crossing is computed. Energy gains obtained are compared Liebermann's approximation [30]. Part of the contents of this chapter are based on a conference paper [56].
- Chapter 4 describes ATHAMES code, which uses a full-wave model to solve for the electromagnetic waves in magnetized plasma featuring multiple cutoffs and resonances. Predictive mesh refinement used by the model is explained and shown to apply local mesh refinement based on the local resolution requirements given by the propagating modes dispersion relations. Both a preliminary planar version and the axisymmetric two dimensional code are explained and its verification is shown. Part of the contents of this chapter have been published in a peer-reviewed journal publication [57] and two conference papers [58, 59].
- Chapter 5 shows the contents published in the peer-reviewed journal Plasma Sources Science and Technology [57]. A reference ECRT prototype is simulated with coupled simulations of ATHAMES with HYPHEN [60], obtaining results of the two dimensional plasma transport and electromagnetic wave properties and derived thruster performance figures. Comparison of the results with existing experimental data showed fair agreement on estimated macroscopic variables as well as thruster performance figures.
- Chapter 6 details a parametric investigation on the operational point and design of the ECRT analyzed in chapter 5 for a single operating point. The chapter demonstrates the capabilities of the coupled simulations to characterize the operation of ECRTs at different operating points showing both consistency and robustness of the results obtained in the reference case. Modifications on the design as the displacement of the resonance location and the injector orientation, and their associated impact on plasma transport and electromagnetic properties are thoroughly analyzed, highlighting some recommended thruster design choices. A sensitivity analysis to anomalous transport coefficient is also detailed. Part of the contents of this chapter are based on a conference paper [61], and are being prepared for submission to the peer reviewed journal Plasma Sources Science and Technology [62].
- Chapter 7 applies the capabilities of HYPHEN to test the influence of different alternative propellants, providing a detailed comparison of the thruster performance and plasma transport and electromagnetic properties obtained.

-
- Chapter 8 analyzes the effects of scaling up the ECRT geometry, comparing a high power (200 W) ECRT prototype with the ECR30 utilized in chapters 5, 6 and 7. The 200 W ECRT is proven to outperform the low power version, while maintaining multiple features characteristic of the low power version.
 - Chapter 9 shows the results of both a numerical and experimental campaigns carried out on the ECRT in collaboration with ONERA research group, to test the capabilities of the code and highlight its main limitations. In the investigation, the effect of anomalous transport coefficient on the solutions is analyzed and the code is shown to be capable of reproducing partially the plasma properties in the plume. The contents of this chapter are based on a publication being prepared in collaboration with ONERA to be published in a peer-reviewed journal [63].
 - Chapter 10 gathers the principal conclusions of the thesis and provides a list of key future directives to continue this research.
 - Appendix A gathers the principal simulation results for the parametric investigation shown in chapter 6.

Chapter 2

Electromagnetic waves in cold plasmas

The purpose of this chapter is to introduce the fundamental concepts of electromagnetic propagation and absorption in arbitrary plasmas, revisited in [27, 64, 65]. The formulation shown here uses the International System of Units. Starting with Maxwell's equations we define the concepts of susceptibility and dielectric tensor, thus reaching the wave equation in plasmas assuming all plasma species can be treated as a fluid with negligible temperature and featuring an effective collisionality with other species. Additionally, the dispersion relation and the principal electromagnetic waves resulting from the plasma response to electromagnetic excitation in a magnetized uniform plasma is explained, introducing the concepts of cutoff and resonance. The CMA diagram is utilized to comprehend a complete picture of the different waves appearing the plasma in parametric space. Other concepts as wave polarization, Poynting's theorem and the definition and appearance of an electromagnetic power absorption in cold plasmas are reviewed.

2.1 Maxwell's Equations

The propagation of electromagnetic waves is governed by Maxwell's equations, i.e.

$$\nabla \times \mathbf{E} = -\frac{\partial \mathbf{B}}{\partial t}, \quad (2.1-1)$$

$$\nabla \cdot \mathbf{E} = \frac{\rho + \rho_a}{\epsilon_0}, \quad (2.1-2)$$

$$\nabla \times \mathbf{B} = \mu_0 \epsilon_0 \frac{\partial \mathbf{E}}{\partial t} + \mu_0 (\mathbf{j} + \mathbf{j}_a), \quad (2.1-3)$$

$$\nabla \cdot \mathbf{B} = 0, \quad (2.1-4)$$

being \mathbf{j} and ρ the plasma electric current and charge densities that result from the sum of the contributions of all charged species, and \mathbf{j}_a and ρ_a the electric current and charge densities that act as generic source terms modeling the electromagnetic excitation of antennas, radiating elements, etc. present in the domain.

Equations (2.1-1)-(2.1-4) must be solved together with the kinetic equations of each plasma species to close the model. The general problem is nonlinear, and the plasma current and charge \mathbf{j}, ρ depend on the electromagnetic fields and the distribution function of each plasma species in the past light cone [27, 66]. Several approximations of varying level of sophistication are used to reduce the complexity of the approach. Starting of with the standard kinetic tensor description of the plasma, the kinetic equations are linearized and the plasmas is assumed *infinite* and *uniform*. A Fourier/Laplace analysis in time and space allows expressing the plasma contributions \mathbf{j}, ρ through

a dielectric tensor form $\boldsymbol{\kappa}$, which is a function of the applied frequency ω and the wave vector \mathbf{k} [27]. Plasma inhomogeneities and boundaries limit the validity of this solution [67].

2.2 The cold plasma approximation

A further approximation, which ends up with the model used in this thesis, is treating the plasma as cold. The cold plasma approximation assumes thermal kinetic energy of each plasma species is negligible and that each species macroscopic velocity is negligible. As a result, the \mathbf{j}, ρ can be defined as *local*, so the tensor $\bar{\bar{\kappa}}$ is no longer a function of the wavenumber. Specifically, the cold plasma approximation is sufficient [68] given that

$$\frac{\ell_{th,s}^2}{\lambda_{\perp}^2} \ll 1, \quad (2.2-1)$$

$$\left| \frac{\omega - N\omega_{cs}}{k_{\parallel}v_{th,s}} \right|^2 \gg 1, \quad (2.2-2)$$

where $\ell_{th,s} = v_{th,s}/\omega_{cs}$ is the thermal Larmor radius being $v_{th,s}$ and ω_{cs} the thermal velocity and cyclotron frequency of plasma species s , λ_{\perp} is the perpendicular (w.r.t. the magnetic field) wavelength, N is the cyclotron harmonic number and k_{\parallel} is the parallel wavenumber. Condition (2.2-1) states that the perpendicular thermal spatial dispersion is negligible. Condition (2.2-2) states that for $N = 0$ the thermal velocity of particles must be smaller than the parallel wave phase velocity $|\mathbf{v}_{\parallel}| = \omega/k_{\parallel}$. For $N \geq 1$, it states that this approximation cannot reproduce the resonance phenomena between particles and electromagnetic waves close to the different cyclotron harmonics.

2.3 Susceptibility and the cold plasma dielectric tensor

The plasma electric current and charge densities are to be included in Eqs.(2.1-1)-(2.1-4). Heald et al. [64] models the plasma current as a conductive current. An equivalent approach is defined by Stix [27], where \mathbf{j} is included as a displacement current in a dielectric medium. Thus, in absence of applied excitation currents Eq. (2.1-3) can be written as

$$\nabla \times \mathbf{B} = \mu_0 \left(\varepsilon_0 \frac{\partial \mathbf{E}}{\partial t} + \mathbf{j} \right) = \mu_0 \frac{\partial \mathbf{D}}{\partial t}. \quad (2.3-1)$$

Let us assume that the background magnetic field \mathbf{B}_0 and plasma density n_0 are steady and uniform in space and that electromagnetic response induces first-order quantities for any component of \mathbf{E} , \mathbf{B} , or scalar quantities as the perturbed plasma density n_1 , etc. that evolve as the harmonic plane wave solutions as

$$\tilde{\mathfrak{F}} = \Re \left\{ \tilde{\mathfrak{F}} e^{i(\mathbf{k} \cdot \mathbf{r} - \omega t)} \right\}. \quad (2.3-2)$$

In Eq. 2.3-2 symbol \Re represents “the real part of”, $\tilde{\mathfrak{F}}$ denotes the complex amplitude of variable \mathfrak{F} and \mathbf{k} is the wave propagation vector, whose direction defines the propagation of the wave and its magnitude the wavenumber. The sign convention for the exponential implies that the propagation for positive ω takes place in the \mathbf{k} direction as $t > 0$.

From equation (2.3-1) one may find that

$$\bar{\mathbf{D}}(\omega, \mathbf{k}) = \varepsilon_0 \bar{\bar{\kappa}}(\omega, \mathbf{k}) \cdot \bar{\mathbf{E}} = \varepsilon_0 \bar{\mathbf{E}}(\omega, \mathbf{k}) + \frac{i}{\omega} \bar{\mathbf{j}}(\omega, \mathbf{k}), \quad (2.3-3)$$

where

$$\bar{\bar{\kappa}}(\omega, \mathbf{k}) = \bar{\bar{1}} + \sum_s \bar{\bar{\chi}}_s(\omega, \mathbf{k}). \quad (2.3-4)$$

is the dimensionless dielectric tensor, being $\bar{\chi}_s$ the susceptibility tensor of each plasma species s . The dielectric tensor description allows to describe *homogeneous* plasmas composed of multiple species by addition of their different susceptibility contributions.

The plasma current is defined by the macroscopic velocities $\bar{\mathbf{u}}_s$ of each species s

$$\bar{\mathbf{j}} = \sum_s \bar{\mathbf{j}}_s = \sum_s q_s n_s \bar{\mathbf{u}}_s, \quad (2.3-5)$$

where q_s and n_s are their respective signed charge and density. The contribution to plasma current by the susceptibility is

$$\bar{\mathbf{j}}_s = \bar{\sigma}_s \cdot \bar{\mathbf{E}} = -i\omega\epsilon_0\bar{\chi}_s \cdot \bar{\mathbf{E}}, \quad (2.3-6)$$

being $\bar{\sigma}_s(\omega, \mathbf{k})$ the s plasma species contribution to the conductivity tensor $\bar{\sigma}(\omega, \mathbf{k})$. Using definition (2.3-6), the dielectric tensor can also be expressed in terms of the conductivity as

$$\bar{\kappa}(\omega, \mathbf{k}) = \bar{\mathbf{1}} + \frac{i}{\omega\epsilon_0} \sum_s \bar{\sigma}_s(\omega, \mathbf{k}). \quad (2.3-7)$$

2.3.1 Cold plasma dielectric tensor including collisions

Eqs. (2.3-3) and (2.3-5) show that the dielectric tensor relates the plasma currents with the electromagnetic fields, specifically the electric field. In order to find this correlation, let us study the equation of motion for particle s in a cold plasma limit.

The momentum conservation equation for species s with mass m_s , signed charge q_s , and velocity \mathbf{u}_s , including its effective collision or damping frequency ν_s , is

$$m_s \frac{d\mathbf{u}_s}{dt} = q_s (\mathbf{E} + \mathbf{u}_s \times \mathbf{B}_0) - m_s \nu_s \mathbf{u}_s. \quad (2.3-8)$$

Application Fourier analysis in time to Eq.(2.3-8) and projecting in Cartesian basis $\{\mathbf{1}_x, \mathbf{1}_y, \mathbf{1}_z\}$ assuming a purely axial applied magnetic field $\mathbf{B}_0 = B_0 \mathbf{1}_z$, the system results in

$$-i(\omega + i\nu_s) \hat{u}_x = \frac{q_s}{m_s} \hat{E}_x + \Omega_s \hat{u}_y, \quad (2.3-9)$$

$$-i(\omega + i\nu_s) \hat{u}_y = \frac{q_s}{m_s} \hat{E}_y - \Omega_s \hat{u}_x, \quad (2.3-10)$$

$$-i(\omega + i\nu_s) \hat{u}_z = \frac{q_s}{m_s} \hat{E}_z, \quad (2.3-11)$$

where

$$\Omega_s = \omega_{cs} = \frac{q_s B_0}{m_s}, \quad (2.3-12)$$

is the signed gyrofrequency of species s , which changes sign with q_s . In Eqs. (2.3-9) -(2.3-11) the temporal evolution in the exponential is canceled out while the Fourier complex amplitude components $\hat{\mathfrak{F}}_j$ of the fields and oscillating variables defined as

$$\mathfrak{F}_j = \Re \left\{ \hat{\mathfrak{F}}_j e^{-i\omega t} \right\}, \quad (2.3-13)$$

has been maintained.

Note that equations (2.3–9)–(2.3–10) are coupled, contrary to Eq. (2.3–10). The macroscopic velocity components resulting from electromagnetic excitation are then

$$\hat{u}_x = \frac{q_s}{m_s} \frac{i(\omega + i\nu_s)\hat{E}_x - \Omega_s\hat{E}_y}{(\omega + i\nu_s)^2 - \Omega_s^2}, \quad (2.3-14)$$

$$\hat{u}_y = \frac{q_s}{m_s} \frac{\Omega_s\hat{E}_x + i(\omega + i\nu_s)\hat{E}_y}{(\omega + i\nu_s)^2 - \Omega_s^2}, \quad (2.3-15)$$

$$\hat{u}_z = i \frac{q_s}{m_s} \frac{\hat{E}_z}{(\omega + i\nu_s)}, \quad (2.3-16)$$

where the motion in the z direction is independent of the magnetic field.

Using (2.3–5) the resulting plasma current is

$$\hat{\mathbf{j}} = \sum_s q_s n_s \begin{pmatrix} \frac{iq_s}{m_s} \frac{(\omega + i\nu_s)}{(\omega + i\nu_s)^2 - \Omega_s^2} & -\frac{q_s}{m_s} \frac{\Omega_s}{(\omega + i\nu_s)^2 - \Omega_s^2} & 0 \\ \frac{q_s}{m_s} \frac{\Omega_s}{(\omega + i\nu_s)^2 - \Omega_s^2} & \frac{iq_s}{m_s} \frac{(\omega + i\nu_s)}{(\omega + i\nu_s)^2 - \Omega_s^2} & 0 \\ 0 & 0 & i \frac{q_s}{m_s} \frac{1}{(\omega + i\nu_s)m_s} \end{pmatrix} \cdot \begin{pmatrix} \hat{E}_x \\ \hat{E}_y \\ \hat{E}_z \end{pmatrix}. \quad (2.3-17)$$

Applying the definition given in Eq. (2.3–7) provides the $\bar{\kappa}$, usually expressed as in Ref. [27, 30]

$$\bar{\kappa} = \begin{pmatrix} \kappa_{\perp} & -i\kappa_{\times} & 0 \\ i\kappa_{\times} & \kappa_{\perp} & 0 \\ 0 & 0 & \kappa_{\parallel} \end{pmatrix}, \quad (2.3-18)$$

where

$$\kappa_{\perp} = 1 - \frac{\omega + i\nu_s}{\omega} \sum_s \frac{\omega_{ps}^2}{(\omega + i\nu_s)^2 - \Omega_s^2}, \quad (2.3-19)$$

$$\kappa_{\times} = \sum_s \frac{\Omega_s}{\omega} \frac{\omega_{ps}^2}{(\omega + i\nu_s)^2 - \Omega_s^2}, \quad (2.3-20)$$

$$\kappa_{\parallel} = 1 - \sum_s \frac{\omega_{ps}^2}{\omega(\omega + i\nu_s)}, \quad (2.3-21)$$

being ω_{ps} the *plasma frequency* of species s , defined as

$$\omega_{ps}^2 = \frac{q_s^2 n_s}{m_s \epsilon_0}. \quad (2.3-22)$$

2.3.1.1 Cold-plasma collisionless dielectric tensor

When no damping is included (i.e. $\nu_s = 0$) the classical cold plasma dielectric tensor is obtained. For that case, the velocity, current, and dielectric tensor are:

$$\hat{v}_x = \frac{q_s}{m_s} \frac{i\omega\hat{E}_x - \Omega_s\hat{E}_y}{\omega^2 - \Omega_s^2}, \quad (2.3-23)$$

$$\hat{v}_y = \frac{q_s}{m_s} \frac{\Omega_s\hat{E}_x + i\omega\hat{E}_y}{\omega^2 - \Omega_s^2}, \quad (2.3-24)$$

$$\hat{v}_z = i \frac{q_s}{m_s} \frac{\hat{E}_z}{\omega}, \quad (2.3-25)$$

$$\hat{\mathbf{j}} = \begin{pmatrix} \hat{j}_x \\ \hat{j}_y \\ \hat{j}_z \end{pmatrix} = \sum_s q_s n_s \begin{pmatrix} \frac{iq_s}{m_s} \frac{\omega}{(\omega^2 - \Omega_s^2)} & -\frac{q_s}{m_s} \frac{\Omega_s}{(\omega^2 - \Omega_s^2)} & 0 \\ \frac{q_s}{m_s} \frac{\Omega_s}{(\omega^2 - \Omega_s^2)} & \frac{iq_s}{m_s} \frac{\omega}{(\omega^2 - \Omega_s^2)} & 0 \\ 0 & 0 & \frac{iq_s}{\omega m_s} \end{pmatrix} \begin{pmatrix} \hat{E}_x \\ \hat{E}_y \\ \hat{E}_z \end{pmatrix}, \quad (2.3-26)$$

$$\bar{\bar{\kappa}} = \begin{pmatrix} \kappa_{\perp} & -i\kappa_{\times} & 0 \\ i\kappa_{\times} & \kappa_{\perp} & 0 \\ 0 & 0 & \kappa_{\parallel} \end{pmatrix} = \begin{pmatrix} 1 - \sum_s \frac{\omega_{ps}^2}{(\omega^2 - \Omega_s^2)} & -i \sum_s \frac{\Omega_s}{\omega} \frac{\omega_{ps}^2}{(\omega^2 - \Omega_s^2)} & 0 \\ i \sum_s \frac{\Omega_s}{\omega} \frac{\omega_{ps}^2}{(\omega^2 - \Omega_s^2)} & 1 - \sum_s \frac{\omega_{ps}^2}{(\omega^2 - \Omega_s^2)} & 0 \\ 0 & 0 & 1 - \sum_s \frac{\omega_{ps}^2}{\omega^2} \end{pmatrix}. \quad (2.3-27)$$

2.3.2 Diagonalization of the dielectric tensor

The dielectric tensor defined by Eqs.(2.3-18)-(2.3-21) is generally given with the following notation

$$\bar{\bar{\kappa}} = \begin{pmatrix} \mathcal{S} & -i\mathcal{D} & 0 \\ i\mathcal{D} & \mathcal{S} & 0 \\ 0 & 0 & \mathcal{P} \end{pmatrix}. \quad (2.3-28)$$

In this section, a derivation of this notation and the physical meaning of \mathcal{S} , \mathcal{D} and \mathcal{P} is provided.

According to matrix diagonalization theory, a square matrix $\bar{\bar{A}}$ can be converted into a diagonal matrix $\bar{\bar{D}}$ that shares the fundamental properties of $\bar{\bar{A}}$.

For $\bar{\bar{A}} \in \mathbb{C}^{n \times n}$ to be diagonalizable, $\exists \bar{\bar{T}}$ s.t:

$$\bar{\bar{D}} = \bar{\bar{T}}^{-1} \bar{\bar{A}} \bar{\bar{T}}, \quad (2.3-29)$$

where

- $\bar{\bar{D}} = \text{diag} \{ \sigma_1, \sigma_2, \dots, \sigma_n \}, \sigma_i \in |\bar{\bar{A}} - \sigma_i \bar{\bar{1}}| = 0$.
- $\bar{\bar{T}} = [\mathbf{v}_1, \mathbf{v}_2, \dots, \mathbf{v}_n], (\bar{\bar{A}} - \sigma_i \bar{\bar{1}}) \cdot \mathbf{v}_i = \mathbf{0}, \mathbf{v}_i \in \mathbb{C}$.

In other words, there exists a basis in which the $\bar{\bar{A}}$ is found to be diagonal. The generalized dielectric tensor given in Eq.(2.3-18) is found to be diagonalizable and therefore to have solutions for the eigenvalue problem

$$|\bar{\bar{\kappa}} - \sigma \bar{\bar{1}}| = 0; \quad (\bar{\bar{\kappa}} - \sigma \bar{\bar{1}}) \cdot \mathbf{v}_i = \mathbf{0}, \quad (2.3-30)$$

being the eigenvalues σ_i and eigenvectors \mathbf{v}_i

1. $\sigma_+ = \kappa_{\perp} - \kappa_{\times} = \mathcal{L}, \quad \mathbf{1}_+ = [1, -i, 0]$.
2. $\sigma_- = \kappa_{\perp} + \kappa_{\times} = \mathcal{R}, \quad \mathbf{1}_- = [1, i, 0]$.
3. $\sigma_{\parallel} = \kappa_{\parallel} = \mathcal{P}, \quad \mathbf{1}_{\parallel} = [0, 0, 1]$.

where

$$\mathcal{L} \equiv 1 + \sum_s \chi_s^+ = 1 - \sum_s \frac{\omega_{ps}^2}{\omega(\omega + i\nu_s - \Omega_s)}, \quad (2.3-31)$$

$$\mathcal{R} \equiv 1 + \sum_s \chi_s^- = 1 - \sum_s \frac{\omega_{ps}^2}{\omega(\omega + i\nu_s + \Omega_s)}, \quad (2.3-32)$$

$$\mathcal{P} \equiv 1 - \sum_s \frac{\omega_{ps}^2}{\omega(\omega + i\nu_s)}. \quad (2.3-33)$$

where \mathcal{L} , \mathcal{R} , and \mathcal{P} , stand for “left-hand”, “right-hand”, and “parallel”, which as it is shown in §2.5, are referring to propagation wave modes in a cold plasma. Thus, dielectric tensor formulation given in (2.3–18) is preferred by most literature [27, 65], defining

$$\mathcal{S} = \frac{1}{2}(\mathcal{R} + \mathcal{L}) \equiv \kappa_{\perp}, \quad (2.3-34)$$

$$\mathcal{D} = \frac{1}{2}(\mathcal{R} - \mathcal{L}) \equiv \kappa_{\times}, \quad (2.3-35)$$

where S & D stand for “sum” and “difference”.

Therefore, either in the collisionless or collisional limits, the cold plasma dielectric tensor can be expressed in diagonal form as

$$\bar{\kappa}_{\pm} = \begin{pmatrix} \mathcal{L} & 0 & 0 \\ 0 & \mathcal{R} & 0 \\ 0 & 0 & \mathcal{P} \end{pmatrix}. \quad (2.3-36)$$

in the so-called *rotating* basis [64] $\{\mathbf{1}_+, \mathbf{1}_-, \mathbf{1}_{\parallel}\}$ that forms the transformation matrix allowing to correlate components between both basis as

$$\begin{pmatrix} \hat{v}_x \\ \hat{v}_y \\ \hat{v}_z \end{pmatrix} = \underbrace{\begin{pmatrix} 1 & 1 & 0 \\ -i & i & 0 \\ 0 & 0 & 1 \end{pmatrix}}_{\bar{T}} \begin{pmatrix} \hat{v}_+ \\ \hat{v}_- \\ \hat{v}_z \end{pmatrix}, \quad \text{and} \quad \begin{pmatrix} \hat{v}_+ \\ \hat{v}_- \\ \hat{v}_z \end{pmatrix} = \underbrace{\begin{pmatrix} \frac{1}{2} & \frac{i}{2} & 0 \\ \frac{1}{2} & -\frac{i}{2} & 0 \\ 0 & 0 & 1 \end{pmatrix}}_{\bar{T}^{-1}} \begin{pmatrix} \hat{v}_x \\ \hat{v}_y \\ \hat{v}_z \end{pmatrix}, \quad (2.3-37)$$

or

$$\hat{E}_{\pm} = \frac{1}{2}(\hat{E}_x \pm i\hat{E}_y), \quad \hat{v}_{\pm} = \frac{1}{2}(\hat{v}_x \pm i\hat{v}_y). \quad (2.3-38)$$

2.3.3 Hermitian and antihermitian parts of the dielectric tensor

In the collisionless case (i.e. $\nu_s = 0$), the cold plasma dielectric tensor is Hermitian, i.e. equal to its conjugate transpose, so that $\bar{\kappa} = \bar{\kappa}^H$ where

$$\bar{\kappa}^H = \bar{\kappa}^*, \quad (2.3-39)$$

where operator $*$ stands for the complex conjugate transpose. According to the *spectral theorem* any Hermitian matrix can be diagonalized and its eigenvalues are *purely real*, which it is the case for \mathcal{L} , \mathcal{R} , and \mathcal{P} with $\nu_s = 0$.

Inclusion of collisions leads to the appearance of an antihermitian part of the dielectric tensor such that

$$\bar{\kappa} = \bar{\kappa}^H + \bar{\kappa}^A, \quad (2.3-40)$$

where

$$\bar{\kappa}^H = \frac{1}{2}(\bar{\kappa} + \bar{\kappa}^\dagger) = \begin{pmatrix} \Re\{\mathcal{S}\} & -i\Re\{\mathcal{D}\} & 0 \\ i\Re\{\mathcal{D}\} & \Re\{\mathcal{S}\} & 0 \\ 0 & 0 & \Re\{\mathcal{P}\} \end{pmatrix}, \quad (2.3-41)$$

and

$$\bar{\kappa}^A = \frac{1}{2}(\bar{\kappa} - \bar{\kappa}^\dagger) = i \begin{pmatrix} \Im\{\mathcal{S}\} & -i\Im\{\mathcal{D}\} & 0 \\ i\Im\{\mathcal{D}\} & \Im\{\mathcal{S}\} & 0 \\ 0 & 0 & \Im\{\mathcal{P}\} \end{pmatrix}. \quad (2.3-42)$$

As could be expected, in the rotating basis, these matrices are

$$\bar{\kappa}_{\pm}^H = \begin{pmatrix} \Re\{\mathcal{L}\} & 0 & 0 \\ 0 & \Re\{\mathcal{R}\} & 0 \\ 0 & 0 & \Re\{\mathcal{P}\} \end{pmatrix}, \quad (2.3-43)$$

and

$$\bar{\kappa}_{\pm}^A = i \begin{pmatrix} \Im\{\mathcal{L}\} & 0 & 0 \\ 0 & \Im\{\mathcal{R}\} & 0 \\ 0 & 0 & \Im\{\mathcal{P}\} \end{pmatrix}. \quad (2.3-44)$$

where the eigenvalues are purely real for $\bar{\kappa}^H$ and purely imaginary for $\bar{\kappa}^A$. Thus, for a dielectric tensor with collisions, the eigenvalues given in Eqs. (2.3-31):(2.3-33) are complex, and their real and imaginary parts correspond to the eigenvalues of $\bar{\kappa}^H$ and $\bar{\kappa}^A$, respectively. The real or complex character of the eigenvalues have a key implication in the propagation of waves. The imaginary part acts as wave *damping*.

2.4 The wave equation

Including the definition of the dielectric tensor in equations (2.1-3)-(2.1-4), and expressing the equations in frequency domain results in

$$\nabla \times \hat{\mathbf{E}} = i\omega \hat{\mathbf{B}}, \quad (2.4-1)$$

$$\nabla \cdot (\varepsilon_0 \bar{\kappa} \cdot \hat{\mathbf{E}}) = \hat{\rho}_a, \quad (2.4-2)$$

$$\nabla \times \hat{\mathbf{B}} = -i\omega\mu_0\varepsilon_0 \bar{\kappa} \cdot \hat{\mathbf{E}} + \mu_0 \hat{\mathbf{J}}_a, \quad (2.4-3)$$

$$\nabla \cdot \hat{\mathbf{B}} = 0. \quad (2.4-4)$$

Taking the curl of Eqs. (2.4-1) and combining with Eq. (2.4-3), the so-called *inhomogeneous Maxwell's wave equation* is found, i.e.

$$\nabla \times \nabla \times \hat{\mathbf{E}} - \frac{\omega^2}{c^2} \bar{\kappa} \cdot \hat{\mathbf{E}} = i\omega\mu_0 \hat{\mathbf{J}}_a, \quad (2.4-5)$$

where inhomogeneous stands for the presence of excitation source term $\hat{\mathbf{J}}_a$, and $c = \frac{1}{\sqrt{\mu_0\varepsilon_0}}$ is the propagation speed of electromagnetic waves in free space (i.e. vacuum).

Let us project the homogeneous form of Eq. (2.4-5) (i.e. $\hat{\mathbf{J}}_a = \mathbf{0}$) in basis $\{\mathbf{1}_+, \mathbf{1}_-, \mathbf{1}_z\}$. For that, the left hand side of Eq. (2.4-5) can be expressed as

$$\nabla \times \nabla \times \hat{\mathbf{E}} = \nabla (\nabla \cdot \hat{\mathbf{E}}) - \nabla^2 \hat{\mathbf{E}}. \quad (2.4-6)$$

For the purely axial case in Cartesian coordinates, $\partial/\partial x = \partial/\partial y = 0$, so that Eq. (2.4-6) is

$$\nabla (\nabla \cdot \hat{\mathbf{E}}) - \nabla^2 \hat{\mathbf{E}} = -\frac{\partial^2 \hat{E}_x}{\partial z^2} \mathbf{1}_x - \frac{\partial^2 \hat{E}_y}{\partial z^2} \mathbf{1}_y, \quad (2.4-7)$$

so that one-dimensional (1D) the wave equation can be expressed as

$$-\begin{pmatrix} \hat{E}_x'' \\ \hat{E}_y'' \\ 0 \end{pmatrix} = \frac{\omega^2}{c^2} \bar{\kappa} \begin{pmatrix} \hat{E}_x \\ \hat{E}_y \\ \hat{E}_z \end{pmatrix}, \quad (2.4-8)$$

where $(\)' \equiv \partial/\partial z$. Then it follows that,

$$\begin{aligned} -\hat{\mathbf{E}}_{xy}'' &= k_0^2 \bar{\kappa}_{xy} \hat{\mathbf{E}}_{xy}, \\ -\bar{T} \hat{\mathbf{E}}_{\pm}'' &= k_0^2 \bar{\kappa}_{xy} \bar{T} \hat{\mathbf{E}}_{\pm}, \\ -\hat{\mathbf{E}}_{\pm}'' &= k_0^2 \underbrace{\bar{T}^{-1} \bar{\kappa}_{xy} \bar{T}}_{\bar{\kappa}_{\pm}} \hat{\mathbf{E}}_{\pm}. \end{aligned}$$

where transformation matrix \bar{T} is defined in (2.3–37), subscripts $(\)_{xy}$ and $(\)_{\pm}$ refer to Cartesian and rotating basis, respectively, and $k_0 = \omega/c$ is the electromagnetic wavenumber in free space.

As a result, the 1D homogeneous wave equation can be expressed in the rotating basis as

$$\hat{\mathbf{E}}_{\pm}'' + k_0^2 \bar{\kappa}_{\pm} \hat{\mathbf{E}}_{\pm} = \mathbf{0}. \quad (2.4-9)$$

Note that by using this change of basis for parallel propagation in the only-axial limit, the \hat{E}_+ , \hat{E}_- and \hat{E}_z components of the electric field are fully uncoupled, and being \hat{E}_z constant. The evolution of each \hat{E}_+ and \hat{E}_- can be then analyzed independently by solving

$$\frac{\partial^2 \hat{E}_+}{\partial z^2} + k_0^2 \mathcal{L} \hat{E}_+ = 0, \quad (2.4-10)$$

$$\frac{\partial^2 \hat{E}_-}{\partial z^2} + k_0^2 \mathcal{R} \hat{E}_- = 0. \quad (2.4-11)$$

Solutions of equation (2.4–11) are governed by the *single-turning point* theory [27, 55], of special interest for the thesis, and are revisited in Chapter 3.

2.5 The infinite homogeneous plasma dispersion relation

Application of space harmonics expansion ¹ (see Eq. (2.3–2)) for the electromagnetic fields to Eq. (2.4–5), in absence of applied excitation, results in the homogeneous plasma wave equation

$$\mathbf{k} \times (\mathbf{k} \times \bar{\mathbf{E}}) + \frac{\omega^2}{c^2} \bar{\kappa} \bar{\mathbf{E}} = 0. \quad (2.5-1)$$

Normalization of the wave propagation vector with the wavenumber in free space k_0 results in the definition of the refractive index vector

$$\mathbf{n} = \mathbf{k}/k_0 = \mathbf{k}c/\omega = \mathbf{k}/\mathbf{v}, \quad (2.5-2)$$

where $n = |\mathbf{n}|$ is the refractive index and equal to the ratio between the propagation speed of electromagnetic waves in free space and the wave phase velocity \mathbf{v} , which is the rate at propagation of the wave phase through the medium. Combining Eqs. (2.5–1) and (2.5–2) results in equation

$$\bar{\bar{D}} \cdot \bar{\mathbf{E}} = 0, \quad (2.5-3)$$

where

$$\bar{\bar{D}} = \left\{ \mathbf{n}\mathbf{n} - n^2 \bar{\mathbf{1}} + \bar{\kappa} \right\}, \quad (2.5-4)$$

is the dispersion relation matrix. For axial applied magnetic field $\mathbf{B}_0 = B_0 \mathbf{1}_z$, the refractive index vector can be expressed as $\mathbf{n} = \cos \beta \mathbf{1}_z + \sin \beta \mathbf{1}_x$ assuming it is contained in x, z plane, where β is the angle with the symmetry axis. Equation (2.5–3) becomes

$$\begin{pmatrix} \mathcal{S} - n^2 \cos^2 \beta & -i\mathcal{D} & n^2 \cos \beta \sin \beta \\ i\mathcal{D} & \mathcal{S} - n^2 & 0 \\ n^2 \cos \beta \sin \beta & 0 & \mathcal{P} - n^2 \sin^2 \beta \end{pmatrix} \begin{pmatrix} \bar{E}_x \\ \bar{E}_y \\ \bar{E}_z \end{pmatrix} = \begin{pmatrix} 0 \\ 0 \\ 0 \end{pmatrix}. \quad (2.5-5)$$

The non-trivial solution of Eq. (2.5–5) is obtained for a null matrix determinant. This equation gives the *dispersion relation*, that describes the relation between the wave frequency and its wavelength or propagation vector, $\omega = \omega(\mathbf{k})$. The roots of the dispersion relation are the natural modes of oscillation of the electromagnetic system, or the wave modes of the system.

¹Note that $\nabla \times \mathfrak{F} = i\mathbf{k} \times \mathfrak{F}$ if $\mathfrak{F} \sim \exp i(\mathbf{k} \cdot \mathbf{r} - \omega t)$

The general expression for the dispersion relation is

$$\mathcal{A}n^4 - \mathcal{B}n^2 + \mathcal{C} = 0, \quad (2.5-6)$$

where

$$\mathcal{A} = \mathcal{S} \sin^2 \beta + \mathcal{P} \cos^2 \beta, \quad (2.5-7)$$

$$\mathcal{B} = \mathcal{R}\mathcal{L} \sin^2 \beta + \mathcal{P}\mathcal{S} (1 + \cos^2 \beta), \quad (2.5-8)$$

$$\mathcal{C} = \mathcal{P}\mathcal{R}\mathcal{L}. \quad (2.5-9)$$

The solution of (2.5-6) is

$$n^2 = \frac{\mathcal{B} \pm \mathcal{F}}{2\mathcal{A}}, \quad (2.5-10)$$

being

$$\mathcal{F}^2 = (\mathcal{R}\mathcal{L} - \mathcal{P}\mathcal{S})^2 \sin^4 \beta + 4\mathcal{P}^2 \mathcal{D}^2 \cos^2 \beta. \quad (2.5-11)$$

Note that in any of the solutions for n^2 the expressions give two different solutions, one for the positive sign and one for the negative sign. For the propagation at $\mathbf{k} \perp \mathbf{B}_0$ the \pm sign represents the so-called ordinary mode and extraordinary mode respectively. For the case of $\mathbf{k} \parallel \mathbf{B}_0$ they represent the left-hand circularly polarized mode and the right-hand circularly polarized mode.

An alternative form of Eq. (2.5-6) obtained by Åström and Allis is

$$\tan^2 \beta = \frac{-\mathcal{P} (n^2 - \mathcal{R}) (n^2 - \mathcal{L})}{(\mathcal{S}n^2 - \mathcal{R}\mathcal{L}) (n^2 - \mathcal{P})}, \quad (2.5-12)$$

where the modes of propagation appear explicitly, for both principal directions, the parallel and perpendicular.

2.6 Parallel and perpendicular propagation

The fundamental or principal wave modes in a cold plasma can be obtained from the different solutions of Eq. (2.5-12). These are classified generally by the orientation of the propagation vector of each mode. From now on, a two-component plasma will be considered, where notation for electrons and singly-charged ions are subscripts e and i , respectively. In the following expressions as in Ref. [27], terms order $\mathcal{O}(Zm_e/m_i)$ are neglected. In addition to the *parallel* and *perpendicular* nomenclature that is defined with respect to \mathbf{B}_0 direction, the fields are also classified in *longitudinal* (i.e. $\mathbf{k} \parallel \mathbf{E}$) and *transverse* (i.e. $\mathbf{k} \perp \mathbf{E}$), referring to the orientation of the electric field of the wave with respect to the propagation vector. Although propagation can take place at any angle β , here we show the waves appearing in the parallel and perpendicular directions.

2.6.1 Parallel propagation

The propagating modes with propagation vector parallel to the applied magnetic field (i.e. $\beta = 0$) are obtained when the numerator of Eq. (2.5-12) is zero. These are:

- ▷ $\mathcal{P} = 0$: this solution represents the so-called *electron plasma oscillations* and as they are unaffected by the applied magnetic field, they appear in both unmagnetized plasmas (in all directions) and in magnetized plasmas along the parallel direction. The oscillations feature longitudinal electric fields and appear when

$$\omega = \omega_{pe}, \quad (2.6-1)$$

but they do not represent a propagating wave or mode.

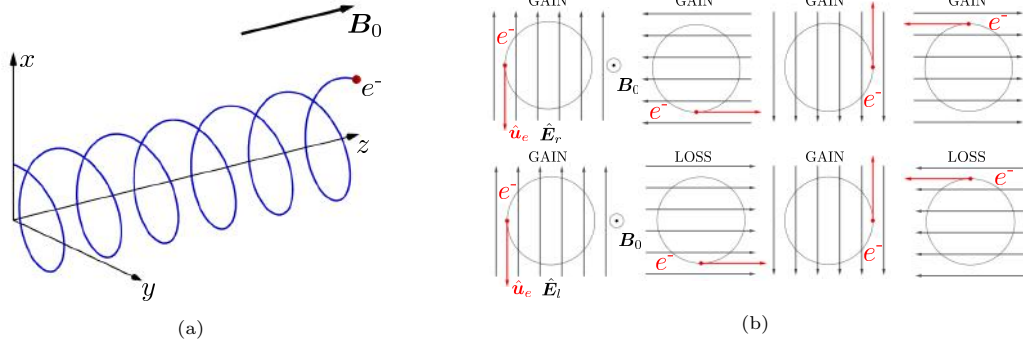


Figure 2.1: (a) Helical motion of an electron under the effect of an axial invariant magnetic field; (b) Sketch of the ECR heating mechanism: the first row shows that the electron gains energy continuously when interacting with a right-hand polarized wave; the second row shows that the electron energy oscillates for left-hand polarized waves.

▷ $n^2 = \mathcal{R}$: this root defines the *right-hand polarized* (RHP) or *R* mode dispersion relation:

$$\frac{k_{\parallel}^2 c^2}{\omega^2} = \frac{\omega^2 + \omega \Omega_e + \Omega_e \Omega_i - \omega_{pe}^2}{(\omega + \Omega_i)(\omega + \Omega_e)}, \quad (2.6-2)$$

where k_{\parallel} represents the wavenumber in the direction of the applied magnetic field. The name of *right-hand polarized* refers to a specific type of polarization. Polarization alludes in this case to the phase relation between transverse electric field components of the wavefield, in this case provided by the second row of Eq. (2.5-5):

$$\frac{i\bar{E}_x}{\bar{E}_y} = \frac{n^2 - \mathcal{S}}{\mathcal{D}}. \quad (2.6-3)$$

For the mode $n^2 = \mathcal{R}$, the ratio $i\bar{E}_x/\bar{E}_y = 1$, which corresponds to a RHP wave given by $\bar{E}_x = a \cos(-\omega t) = a \Re \{e^{-i\omega t}\}$ and $\bar{E}_y = -a \sin(-\omega t) = a \Re \{ie^{-i\omega t}\}$.

In the presence of a magnetic field, electrons rotate around magnetic field lines following the right-hand rule as it is shown in Figure 2.1a. Since the electrons and the RHP wave rotate in the same sense, when the electron gyrofrequency matches the wave frequency so that

$$\Omega_{ce} = -\omega, \quad (2.6-4)$$

a work done by the right hand polarized electric field \hat{E}_r (see top row of Figure 2.1b) on the electrons along their motion causes an increase in the Larmor radius of their orbits, and resulting in a kinetic energy gain. This process is the electron cyclotron *resonance* (ECR) and can be applied to deposit electromagnetic energy in the electron species. For that absorption some wave damping is necessary, either collisional or collisionless. Moreover, this is the fundamental mechanism that characterizes the ECRIS and ECRT technologies.

▷ $n^2 = \mathcal{L}$: this root defines the left-hand polarized (LHP) or *L* wave dispersion relation, for which the ratio $i\bar{E}_x/\bar{E}_y = -1$. Similarly to Eq. (2.6-2), its dispersion relation is:

$$\frac{k_{\parallel}^2 c^2}{\omega^2} = \frac{\omega^2 - \omega \Omega_e + \Omega_e \Omega_i - \omega_{pe}^2}{(\omega - \Omega_i)(\omega - \Omega_e)}, \quad (2.6-5)$$

where in this case the resonance occurs whenever

$$\Omega_{ci} = \omega. \quad (2.6-6)$$

This is the so-called *ion cyclotron resonance* (ICR). In general this wave is employed for heating plasmas featuring magnetized ions (i.e. strong applied magnetic fields) or low frequency excitation.

2.6.2 Perpendicular propagation

The modes with propagation vector perpendicular to the applied magnetic field (i.e. $\beta = \pi/2$) are obtained when the denominator of Eq. (2.5–12) vanishes. The roots are:

- ▷ $n^2 = \mathcal{P}$: this wave is the so-called *ordinary* (O) mode, as it corresponds to the modes propagating in an unmagnetized plasma. The electric field of this wave is linearly polarized and is aligned with the magnetic field direction and affects only electron parallel velocities. Its dispersion relation reads

$$k_{\perp}^2 c^2 = \omega^2 - \omega_{pe}^2, \quad (2.6-7)$$

where a cutoff is obtained at the critical plasma density

$$n_{cr} = \frac{\omega^2 \epsilon_0 m_e}{e^2}, \quad (2.6-8)$$

obtained when the electron plasma frequency matches the excitation frequency, also given by $\mathcal{P} = 0$.

- ▷ $n^2 = \mathcal{R}\mathcal{L}/\mathcal{S}$: this wave is the so-called *extraordinary* (X) mode, as it depends on the applied magnetic field. The mode features only a perpendicular electric field but with both a longitudinal and transverse components. The dispersion relation for this mode is

$$\frac{k_{\perp}^2 c^2}{\omega^2} = \frac{(\omega^2 + \omega\Omega_e + \Omega_e\Omega_i - \omega_{pe}^2)(\omega^2 - \omega\Omega_e + \Omega_e\Omega_i - \omega_{pe}^2)}{(\omega^2 - \omega_{LH}^2)(\omega^2 - \omega_{UH}^2)}, \quad (2.6-9)$$

where two cutoffs are found, and are those for the Eq. (2.6–2) and Eq. (2.6–5), and two resonances can be found. The cutoffs appear for both the RHP and LHP waves and the resonances at $\mathcal{S} = 0$ are found at two different frequencies called the lower hybrid resonance (LHR) frequency

$$\frac{1}{\omega_{LH}^2} = \frac{1}{\Omega_i^2 + \omega_{pi}^2} + \frac{1}{|\Omega_i\Omega_e|}, \quad (2.6-10)$$

and the upper hybrid resonance (UHR) frequency,

$$\omega_{UH}^2 = \Omega_e^2 + \omega_{pe}^2. \quad (2.6-11)$$

2.7 Cutoffs and resonances

For several combinations of the problem parameters, the refractive index squared n^2 is zero or infinity. These conditions are called *cutoffs* and *resonances*, respectively. They are functions of the plasma and magnetic field parameters, and in 3D can be understood as parametric surfaces that act as boundaries for the propagation of the different modes.

2.7.1 Cutoffs

From Eq.(2.5–6), a cutoff (i.e. $n^2 = 0$) appears whenever the independent term $\mathcal{C} = 0$. Using its definition given in Eq. (2.5–9), this occurs whenever either of these conditions apply:

$$\mathcal{P} = 0, \quad (2.7-1)$$

$$\mathcal{R} = 0, \quad (2.7-2)$$

$$\mathcal{L} = 0, \quad (2.7-3)$$

which are respectively, the cutoffs for the O , R , and L waves. After crossing the cutoff $n^2 < 0$ and the wave becomes *evanescent*, exhibiting a spatial decay of its amplitude as it propagates. Contrary to other processes where this decay is produced by an absorption mechanism of the medium, in this case, the decay manifests as the wave is not able to propagate freely past this region. For that, these regions are known as surfaces of wave reflection.

2.7.2 Resonances

Resonances (i.e. $n^2 \rightarrow \pm\infty$) occur whenever, from Eq. (2.5-7), $\mathcal{A} = 0$. From this condition we find that resonances occur at a when the propagation angle fulfills

$$\tan^2 \beta = -\frac{\mathcal{P}}{\mathcal{S}}. \quad (2.7-4)$$

Along the direction of the magnetic field ($\beta = 0$), resonance occurs for $\mathcal{S} = (\mathcal{R} + \mathcal{L})/2 \rightarrow \pm\infty$ and $\mathcal{P} = 0$. The first one, is given by

$$\mathcal{R} \rightarrow \pm\infty, \quad (2.7-5)$$

$$\mathcal{L} \rightarrow \pm\infty, \quad (2.7-6)$$

which are respectively the ECR and the ICR. For $\mathcal{P} = 0$, all coefficients of Eq. (2.5-6) vanish, and the value of n^2 at this double limit (resonance, cutoff) depends on the specific path of approach in the β, \mathcal{P} plane. In fact for any other propagation direction, $\mathcal{P} = 0$ is no longer a resonance.

For perpendicular propagation, the resonances are determined by

$$\mathcal{S} = 0, \quad (2.7-7)$$

which occurs at the two hybrid resonances, the LHR and the UHR, which occur at the frequencies

$$\omega_{\text{LH}} = \omega, \quad (2.7-8)$$

$$\omega_{\text{UH}} = \omega, \quad (2.7-9)$$

respectively. Note that, generally, $\omega_{\text{LHR}} < \omega_{\text{UHR}}$, so that the UHR occurs at much higher excitation frequencies than the LHR.

Resonances not only occur at the boundary surfaces of the principal resonances, but also at every bounded volume where \mathcal{P} and \mathcal{S} have different sign, so that a real angle β_{res} exists given by Eq. (2.7-4). In these regions the propagation of some modes is restricted to an specific range of propagation angles, so that their wave normal surfaces are dumbbell or wheel lemniscoids [29]. Those regions are: III and X for \mathcal{X} mode; VII, VIIIa & b for \mathcal{R} mode; and region XIII for \mathcal{L} mode. The range of possible propagation angles is given by the resonant angle, featuring a resonance at that propagation direction. Overall, in the plasmas featuring one of these wave propagation regimes, there is a resonance for propagation directions β_{res} and $\pi - \beta_{\text{res}}$ at every point in the bounded volume.

2.8 Clemmow-Mullaly-Allis diagram for a two-component plasma

The CMA diagram, shown in Fig. 2.2, is a parametric diagram of interest for the understanding of the different propagating regimes in a cold plasma formed only by singly-charged ions and electrons. The diagram represents the key propagating electromagnetic modes in *parameter space*, where the horizontal axis represents a normalized plasma density, by parameter $(\omega_{pe}^2 + \omega_{pi}^2)/\omega^2$, and the vertical axis refers to a normalized magnetic field intensity, $|\Omega_e|/\omega$. The principal cut-offs and resonances given in Eqs.(2.7-1)(2.7-3), and Eqs. (2.7-5) (2.7-7), respectively, are shown as *boundary surfaces*. These surfaces represent boundaries from the different regions of propagation or *bounded volumes*, from I-XIII in this map. Crossing each region, a propagating mode appears/dissappears depending on whether it existed before the crossing. An additional bounding surface, introduced by Stix [27], is shown in dashed-dotted line separating regions from *a* and *b* by condition $\mathcal{R}\mathcal{L} = \mathcal{P}\mathcal{S}$. This surface accounts for the mode-switching between \mathcal{X} and \mathcal{O} waves.

Plasmas can be classified according to their density into two categories. The boundary surface limiting these two categories is the $\mathcal{P} = 0$ cutoff. This condition is equivalent to $\omega_{pe}^2 + \omega_{pi}^2 \approx$

$\omega_{pe}^2 = \omega^2$, which occurs for a plasma with critical plasma density n_{cr} given in Eq. (2.6–8). While plasmas with $n_e < n_{cr}$, referred to as *underdense*, features $\mathcal{P} > 0$, plasmas with $n_e > n_{cr}$, namely *overdense*, present $\mathcal{P} < 0$.

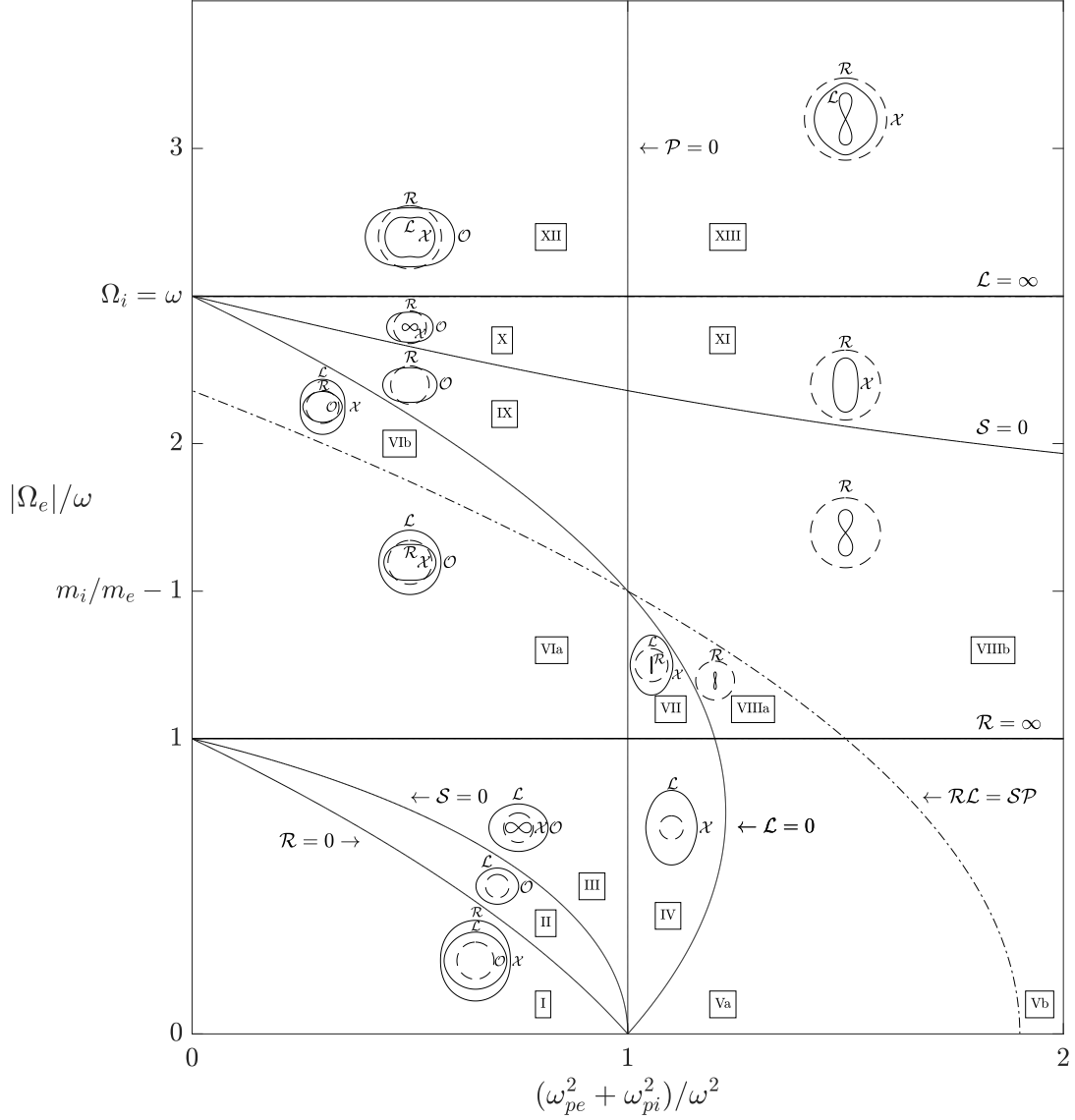


Figure 2.2: CMA diagram for a two component plasma, for a singly-charged ion to electron mass ratio of 2.5. The solid lines represent bounding surfaces representing cutoffs and resonances. The wave normal surfaces' cross-sections at specific points of each region, representative of the type of waves present, are shown where the corresponding propagating modes in the parallel and perpendicular direction are represented.

The propagating modes in a cold-plasma are generally represented by their *wave normal surfaces*, as represented in each bounded volume in Fig. 2.2. These plots represent the locus of the phase-velocity vector $\mathbf{v} = (\omega/k^2)\mathbf{k}$. They are figures of revolution about the $\mathbf{1}_{\parallel}$ axis whose cross-section is represented in the ω/k vs β plane and the dashed circle is the speed of electromagnetic waves in vacuum. Their solution is obtained from equation (2.5–6), given that the dimensionless wave

phase velocity $u = 1/n$, so that the solutions are obtained from

$$Cu^4 + Bu^2 + A = 0, \quad (2.8-1)$$

being A, B, and C defined in Eqs. (2.5-7)-(2.5-9). Figure 2.2 includes several sub-figures showing the wave normal surfaces of all the different propagating modes obtained numerically at the point in the center of each sub-figure, which are representative of the morphological shapes for the entire bounded volume.

Note that the positive or negative sign of \mathcal{R} represents the regions where the \mathcal{R} mode propagates or not, respectively. This occurs for all the modes, and it is a useful tool to understand their propagation. For instance, whenever $\mathcal{R} < 0$, the refractive index squared of the \mathcal{R} wave is $n_{\mathcal{R}}^2 < 0$, so that the solutions have imaginary indexes, so that the waves are evanescent, or non propagating in this region. In regions Va and Vb, all modes are evanescent, so no wave normal surfaces are represented.

The principal regions of interest for ECRTs are overdense regions VIII and VII, where Whistler waves appear and feature resonant absorption at specific propagation angles, and region V which is an evanescent region. As it will be shown in chapter 5, region V dominates most of the plasma volume contained within the ECRT chamber volume as the plasma is still overdense there, and the ECR location is close to the backplate. A plasma density depletion is observed close to the inner rod, leading to the appearance of a small bounded plasma volume presenting propagation properties of region VIa. As the plasma expands downstream with $B_0 < B_{res}$, the plasma density decreases and bounded volumes with parametric regimes III II and I appear. Boundary surfaces $\mathcal{P} = 0$ and $\mathcal{S} = 0$ appear there and accurate description of electromagnetic solutions close to them will be discussed in chapter 4.

2.9 Poynting's theorem for harmonic fields in cold plasmas

The conservation of energy for a system of charged particles and electromagnetic fields, is the so-called *Poynting's theorem*[69]. For harmonic fields (i.e. time dependence $e^{i\omega t}$) as given in Eq. (2.3-13), such that

$$\mathbf{E}(\mathbf{r}, t) = \Re \left\{ \hat{\mathbf{E}}(\mathbf{r})e^{-i\omega t} \right\} = \frac{1}{2} \left[\hat{\mathbf{E}}(\mathbf{r})e^{-i\omega t} + \hat{\mathbf{E}}^*(\mathbf{r})e^{i\omega t} \right], \quad (2.9-1)$$

the Poynting's theorem can be expressed, in integral form, as

$$\frac{1}{2} \int_{V_p} \hat{\mathbf{j}}_{cond}^* \cdot \hat{\mathbf{E}} dV + 2i\omega \int_{V_p} (w_e - w_m) dV + \oint_{A_p} \mathbf{S} \cdot d\mathbf{A} = 0, \quad (2.9-2)$$

where V_p is the plasma volume enclosed by surface A_p with differential volume dV and differential surface normal vector $d\mathbf{A}$, respectively, $\hat{\mathbf{j}}_{cond}$ is the conduction current in the media,

$$w_e = \frac{1}{4} \left(\hat{\mathbf{E}} \cdot \hat{\mathbf{D}}^* \right), \quad w_m = \frac{1}{4} \left(\hat{\mathbf{B}} \cdot \hat{\mathbf{H}}^* \right), \quad (2.9-3)$$

are the electric and magnetic energy densities stored in the harmonic fields, respectively, and

$$\mathbf{S} = \frac{1}{2} \left(\hat{\mathbf{E}} \times \hat{\mathbf{H}}^* \right), \quad (2.9-4)$$

is the *Poynting* vector. The Poynting vector magnitude is the flux of electromagnetic energy and the unitary vector defined by $\mathbf{S}/|\mathbf{S}|$ points in the propagation direction of electromagnetic energy. Equation (2.9-2) is a complex equation whose real part provides the energy conservation for time-averaged harmonic fields (as in Eq. (2.9-1)). The imaginary part of Eq. (2.9-2) represents the reactive part of the energy stored in the plasma and its alternating energy flow.

Whenever the contribution to current is included in the dielectric response formulation, as shown in §2.3, the term $\hat{\mathbf{j}}_{cond}^* \cdot \mathbf{E}$ in Equation (2.9-2) is disregarded. Taking the resistive (i.e. real) part of Eq.(2.9-2) in its differential form it can be found that

$$\frac{1}{2\mu_0} \Re \left\{ \nabla \cdot (\hat{\mathbf{E}} \times \hat{\mathbf{B}}) \right\} = -\frac{\omega\epsilon_0}{2} \Im \left\{ \hat{\mathbf{E}}^* \cdot \bar{\bar{\kappa}}^* \cdot \hat{\mathbf{E}} \right\} = Q_a, \quad (2.9-5)$$

so that the divergence in the time-averaged electromagnetic power flux vector is due to dielectric losses or heating, or the so-called electromagnetic power absorption Q_a . Integration of Q_a over the total plasma volume V_p results in the total electromagnetic power absorbed by the plasma

$$P_a = \int_V Q_a dV. \quad (2.9-6)$$

2.9.1 Electromagnetic power absorption: the antihermitian part of the dielectric tensor

Combining Eq. (2.9-5) with the definition of a dielectric tensor with both Hermitian and antihermitian contributions given in Eqs. (2.3-40)-(2.3-42), the electromagnetic power absorption is

$$Q_a = -\frac{\omega\epsilon_0}{2} \Im \left\{ \hat{\mathbf{E}}^* \cdot (\bar{\bar{\kappa}}^H + \bar{\bar{\kappa}}^A)^* \cdot \hat{\mathbf{E}} \right\} = \frac{\omega\epsilon_0}{2i} \hat{\mathbf{E}}^* \cdot \bar{\bar{\kappa}}^A \cdot \hat{\mathbf{E}}. \quad (2.9-7)$$

Here, the contribution of the Hermitian part of the dielectric tensor to electromagnetic power absorption is found to be null, as the Hermitian matrix is such that any product of the type $\mathbf{w}^* \cdot \bar{\bar{A}}^H \cdot \mathbf{w}$, is a real number as the eigenvalues of $\bar{\bar{A}}^H$ are purely real, being \mathbf{w} a complex vector. The opposite occurs for antihermitian matrices, where that product is purely imaginary. Additionally, the property $(\bar{\bar{\kappa}}^A)^* = -\bar{\bar{\kappa}}^A$ of antihermitian matrices has been applied in Eq. (2.9-7).

Chapter 3

One-dimensional ECR model

In §2 we revisited the fundamentals of the cold-plasma model including collisional damping in the electron response to electromagnetic excitation. This model describes the plasma response to time harmonic electromagnetic fields, treating its constituents as fluids with negligible temperature. That model predicts the location of the cutoffs and resonances in parametric space for a two-component magnetized uniform plasma. The CMA diagram locates these resonances in parametric space given by fluid properties as electron and ion densities and the magnetic field intensity. The first aspect investigated in this chapter is the use of a dielectric tensor model for the solution of the wave propagation in a medium with an inhomogeneous dispersion. The second and most important aspect is the use of an effective damping parameter to model electromagnetic power absorption in a cyclotron resonance, in this case the ECR. The model utilizes an effective collisionality that introduces damping resulting in finite dispersion relation of the right hand polarized (RHP) wave at the ECR. Solutions of the RHP wave propagation and absorption in cutoff-ECR media are obtained, depending on the propagation direction. The problem is adimensionalized and parametrized as in [34], where the influence of each parameter are analyzed. The wave solutions, transmission, reflection, and absorption coefficients are compared to the estimations obtained in the collisionless limit by Budden [55]. Finally, the electron dynamics under the influence of a RHP wave-fields obtained with this model are solved for different parametric conditions and starting phase shifts to establish a simplified ECR heating model. Numerical estimations are compared to the collisionless electron cyclotron heating model introduced by Liebermann [30]. The model results agree with the analytical estimations in the collisionless limit denoting that for limited collisionality, it is capable to reproduce the main mechanisms of wave propagation and absorption in ECR plasmas. Part of the contents of this chapter were shown in a conference paper published in the International Electric Propulsion Conference [56].

3.1 1D RHP wave model

A formalism to solve the one-dimensional propagation and absorption of right hand polarized waves was introduced by Williamson [34]. The ion contribution to the dielectric tensor is neglected as $\omega_{pi}/\omega_{pe} = m_e/m_i \ll 1$. The model includes an effective collisionality into the electron momentum equation, as shown in §2.3.1. The formalism is revisited and explored to investigate the behavior of the independent wave solutions depending on the approaching direction to the cutoff-resonance system. Additionally the impact of the problem parameters on the wave solutions is explored for each scenario.

3.1.1 RHP wave equation

Let us consider the one dimensional wave equation for the RHP wave with collisions as defined in Eq. (2.4–11). Note that from the result obtained in 2.4 it was shown that for the parallel axial case, the RHP and LHP waves are decoupled. Neglecting the ion contribution from Eq. (2.3–32), Eq. (2.4–11) can be written as

$$\frac{d^2 \hat{E}_-}{dz^2} + k_0^2 \underbrace{\left(1 - \frac{\omega_{pe}^2(z)}{\omega[\omega - \omega_{ce}(z) + i\nu_e(z)]}\right)}_{n^2} \hat{E}_- = 0, \quad (3.1-1)$$

where n^2 is the squared refractive index of the medium, and $\omega_{pe}^2(z) = e^2 n_0(z) / \epsilon_0 m_e$ and $\omega_{ce}(z) = -\Omega_{ce}(z) = e|B(z)|/m_e$ are the plasma and electron cyclotron frequencies correspondingly. This equation is a second order ordinary differential equation in z with parameters (*i*) the plasma density $n_0(z)$, (*ii*) the excitation frequency ω , (*iii*) the external magnetic field $B_0(z)$ and (*iv*) the electron effective collisional frequency ν_e .

The introduction of an imaginary part to the dispersion relation, includes wave damping in the wave as it propagates. There are multiple phenomena that can produce wave damping, which may have a collisionless character as it is the case for instance, of Landau and cyclotron damping [27], or simply collisional damping. Wave damping has been included in the cold-plasma model using a collisional approach through the inclusion of effective collisionality for each species in Eq. (2.3–8). As shown in §2.3.1, the effect of effective collisionality is to add an imaginary part to quantities \mathcal{P} , \mathcal{R} , \mathcal{L} in Eqs. (2.3–31)-(2.3–33), and therefore on \mathcal{S} and \mathcal{D} .

Given that n_e and ν_e are independent of z , this problem can be solved by linearizing ω_{ce} around the resonance point as

$$\omega_{ce}(z') = \omega(1 + \alpha z'), \quad (3.1-2)$$

where $z' = z - z_{\text{res}}$, being z_{res} the resonance axial position, and

$$\alpha = \left| \frac{1}{B_{\text{res}}} \left(\frac{dB}{dz} \right)_{\text{res}} \right|, \quad (3.1-3)$$

which is computed taking both the values of the applied magnetic field intensity B and its axial derivative, at the resonance. Equation (3.1–1) can be then expressed as

$$\frac{d^2 \hat{E}_-}{ds^2} + \left(1 + \frac{\eta}{s - i\gamma}\right) \hat{E}_- = 0, \quad (3.1-4)$$

by defining

$$\eta = \frac{\omega_{pe}^2}{\omega c \alpha}, \quad (3.1-5)$$

$$\gamma = \frac{\nu_e}{c \alpha}, \quad (3.1-6)$$

$$s = k_0 z'. \quad (3.1-7)$$

Parameters η and γ represent normalized electron density and wave damping (in this case through collisions). The refractive index has as pole (i.e. infinite) and a zero given, respectively, by

$$s = i\gamma, \quad (3.1-8)$$

$$s = -\eta + i\gamma, \quad (3.1-9)$$

representing a resonance and a cutoff. Note that definition (3.1–2) requires that $z' \geq -\alpha^{-1}$, or equivalently, that $s \geq -k_0/\alpha$. Therefore, the zero defined in Eq. (3.1–9) exists in the simulation domain only if $\eta \leq k_0/\alpha$.

3.1.2 Asymptotic solutions in the collisionless limit

The solution to equation (3.1-1) with $\nu_e = 0$ can be obtained by the application of WKB expansion whenever the refractive index changes smoothly or that $\frac{dn}{dz}$ and $\frac{d^2n}{dz^2}$ are small. In the vicinity of the resonance region, the variations in the refractive index are steep. In practice, this means that away from the cutoff-resonance region

$$\hat{E}_-(z) = n^{-1/2}(z)\hat{E}_-(0) \exp\left(\pm i\frac{\omega}{c} \int^z n(z')dz'\right), \quad (3.1-10)$$

which are valid only when

$$\frac{c^2}{\omega^2} \left| \frac{3}{4} \left(\frac{1}{n^2} \frac{dn}{dz} \right)^2 - \frac{1}{2n^3} \frac{d^2n}{dz^2} \right| \ll 1. \quad (3.1-11)$$

Budden [55] provided analytical solutions based on the WKB method ¹ to Eq. (3.1-4) in the context of radio waves propagation through ionosphere, and specifically a medium with a refractive index featuring both a linear turning point (i.e. zero) and a singular turning point (i.e. infinite). This case is of relevance for the crossing of a resonance-cutoff system, which in this case is particularized for the dispersion relation of \mathcal{R} waves. The same physical situation is found when wave propagation takes place along other paths in the parametric space of the CMA diagram (see Fig. 2.2). The solutions are revisited by Stix [27] and summarized here as they will be used in the comparison with numerical solutions obtained for Eq. (3.1-4). The validity of this solutions is still restricted to regions far from the cutoff-resonance system.

For large s , Eq. (3.1-4) is simplified to

$$\frac{d^2\hat{E}_-}{ds^2} + \left(1 + \frac{\eta}{s}\right) \hat{E}_- = 0, \quad (3.1-12)$$

which is a specific case of *Whittaker's equation* [70]

$$\frac{d^2W}{d\xi^2} + \left(-\frac{1}{4} + \frac{a}{\xi} + \frac{\frac{1}{4} - b^2}{\xi^2}\right) W = 0, \quad (3.1-13)$$

for $b = \pm\frac{1}{2}$, and the two combinations of $a = \pm\frac{1}{2}i\eta$ together with $\xi = \mp 2is$. The solutions to this problem are

$$\hat{E}_- = W_{a,b}(\xi), \quad (3.1-14)$$

the *Whittaker functions*, a form of the confluent hypergeometric function [71].

3.1.2.1 Case (i): wave propagating in the direction of increasing magnetic field

Let $\xi = -2is$ and $a = \frac{1}{2}i\eta$, Eq. (3.1-12) turns into

$$\frac{d^2\hat{E}_-}{d\xi^2} + \left(-\frac{1}{4} + \frac{\frac{1}{2}i\eta}{\xi}\right) \hat{E}_- = 0, \quad (3.1-15)$$

which has asymptotic solutions for $\xi \rightarrow -\infty$ of the form [70]

$$W_{a,b}(\xi) \sim e^{-\frac{1}{2}\xi} \xi^a = e^{-\frac{1}{2}\xi + a \ln \xi}, |\arg \xi| \leq \frac{3}{2}\pi - \delta, \quad (3.1-16)$$

when $b - a \notin -\frac{1}{2}, -\frac{3}{2}, \dots$ and being δ an arbitrarily small positive constant. As the argument of ξ is $-\frac{\pi}{2}$, for the specific case of $b = \pm\frac{1}{2}$ and $a = \frac{1}{2}i\eta$ the solution is

$$\hat{E}_- \sim \exp\left(is + \frac{1}{2}i\eta \ln(2s)\right) \exp\left(\frac{1}{4}\pi\eta\right), \quad (3.1-17)$$

¹Note that the solutions given in these references are for waves of the form $\exp\{i(\omega t - \mathbf{k} \cdot \mathbf{r})\}$ so for a refractive index with a pole at $s = -i\gamma$. Those solutions have been adapted to the convention used throughout the Thesis which is that defined in (2.3-2) (i.e. $\exp\{i(\mathbf{k} \cdot \mathbf{r} - \omega t)\}$).

for s real and positive and large $|s|$. Solution (3.1–17) is a wave propagating in the positive s direction after having passed through a resonance facing positive magnetic field gradient. The solution may therefore be used to find the reflection and transmission coefficients of the resonance region for a wave facing a positive magnetic field gradient. In order to do so, the asymptotic solutions (3.1–14) when $s < 0$ and $|s|$ must be analyzed.

As $\xi \rightarrow \infty$, so that s real, negative and large, $|\arg(\xi)|$ is either $-\frac{3\pi}{2}$ or $\frac{\pi}{2}$. Introducing a small amount of damping as collisions, the singularity of the equation (3.1–12) at $s = 0$ is displaced slightly (with our nomenclature) above the real axis. The solution is then continuous for real values of s . Reducing collisions must preserve continuity so that the path along which s varies must still pass below the singularity at $s = 0$, so as $\arg \xi$ increases from 0 to $-\pi$, $\arg \xi$ is $-\frac{3}{2}\pi$. This argument is outside the validity range of Eq. (3.1–16). The correct asymptotic solution for $\xi \rightarrow \infty$ is given by Budden [55], which adapted to our sign convention and nomenclature is

$$W_{a,b}(\xi) \sim e^{-\frac{1}{2}\xi} \xi^a - \frac{2\pi i \exp(-2\pi i a)}{(-\frac{1}{2} - b - a)! (-\frac{1}{2} + b - a)!} e^{\frac{1}{2}\xi} \xi^{-a}. \quad (3.1-18)$$

Solution (3.1–18) can be written² as

$$\hat{E}_- \sim \exp(is + \frac{1}{2}i\eta \ln |2s| + \frac{3}{4}\pi\eta) - \frac{2\pi i \exp(\pi\eta)}{(-\frac{1}{2}i\eta)!(-1 - \frac{1}{2}i\eta)!} \exp(-is - \frac{1}{2}i\eta \ln |2s| - \frac{3}{4}\pi\eta), \quad (3.1-19)$$

which represents a combination of two waves. The first term in (3.1–19) is a right-going wave, the so-called incident wave, and the second is a left-going wave or the so-called reflected wave.

Normalization of the asymptotic solutions with respect to the amplitude of the incident wave results in

$$\hat{E}_-(s) = \begin{cases} \exp(is + \frac{1}{2}i\eta \ln(2s)) \exp(-\frac{1}{2}\pi\eta), & s \rightarrow \infty \\ \exp(is + \frac{1}{2}i\eta \ln |2s|) - \frac{2\pi i \exp(-\frac{1}{2}\pi\eta)}{(-\frac{1}{2}i\eta)!(-1 - \frac{1}{2}i\eta)!} \exp(-is - \frac{1}{2}i\eta \ln |2s|), & s \rightarrow -\infty \end{cases} \quad (3.1-20)$$

The reflection and transmission coefficients along this cutoff-resonance system for a wave propagating in the direction of increasing magnetic field is computed by the ratios of the reflected and transmitted waves, with respect to the incident wave, respectively

$$|R| = \frac{|\hat{E}_-^{\text{REF}}|}{|\hat{E}_-^{\text{INC}}|} = \frac{2\pi \exp(-\frac{1}{2}\pi\eta)}{[(\frac{1}{2}i\eta)!(-1 + \frac{1}{2}i\eta)!]} = 1 - e^{-\pi\eta}, \quad (3.1-21)$$

$$|T| = \frac{|\hat{E}_-^{\text{TR}}|}{|\hat{E}_-^{\text{INC}}|} = e^{-\frac{1}{2}\pi\eta}. \quad (3.1-22)$$

In any case, energy conservation ensures that the sum of the wave-power reflection coefficient $|R|^2$ and the wave-power transmission coefficient $|T|^2$ must fulfill

$$|R|^2 + |T|^2 = 1 - e^{-\pi\eta} + e^{-2\pi\eta} < 1; \quad (3.1-23)$$

the non-absorptive case corresponding to $|R|^2 + |T|^2 = 1$ and the $|R|^2 + |T|^2 < 1$ corresponding to the presence of a resonance (absorptive) layer.

3.1.2.2 Case (ii): wave propagating in the direction of decreasing magnetic field

Let $\zeta = 2is$ and $a = -\frac{1}{2}i\eta$ so that Eq. (3.1–12) turns into

$$\frac{d^2 \hat{E}_-}{d\zeta^2} + \left(-\frac{1}{4} - \frac{\frac{1}{2}i\eta}{\zeta} \right) \hat{E}_- = 0, \quad (3.1-24)$$

²Note that $\ln \xi = \ln |\xi| + i \arg \xi$ has been applied here, knowing that $\arg \xi = -\frac{3}{2}\pi$.

for which solutions are also

$$\hat{E}_- = W_{a,b}(\zeta), \quad (3.1-25)$$

where $a = -\frac{1}{2}i\eta$ and $b = \pm\frac{1}{2}$. When $\zeta \rightarrow \infty$ being s both real and positive, $\arg \zeta = \frac{1}{2}\pi$ and thus the asymptotic solution for large $|s|$ is [71]

$$\hat{E}_- \sim e^{-\frac{1}{2}\zeta} \zeta^a = \exp\left(-is - \frac{1}{2}i\eta \ln(2s) + \frac{1}{4}\pi\eta\right), \quad (3.1-26)$$

which is a wave traveling in the negative s direction.

For s both real and negative so that $\zeta \rightarrow -\infty$, $\arg \zeta = -\frac{1}{2}\pi$, and for large $|s|$ (3.1-26) is still valid, so that

$$\hat{E}_- \sim e^{-\frac{1}{2}\zeta} \zeta^a = \exp\left(-is - \frac{1}{2}i\eta \ln|2s| - \frac{1}{4}\pi\eta\right). \quad (3.1-27)$$

Similarly to what was made for Case(i), normalization with respect to the incident wave results in

$$\hat{E}_-(s) = \begin{cases} \exp\left(-is - \frac{1}{2}i\eta \ln(2s)\right), & s \rightarrow \infty \\ \exp\left(-is - \frac{1}{2}i\eta \ln|2s|\right) \exp\left(-\frac{1}{2}\pi\eta\right), & s \rightarrow -\infty \end{cases} \quad (3.1-28)$$

The reflection and transmission coefficients are

$$|R| = 0, \quad (3.1-29)$$

$$|T| = e^{-\frac{1}{2}\pi\eta} \quad (3.1-30)$$

where the conservation of energy gives

$$|R|^2 + |T|^2 = e^{-\pi\eta} < 1. \quad (3.1-31)$$

In this case, since the absorption coefficient is $1 - e^{-\pi\eta}$, the optimal absorption occurs for $\eta \rightarrow \infty$.

3.1.2.3 Behavior of the energy close to an infinite refractive index

For $\gamma \ll \eta$, the RHP wave is evanescent between $s = -\eta$ and $s = 0$. For a wave propagating in the direction of increasing magnetic field, the decay in the cutoff-resonance system is due to the evanescent region and also the reflection produced at the cutoff. The infinite value of the refractive index at $s = 0$ is not relevant for the reflection process.

On the contrary, the wave incident from the right, propagating in the direction of decreasing magnetic field, exhibits no reflection, but the transmitted wave energy is still very small. This phenomena would be straightforward to explain in the presence of damping, as the refractive index would feature an imaginary part and the wave could be absorbed by the media. In the collisionless case this argument is not applicable. The explanation provided by Budden for that case is related to the propagation direction of the energy flow close to $s = 0$, which becomes perpendicular to the resonance in a two dimensional problem as the electromagnetic energy approaches from $s > 0$ ³, arguing that the same applies in the case of an infinite plane wave with wave normal along s . In that case the axial component U_z of the group velocity

$$U_z \approx As^{3/2}, \quad (3.1-32)$$

being A constant. Then the time it takes the wave to arrive to the resonance at $s = \delta > 0$ from the right is

$$T = \int_+^\delta \frac{ds}{kU_z} \approx A\delta^{-\frac{1}{2}} + B, \quad (3.1-33)$$

³In this case the direction of decreasing magnetic field also defined by other authors as Williamson [34], or in the direction from above in the context of propagation of radio waves in the ionosphere [55]

where B is also a constant. As can be noticed the time increases indefinitely as $\delta \rightarrow 0$. Thus, as $s \rightarrow 0$ the wave the energy increases, concentrating electromagnetic energy density in the resonance vicinity.

When the wave is approaching the cutoff-resonance system from the cutoff side (i.e. in the direction of increasing magnetic field intensity) the axial component of the group velocity is

$$U_z \approx B\sqrt{s_0 - s}, \quad (3.1-34)$$

where B is constant and $s = s_0$ is the cutoff location. In that case the integral is definite so that the time it takes to reach point s_0 is discrete and the energy is not stored or accumulated.

3.1.3 Numerical solutions including damping

Having revisited the analytical solutions in the asymptotic limits (i.e. $s \rightarrow \pm\infty$) for the collisionless case, a numerical solution including wave damping is investigated here. This problem was introduced by Williamson [34] and allows to obtain the full-wave solutions for all s in the presence of a resonance.

Equation (3.1-4) is a second order differential equation which is equivalent to the following set of ordinary differential equations (ODE's)

$$\frac{dE_R}{ds} = G_R, \quad (3.1-35)$$

$$\frac{dE_I}{ds} = G_I, \quad (3.1-36)$$

$$\frac{dG_R}{ds} = (n^2)_I E_I - (n^2)_R E_R, \quad (3.1-37)$$

$$\frac{dG_I}{ds} = -(n^2)_R E_I - (n^2)_I E_R, \quad (3.1-38)$$

where E_R and E_I are the real and imaginary parts of \hat{E}_- , n^2 is the refractive index squared, and G_R and G_I are the derivatives of the real and imaginary parts of \hat{E}_- , respectively. The inclusion of collisions adds and modifies the refractive index so that its real $(n^2)_R$ and imaginary $(n^2)_I$ parts are

$$(n^2)_R = \Re \{n^2\} = 1 + \frac{\eta s}{s^2 + \gamma^2}, \quad (3.1-39)$$

$$(n^2)_I = \Im \{n^2\} = \frac{\eta \gamma}{s^2 + \gamma^2}, \quad (3.1-40)$$

where the real part is slightly modified, and an imaginary part appears.

As a reference case, an underdense plasma discharge is considered, whose parameters are shown in Tab. 3.1. Other plasma discharges as overdense ECR plasma discharges and other parametric ranges are covered in the parametric investigation section given in §3.1.4.

n_0 [m ⁻³]	ω_{pe} [rad/s]	f [Hz]	ω [rad/s]	α [m ⁻¹]	ν_e [rad/s]
0.7×10^{15}	1.4930×10^9	2.45×10^9	1.5394×10^{10}	0.5	10^6

Table 3.1: Reference case parameters.

Taking these values as the reference case, $\eta = \eta_0 = 0.9653$ and $\gamma_0 = 0.0067$. Figure 3.1(a) shows the real and imaginary parts of the refractive index for the reference case, which features low collisional underdense plasma. Whilst the imaginary part of n^2 is symmetric with respect to the resonance location s , its real part is asymmetric. As explained before, this asymmetry is a

consequence of the presence of a cutoff at $s < 0$ and leads to two differentiated cases are found depending on the wave approach direction.

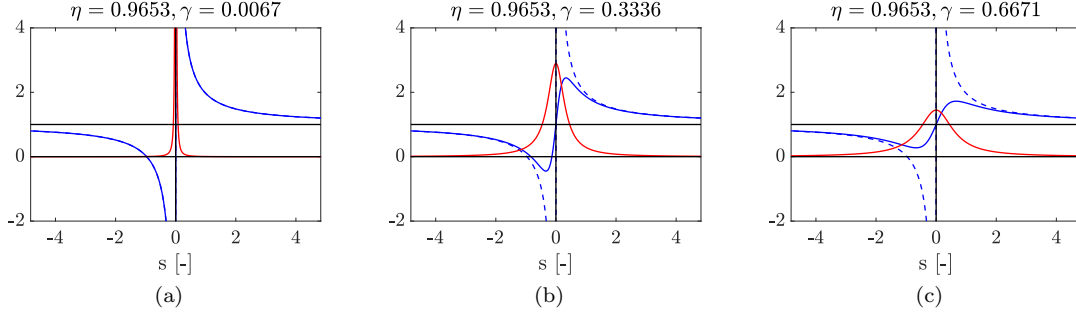


Figure 3.1: Evolution of the real (blue) and imaginary (red) parts of the refractive index squared along a channel where B_0 increases linearly with s , for $\eta \approx 0.9653$ and (a) $\gamma \approx 0.0067$ (b) $\gamma \approx 0.3336$ (c) $\gamma \approx 0.6671$. The dashed lines represent the near collisionless limit for reference case.

The electromagnetic power flow of the wave is the real part of Eq. (2.9-4), which for a planar case and a wave of type $\hat{\mathbf{E}} = \hat{E}_- \mathbf{1}_x + i\hat{E}_- \mathbf{1}_y$ is

$$\mathbf{S} = \frac{1}{2\mu_0} \Re \left\{ \hat{\mathbf{E}} \times \hat{\mathbf{B}}^* \right\} = \frac{1}{\mu_0 \omega} \Im \left\{ -\hat{E}_- \frac{\partial \hat{E}_-^*}{\partial z} \right\} \mathbf{1}_z, \quad (3.1-41)$$

so that the power flows along z , where the propagation direction is determined by the sign of \mathbf{S} .

The numerical solution of Eqs. (3.1-35)-(3.1-38) is obtained using Eqs. (3.1-20) and (3.1-28) and their derivatives to set up the boundary conditions for integration. The domain extension is such that $s \in [s_a, s_b]$, being a and b the negative and positive limits of the simulation domain, and both equidistant to the resonance location. Whether the damping does not play a major role in this problem, the numerical solution will converge to the asymptotic solutions in the collisionless limit as $s_b \rightarrow \infty$ (i.e. and also $s_a \rightarrow -\infty$). The numerical solver used is the *ode45* algorithm based on a Runge-Kutta method that uses adaptive step refinement based on tolerances specified.

3.1.3.1 Case (i): a single wave propagating towards $s \rightarrow \infty$ at boundary b . Propagation with increasing magnetic field.

Imposing the $s \rightarrow \infty$ solution given in Eq. (3.1-20) as boundary conditions at point b results in

$$E_R = \exp\left(-\frac{1}{2}\pi\eta\right) \cos\left(s_b + \frac{1}{2}\eta \ln|2s_b|\right), \quad (3.1-42)$$

$$E_I = \exp\left(-\frac{1}{2}\pi\eta\right) \sin\left(s_b + \frac{1}{2}\eta \ln|2s_b|\right), \quad (3.1-43)$$

$$G_R = -(1 + \frac{1}{2}\eta s_b) E_I, \quad (3.1-44)$$

$$G_I = (1 + \frac{1}{2}\eta s_b) E_R. \quad (3.1-45)$$

Figure 3.2a shows the numerical wave solution for $s_b = 20$. Solutions match the behavior predicted by the collisionless limit, as for a wave solution to be pure after passing through a resonance in the increasing magnetic field direction, the wave field at $s < 0$ is a standing wave resulting from the composition of an incident wave and a reflected wave. The standing wave converges to the asymptotic solution as $|s| \rightarrow \infty$. The imposition of an asymptotic solution in a finite boundary at $s = s_b$ leads to the accumulation of mismatch between asymptotic and numerical solutions at the opposite boundary, in this case, at $s = s_a$.

The Poynting vector z component obtained using Eq. (3.1-41) is shown in Figure 3.2b. The propagation direction is in the positive z direction. Approaching from the cutoff side, S_z features a slow decrease produced by the reflection induced by the cutoff. After crossing this point the wave

is evanescent and decreases rapidly, even more when the resonance is crossed. As can be seen some power is still capable of tunneling through this turning point system.

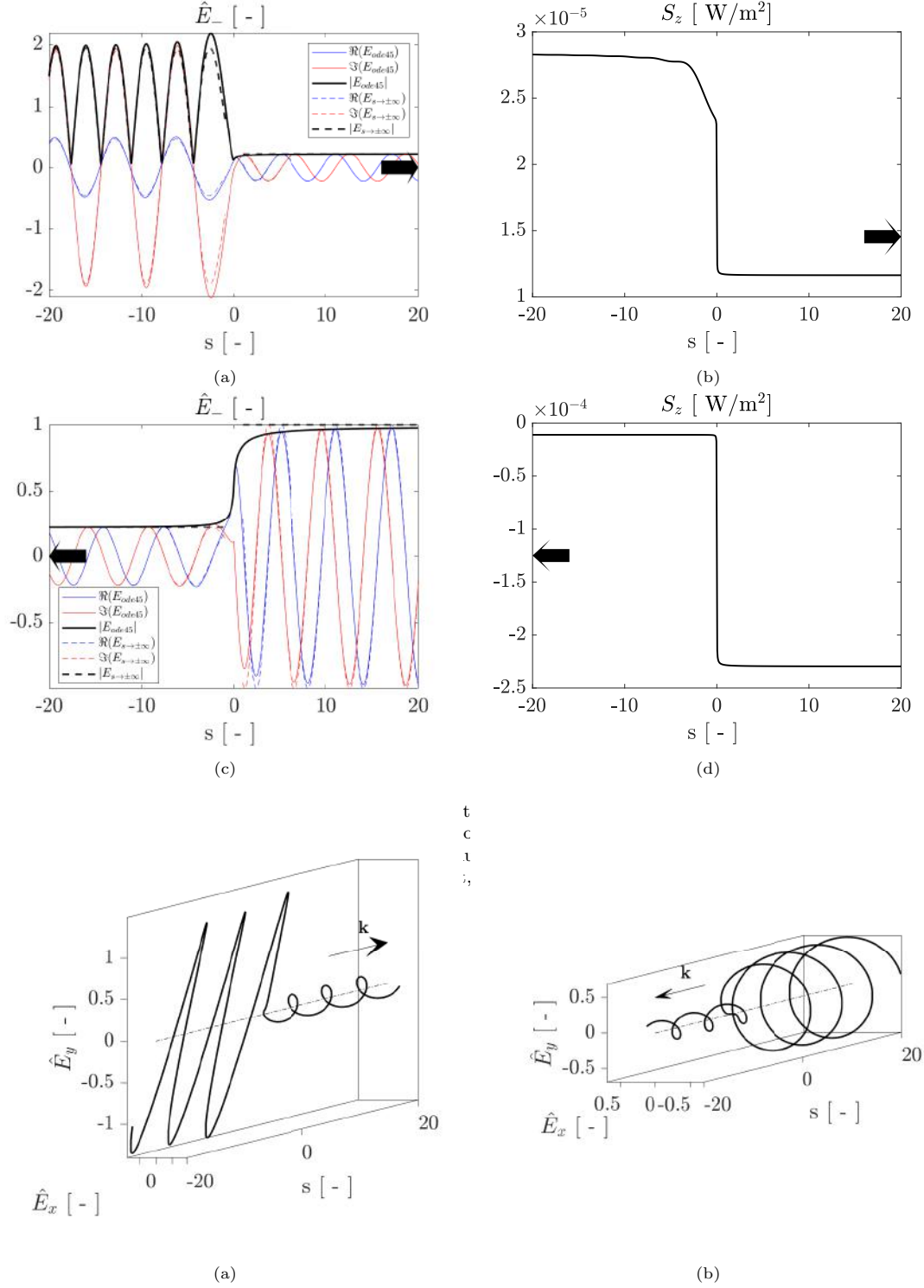


Figure 3.3: Electric field complex amplitude in Cartesian basis for (a) case (i) and (b) case (ii).

3.1.3.2 Case (ii): a single wave propagating towards $s \rightarrow -\infty$ at boundary a . Propagation with decreasing magnetic field.

Imposing the $s \rightarrow -\infty$ solution given in Eq. (3.1–28) as boundary conditions at point a results in

$$\begin{cases} E_R = \cos(s_a + \frac{1}{2}\eta \log|2s_a|), \\ E_I = -\sin(s_a + \frac{1}{2}\eta \log|2s_a|), \\ G_R = (1 + \frac{1}{2}\eta s_a)E_I, \\ G_I = -(1 + \frac{1}{2}\eta s_a)E_R. \end{cases} \quad (3.1-46)$$

The solution, shown in Fig. 3.2c and its corresponding S_z in Fig. 3.2d, is a wave propagating in the decreasing magnetic field direction, the one detailed in [34] and generally used for power absorption at an ECR region. As for case (i), the solutions also match the asymptotic limits shown in §3.1.2 as $s_b \rightarrow \infty$. The wave passes through the resonance and it is not influenced by the cutoff, so that there is no reflection. Instead, the solution is uniquely determined by the resonance, and as it will be shown hereinafter, by the problem parameters η , γ .

3.1.4 Parametric study

Assuming that the collisional and collisionless problems are equivalent and that the solution is unaffected by damping, the numerical solutions of the collisional model should converge to the analytic solutions of the collisionless case as $|s_a = -s_b| \rightarrow \infty$. Thus, one of the first effects to be investigated here is the use of damping and whether this affects electromagnetic wave propagation and absorption in ECR plasmas. The second aspect is to compare the numerical results to the analytic, which estimate that the transmission and reflection ratios for both Cases (i) and (ii) are only determined by parameter η , in the range of parameters relevant for an ECRT.

Examples of the problem parameters can be found in Tab. 3.2.

Prototype	Miller[22, 23]	Sercel[9, 24, 25]	ONERA[26]
Diameter [mm]	51	128	13 – 27
Length [mm]	51	~ 50	15
Propellant species	Xe/Ar	Ar	Xe/Ar
Power range [W]	$10^3 - 10^4$	$10^2 - 10^4$	10^2
Frequency [GHz]	8.35	2.12	2.45
Applied field B_0 [G]	2983	755	875
Axial field gradient α [m^{-1}]	~ 6.5	~ 2	~ 0.07
Electron temperature T_e [eV]	10^2	35	10 – 30

Table 3.2: Illustrative parameter values of the existing ECR thruster, based on or estimated from the references given.

The range of η and γ parameters used allows us to predict the behaviour of the configurations of interest given in Table 3.2. The parametric study is performed fixing $\eta = \eta_0$ when changing γ and vice-versa. Recall $\eta_0 \approx 0.9653$ and $\gamma_0 \approx 0.0067$. The influence on both case (i) and (ii) is explored.

Figures 3.4(a) and 3.4(b) show the results of the parametric analysis for η for cases (i) and (ii), respectively. Parameter η controls the length of the evanescent region. If this length is relatively small with respect to the wavelength, i.e., if $\eta \ll 1$, the incident wave tunnels through the evanescent region. However, when $\eta \sim 1$, tunneling is negligible, and the absorption and reflection is dominated by the first turning point found by the wave (i.e., the cutoff or the resonance, depending the direction of propagation).

In this system, the energy is conserved so that part of the energy reaching the resonance is reflected (in case (i)), part is transmitted, and part is absorbed. Note that independently of the

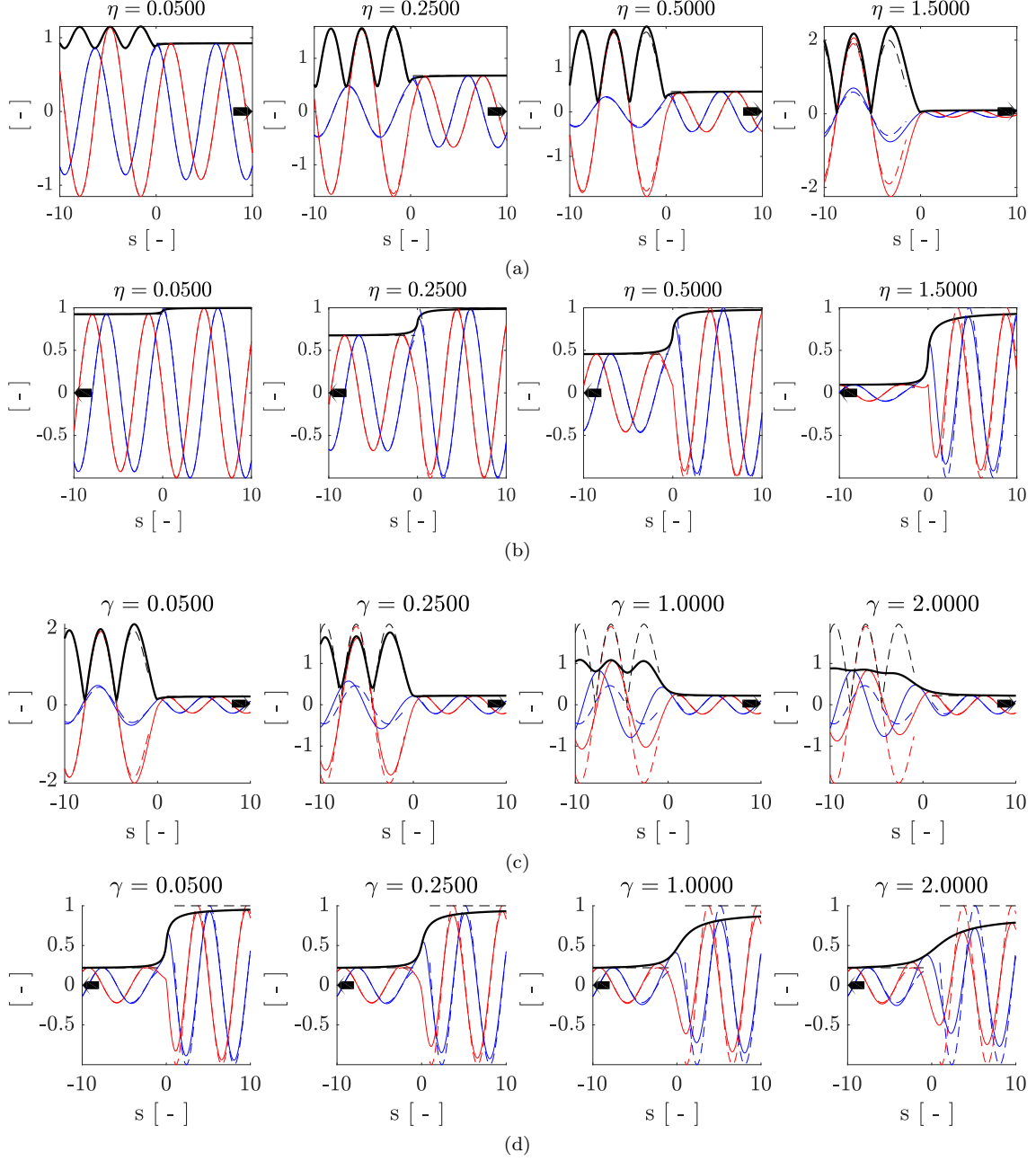


Figure 3.4: Effect of dimensionless parameters η, γ in the normalized right-hand-side polarized electric field \hat{E} through an ECR resonance: (a) and (b) $\eta = [0.05, 0.25, 0.5, 1.5], \gamma = 0.0067$; (c) and (d) $\eta = 0.9653, \gamma = [0.05, 0.25, 1, 2]$. Blue, red, and black lines represent real part, imaginary part, and magnitude of the R wave electric field complex amplitude (\hat{E}), respectively. Numerical solutions are shown in solid and analytical in dashed. Plots (a) and (c) correspond to case I, and (b) and (d) to case II.

case, there is always a net absorption so that $|R|^2 + |T|^2 < 1$. Additionally it can be noticed that for all cases, the numerical solution approaches the asymptotic solution in all cases for $|s| \gg \eta$.

The inclusion of damping in the model, described by the parameter γ , displaces the pole to the imaginary axis. Figure 3.1 shows the effect of increasing γ on the real and imaginary parts of n^2 . First, the imaginary part is modified, increasing in all s except at close to $s = 0$. As a result, the resonance width is increased and the absorption takes place in a wider region. This is the principal effect due to collisions for the case of ECR wave absorption when wave propagation occurs in the decreasing B direction. Second, increasing γ also modifies the real part of n^2 . For low damping, $\Re\{n^2\}$ is very close to that of the collisionless limit. However, inclusion of collisions modifies the real part so that the refractive index now features another zero. The two new cutoffs are found for the zeros of Eq. (3.1-39), i.e. $s = -\eta/2 \pm \sqrt{\eta^2 - 4\gamma^2}/2$. The location of both cutoffs approach each other as γ increases, merging when $\gamma = \eta/2$ so that for $\gamma > \eta$, $\Re\{n^2\} > 0 \forall s$. Nevertheless, the refractive index gradient also plays a role in the reflection, as can be seen in Fig. 3.4(c), where reflection is observed for $\gamma > \eta/2$ at $s < 0$. As can be seen from Fig. 3.4(c) for $\gamma = 2$, where $\gamma \gg \eta$, the wave solutions of case (i) start to resemble those of case (ii). In fact, the evolution of case (i) with increasing γ shows that the amplitude of the reflected wave decreases when increasing γ as the ratio of maximum to minimum voltages of the standing wave decreases.

3.1.4.1 Transmission factor for case (ii)

In order to verify our results, the transmission factor is compared to the analytic expression obtained by [55] as was done in [34]. A range of values for the plasma density $n_0 \in [0, 1, \dots, 10] \times 10^9 \text{cm}^{-3}$ is evaluated. The comparison is made using two collisional frequencies, $5.3 \times 10^7 \text{s}^{-1}$ and $5.3 \times 10^9 \text{s}^{-1}$, equivalent to $\gamma \approx 0.02$ and $\gamma = 2.16$ respectively. The wave frequency used is $f = 2.45 \text{ GHz}$ and the magnetic field slope $\alpha = k_0/2\pi$. The results depend on the maximum size of the simulation domain. For that, cases with $s_b = 10$ and $s_b = 100$ are shown in Figs. 3.5a and 3.5b, respectively. The transmission coefficient obtained numerically follows the trend estimated by the collisionless limit, specially whenever the size of the domain is increased and the effect of the resonance is no longer important. Although for short domains the higher the damping the agreement between numerical and analytical estimations decreases, for sufficiently large domains, the effect is mitigated and negligible.

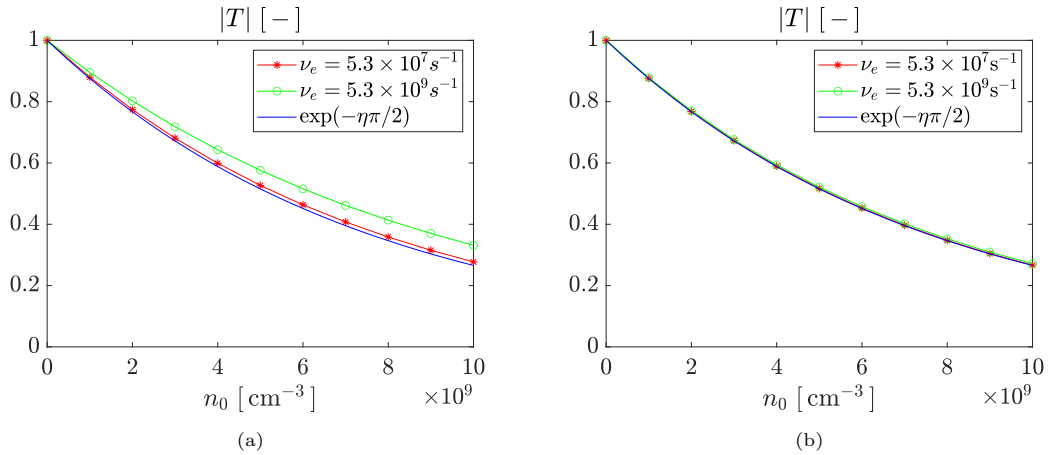


Figure 3.5: Evolution of the transmission factor as a function of the plasma density. Analytic expression (in blue) is compared to numerical model using a low (red-star) and high (green-circled) electron effective collisionalities for two different domain sizes (a) $s_b = 10$ and (b) $s_b = 100$.

3.1.4.2 Transmission and reflection factors for case (i)

Expressions for the estimated transmitted, reflected and absorbed power for a wave propagating in the direction of the magnetic field intensity gradient are given in Eqs. (3.1–21). These values are compared to those obtained numerically for $\eta \in [10^{-3}, 1]$. The values are computed obtaining the forward and reflected waves knowing the standing wave created in the channel for this case, applying the VSWR definition given in Eq. (4.2–38), and relations (4.2–35)–(4.2–36). Note that solutions are found for $s_b = 100$.

Figure 3.6 shows two cases for two different γ , being Fig. 3.6a for $\gamma \approx 0.022$ and Fig. 3.6b for $\gamma \approx 2.2$, respectively. For low values of γ , in this case given by $\nu_e = 5 \times 10^7 \text{s}^{-1}$, the power reflection, transmitted and absorption factors are close to those estimated by Budden in the collisionless limit. Although the transmitted power is slightly affected by collisions, the main difference is found in the reflected power, and both combined affect the estimated absorption, which in this case, is higher in the presence of collisions. Note that the maximum absorption in the collisionless limit occurs for

$$\frac{d}{d\eta} ((1 - |R|^2 - |T|^2)) = \pi (-e^{-2\pi\eta}) (e^{\pi\eta} - 2) = 0, \quad (3.1-47)$$

which is obtained at an specific value of η ,

$$\eta_* = \frac{\log 2}{\pi}. \quad (3.1-48)$$

The effect of damping on the reflection coefficient was observed both in n^2 (see Fig. 3.1) and in the wave solutions shown in Fig. 3.4(c), where the cutoff location is modified by γ and for $\gamma > \eta/2$, there is no longer a cutoff and the reflection occurs due to the gradients of the refractive index. This effect is observed clearly comparing Fig. 3.6a with the high damping (i.e. electron collisionality $\nu_e \sim \mathcal{O}(\omega)$ for $\alpha =$) case shown in Fig. 3.6b. The reflection, as shown before in Fig. 3.4(c), is affected so that for $\gamma > \eta/2$ there is no longer a cutoff and this affects the behavior of the resonance cutoff system investigated. As a result, with increasing γ the reflected coefficient decreases (for a fixed η), and the opposite occurs absorption coefficient. In all cases, as mentioned in Ref. [34], maximum absorption occurs for $\eta \sim \mathcal{O}(1)$, being the optimal η for absorption greater the higher the gamma.

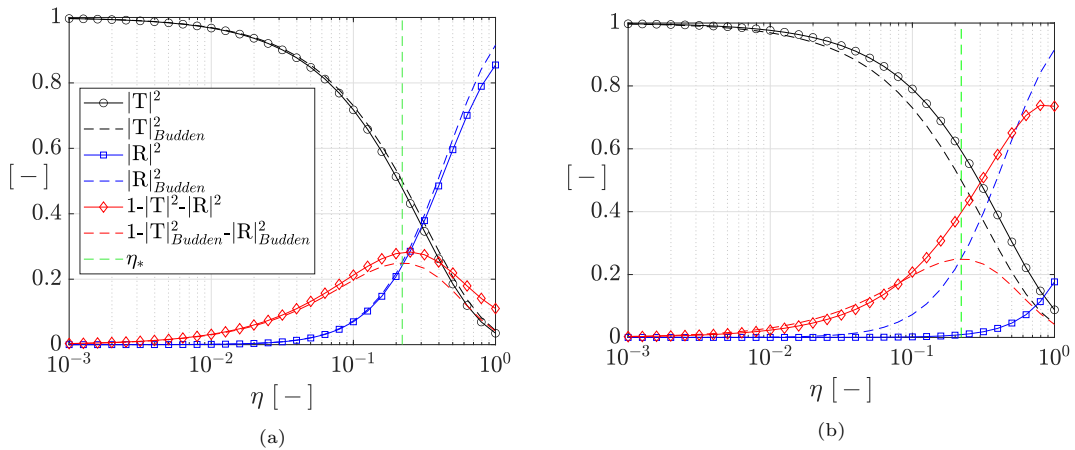


Figure 3.6: Evolution of transmitted (black), reflected (blue) and absorbed (red) power for (a) $\gamma \approx 0.022$ and (b) $\gamma \approx 2.2$. The numerical solutions are shown with solid lines and analytical with dashed lines. Parameter η_* is the maximum absorption in the collisionless limit, defined in Eq. (3.1–48).

3.1.5 Concluding remarks

The results obtained from the model shown here, which includes wave damping, are in good agreement with the estimations obtained in [55], specially for the case of interest to ECR discharges, to be investigated in the Thesis. In those discharges, the waves are launched approaching the resonance in the decreasing magnetic field direction (i.e. case (ii)). In that case, one of the main conclusions of this model is that the wave damping (either collisional or kinetic), which adds an antihermitian part of the dielectric tensor, only affects the resonance region width. Then, the absorption is determined only by parameter η which is a function of the electron density, the magnitude of the magnetic field gradient and the excitation frequency. This result is consistent with other studies [32, 34–36, 55]. Thus, although the collisionless plasma model cannot reproduce resonant behavior it is possible to model absorption and wave damping by the inclusion of an antihermitian part of the dielectric tensor through effective damping using a collisional cold-plasma tensor, as shown in §2.3. Regardless of the damping mechanism (kinetic, collisional), a small value of the collisional parameter suffices to absorb power, without affecting either the transmitted or the reflected amount of power through the resonance. With these results we can conclude that the model used, although not capable of describing kinetic absorption mechanisms not covered by the cold plasma approximation, it is capable of providing robust power absorption solutions.

In the case of waves approaching the resonance in the increasing magnetic field direction, the reflection behavior is affected by damping. However, this effect is clearly observed to decrease whenever wave damping is such that $\gamma \ll \eta$, which is the case for the devices considered.

3.2 Electron particle response

For a known electric field, as the RHP electromagnetic wave solutions of the type obtained in case (ii) (see §3.1.2), the collisionless electron motion is formally integrable assuming constant parallel velocity of the electrons (i.e., $v_z = \text{const}$), thus neglecting magnetic mirror effect and the axial electric field. The magnetic field is assumed to vary linearly with distance as in Eq. (3.1–2). Knowing that the RHP electric field and the electron velocities can be expressed as

$$\mathbf{E}_\perp = \Re \{ \bar{\mathbf{E}}_\perp (\mathbf{1}_x + i\mathbf{1}_y) e^{-i\omega t} \}, \quad (3.2-1)$$

$$\mathbf{v}_\perp = \Re \{ \bar{\mathbf{v}}_\perp (\mathbf{1}_x + i\mathbf{1}_y) e^{-i\omega t} \}, \quad (3.2-2)$$

being $\bar{\mathbf{E}}_\perp = \bar{E}_x - i\bar{E}_y$ and $\bar{\mathbf{v}}_\perp = \bar{v}_x - i\bar{v}_y$ as defined in Eqs. (2.3–38). The equation governing the perpendicular RHP electron velocity response v_\perp is

$$\frac{d\bar{\mathbf{v}}_\perp}{dt} + i(\omega_{ce} - \omega) \bar{\mathbf{v}}_\perp = -\frac{e}{m_e} \bar{\mathbf{E}}_\perp, \quad (3.2-3)$$

where the cyclotron frequency $\omega_{ce} = eB(z)/m_e$ is given by (3.1–2) and depends on z . Note that the fast electron response given by the phasor $\exp(-i\omega t)$ is canceled out. As a result, the magnetized electron response due to a RHP wave can be studied uniquely with the slow frequency response of the electrons described by $\bar{\mathbf{v}}_\perp$. Assuming that the distance traveled from the resonance is given by $z - z_{res} = v_z t$, being v_z the electron parallel speed near the ECR, Eq. (3.2–3) can be expressed as

$$\frac{d\bar{\mathbf{v}}_\perp}{dt} + i\omega\alpha v_z t \bar{\mathbf{v}}_\perp = -\frac{e}{m_e} \bar{\mathbf{E}}_\perp. \quad (3.2-4)$$

3.2.1 Analytical solution

The solution for Eq. (3.2–4) is of the form

$$\bar{\mathbf{v}}_\perp(t) = A(t) \exp\left(-\frac{1}{2}i\omega\alpha v_z t^2\right). \quad (3.2-5)$$

Applying the method of variation of parameters the solution to the complete Eq. (3.2-3) is given by

$$\int dA = - \int \frac{e}{m_e} \bar{E}_-(v_z t) \underbrace{\exp\left(\frac{1}{2}i\omega\alpha v_z t^2\right)}_{\text{Fast phasor } t \neq 0} dt. \quad (3.2-6)$$

Assuming that the electric field constant at the resonance and using the stationary phase method to integrate Eq. (3.2-6), we find

$$\Delta A \simeq -\frac{e}{m_e} \bar{E}_-(0) \int_{-\infty}^{\infty} \exp\left(\frac{1}{2}i\omega\alpha v_z t^2\right) dt = -\frac{e\bar{E}_-(0)}{m_e} \sqrt{\frac{\pi}{\omega\alpha v_z}} (1+i). \quad (3.2-7)$$

As a result the energy gain per single electron pass through the resonance is found to be [30, 34]

$$\langle W_{ecr} \rangle = \frac{1}{2} m_e \Delta \bar{A} \cdot \Delta \bar{A}^* = \frac{\pi e^2 |\bar{E}_-(0)|^2}{\omega\alpha v_z m_e}. \quad (3.2-8)$$

Equation (3.2-7) describes the complex velocity gain ΔA added to each electron after a single resonance crossing. Note that the changes in the magnitude $|v_-|$ are given by those of $|A|$. From the integral given in Eq. (3.2-6), A is nearly constant away from the resonance, while its variation occurs in the resonance neighborhood. A sample of electrons with different phases but the same initial perpendicular kinetic energy and thus RHP velocity magnitude $|A_{-\infty}|$ and parallel velocity v_z lay on a circle of radius $|A_{-\infty}|$ in the v_- complex plane, represented in red in Figs. 3.7(a)-(c). A single pass through resonance then translates this circle away from the origin by the quantity ΔA , shown in black. After the resonance pass, the complex amplitudes of the velocity A lie on a circle of the same radius, and represented in blue, and the electrons continue to gyrate with $\exp(-i\omega t) \exp(-i\omega\alpha v_z t^2/2)$, so that this circle rotates about the origin with time. Depending on the initial gyrophase, the electrons can gain more or less energy in the resonance pass, and some can even *lose* energy to the field, depending on the value of $|\Delta A|$.

Figures 3.7(d)-(f) show the resulting energy gains as a function of the initial electron gyrophase. For $|\Delta A| > 2|A(-\infty)|$, independently of their phase, electrons cannot lose energy on a resonance crossing. For $|\Delta A| < 2|A(-\infty)|$ some electrons start to lose energy, and the lower $|\Delta A|$ the higher the amount of electron phases featuring energy loss. The contributions to energy gain and loss are represented with green and red areas, respectively. Note however that for any $|\Delta A|$, $\langle W_{ecr} \rangle > 0$, being $\langle W_{ecr} \rangle$ the mean energy per electron for a homogeneous phase electron population. A physical explanation for this is that electrons changing progressively their energy in the resonance feature spirals. The electrons losing energy describe converging spirals and those gaining energy, follow diverging spirals when crossing the resonance. The path and thus the work done by the field on the electrons is greater for electrons gaining energy than the negative counterpart.

An additional effect of resonance crossing is that the higher $|\Delta A|$, the higher the effect of electron phase coalescing. Electron phases coalesce as when crossing the resonance, the phases focus towards the direction given by ΔA .

Analyzing the Eq. (3.2-8) it can be noticed that:

1. The mean energy gain by electrons due to ECR heating is always positive.
2. Second, the higher (i) the magnetic field gradient and (ii) the electron parallel velocity at the resonant zone, the lower the energy gain.
3. Third, the energy gain per pass is proportional to the square of the amplitude of the wave electric field at the resonance, so that the exact value at the resonance affects considerably the absorption.

4. Forth, the higher $A(-\infty)$ the higher the electric field required to produce an energy gain to all phases. Therefore, ECR heating would be more effective when heating electrons with low initial perpendicular energy. Although it would be possible to heat without limit with consecutive resonance crossings, the law of diminishing returns would apply so that less efficient heating would be obtained after each resonance crossing.
5. Fifth, for an increasing ratio $\Delta A/A(-\infty)$, the electron phases approach to a single gyrophase. As a result, after a resonance crossing with significant heating, electrons “lose track” of their initial gyrophase and the resulting electron population results in a coalescence of phases in a specific phase span. This span decreases the higher the $\Delta A/A(-\infty)$, increasing the electron phase synchronization.

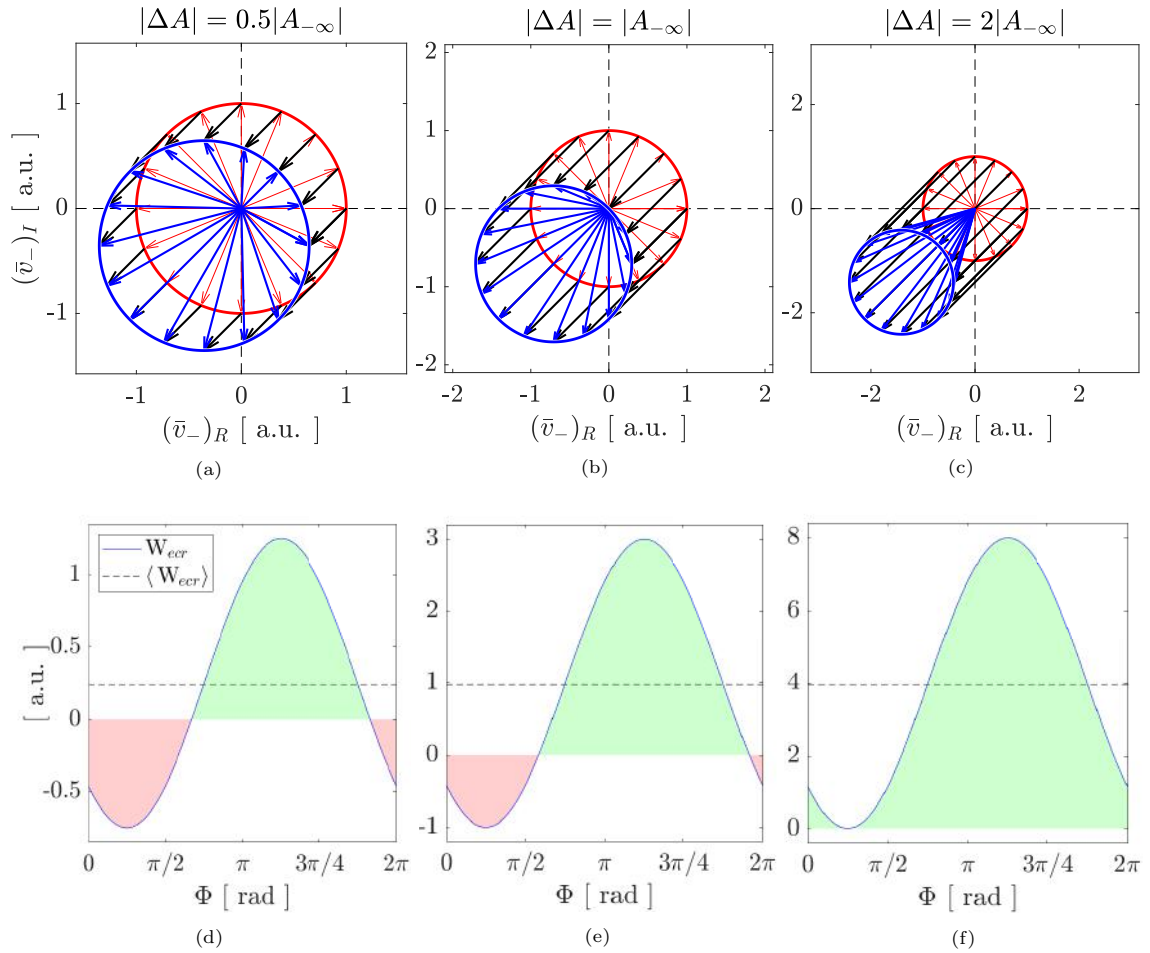


Figure 3.7: Evolution the complex magnitude of the electron velocity vector in a single resonance crossing for different phases Φ . For each Φ , an initial velocity $A_{-\infty}$ changes in the complex plane by ΔA in black, resulting in a final velocity A in blue. Three cases for ΔA equal to (a) $0.5A_{-\infty}$, (b) $A_{-\infty}$, and (c) $2A_{-\infty}$. The respective heating as a function of the phase is shown below with the mean energy in dashed black lines. The green and red regions in (d)-(f) represent the positive and negative contributions to electron heating.

3.2.2 Numerical solution

In order to quantify the impact of the stationary phase method on the solution to the problem and the validity of the approximation, Eq. (3.2-3) is solved numerically using a Runge-Kutta based variable step ordinary differential equation (ODE) solver as *ode45*, by separating both real and imaginary parts of the equation as

$$\frac{d(\bar{v}_\perp)_R}{dt} = -\frac{e}{m_e} \bar{E}_R + (\omega_{ce} - \omega) (\bar{v}_\perp)_I, \quad (3.2-9)$$

$$\frac{d(\bar{v}_\perp)_I}{dt} = -\frac{e}{m_e} \bar{E}_I - (\omega_{ce} - \omega) (\bar{v}_\perp)_R, \quad (3.2-10)$$

where $\bar{v}_\perp = (\bar{v}_\perp)_R + i(\bar{v}_\perp)_I$ and $\bar{E} = (\bar{E})_R + i(\bar{E})_I$, and subscripts R and I refer to the real and imaginary parts, respectively. In this case, the solution of the electron individual response is obtained for imposing exactly the solution of the RHP wavefield obtained from case (ii). Two alternative approaches are used here: A) use a stationary electric field which is that of the solution at the resonance, $\bar{E} = \bar{E}_-(0)$; B) use the complete solution of case (ii), i.e. $\bar{E} = \bar{E}_-(k_0 v_z t)$. Solution of A) is expected to reflect the solution obtained analytically, whilst approach B) would reveal the validity of the stationary phase method approximation.

An initial phase difference Φ between \bar{v}_\perp and \bar{E}_- between the velocity vector and the electric field at the electron initial location s_i . Note that for approach A, the phase of \bar{E}_- is that of the field. For the simulations shown the electrons are launched at $s_i = 6$. The phase is defined as a positive angle taken from the velocity vector phase in the complex plane. An initial value of the perpendicular kinetic energy K_\perp is provided so that initially

$$(\bar{v}_\perp)_R = \sqrt{\frac{2K_\perp}{m_e}} \cos \Phi, \quad (3.2-11)$$

$$(\bar{v}_\perp)_I = \sqrt{\frac{2K_\perp}{m_e}} \sin \Phi. \quad (3.2-12)$$

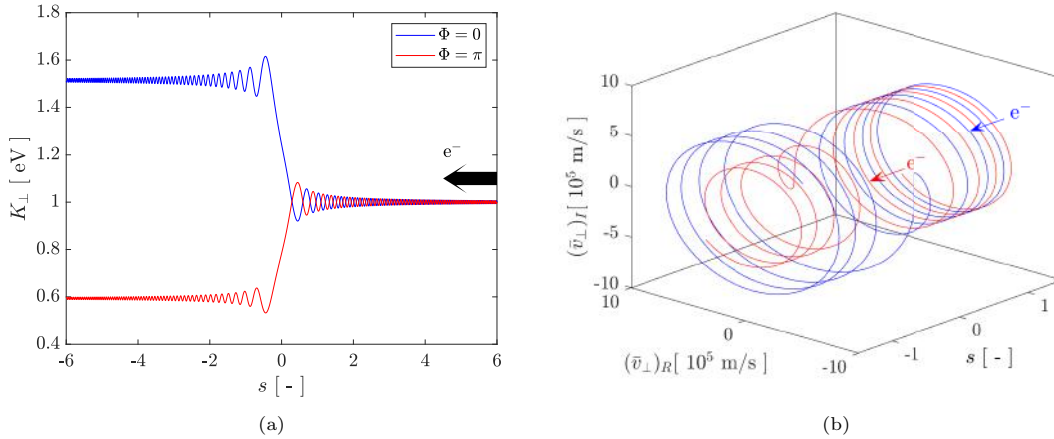


Figure 3.8: Evolution with respect to s of an electron (a) perpendicular kinetic energy and (b) \bar{v}_\perp . Two electrons with phase $\Phi = 0$ (blue) and π (red) are launched in the decreasing magnetic field direction crossing the ECR resonance under the action of a RHP wave. Initial electron parameters are $K_\parallel = 5$ eV, $K_\perp = 1$ eV, $E_0 = 100$ V/m.

Figure 3.8 shows a solution example using approach A) for two electrons launched in the decreasing magnetic field gradient direction under the influence of the an electric field given by the value of $E_-(s)$ from a RHP wave solution of case (ii) for approach A). Figure 3.8 (a) shows the

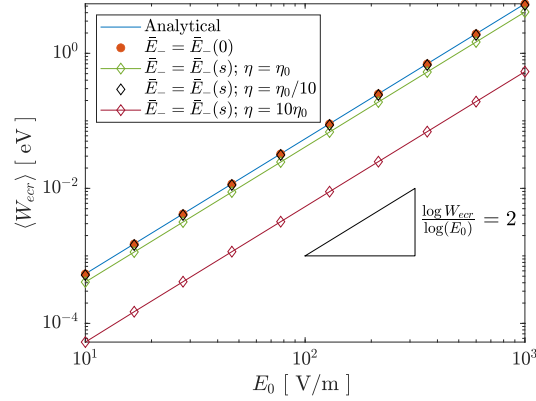


Figure 3.9: Comparison of the mean energy gain computed by the analytical expression given in Eq. (3.2–7) (blue solid), the numerical solution using a constant RHP electric field (red circles), and the numerical solution where the electric field of the RHP wave evolves in space as the solutions of case (ii) in §3.1.3.2.

evolution of the perpendicular kinetic energy for these electrons, which for different phases, one exhibits energy gain and another one energy loss. Note that in both cases, and as it was mentioned above this perpendicular energy change takes place in the vicinity of the resonance. Figure 3.8 (b) shows the evolution of \bar{v}_\perp , where for the electron with $\Phi = 0$ (i.e. in blue), the magnitude of \bar{v}_\perp increases. The opposite occurs for the case with $\Phi = \pi$. Note that the frequency of \bar{v}_\perp increases far from the resonance, as detailed by the analytical solution.

In order to recover the full perpendicular velocity field, the solution for \bar{v}_\perp is inserted in Eq. (3.2–2). The resulting electron motion is helical with a perpendicular right-handed velocity (given by the direction of the magnetic field) which increases its Larmor radius as the electron crosses the resonance, or more accurately, when the ECR condition given by Eq. (2.6–4) is fulfilled. As seen in Fig. 3.8b, the electrons gain perpendicular energy in the vicinity of the ECR in a continuous manner.

Figure 3.9 shows the comparison between the analytical estimation given in Eq. (3.2–7) and the numerical solutions of cases (A) and (B). As expected, the solution of case (A) matches perfectly the numerical computation of (A). For the response using the RHP wave electric field solution obtained by case (ii) using reference parameters η_0 and γ_0 , the estimated energy gain decreases while still being proportional to E_0^2 . The effect of η is analyzed including cases with $\eta/10$ and $10\eta_0$. The proportionality constant is kept for all η . However, energy gain decreases below the constant \bar{E}_- value, the higher η . This is a result of the wave profile whose average in the resonance zone decreases for higher η (see Fig. 3.4(b)).

3.2.3 Concluding remarks

In this section the collisionless electron individual response to right hand polarized wave fields is investigated. The analytical solution based on the stationary phase method shown in Ref. [30] is revisited and the main conclusions on the heating mechanism are highlighted: (i) the mean energy gain of the electrons due to ECR is always positive, for a uniformly distributed electron population in phase; (ii) the higher the magnetic field gradient and electron parallel velocity at the ECR region, the lower the gain; (iii) the energy gain is proportional to the RHP wave amplitude at the resonance squared, leading to need to determine accurately the electric field wave; (iv) the higher the initial perpendicular velocity of electrons, the higher the electric field required to produce an energy gain to all phases; thus, electrons with lower initial perpendicular energy are easier to be heated; (v) for an increasing ratio $\Delta A/A(-\infty)$, the electron phases approach to a single gyrophase, with a phase span that decreases with that ratio; as a result, after a resonance crossing with significant heating, electrons “lose track” of their initial gyrophase and the resulting electron

population features a phase synchronization or coalescence.

The analytical solutions based on the stationary phase method are compared to the exact numerical solution utilizing (i) a stationary electric field which is that of the solution at the resonance, i.e. $\bar{E} = \bar{E}_-(0)$; (ii) the solution of the RHP wavefield which include the axial dependence i.e. $\bar{E} = \bar{E}_-(k_0 v_z t)$. The results verify that for case (i) the analytical formula is the numerical solution. However, it is shown that the energy absorption computed using the complete axial evolution of the RHP electric wave field is smaller than the analytical expression given by the stationary phase method. Although this difference is negligible for $\eta \ll 1$, in cases with $\eta \geq 1$ the analytical solution overestimates absorption, so that the validity of the stationary phase approximation is limited for $\eta \ll 1$.

Chapter 4

ATHAMES: A finite element electromagnetic wave code

This Chapter provides a detailed portrayal of the Axisymmetric Time Harmonic Maxwell's Equations Solver (ATHAMES) developed during the thesis. ATHAMES is a novel two-dimensional axisymmetric code that solves Maxwell's equations in frequency domain. Specifically, the code solves for the electromagnetic (EM) fields in the presence of magnetized inhomogeneous plasmas featuring EM propagation boundary surfaces such as cutoffs and resonances. The code utilizes the Finite Element Method (FEM) for the solution in contrast to other methods previously used, as the Finite Difference Method (FDM) using Yee's scheme [44, 54]. Although Yee's scheme allows to solve for the EM fields and power absorption maps in HPTs, the solutions require interpolation from two staggered structured grids. Additionally, some other advantages can be obtained from the use of the FE instead of FD. Amongst these, its capability to solve problems in complex geometries by the use of unstructured meshes, to provide local mesh refinement according to the specific local requirements at every domain region, and allowing for scalability given its computationally efficient cost, are some of the many advantages which make the use of FEM appealing for the solution of EM problems. For the purposes of this Thesis, the use of local refinement is a key factor in order to select this approach over other methods, as it allows to perform predictive mesh refinement based on estimated wavelengths prior to the solution given the plasma properties and applied magnetic field. In particular, this choice enables the solution of EM wave fields in the presence of ECR regions. Both a planar [58] (THAMES) and axisymmetric (ATHAMES) versions of the code have been implemented. The axisymmetric has been coupled with HYPHEN, a hybrid plasma simulation platform [60, 72, 73], to obtain the coupled EM and plasma transport response in ECR thrusters. This is shown in Chapter 5. Part of the contents of this chapter have been published in Space Propulsion Conference 2018 [58], International Electric Propulsion Conference [59] and in Plasma Sources Science and Technology journal [57]. The contents of this chapter are part of EP2's contributions to MINOTOR project.

4.1 Objectives and capabilities

Amongst the objectives of this Thesis, the role of ATHAMES is to provide accurate and computationally cost-efficient solutions of the EM wave-fields in ECR plasmas. The plasmas simulated are magnetized, bounded and inhomogeneous. The code is required to describe EM propagation considering multiple nonuniform cutoffs and resonances. The conditions reproduced by the code must resemble the most those presented in real ECRT prototypes.

The code presents the following capabilities:

- Definition of the simulation domain properties and the excitation sources location.
- Specification of different boundary conditions, including perfect electric conductor (PEC), perfect magnetic conductor (PMC), and a coaxial waveport.
- A coaxial waveport simulated with a lumped element, key to reproduce the coaxial ECR thruster [26].
- Solution of Maxwell's equations in frequency domain, returning the EM waves within an arbitrary media containing inhomogeneous plasmas.
- Description of cutoffs and resonances featured by arbitrary low temperature ECR plasmas.
- Description of complex geometries, including domain boundaries and excitation sources by the use of arbitrary unstructured meshes.
- Predictive mesh refinement (see §4.3) based on the characteristic minimum wavelength estimated from the local plasma properties and applied magnetic field \mathbf{B}_0 .
- Computation of the EM power absorption density spatial distribution Q_a .
- Computation of the reflection coefficient R of the coaxial transmission line.
- Computation of the Poynting flux vector \mathbf{S} describing the direction of the stationary EM power flow.
- Data intercommunication communication with HYPHEN, performing the necessary interpolations: (i) the plasma density n_e , the effective electron collisionality ν_e , from the PIC mesh to the wave (W-) mesh, (ii) the applied magnetic field intensity \mathbf{B}_0 and angle β from the magnetic field file mesh (higher resolution) to the W-mesh, and (iii) the EM power absorbed density from the W-mesh to the MFAM element centers..

4.2 The full wave model

As detailed in §1.1, ray tracing algorithms are not useful to model ECR thrusters as their typical characteristic length is greater than that of the electromagnetic waves to be modeled. Instead, the ATHAMES model utilizes a full-wave approach, which solves simultaneously for all EM propagation directions. As a result of the investigation on the accuracy of full-wave numerical schemes shown in Ref. [56], a 2D full-wave Galerkin's finite element (FE) formulation based on the use of a mixed basis of shape functions was selected to solve the curl-curl equation (2.4-5) in the meridional plane. The mixed basis (see §4.2.2.2), is composed of:

1. Nédélec edge ($H(\text{curl})$ -conforming) elements [74] for the in-plane or tangential components of \mathbf{E} ,
2. Lagrange (H^1 -conforming) nodal elements for the out-of-plane component of \mathbf{E}

This choice was based on several considerations:

- FE methods do not rely on structured grids. Thus, FE allows for proper treatment highly nonuniform problems and complex geometries. This enables a finer description of the ECR region, which features a rapid change in the propagation properties, thus requiring non-uniform complex refinement to be capable of characterizing the minimum wavelengths of the problem.

- The use of curl-curl formulation for Maxwell’s equations with respect to first-order Maxwell’s curl equations provides with several advantages and drawbacks. On the one hand, double curl formulation allows to solve independently for the wave electric field in all the mesh nodes and requires no treatment for non-self-adjoint first order derivatives as in for Yee’s scheme [75]. On the other hand, it is known that the double curl equations have more solutions than first order equations [76] (i.e. spurious solutions) under certain circumstances. In FE, this is treated either by penalizing the non-zero divergence as in Ref. [77], or using Nédélec edge elements discretization, which solves for the difficulties of spurious solutions [74, 78, 79]. The latter is limited to divergence-free cases, and provides hindered computational efficiency and accuracy [78] with respect to nodal element formulation. However, the latter requires appropriate treatment of singularities in PEC corners.

In this Thesis, we have taken advantage of the FEM functionalities provided by the open-source FE discretization library MFEM [80] and its associated basis functions, linear and bilinear integrators, developed by the Lawrence Livermore National Laboratory (LLNL). The library was chosen amongst others due to its applicability to the EM wave problem and long-term capabilities, given the extensive background of its developers and previous experience of other groups as the Plasma Science and Fusion Center (PSFC), that applied the library also for full-wave simulations in cold-plasmas, and in that case, located at the scrap-off layer (SOL) of fusion reactors [81].

4.2.1 Physical model

The model solves Maxwell’s inhomogeneous wave equation in frequency domain (i.e. Eq. (2.4–5)), also called the curl-curl wave-equation for the electric field

$$\nabla \times (\nabla \times \hat{\mathbf{E}}) - k_0^2 \bar{\kappa} \cdot \hat{\mathbf{E}} = i\omega\mu_0 \hat{\mathbf{J}}_a, \quad (4.2-1)$$

where $\mathbf{E} = \Re[\hat{\mathbf{E}} \exp(-i\omega t)]$, k_0 is the wave number in vacuum, and $\bar{\kappa}$ is the dielectric tensor which models the plasma EM response. A cold-plasma dielectric tensor description is used, including effective collisionalities for each species as in Eqs. (2.3–28), (2.3–31)-(2.3–33). The cold-plasma model (see §2.3.1) assumes that (i) the electric fields are linear, (ii) the thermal speed of electrons is negligible, (iii) the velocity of the plasma constituents is negligible to the wave phase velocity, (iv) and also disregarding the pressure contribution. As a result of these assumptions the plasma response obtained is local, so that the wave propagation and absorption properties at each point depend on the local dielectric tensor. The collisionless cold-plasma model is known to be unable to reproduce the ECR. The effects of including wave damping in terms of an effective collisionality into the cold-plasma model were shown for a 1D model in §3.1.4. Collisions were shown to determine the width of the resonance layer for the case of EM power propagating in the decreasing magnetic field direction. In the case of wave propagation in the increasing magnetic field direction, for low damping the reflection, transmission and absorption coefficients were kept unaffected.

As a result the model retains the relevant physics to study many of the wave-plasma interaction problems, including propagation, cutoffs, and accessibility [27], including that of the plasmas appearing in ECRTs.

The wave-particle interaction is timely coupled whenever the characteristic transport time τ_c and wave period are similar. In this technology, $2\pi/\omega \ll \tau_c$ so that the wave equation can be solved in frequency domain and the electromagnetic problem can be treated as “fast” and the transport problem as “slow”. In other words, the EM waves perform many complete cycles before the plasma properties are modified due to transport phenomena. The plasma-wave response is then termed as “fast” and the plasma transport response as “slow”. As a consequence, the results of the waves can be obtained for “frozen” plasma properties.

As the form of Maxwell’s wave equation solved has been also linearized, the superposition principle applies, so that for excitation of more than one frequency mode in time, the individual mode solutions to each excitation can be added to obtain the complete EM field solution.

4.2.2 Mathematical model

4.2.2.1 Variational formulation

Applying the dot product of Eq. (2.4-5) with the complex conjugate of a trial function $\hat{\mathbf{W}}$, and integrating in the simulation domain Ω , we obtain

$$\iiint_{\Omega} \nabla \times (\nabla \times \hat{\mathbf{E}}) \cdot \hat{\mathbf{W}}^* dV - k_0^2 \iiint_{\Omega} \bar{\kappa} \hat{\mathbf{E}} \cdot \hat{\mathbf{W}} dV = i\omega\mu_0 \iiint_{\Omega} \hat{\mathbf{j}}_a \cdot \hat{\mathbf{W}}^* dV. \quad (4.2-2)$$

Manipulation of Eq. (4.2-2), and applying both integration by parts and Gauss theorem, results in

$$\iiint_{\Omega} \nabla \times (\nabla \times \hat{\mathbf{E}}) \cdot \hat{\mathbf{W}}^* dV = \iiint_{\Omega} (\nabla \times \hat{\mathbf{W}}^*) \cdot (\nabla \times \hat{\mathbf{E}}) dV + \iint_{\partial\Omega} \hat{\mathbf{W}}^* \cdot (\hat{\mathbf{n}} \times \nabla \times \hat{\mathbf{E}}) dA, \quad (4.2-3)$$

where $\partial\Omega$ is the boundary enclosing domain Ω , $\hat{\mathbf{n}}$ is the local normal vector to each boundary element of $\partial\Omega$. As a result, the weak form of Eq. (2.4-5) is [78]

$$\begin{aligned} & \iiint_{\Omega} [(\nabla \times \hat{\mathbf{W}}^*) \cdot (\nabla \times \hat{\mathbf{E}}) - k_0^2 \hat{\mathbf{W}}^* \cdot \bar{\kappa} \cdot \hat{\mathbf{E}}] dV + \\ & \iint_{\partial\Omega} \hat{\mathbf{W}}^* \cdot [\mathbf{1}_n \times (\nabla \times \hat{\mathbf{E}})] dS = i\mu_0\omega \iiint_{\Omega} \hat{\mathbf{W}}^* \cdot \hat{\mathbf{j}}_a dV. \end{aligned} \quad (4.2-4)$$

The second term of Eq. 4.2-4 represents the boundary conditions. The boundaries can be classified in

$$\partial\Omega = \partial\Omega_D + \partial\Omega_N, \quad (4.2-5)$$

which represent homogeneous Dirichlet (i.e. perfect electric conductors PEC) and Neumann (i.e. perfect magnetic conductor PMC) boundary conditions, defined as

$$\hat{\mathbf{n}} \times \hat{\mathbf{E}} = 0, \quad \partial\Omega \in \partial\Omega_D, \quad (4.2-6)$$

$$\hat{\mathbf{n}} \times (\nabla \times \hat{\mathbf{E}}) = 0, \quad \partial\Omega \in \partial\Omega_N. \quad (4.2-7)$$

Application of Neumann boundary conditions results in

$$\iint_{\partial\Omega_N} \hat{\mathbf{n}} \times (\nabla \times \hat{\mathbf{E}}) \cdot \hat{\mathbf{W}}^* dS = 0. \quad (4.2-8)$$

In the case of Dirichlet conditions, rearranging the terms in the expression one finds

$$\hat{\mathbf{W}}^* \cdot [\hat{\mathbf{n}} \times (\nabla \times \hat{\mathbf{E}})] = -\hat{\mathbf{n}} \times \hat{\mathbf{W}}^* \cdot (\nabla \times \hat{\mathbf{E}}). \quad (4.2-9)$$

Given that Galerkin's formulation is used so that the weighting and test functions are both of the same functional space, the Dirichlet homogeneous boundary condition is taken as essential boundary condition on PEC. Thus, $\hat{\mathbf{n}} \times \hat{\mathbf{W}}^* = 0$ at $\partial\Omega_D$, and it is straightforward to find that

$$\iint_{\partial\Omega_D} \hat{\mathbf{n}} \times (\nabla \times \hat{\mathbf{E}}) \cdot \hat{\mathbf{W}}^* dS = 0. \quad (4.2-10)$$

As a result, after the application of boundary conditions given in Eq. (4.2-6) and (4.2-7), Eq. (4.2-4) reads

$$\iiint_{\Omega} [(\nabla \times \hat{\mathbf{W}}^*) \cdot (\nabla \times \hat{\mathbf{E}}) - k_0^2 (\bar{\kappa} \hat{\mathbf{E}}) \cdot \hat{\mathbf{W}}^*] dV = i\mu_0\omega \iiint_{\Omega} \hat{\mathbf{W}}^* \cdot \hat{\mathbf{j}}_a dV. \quad (4.2-11)$$

Equation (4.2-11) can be formulated by bilinear and linear forms so that we seek to find $\hat{\mathbf{E}}$ fulfilling:

$$a(\hat{\mathbf{W}}, \hat{\mathbf{E}}) = b(\hat{\mathbf{W}}), \quad (4.2-12)$$

where $a(\hat{\mathbf{W}}, \hat{\mathbf{E}})$ is a bilinear form and $b(\hat{\mathbf{W}})$ is a linear form defined as

$$a(\hat{\mathbf{W}}, \hat{\mathbf{E}}) = \iiint_{\Omega} \left[(\nabla \times \hat{\mathbf{W}}^*) \cdot (\nabla \times \hat{\mathbf{E}}) - k_0^2 (\bar{\kappa} \hat{\mathbf{E}}) \cdot \hat{\mathbf{W}}^* \right] dV, \quad (4.2-13)$$

$$b(\hat{\mathbf{W}}) = i\mu_0\omega \iiint_{\Omega} \hat{\mathbf{j}}_a \cdot \hat{\mathbf{W}}^* dV. \quad (4.2-14)$$

The FE method splits the domain Ω into finite elements where the discretization of $\hat{\mathbf{E}}, \hat{\mathbf{W}}$ is chosen, depending on the problem. Application of the bilinear and linear integrators onto the domain results in a sparse linear system $\mathbf{A}\mathbf{x} = \mathbf{b}$ that is solved by sparse matrix solvers.

4.2.2.2 Mixed finite element discretization

In the problems discussed here, solutions obtained are for modal expansions in one of the three dimensions in Euclidean space. Solutions are obtained for each mode in the other two dimensions. Two cases have been implemented:

- A planar solver (THAMES), where the solutions are obtained in Cartesian coordinates (x, y) and the modal expansion is applied in z . In this case the modes wave number $k_z \in \mathbb{R}$;
- An axisymmetric solver (ATHAMES) where the solution is obtained in cylindrical coordinates (z, r) , and the modal expansion is applied in θ for which the azimuthal mode number $m \in \mathbb{Z}$.

The planar case is not of special interest for ECR thruster geometry but its implementation allowed to verify the code behavior of other features as using an inhomogeneous dielectric tensor including resonances and cutoffs, the imposition of boundary condition, and, in general, a similar implementation structure to that of the axisymmetric code version. The axisymmetric code adds extra complexity to the solution since it modifies the integrators required, also including the axisymmetric boundary conditions. However, the overall code structure is maintained. The axisymmetric case is of greater interest for the simulation of ECRTs, as in general these thrusters present a high level of axisymmetry, some of them as the coaxial ECRT being almost purely axisymmetric (except the propellant injection ports).

In both cases, the fields are decomposed into *in-plane* (e.g. x_1 and x_2) and *out-of-plane* (e.g. x_3) components, where the simulation plane is that formed by the two coordinates without modal expansion. Nédélec ($H(\text{curl}, \Omega)$ -conforming¹) elements [74, 82] are used for the in-plane components and Lagrange nodal ($H^1(\Omega)$ -conforming²) elements for the *out-of-plane* components of $\vec{\mathbf{E}}$ vector. These functional bases depend on the polynomial degree or functional base orders p_N and p_L . The element order determines the amount of degrees of freedom (d.o.f.) per element. For orders $p_N = p_L = p = 1$ we write

$$\vec{\mathbf{E}}(x_1, x_2) = \sum_i a_i \tilde{\mathbf{N}}_i(x_1, x_2) + \sum_l b_l \tilde{\mathbf{L}}_l(x_1, x_2) \mathbf{1}_{x_3}, \quad (4.2-15)$$

where i and l correspond to the indexes covering all elements edges and vertices, $\tilde{\mathbf{N}}_i$ are the $H(\text{curl})$ continuous Nédélec vector basis functions of order $p = 1$, a_i is each d.o.f. representing the tangential value of the electric field at each edge in the mesh, $\tilde{\mathbf{L}}_l$ represents $H^1(\Omega)$ continuous Lagrange basis functions used for the out-of-plane electric component, and b_l each d.o.f. representing the field component values at the nodes.

¹Nédélec elements are *curl conforming* i.e. their functional space is a subspace of $H(\text{curl}, \Omega)$, where for $\Omega \in \mathbb{R}^n$ $H(\text{curl}, \Omega) = \{ \mathbf{v} \in (L^2(\Omega))^n \mid \nabla \times \mathbf{v} \in (L^2(\Omega))^n \}$, being $L^2(\Omega)$ the subspace of square integrable functions in Ω [78].

²For $\Omega \in \mathbb{R}^n$ Sobolev space $H^1(\Omega) := \{ f \in L^2(\Omega); \partial_j f \in L^2(\Omega), j \in 1, \dots, n \}$.

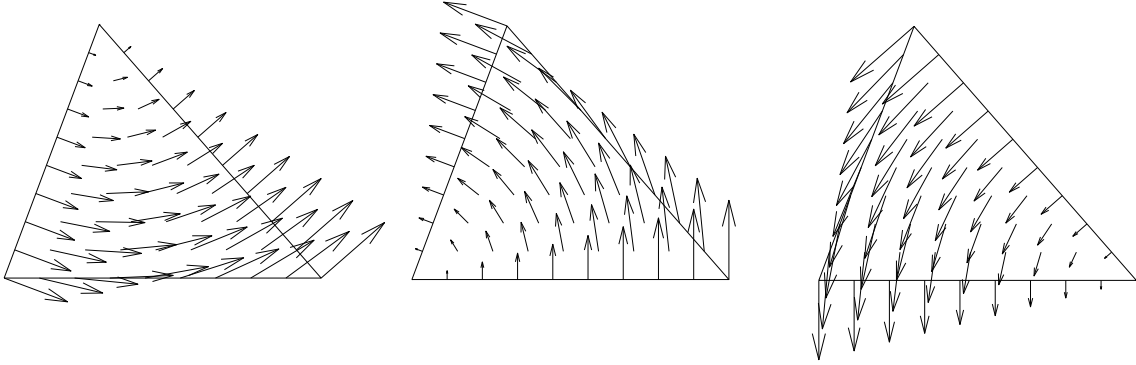


Figure 4.1: Nédélec vector basis functions of order $p_N = 1$ for a triangular element.

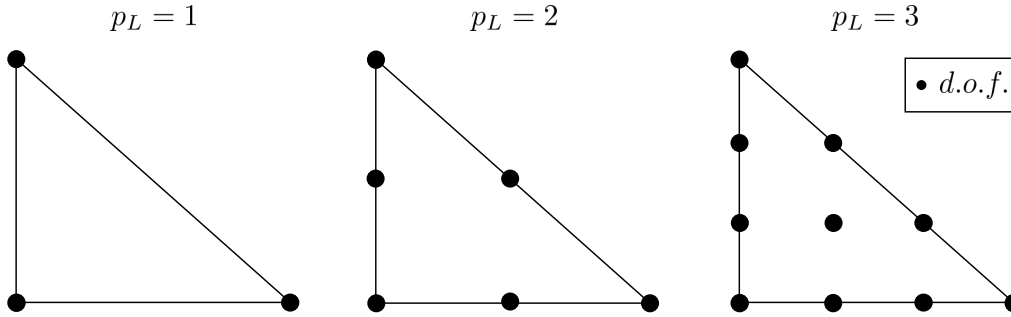


Figure 4.2: Degrees of freedom in a Lagrange triangular element for different p_L .

The local Nédélec shape functions associated with the edge i connecting nodes i and j can be expressed [79] in terms of barycentric coordinates λ_i where $i = 1, 2, 3$, as

$$\tilde{\mathbf{N}}_i = l_{ij} (\lambda_i \nabla \lambda_j - \lambda_j \nabla \lambda_i), \quad (4.2-16)$$

being l_{ij} the edge length connecting the nodes i and j . Figure 4.1 shows the Nédélec vector basis functions $\tilde{\mathbf{N}}_i$ for a linear triangular element. Each function is associated to an edge, featuring a constant tangential field value at the associated edge and a perpendicular field at the other two edges [79]. The vector functions are zero at the opposite node of the associated edge. These elements ensure tangential continuity of the interpolated field allowing also discontinuous normal field, for instance at a material discontinuity. Additionally, they are also known to be divergence free [83]. Due to these two last properties, this functional space is useful for the simulation of divergence free electric fields obtained from EM FEM codes. Moreover, this basis allows to specify directly boundary tangential boundary conditions, being a homogeneous Dirichlet that of a PEC. The modulus of the vector basis functions associated to each degree of freedom is represented in Figs. 4.3a-4.3c, using MFEM's tool *display-basis* and visualized using software GLVIS [84].

The Lagrange functional space is used to describe scalar variables. In this case, they are used for the modeling of the out-of-plane component. The value of each scalar function \tilde{P}_l for a first order Lagrange ($p_L = 1$) element is shown in Figs. 4.3d-4.3f. The magnitude of each function is maximum at the vertex of the associated degree of freedom, and zero at the other two. Within the element, the functions increase linearly from the non-associated vertices towards the location of the associated degree of freedom. The degrees of freedom are in this case the values of the field at nodes in the triangle. For a linear element that is at the three vertices of the triangle and increasing in order, the degrees of freedom scale as shown in Fig. 4.2.

Note that the number of degrees of freedom (d.o.f.) per element does not scale linearly with the element order. For instance for $p_N = 1$, Nédélec elements features 3 d.o.f., while for $p_N = 2$ is 8

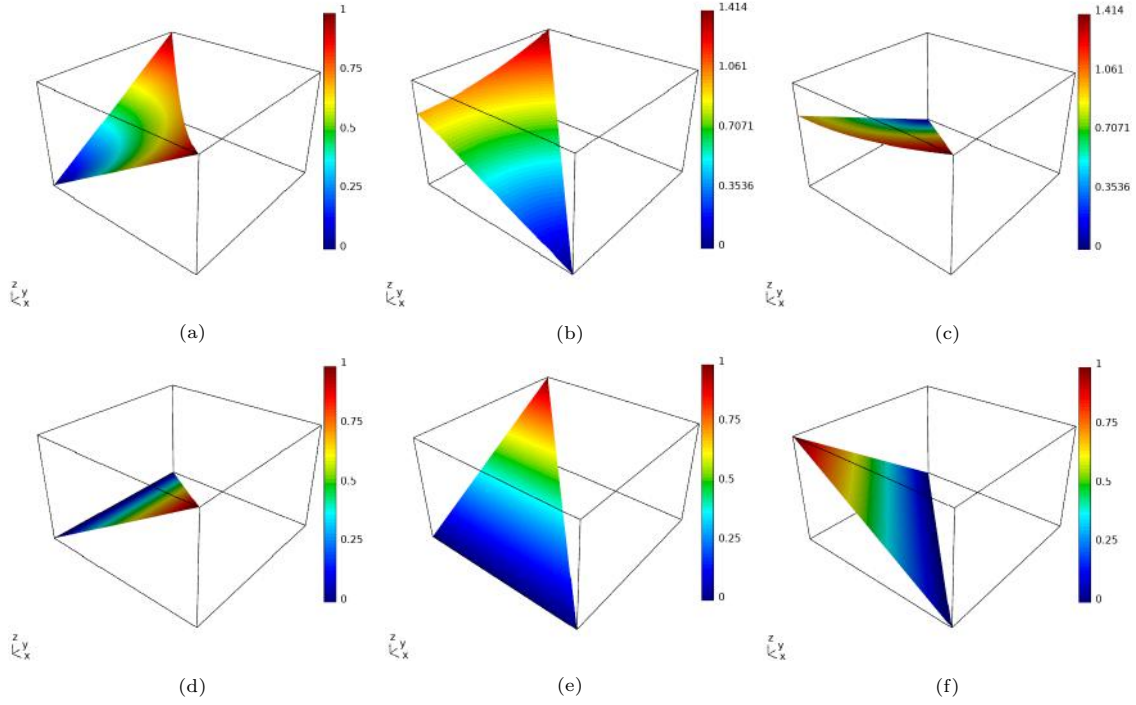


Figure 4.3: Representation in a reference element of the magnitude of the basis functions associated to each degree of freedom for (a)-(c) the Nédélec first order vector basis functions, and (d)-(f) for the Lagrange first order nodal functions [80].

(6 for the values at the edges and 2 for values inside the triangle) and for $p_N = 3$ is 15 (9 for the values at the edges and 6 for values inside the triangle). In the cases of Lagrange elements, the d.o.f. number per element is 3 for $p_L = 1$, 6 for $p_L = 2$, and 10 for $p_L = 3$.

The increase in d.o.f. number allows to reduce the local approximation error without further refining the spatial discretization. As a result, the local approximation error is directly related to the functional basis type and order, analogously to the scheme in a finite difference method. For a $p_L = 1$ Lagrange triangular element the approximation error is $\mathcal{O}(h^2)$, being h the largest triangle edge length. For the Nédélec linear elements, the error is proportional to $\mathcal{O}(h)$ due to their constant value in a specific spatial direction [83]. The approximation error order scales with the element order, so that the approximation error for Lagrange elements is found to be $\mathcal{O}(h^{(p_L+1)})$ while for Nédélec it is $\mathcal{O}(h^{(p_N)})$.

4.2.2.3 Planar problem

Assuming planar wave propagation in z coordinate, the electric field can be expressed as

$$\mathbf{E}(x, y, z) = \Re \left\{ \tilde{\mathbf{E}}(x, y) \exp(ik_z z - i\omega t) \right\}, \quad (4.2-17)$$

so that $\hat{\mathbf{E}} = \tilde{\mathbf{E}} \exp(ik_z z)$. The electric field is then decomposed into in-plane and out-of-plane components as

$$\tilde{\mathbf{E}} = \tilde{\mathbf{E}}_{xy} + \tilde{E}_z \mathbf{1}_z, \quad (4.2-18)$$

where $\tilde{\mathbf{E}}_{xy} = \tilde{E}_x \mathbf{1}_x + \tilde{E}_y \mathbf{1}_y$, and $\tilde{E}_{(\cdot)}$ are complex-valued functions of x and y coordinates. Planar propagation in z substitutes $\nabla \rightarrow \bar{\nabla} + ik_z$, in which $\bar{\nabla} = (\partial/\partial x, \partial/\partial y)$. Using vector differential operator identities³, the curl of field $\tilde{\mathbf{E}}$ is then given by

$$\nabla \times \tilde{\mathbf{E}} = \bar{\nabla} \times \tilde{\mathbf{E}}_{xy} + ik_z \mathbf{1}_z \times \tilde{\mathbf{E}}_{xy} + \bar{\nabla} \tilde{E}_z \times \mathbf{1}_z. \quad (4.2-19)$$

³ $\nabla \times (f\mathbf{A}) = f\nabla \times \mathbf{A} + \nabla f \times \mathbf{A}$ and $\nabla(fg) = f\nabla g + g\nabla f$

As a result of using the field expansion shown in Eq. (4.2–17), Eq. (4.2–11) is simplified to a two dimensional problem where the variables to be solved are in x, y coordinates and the volume integrals turn into surface integrals. All the differential operators are then substituted for the planar version, where the curl is given by Eq. (4.2–19). Since the electric field components feature complex amplitudes, if real value solvers are to be used, a solution is to decompose the fields into real and imaginary parts, each of them modeled by independent FE functions. Taking the real value of the resulting equation, which involves both real and imaginary parts of the fields, the solution can be obtained using a block matrix of the bilinear integrators. This block matrix is shown in Tab. 4.1. Each row and column of that block matrix provides the bilinear integrators which relate each trial function (real, imaginary, and in/out of plane component) with a test function. Each entry of the block matrix will be represented by a $M \times N$ large matrix, being M the size of the corresponding W degrees of freedom and N the number of degrees of freedom of the corresponding electric field E . Note that the terms arising from the dielectric tensor have been subdivided into matrix $\bar{\kappa}_{xy,xy}$, vectors $\kappa_{xy,z}$ and $\kappa_{z,xy}$ and element $\kappa_{z,z}$, where sub-indexes represent the index of the matrix related to the corresponding coordinates.

	$\tilde{\mathbf{E}}_{xy}^R$	$\tilde{\mathbf{E}}_{xy}^I$	\tilde{E}_z^R	\tilde{E}_z^I
$\tilde{\mathbf{W}}_{xy}^R$	$(\nabla \times \tilde{\mathbf{W}}_{xy}^R) \cdot (\nabla \times \tilde{\mathbf{E}}_{xy}^R)$ $-k_0^2 [\bar{\kappa}_{xy,xy}^R \cdot \tilde{\mathbf{E}}_{xy}^R] \cdot \tilde{\mathbf{W}}_{xy}^R$ $+k_z^2 \tilde{\mathbf{E}}_{xy}^R \cdot \tilde{\mathbf{W}}_{xy}^R$	$k_0^2 [\bar{\kappa}_{xy,xy}^I \cdot \tilde{\mathbf{E}}_{xy}^I] \cdot \tilde{\mathbf{W}}_{xy}^R$	$-k_0^2 \tilde{E}_z^R \kappa_{xy,z}^R \cdot \tilde{\mathbf{W}}_{xy}^R$	$-k_z \nabla \tilde{E}_z^I \tilde{\mathbf{W}}_{xy}^R$ $+k_0^2 \tilde{E}_z^I \kappa_{xy,z}^I \cdot \tilde{\mathbf{W}}_{xy}^R$
$\tilde{\mathbf{W}}_{xy}^I$	$-k_0^2 [\bar{\kappa}_{xy,xy}^I \cdot \tilde{\mathbf{E}}_{xy}^I] \cdot \tilde{\mathbf{W}}_{xy}^I$	$(\nabla \times \tilde{\mathbf{W}}_{xy}^I) \cdot (\nabla \times \tilde{\mathbf{E}}_{xy}^I)$ $-k_0^2 [\bar{\kappa}_{xy,xy}^R \cdot \tilde{\mathbf{E}}_{xy}^I] \cdot \tilde{\mathbf{W}}_{xy}^I$ $+k_z^2 \tilde{\mathbf{E}}_{xy}^I \cdot \tilde{\mathbf{W}}_{xy}^I$	$k_z \nabla \tilde{E}_z^R \tilde{\mathbf{W}}_{xy}^I$ $-k_0^2 \tilde{E}_z^R \kappa_{xy,z}^I \cdot \tilde{\mathbf{W}}_{xy}^I$	$-k_0^2 \tilde{E}_z^I \kappa_{xy,z}^R \cdot \tilde{\mathbf{W}}_{xy}^I$
\tilde{W}_z^R	$-k_0^2 \kappa_{z,xy}^R \cdot \tilde{\mathbf{E}}_{xy}^R \tilde{W}_z^R$	$k_z \nabla \tilde{W}_z^R \tilde{\mathbf{E}}_{xy}^I$ $+k_0^2 \tilde{W}_z^R \kappa_{z,xy}^I \cdot \tilde{\mathbf{E}}_{xy}^I$	$\nabla \tilde{W}_z^R \cdot \nabla \tilde{E}_z^R$ $-k_0^2 \kappa_{zz}^R \tilde{E}_z^R \tilde{W}_z^R$	$k_0^2 \kappa_{zz}^I \tilde{E}_z^I \tilde{W}_z^R$
\tilde{W}_z^I	$-k_z \nabla \tilde{W}_z^I \tilde{\mathbf{E}}_{xy}^R$ $-k_0^2 \tilde{W}_z^I \kappa_{z,xy}^I \cdot \tilde{\mathbf{E}}_{xy}^R$	$-k_0^2 \kappa_{z,xy}^R \cdot \tilde{\mathbf{E}}_{xy}^I \tilde{W}_z^I$	$-k_0^2 \kappa_{z,z}^I \tilde{E}_z^R \tilde{W}_z^I$	$\nabla \tilde{W}_z^I \cdot \nabla \tilde{E}_z^I$ $-k_0^2 \kappa_{z,z}^R \tilde{E}_z^I \tilde{W}_z^I$

Table 4.1: 4x4 Block matrix of bilinear integrator forms splitting real and imaginary parts (represented by superscripts R and I) of both in-plane and out-of-plane components of the electric field, assuming plane wave propagation in z direction.

4.2.2.4 Axisymmetric problem

In the further complex axisymmetric formulation, the simulation domain is expressed in cylindrical coordinates and plane waves are assumed along θ coordinate for all quantities so that

$$\begin{aligned} \hat{\mathbf{E}}(z, r, \theta) &= \sum_{m=-\infty}^{\infty} \tilde{\mathbf{E}}^{(m)}(z, r) e^{im\theta}, \\ \hat{\mathbf{j}}_a(z, r, \theta) &= \sum_{m=-\infty}^{\infty} \tilde{\mathbf{j}}_a^{(m)}(z, r) e^{im\theta}. \end{aligned} \quad (4.2-20)$$

This expansion allows to solve the system for all the modes. However, depending on the problem some modes will contribute more significantly to the global solution than others. Due to the linear character of Eq. (4.2–11), each mode equation (i.e. for a value of $m \in \mathbb{Z}$) can be solved independently and depends on the value of m .

Let us solve now the problem for a single mode m so that we will omit superscript (m) . Splitting $\tilde{\mathbf{E}} = \tilde{\mathbf{E}}_t(z, r) + \tilde{E}_\theta(z, r)\mathbf{1}_\theta$, where $\tilde{\mathbf{E}}_t$ represents the tangential fields to the plane zr , and taking the curl of this field of mode m , it is straightforward to find that

$$\nabla \times \hat{\mathbf{E}} = e^{im\theta} \left(\nabla \times \tilde{\mathbf{E}}_t - \frac{\mathbf{1}_\theta}{r} \times \nabla (r\tilde{E}_\theta) + \frac{im}{r} \times \tilde{\mathbf{E}}_t \right), \quad (4.2-21)$$

and similarly for the trial functions

$$\nabla \times \hat{\mathbf{W}}^* = e^{-im\theta} \left(\nabla \times \tilde{\mathbf{W}}_t^* - \frac{\mathbf{1}_\theta}{r} \times \nabla (r\tilde{W}_\theta^*) - \frac{im}{r} \times \tilde{\mathbf{W}}_t^* \right). \quad (4.2-22)$$

Taking the dot product of Eqs. (4.2-21) and (4.2-22) results in

$$\begin{aligned} (\nabla \times \hat{\mathbf{E}}) \cdot (\nabla \times \hat{\mathbf{W}}^*) &= \nabla \times \tilde{\mathbf{E}}_t \cdot \nabla \times \tilde{\mathbf{W}}_t^* + \frac{m^2}{r^2} \tilde{\mathbf{E}}_t \cdot \tilde{\mathbf{W}}_t^* - \frac{im}{r^2} \tilde{\mathbf{E}}_t \cdot \nabla (r\tilde{W}_\theta^*) \\ &\quad + \frac{im}{r^2} \tilde{\mathbf{W}}_t^* \cdot \nabla (r\tilde{E}_\theta) + \frac{1}{r^2} \nabla (r\tilde{E}_\theta) \cdot \nabla (r\tilde{W}_\theta^*). \end{aligned} \quad (4.2-23)$$

Let us decompose the dielectric tensor as

$$\bar{\bar{\kappa}} = \begin{pmatrix} \bar{\kappa}_{tt} & \boldsymbol{\kappa}_{t,\theta} \\ \boldsymbol{\kappa}_{\theta,t} & \kappa_{\theta,\theta} \end{pmatrix}, \quad (4.2-24)$$

so that combining combining Eqs. (4.2-20)-(4.2-24) with Eq. (4.2-11) we can find a real equation that involves both the real and imaginary degrees of freedom of the problem representing the electric field complex amplitude vector $\tilde{\mathbf{E}}$. Such equation is composed by the addition of multiple bilinear integrators that can be ordered in a block matrix, which is shown in Tab. 4.2. As the differential $dV = r d\theta dr dz$ the integration in a 3D domain Ω turns into the meridional plane Σ (i.e. z, r) so that

$$\iiint_{\Omega} dV \rightarrow 2\pi \iint_{\Sigma} r dr dz, \quad (4.2-25)$$

so that for all the volume integrals in Eq. (4.2-11) the integrands are scaled by a factor r .

	$\tilde{\mathbf{E}}_t^R$	$\tilde{\mathbf{E}}_t^I$	\tilde{E}_θ^R	\tilde{E}_θ^I
$\tilde{\mathbf{W}}_t^R$	$r(\nabla \times \tilde{\mathbf{W}}_t^R) \cdot (\nabla \times \tilde{\mathbf{E}}_t^R)$ $-rk_0^2(\bar{\kappa}_{t,t}^R \cdot \tilde{\mathbf{E}}_t^R) \cdot \tilde{\mathbf{W}}_t^R$ $+\frac{m^2}{r} \tilde{\mathbf{E}}_t^R \cdot \tilde{\mathbf{W}}_t^R$	$rk_0^2(\bar{\kappa}_{t,t}^I \cdot \tilde{\mathbf{E}}_t^I) \cdot \tilde{\mathbf{W}}_t^R$	$-rk_0^2 \tilde{E}_\theta^R \boldsymbol{\kappa}_{t,\theta}^R \cdot \tilde{\mathbf{W}}_t^R$	$-\frac{m}{r} \nabla(r\tilde{E}_\theta^I) \cdot \tilde{\mathbf{W}}_t^R$ $+rk_0^2 \tilde{E}_\theta^I \boldsymbol{\kappa}_{t,\theta}^I \cdot \tilde{\mathbf{W}}_t^R$
$\tilde{\mathbf{W}}_t^I$	$-rk_0^2 [\bar{\kappa}_{t,t}^I \cdot \tilde{\mathbf{E}}_t^I] \cdot \tilde{\mathbf{W}}_t^I$	$r(\nabla \times \tilde{\mathbf{W}}_t^I) \cdot (\nabla \times \tilde{\mathbf{E}}_t^I)$ $-rk_0^2 [\bar{\kappa}_{t,t}^R \cdot \tilde{\mathbf{E}}_t^I] \cdot \tilde{\mathbf{W}}_t^I$ $+\frac{m^2}{r} \tilde{\mathbf{E}}_t^I \cdot \tilde{\mathbf{W}}_t^I$	$\frac{m}{r} \nabla(r\tilde{E}_\theta^R) \cdot \tilde{\mathbf{W}}_t^I$ $-rk_0^2 \tilde{E}_\theta^R \boldsymbol{\kappa}_{t,\theta}^I \cdot \tilde{\mathbf{W}}_t^I$	$-rk_0^2 \tilde{E}_\theta^I \boldsymbol{\kappa}_{t,\theta}^R \cdot \tilde{\mathbf{W}}_t^I$
\tilde{W}_θ^R	$-rk_0^2 \tilde{W}_\theta^R \boldsymbol{\kappa}_{\theta,t}^R \cdot \tilde{\mathbf{E}}_t^R$	$\frac{m}{r} \nabla(r\tilde{W}_\theta^R) \cdot \tilde{\mathbf{E}}_t^I$ $+rk_0^2 \tilde{W}_\theta^R \boldsymbol{\kappa}_{\theta,t}^I \cdot \tilde{\mathbf{E}}_t^I$	$\frac{1}{r} \nabla(r\tilde{W}_\theta^R) \cdot \nabla(r\tilde{E}_\theta^R)$ $-rk_0^2 \boldsymbol{\kappa}_{\theta,\theta}^R \tilde{E}_\theta^R \tilde{W}_\theta^R$	$rk_0^2 \boldsymbol{\kappa}_{\theta,\theta}^I \tilde{E}_\theta^I \tilde{W}_\theta^R$
\tilde{W}_θ^I	$-\frac{m}{r} \nabla(r\tilde{W}_\theta^I) \cdot \tilde{\mathbf{E}}_t^R$ $-rk_0^2 \tilde{W}_\theta^I \boldsymbol{\kappa}_{\theta,t}^I \cdot \tilde{\mathbf{E}}_t^R$	$-rk_0^2 \tilde{W}_\theta^I \boldsymbol{\kappa}_{\theta,t}^R \cdot \tilde{\mathbf{E}}_t^I$	$-rk_0^2 \boldsymbol{\kappa}_{\theta,\theta}^I \tilde{E}_\theta^R \tilde{W}_\theta^I$	$\frac{1}{r} \nabla(r\tilde{W}_\theta^I) \cdot \nabla(r\tilde{E}_\theta^I)$ $-rk_0^2 \boldsymbol{\kappa}_{\theta,\theta}^R \tilde{E}_\theta^I \tilde{W}_\theta^I$

Table 4.2: 4x4 Block system of bilinear integrator forms splitting real and imaginary parts (represented by superscripts R and I) of both in-plane and out-of-plane components of the electric field, assuming plane wave propagation in θ direction for any mode number m .

In order to satisfy the axisymmetric boundary conditions at the z -axis, the discretization of $\tilde{\mathbf{E}}^{(m)}$ and $\tilde{\mathbf{W}}^{(m)}$ in the axisymmetric case depends on the mode number m . The conditions are [79]:

$$E_r^{(0)} = E_\theta^{(0)} = 0, \quad (4.2-26)$$

$$E_r^{(\pm 1)} = \mp i E_\theta^{(\pm 1)} = 0, \quad E_z^{(\pm 1)} = 0, \quad (4.2-27)$$

$$E_r^{(m)} = E_\theta^{(m)} = E_z^{(m)} = 0, \quad |m| > 1. \quad (4.2-28)$$

The discretization that fulfills such conditions [79, 85] is:

$$\mathbf{E}^{(m)} = \begin{cases} \sum_{i=1}^{N_{\text{edge}}} \mathbf{N}_i(r, z) e_{t,i}^{(m)} + \mathbf{1}_\theta \sum_{i=1}^{N_{\text{node}}} N_i(r, z) e_{\theta,i}^{(m)}, & m = 0, \\ \sum_{i=1}^{N_{\text{edge}}} r \mathbf{N}_i(r, z) e_{t,i}^{(m)} + (\mathbf{1}_\theta \mp i \mathbf{1}_r) \sum_{i=1}^{N_{\text{node}}} N_i(r, z) e_{\theta,i}^{(m)}, & m = \pm 1, \\ \sum_{i=1}^{N_{\text{edge}}} r \mathbf{N}_i(z, r) e_{t,i}^{(m)} + \mathbf{1}_\theta \sum_{i=1}^{N_{\text{node}}} N_i(z, r) e_{\theta,i}^{(m)}, & |m| > 1. \end{cases} \quad (4.2-29)$$

The conditions provided in Eqs. (4.2-26) and (4.2-28) are satisfied imposing PEC boundary conditions on the azimuthal fields at the nodes on the z -axis.

Note that ATHAMES current version assumes the field is purely axisymmetric (i.e. $m = 0$), as it is the one of main interest for ECRT simulations.

Having solved for $\tilde{\mathbf{E}}$, the wave magnetic field complex amplitude vector can be obtained using Eqs. (2.4-1) and (4.2-21) so that

$$\tilde{\mathbf{B}} = -\frac{i}{\omega} \left(\nabla \times \tilde{\mathbf{E}}_t - \mathbf{1}_\theta \times \frac{\nabla(r\tilde{E}_\theta)}{r} \right). \quad (4.2-30)$$

4.2.3 Coaxial transmission line model

In the coaxial ECRT, the power is transmitted to the plasma through a coaxial line that ends in a dielectric window at the thruster chamber. In order to simulate this condition, a lumped element model is used in which a small element upstream the coaxial line is excited with a current source. The boundary condition of the port is set to Neumann and as a result a TEM mode is excited along the coaxial line.

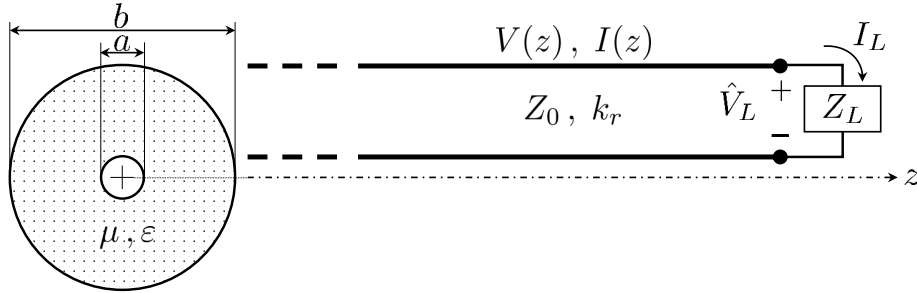


Figure 4.4: Coaxial lossless transmission line terminated in a load [86].

The coaxial transmission line and the plasma form an electromagnetic system as shown in Fig. 4.4. Often, in such systems, standing waves appear whenever there is an impedance mismatch between the loads applied on a line, Z_L , and the characteristic impedance of a transmission line, Z_0 . Let us assume that (i) a source located at $z < 0$, (ii) the line is lossless, (iii) and that is aligned with the z axis as depicted in Figure 4.4. A standing wave appearing in the coaxial can be represented by a total line voltage that results from the sum of an incident/forward wave and a reflected wave [86]

$$V(z) = V_f e^{ik_r z} + V_r e^{-ik_r z}. \quad (4.2-31)$$

Equivalently, the total current on the line is

$$I(z) = \frac{V_f(z)}{Z_0} e^{ik_r z} - \frac{V_r(z)}{Z_0} e^{-ik_r z}. \quad (4.2-32)$$

For a coaxial line (see Fig. 4.4)

$$Z_0 = \sqrt{\frac{\mu}{\varepsilon}} \frac{\ln b/a}{2\pi}, \quad (4.2-33)$$

where μ and ε are the permeability and permittivity of the material between the inner and outer conductors of the coaxial line, with respective diameters a and b .

The total voltage and current at the load are related by the load impedance as

$$Z_L = \frac{V_f + V_r}{V_f - V_r} Z_0. \quad (4.2-34)$$

Therefore, the *voltage reflection coefficient* or normalized reflected voltage wave ratio is

$$R = \frac{V_r}{V_f} = \frac{Z_L - Z_0}{Z_L + Z_0}, \quad (4.2-35)$$

where R is a complex number, which is only zero whenever the impedance of the load is equal to that of the line, so that the line is said to be *matched*.

Since there is a standing wave, the voltage on the line is not constant and the maximum and minimum voltages on the line are equal to

$$V_{max} = |V_f|(1 + |R|), \quad (4.2-36)$$

$$V_{min} = |V_f|(1 - |R|). \quad (4.2-37)$$

Thus the difference between V_{max} and V_{min} is directly related to the impedance mismatch of the line, and thus the *voltage standing wave ratio* (VSWR)

$$\text{VSWR} = \frac{|V_{max}|}{|V_{min}|} = \frac{1 + |R|}{1 - |R|}, \quad (4.2-38)$$

can be used as an indicator of the level of reflection on the transmission line.

4.3 Numerical implementation

4.3.1 Code architecture

The ATHAMES architecture is designed similarly to that of HYPHEN modules [60]. The design is based on modularity, to allow for adequate code debugging and verification. The code development is based on strict verification standards. Section §4.4 shows the different unit, functional, and integration tests developed. The code makes use of various programming languages. For pre-processing and post-processing routines (i.e. SET and POST), MATLAB is chosen due to its functionalities and packages. The computational code, named as CORE, is written in C++, as the code takes advantage of packages written in this language, specially the FE discretization library MFEM [80]. This library accounts for high-order FE spaces both in 2D and 3D including H^1 -conforming, $H(\text{div})$ -conforming, $H(\text{curl})$ -conforming spaces, discontinuous L^2 spaces, etc. It allows to deal with triangular, quadrilateral, tetrahedral, hexahedral elements, using different forms of refinement (e.g. uniform, local, non-conforming) depending on the element type and to optimize the mesh. Additionally, the code provides with compatibility to apply multiple solvers depending on the type of linear algebra system found, including GMRES, MINRES, PCG, hypre solvers, PETSc suite linear and non linear solvers and preconditioners, parallel and serial sparse direct solvers as SuperLU, KLU, STRUMPACK or UMFPACK from the SuiteSparse library.

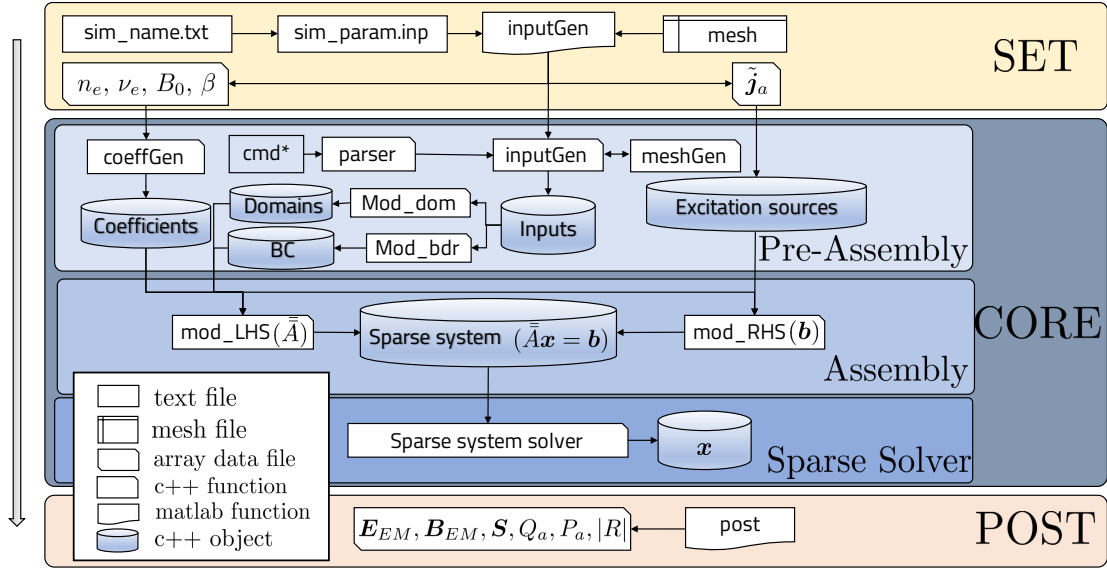


Figure 4.5: ATHAMES overall architecture

The overall structure of the code is depicted in Fig. 4.5. The code is comprised by three differentiated parts: (i) the SET, (ii) the CORE, and (iii) the POST units.

The SET unit comprises a series of subroutines that generate the necessary inputs for an EM simulation. These inputs are:

- `sim_name.txt` where the simulation name is written and all files are saved;
- the plasma properties (n_e, ν_e) obtained either with a preprocessing routine or from HYPHEN simulation outputs;
- the magnetic field topology file (or in absence of one the magnetic field data contained in HYPHEN simulation file);
- the `sim_params.inp` file where simulation parameters are detailed as simulation paths (e.g. mesh path), mesh information, domain types and boundary conditions, problem variables (e.g. excitation frequency), solution parameters (e.g. order of the finite elements used), and simulation flags (e.g. save BLOCK sparse matrix flag);
- the unstructured mesh file (e.g in formats `.msh`, `.vtk`, `.mesh`, etc).

Secondly, the code CORE is structured in several steps:

1. Input generation (`mod_inputGen.cpp`): in this step the code reads the input data from the SET files and creates the necessary objects to run a simulation.
2. Mesh generation (`mod_meshGen.cpp`): this function takes the mesh path, dimension, and refinement options to generate a mesh object of MFEM class `Mesh`.
3. Finite element space generation (`mod_feGen.cpp`): this function generates the finite element spaces associated to the degrees of freedom of the problem based on the mesh. The finite element spaces to be used are generated, in this case `H(curl)`-conforming function collection `ND_FECollection` for the in-plane electric field components and the `H1`-conforming function collection `H1_FECollection` for the out-of-plane components. The function creates these spaces based on the element orders specified in the input file.

4. Input variable 2D maps reading and objects generation for n_e , ν_e , B_0 , and β and also that for the current excitation sources, using the class `GridFunction` and its member functions.
5. Dielectric tensor generation by application of class `FunctionCoefficient` and its member functions.
6. Boundary condition module (`mod_bdr.cpp`): identifies the boundary condition type associated to the mesh boundary IDs based on the input simulation data. For the PEC boundary conditions it identifies the degrees of freedom associated to that boundary and adds them to the array of essential degrees of freedom.
7. Domain module (`mod_dom.cpp`): identifies the type and number of simulation domain subdivisions attributed to each mesh partition, assigning a mask to each domain depending on whether it is a plasma, vacuum or excitation source.
8. Coefficient generation: definition of the coefficients required by the bilinear and linear integrators using classes: (i) `Coefficient`, `VectorCoefficient` and `MatrixCoefficient` depending on the type of coefficient used, (ii) classes assigned only to a specific region using the mask created identifying each part of the domain named `Restricted`, (iii) additional coefficients were required in order to combine multiple coefficients, based on class inheritance property, (iv) and `VectorArray` and `MatrixArray` coefficients which allow to set vector and array entries defined in other coefficients.
9. RHS building `mod_rhs.cpp`: based on the input data, the linear form Eq. (4.2-14) is implemented using `VectorFEDomainLFIntegrator` for the in-plane components of the excitation current and `DomainLFIntegrator` for the out-of-plane components (i.e. both for the real and imaginary parts).
10. Block matrix assembly (`mod_lhs.cpp`): depending on whether or not the FE space of the test function is the same of the weight function, the module creates either bilinear or mixed-bilinear forms. These are respectively the diagonal and off-diagonal terms of block matrix shown in Tab. 4.2. Integrators used are shown in Table 4.3.
11. The rows and columns corresponding to the essential degrees of freedom found in the boundary definition module, are eliminated from the block matrix.
12. SparseMatrix \bar{A} of the linear system is created using the block matrix assembled.
13. The KLU solver is selected to be applied to solve this linear system, obtaining the final solution stored $\tilde{\mathbf{E}}$ in objects of class `GridFunction`. These data are saved in output text files, including optional data as sparse matrix A and RHS vector, etc.
14. $\tilde{\mathbf{E}}$ is then used to compute the terms of Eq. (4.2-30) which are the curl of the tangential field and the gradient of the azimuthal fields. For every element in `Mesh`, an associated the element transformation object defining all the methods to transform from reference to physical coordinates in the mesh is used in combination with member functions `GetGradient` and `GetCurl` of the class `GridFunction`. The results of `GetGradient` and `GetCurl` of the normal and tangential components of electric field, respectively, are stored into files which are post-processed to compute the magnetic field complex amplitude, and therefore the Poynting vector \mathbf{S} .

Lastly, a POST unit postprocesses the EM wave-fields and obtains the relevant outputs as the Poynting vector \mathbf{S} , the EM power absorption density maps Q_a , the reflection coefficient of the line $|R|$, or the solution. Additionally, it stores relevant variables, depending on the settings, in order to visualize variables as the sparse matrix solved, etc. These variables are controlled by user input flags specified in the `sim_params.inp` file.

Integrator	Trial space	Test Space	Coefficient(λ)	Operator
CurlCurlIntegrator	Nédélec	Nédélec	Scalar, matrix	$(\lambda \nabla \times \tilde{\mathbf{W}}_t, \nabla \times \tilde{\mathbf{E}}_t)$
VectorFEMassIntegrator	Nédélec	Nédélec	Scalar, matrix	$(\lambda \tilde{\mathbf{W}}, \tilde{\mathbf{E}})$
DiffusionIntegrator	H^1	H^1	Scalar, matrix	$(\lambda \nabla(r\tilde{W}_\theta), \nabla(r\tilde{E}_\theta))$
MassIntegrator	H^1	H^1	Scalar	$(\lambda \tilde{W}_\theta, \tilde{E}_\theta)$
MixedVectorMassIntegrator	Nédélec	Nédélec	Scalar, matrix	$(\lambda \tilde{\mathbf{W}}_t, \tilde{\mathbf{E}}_t)$
MixedVectorProductIntegrator	Nédélec	H^1	Vector	$(\lambda \tilde{W}_\theta, \tilde{\mathbf{E}}_t)$
MixedDotProductIntegrator	H^1	Nédélec	Vector	$(\lambda \tilde{E}_\theta, \tilde{\mathbf{W}}_t)$

Table 4.3: List of integrators provided by MFEM applied to build the block matrix system for $m = 0$.

4.3.2 Integration with HYPHEN

The main purpose of the Thesis is to provide complete simulations of ECRT plasma thrusters and perform parametric investigations on specific design and operation parameters. The main details of such coupling can be found in Chapter 5. Here some details regarding the implementation of the coupled simulation launcher and the approach used are provided. Additionally, an overview of the main aspects of the subroutines utilized to transfer data between codes is provided.

ATHAMES is required to be coupled to the HYPHEN [60] simulation transport code. As both codes are programmed in different programming languages (i.e. Fortran for HYPHEN and C++ for ATHAMES) and are independent codes, a wrapper that allows to call both codes and transfer information is required in order to obtain coupled simulations. This routine is implemented in Python.

Several adaptations to HYPHEN were required in order to obtain coupled simulations with a wave module, in this case ATHAMES. Amongst the few updates to HYPHEN required by this new feature, the following are highlighted:

- Definition of meshes of the type of interest for ECRT geometries.
- Addition of wave-module (e.g. ATHAMES) variables (e.g. number of wave module timesteps).
- PostData generation option to define a structure for iterative and sequential HYPHEN launches for coupled simulations.

The interaction between HYPHEN and ATHAMES is given by the inputs and output shown in Table 4.4.

Input	Origin
n_e, ν_e	HYPHEN(Electron fluid module)
B_0, β	Applied magnetic field data
Output	Destination
Q_a	HYPHEN (Electron Fluid module)

Table 4.4: Major inputs and outputs of ATHAMES (see Fig. 5.2).

4.3.2.1 Wrapper structure overview

First of all, the simulation files of each code have to be prepared separately as individual simulations. Then the set of HYPHEN has to be generated with provides with the necessary files to run a simulation (i.e. `SimState.hdf5`) and save printout data (i.e. `PostData.hdf5`). Then, the wrapper implemented reads the HYPHEN input simulation file `sim_params.inp` where the wrapper simulation settings are specified and based on the number of initialization steps (i.e. generally

using a polytropic law for the electrons or an isothermal electron population), simulation steps (i.e. total number of simulation steps of coupled simulation), and number of steps between wave module calls, the code launches HYPHEN and carries out a number of loops where (i) HYPHEN completes a number of steps, (ii) HYPHEN2ATHAMES.m code is called transferring the necessary data from HYPHEN simulation state to ATHAMES, (iii) ATHAMES is launched computing the EM fields, (iv) ATHAMES2HYPHEN.m is used to post-process the data, obtain derived quantities and transfer the data to HYPHEN; (v) HYPHEN is relaunched continuing from the last simulation timestep simulation state and with the updated map of EM power absorption.

4.3.2.2 HYPHEN-ATHAMES intercommunication subroutines

Regarding the implementation details of HYPHEN2ATHAMES.m, the function reads the simulation data and creates the simulation files compatible with ATHAMES for the electron density and collisionality and applied magnetic field. As the meshes utilized by HYPHEN feature much lower resolution than those used by ATHAMES (e.g. from 10^3 HYPHEN mesh cells to 10^5 ATHAMES mesh elements), the profiles require smoothing. The smoothing used is a Gauss filtering applied on the plasma properties. The smoothed plasma properties are then interpolated to W-mesh. In the case of magnetic field data, the magnetic field is interpolated from a finer magnetic mesh used to generate the Magnetic Field Aligned Mesh (MFAM) used by HYPHEN electron fluid module.

After ATHAMES execution process is finished, using the EM fields solution, the subroutine ATHAMES2HYPHEN.m computes the power absorption map, Poynting vector, the total power absorbed by the plasma and the power reflection coefficient. The power reflection coefficient is determined by the voltage standing wave ratio within the coaxial, computed as in Eq. (4.2-38). In the simulation settings, it can be decided whether the total power absorbed by the plasma source or the input or forwarded power is fixed. The former is less realistic but can be useful to investigate a specific thruster operating point. The latter is more adequate as it allows to investigate the behavior of the coupled EM system, as the reflection coefficient depends also on the plasma impedance which is a function of the plasma density and, therefore, on the operating point itself.

Regarding the power absorption map, its interpolation to a coarser mesh (the MFAM) is required. As direct interpolation methods may result in spatial aliasing since the power absorption profile obtained by ATHAMES may present sharp gradients within a MFAM element, a spatial anti-aliasing algorithm is implemented. The algorithm identifies the ATHAMES mesh nodes contained within each element and takes an averaged value assigned to the MFAM cell centers. Afterwards, this power absorption map is integrated in the MFAM and scaled proportionally to result in the target power absorbed obtained in the W-mesh to maintain the total absorbed power P_a .

4.3.3 Meshing

One of the main advantages of applying FEM instead of FDM is the versatility provided by the use of unstructured meshing. The utilization of unstructured meshes against structured alternatives provides several benefits. Firstly, it allows to define problems with arbitrary and complex geometries, for which an structured mesh is not simple to generate and in some cases it not even possible. Additionally, the definition of curved geometries with structured meshes leads to stair stepping issues, which can be avoided by the use of an unstructured approach. Secondly, and more importantly, unstructured meshes provide optimal flexibility in terms of refinement, since it is possible to provide specific mesh resolution attributed to different regions in the domain. This last feature is key for EM wave simulation in ECR plasmas, since mesh resolution requirements are directly influenced by the local media properties. Then, in order to avoid the use of a high-resolution refinement in the entire domain, any sort of local refinement is advisable to obtain computationally cost-effective solutions. For this reason ATHAMES is designed based on unstructured meshing.

Amongst the multiple open-source softwares available for unstructured meshing, in this work

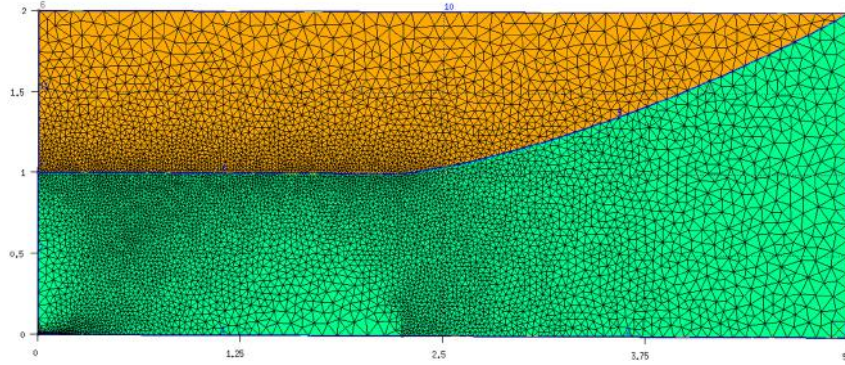


Figure 4.6: Example of unstructured mesh obtained using GMSH using partitions, a curved internal boundary and local refinement.

GMSH⁴ [87] software has been utilized as mesher, as it provides with all the features necessary and also features MFEM-compatible mesh formats. GMSH allows to define a geometry with variables in a `.geo` file, where the meshing options can be coded, physical boundaries defined, as well as local refinements, domain IDs, boundary IDs, etc. Once the geometry file is completed, it only takes a single command line from the terminal to create a mesh, where some parameters allow to configure meshing including 1D, 2D, or 3D generation, typical output filename and type, the meshing algorithm used (e.g. Delaunay, frontal), an also other functionalities related to mesh coarseness. An example mesh featuring all the features above is shown in Fig. 4.6.

4.3.3.1 Predictive mesh refinement

As mentioned before, efficient simulation of ECR plasmas requires the use of some sort of local refinement. GMSH allows to specify a target element size function to the mesher in an input file provided prior mesh generation, without requiring the modification of the `.geo` file. The target element size has to be provided in a GMSH compatible mesh format, in which in our case a roughly uniform mesh is selected, created by Delaunay triangulation method using GMSH. A series of subroutines were implemented to determine the target element size function based on the specific refinement requirements of an ECRT simulation. After creating the target element size vector, the map is interpolated to the uniform mesh obtained by GMSH creating the background mesh (i.e. `.bgm`) file with the associated target element size. Application of GMSH command option `-bm` followed by the name of the `.bgm` file generated allows to generate a mesh featuring predictive refinement.

The target element size is determined directly by the local plasma properties and the applied magnetic field. Based on these properties, the local estimated wavelengths of all the modes propagating at each domain node are computed using their respective dispersion relations. The dispersion relations are given in §2.6 including the electron damping. Taking the minimum of all these wavelengths an estimated local minimum wavelength l_{min} is obtained. A factor $N_\lambda = l_{min}/l_c > 20$, being l_c the characteristic mesh size or target element size. This target element size is then predicting the resolution required for the waves in each region of the domain. Minimum wavelength is typically found close to resonances as it is the case of the ECR (i.e. $\mathcal{R} \rightarrow \infty$) and the UHR (i.e. $\mathcal{S} = 0$) regions. An example of the mesh obtained after the application of predictive refinement is shown in Fig. 4.7. Here the simulation domain of a coaxial ECRT is meshed with an unstructured mesh using the target element size shown in Fig. 4.7a. GMSH refinement algorithm obtains the mesh shown in Fig. 4.7b, where, as expected, the regions featuring the lowest target element size are fundamentally the ECR and in a lesser amount the UHR. For the ECR plasmas found in this type of ECRTs, $l_{min} \sim \mathcal{O}(1 \text{ mm})$ so that the minimum target element size is one order of magnitude below the mm scale. Additionally, the mesh is refined at the vicinity of domain PEC corners as the solutions there may require more resolution due to the sharp discontinuities in the fields

⁴<https://gmsh.info/>

there. Local refinement is also applied to the dielectric window connecting the coaxial line with the thruster chamber, in order to smoothen the transition.

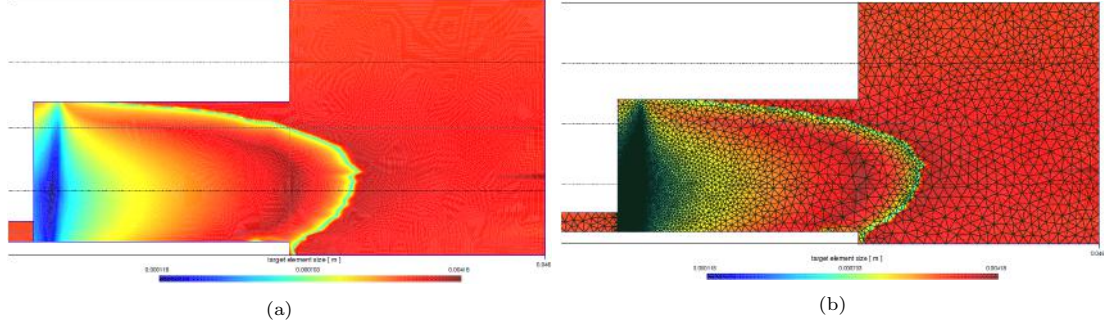


Figure 4.7: (a) Target element size function and (b) resulting mesh after the application of predictive refinement.

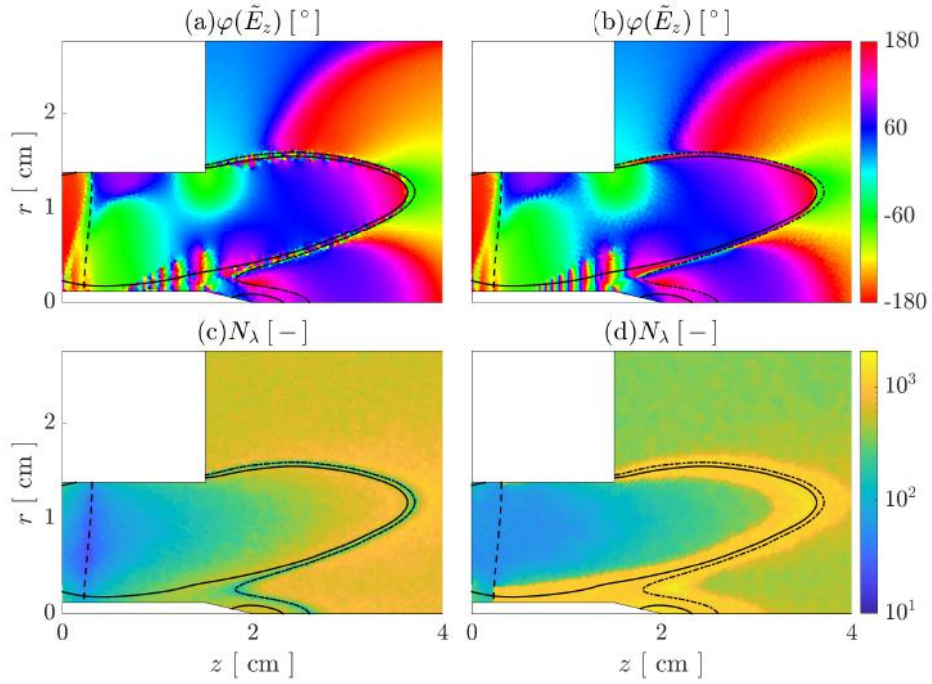


Figure 4.8: Complex phase of the E_z fast electromagnetic field and number of mesh elements per local wavelength for a uniform mesh (left) and for a refined mesh (right).

In order to verify the interest and application of this feature, let us anticipate one of the numerical results obtained for the reference simulation shown in Chapter 5. Figure 4.8 show the numerical results of ATHAMES for the complex phase of the axial component of the wave electric field (i.e. $\varphi(\tilde{E}_z)$) in a (a) uniform very fine mesh (i.e. 96239 elements), against a solution with using predictive refinement, shown in Fig. 4.8(b), (b) predictive refined mesh with 120782 elements. Figures 4.8(c) and (d) display the characteristic number of mesh elements per wavelength, this one computed from the local dielectric tensor. Important EM propagation parametric boundary surfaces are

represented in dashed lines (ECR), solid lines (the \mathcal{P} cutoff) and dashed-dotted lines (UHR). High-wavenumber oscillations are observed in the neighborhood of the UHR and \mathcal{P} boundary surfaces in the uniform mesh simulation results, which are only partially physical. Such oscillations do not correlate with waves as there is a mismatch between the expected wavelengths given by the local properties and the numerical simulation. Furthermore, as the oscillations scale is of the order of the mesh-cell characteristic length, this suggests that such oscillations are in fact, at least partly, spurious noise. Indeed progressive refinement of the mesh in regions II, III and IV of the CMA diagram (see §2.8), as represented in Fig. 4.8(d), shows that the fields converge to those on Fig. 4.8(b), where most of these oscillations have disappeared and therefore are considered error noise. Only some of the oscillations remain in the low-density channel that occurs near the inner rod element in this simulation, as shown in the main text (Fig. 5.9). Noteworthily, while the noise affects the field phase, it was observed that it does not impact significantly the power absorption profile.

As a final observation, it is noted that for the multiple plasma and magnetic field profiles were tested, the location of this noise is in direct correlation with the UHR surface. Similar spurious solutions near this resonance are reported near lower-hybrid resonances in other works [88], which show some mathematical analogy with the UHR. A regularization of the double-curl formulation of the finite elements scheme is suggested there as an alternative route to solve this issue [89, 90].

4.4 Verification

Test Name	Type	Success criteria
FScaledGFCoefficient_test associated to derived class FScaledGFCoefficient.	Functional	Scales a GridFunctionCoefficient with a different Coefficient, in this case a Gaussian. Expected scaling of input coefficient from a file.
MMS for 2D planar module with metallic case geometry and arbitrary plasmas [58].	Integrated	Convergence rate of the order of the method for different model parameters.
MMS for 2D axisymmetric module with annular metallic case geometry and arbitrary plasmas.	Integrated	Convergence rate of the order of the method for different model parameters.
MMS 2D axisymmetric module with cylindrical metallic case geometry and arbitrary plasmas.	Integrated	Convergence rate of the order of the method for different model parameters.
MMS for verification of fulfillment of axisymmetric boundary conditions in the 2D axisymmetric module.	Integrated	Convergence rate of the order of the method for different model parameters.
Comparison against 1D semi-analytic solution.	Integrated	A MATLAB code wave1D is used to verify the operation of the code in simple geometries.
System assembly and solution from input files.	Integrated	Compares simulations with inputs as nodal values given in external files and analytical C++ functions. Errors in the assembled block matrix coefficients between both approaches lie below a tolerance.

Table 4.5: List of major ATHAMES tests.

As ATHAMES integrates several tested packages (e.g. MFEM library, SuiteSparse solvers), a behavior-driven development (BDD) approach has been the leading testing philosophy used for its verification process. This strategy is based on the execution of functional or integration tests. A list of the major tests in the suite has been summarized in Tab. 4.5. Unit tests are not shown in this table for the sake of brevity.

4.4.1 Method of manufactured solutions

Several of the integration tests listed in Tab. 4.5 employ the so-called Method of Manufactured Solutions (MMS) which has been identified to an effective method for the verification process of algorithms that solve differential equations and, in particular, to FEM electromagnetic codes [91]. The method allows to, not only obtain the convergence rate or method order, but also to reveal errors in code implementation. The MMS consists on applying the differential operator of the strong form of the equation to be solved to a designed manufactured solution (i.e. $\tilde{\mathbf{E}}^{mms}$). The manufactured solution is required to be compliant with the boundary conditions imposed. Analytically, a RHS or excitation current in this case can be found (i.e. $\tilde{\mathbf{j}}^{mms}$). This RHS is then taken as input into the numerical differential equation to be solved and the numerical solution (i.e. $\tilde{\mathbf{E}}$) of that problem is found. The numerical solution obtained can be compared with the manufactured solution providing an estimate of the error of the approximation, for instance, in terms of norm error. As a result, the test verifies the matrix building method and its implementation, where the verification is based on convergence rate and convergence itself. The convergence rate is determined by the approximation error of the truncation provided by the use of an specific finite element type.

Following the examples given on the work of Garcia-Doñoro [91], the verification of ATHAMES using MMS has been carried out part by part. MMS is applied to specific terms of the matrix building process, and stacking them until proving the convergence of the method for the complete differential equation to be solved for the most complex scenario to be considered. This approach has been consistently used throughout the development of both the planar (THAMES) [58] and the axisymmetric (ATHAMES) versions [57] of the code. The most relevant tests using this methodology are summarized hereinafter.

4.4.1.1 THAMES verification

In the case of THAMES, the verification is shown in a two dimensional rectangular domain of $H = 2$ m height (along y) and $L = 5$ m length (along x). The domain boundaries are PEC so that at $y = 0$ m and $y = H$, $\tilde{E}_x = \tilde{E}_z = 0$ V/m and at $x = 0$ m and $x = L$, $\tilde{E}_y = \tilde{E}_z = 0$ V/m.

All tests are performed with the following manufactured solution:

$$\tilde{\mathbf{E}}^{mms} = \begin{bmatrix} \sin(k_1 y) + i \sin(k_2 y) \\ \sin(k_1 x) + i \sin(k_2 x) \\ \sin(k_3 x) \sin(k_3 y) + i \sin(k_4 x) \sin(k_4 y) \end{bmatrix}, \quad (4.4-1)$$

which is represented in Fig. 4.9. The order of both the Nédélec (in-plane) and Lagrange (out-of-plane) element functional spaces is selected to be $p_N = p_L = 2$. Simulation parameters as plasma density and magnetic field intensity have been chosen to resemble those of the ECRT [49]. The different scenarios tested are:

- **Case 1:** unmagnetized underdense plasma slab ($B = 0$ T, $n = n_0 = 5 \times 10^{16}$ [m⁻³], CMA region I, $k_z = 0$ m⁻¹, $\nu_e/\omega = 0.01$).
- **Case 2:** magnetized overdense plasma slab ($B = B_0 = 0.1$ T, $n = n_0 = 2 \times 10^{17}$ [m⁻³], CMA region VIII, $k_z = 0$ m⁻¹, $\nu_e/\omega = 0.01$).
- **Case 3:** increasing k_z ($B = B_0 = 0.1$ T, $n = n_0 = 2 \times 10^{17}$ [m⁻³], CMA region VIII, $k_z = 100$ m⁻¹, $\nu_e/\omega = 0.01$).

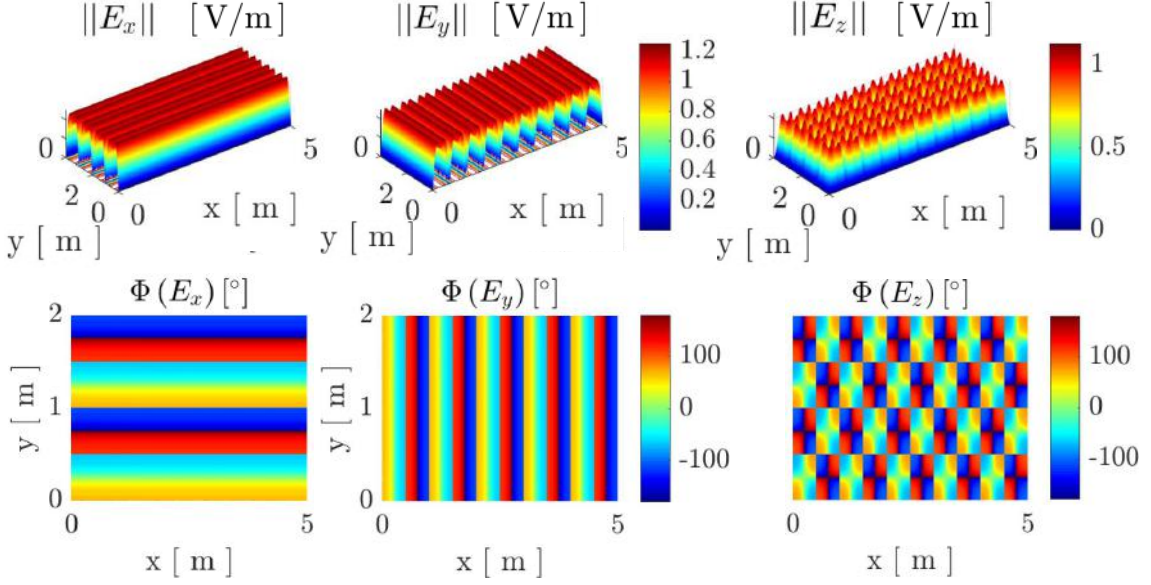


Figure 4.9: Manufactured solution with parameters $k_1 = k_3 = 2\pi$, $k_2 = k_4 = 4\pi$.

- **Case 4:** increasing B_0 ($B = B_0 = 0.3T$, $n = n_0 = 2 \times 10^{17} [\text{m}^{-3}]$, CMA region VIII, $k_z = 10\text{m}^{-1}$, $\nu_e/\omega = 0.01$).
- **Case 5:** increasing ν_e/ω ($B = B_0 = 0.3T$, $n = n_0 = 2 \times 10^{17} [\text{m}^{-3}]$, CMA region VIII, $k_z = 10\text{m}^{-1}$, $\nu_e/\omega = 0.1$).
- **Case 6:** including inhomogeneous plasma density ($B = B_0 = 0.1 \text{ T}$, $n(y) = 2 \times 10^{17}(1 - (y/H)^2) [\text{m}^{-3}]$, $k_z = 10\text{m}^{-1}$, $\nu_e/\omega = 0.1$).

For each scenario, the test forcing functions are computed from Eq.4.4-1 and Eq. (2.4-5). In order to reduce the amount of cases investigated in this study, wave numbers k_1 , k_2 , k_3 , k_4 are set fixed for all test cases as shown in Fig. 4.9.

Passing several test cases is considered as milestones for the code development process, each of them having different sets of simulation parameters. Case 1 shows the simplest simulation performed, which is a case run for an unmagnetized underdense plasma (i.e. $\omega_{pe}^2/\omega^2 < 1$) that is equivalent to EM propagation region I in the CMA diagram[27], equivalent to the far plume. Cases 2-6 are for magnetized overdense plasmas (i.e. $\omega_{pe}^2/\omega^2 > 1$ & $\omega_{ce}/\omega > 1$) corresponding to CMA region VIII. The latter region is characteristic of ECRT plasmas upstream the ECR region. Case 2 reproduces an overdense magnetized homogeneous plasma slab. The inclusion of a magnetic field intensity generates anisotropy in the media and couples the different electric field components (see Eq. (2.3-28)). Case 3 includes a out-of-plane wave number. Case 4 increases by a factor of 3 the magnetic field intensity with respect to case 3. Case 5 increases the effective collisionality by one order of magnitude with respect to case 4. Case 6 takes case 5 and includes inhomogeneous plasma density with quadratic profile in y axis, with maximum at $y = 0$, and zero at $y = H$.

The results of the convergence analysis for each scenario, an their computational time are shown in Table 4.6. The error between the numerical solution and the manufactured solution is computed as the L^2 -norm absolute error defined as

$$e = \int_{\Sigma} \|\tilde{\mathbf{E}} - \tilde{\mathbf{E}}^{mms}\|_2 d\Sigma, \quad (4.4-2)$$

for both in-plane and out-of-plane components of the electric field. The convergence of the data

	N	Case 1	Case 2	Case 3	Case 4	Case 5	Case 6
e_{xy} [V/m]	62	2.184	$1.255 \cdot 10^1$	$2.217 \cdot 10^1$	$1.476 \cdot 10^1$	5.830	$1.157 \cdot 10^1$
	188	1.087	6.766	8.402	$1.130 \cdot 10^1$	3.915	8.526
	652	$2.942 \cdot 10^{-1}$	1.796	2.901	1.710	$6.606 \cdot 10^{-1}$	1.489
	1232	$1.670 \cdot 10^{-1}$	$9.561 \cdot 10^{-1}$	1.363	1.261	$4.153 \cdot 10^{-1}$	$8.393 \cdot 10^{-1}$
	3402	$6.204 \cdot 10^{-2}$	$2.786 \cdot 10^{-1}$	$3.492 \cdot 10^{-1}$	$4.745 \cdot 10^{-1}$	$1.611 \cdot 10^{-1}$	$3.266 \cdot 10^{-1}$
	7504	$2.698 \cdot 10^{-2}$	$1.153 \cdot 10^{-1}$	$1.468 \cdot 10^{-1}$	$1.990 \cdot 10^{-1}$	$6.604 \cdot 10^{-2}$	$1.283 \cdot 10^{-1}$
	16690	$1.262 \cdot 10^{-2}$	$5.102 \cdot 10^{-2}$	$5.810 \cdot 10^{-2}$	$8.969 \cdot 10^{-2}$	$3.007 \cdot 10^{-2}$	$5.171 \cdot 10^{-2}$
	29760	$6.806 \cdot 10^{-3}$	$2.842 \cdot 10^{-2}$	$3.179 \cdot 10^{-2}$	$4.429 \cdot 10^{-2}$	$1.544 \cdot 10^{-2}$	$2.467 \cdot 10^{-2}$
	66056	$3.074 \cdot 10^{-3}$	$1.282 \cdot 10^{-2}$	$1.395 \cdot 10^{-2}$	$1.971 \cdot 10^{-2}$	$6.805 \cdot 10^{-3}$	$1.017 \cdot 10^{-2}$
e_z [V/m]	62	1.381	8.175	9.067	$4.851 \cdot 10^{-1}$	2.435	3.356
	188	$7.132 \cdot 10^{-1}$	4.323	4.537	5.070	2.072	2.576
	652	$1.117 \cdot 10^{-1}$	1.095	1.552	$7.653 \cdot 10^{-1}$	$4.168 \cdot 10^{-1}$	$5.069 \cdot 10^{-1}$
	1232	$5.334 \cdot 10^{-2}$	$6.063 \cdot 10^{-1}$	$7.477 \cdot 10^{-1}$	$5.446 \cdot 10^{-1}$	$2.486 \cdot 10^{-1}$	$3.004 \cdot 10^{-1}$
	3402	$1.639 \cdot 10^{-2}$	$1.744 \cdot 10^{-1}$	$1.962 \cdot 10^{-1}$	$2.292 \cdot 10^{-1}$	$1.094 \cdot 10^{-1}$	$1.262 \cdot 10^{-1}$
	7504	$5.104 \cdot 10^{-3}$	$7.539 \cdot 10^{-2}$	$8.622 \cdot 10^{-2}$	$9.773 \cdot 10^{-2}$	$4.988 \cdot 10^{-2}$	$5.702 \cdot 10^{-2}$
	16690	$1.759 \cdot 10^{-3}$	$3.273 \cdot 10^{-2}$	$3.515 \cdot 10^{-2}$	$4.560 \cdot 10^{-2}$	$2.422 \cdot 10^{-2}$	$2.651 \cdot 10^{-2}$
	29760	$7.120 \cdot 10^{-4}$	$1.853 \cdot 10^{-2}$	$1.963 \cdot 10^{-2}$	$2.303 \cdot 10^{-2}$	$1.316 \cdot 10^{-2}$	$1.403 \cdot 10^{-2}$
	66056	$2.177 \cdot 10^{-4}$	$8.371 \cdot 10^{-3}$	$8.767 \cdot 10^{-3}$	$1.030 \cdot 10^{-2}$	$5.996 \cdot 10^{-3}$	$6.328 \cdot 10^{-3}$
t_c [s]	62	0.029	0.049	0.070	0.023	0.033	0.11273
	188	0.090	0.135	0.128	0.127	0.100	0.139
	652	0.381	0.339	0.324	0.353	0.306	0.304
	1232	0.538	0.495	0.625	0.780	0.521	0.517
	3402	1.340	1.268	1.518	1.621	1.284	1.259
	7504	2.492	2.832	2.902	3.463	3.174	2.915
	16690	6.225	6.810	6.861	9.532	7.236	6.848
	29760	11.122	12.532	13.153	16.924	13.475	12.910
	66056	22.774	32.825	31.803	33.566	35.119	32.725

Table 4.6: Convergence and computational requirements of the simulation are run for increasing number of elements (**N**) depending on the complexity of the simulation, increasing from **Case 1** to **Case 6**. L^2 -norm errors between the manufactured $\hat{\mathbf{E}}^{mms}$ and numerical $\hat{\mathbf{E}}$ solutions are displayed in absolute value. Workstation specifications: 16Gb RAM, Intel Core™i7-6700 CPU @ 3.40GHz x 8.

of the different cases is shown in Fig. 4.10. Comparison of the errors evolution show that the totality of test runs converge to the analytical solution with mesh refinement. For all the in-plane components the convergence rate is that of the Nédélec element functions of order two (i.e. $\mathcal{O}(h^2)$) where $p = \log(e)/\log(h)$. Regarding the out-of-plane convergence, for the unmagnetized case the convergence rate is that of the Lagrange second order elements (i.e. $\mathcal{O}(h^3)$). However, by the introduction of magnetization in the problem, both functional spaces are coupled and the one with higher truncation error dominates on that of the other spaces. As a result, for all magnetized cases the truncation error is $\mathcal{O}(h^2)$ (i.e. $p = 2$).

Comparing cases, one first notices that case **2** convergence is considerably worse than that of case **1** as can be seen in Table 4.6 for both in-plane and out-of-plane solutions. The effect on the computational time is increasing it by almost 50%. This is a result of the increased number of non-zero coefficients per row of the linear system matrix. Comparison of the convergence of case **3** with case **2** shows that both convergence and computational time are barely affected by the increase in k_z . Case **4** convergence compared to Case **2** is slightly worse for the former, suggesting that the magnetic field has higher impact on convergence than k_z . Comparison between cases **5** and **4** shows that increasing the collisionality results in improving the convergence of the simulations. Further information about this topic is provided in §4.5. Convergence of case **6** is similar but slightly worse than that of the homogeneous case (i.e. case **5**).

All test cases feature similar computational times, specially those with magnetization as these

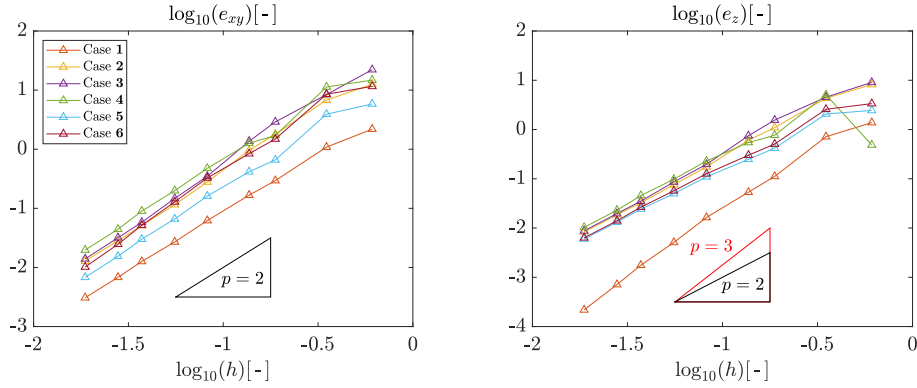


Figure 4.10: Convergence of THAMES verification.

increase considerably the number of non-zero terms in the sparse matrix with respect to the unmagnetized case. Furthermore, the computational time growth with the number of elements is very similar for all cases.

4.4.1.2 ATHAMES verification

For the axisymmetric code several modifications were required with respect to the planar case. First, the presence of different coefficients, including weighting proportional and inversely proportional to the radius. Second different terms and Integrators to be used in the assembly of the block matrix shown in Tab. 4.2 for $m = 0$. Third, the axisymmetric boundary conditions which provide an additional complication in terms of formulation.

Based on the knowledge obtained from the verification of the planar code, several tests were run of an annular geometry and then on a cylindrical geometry, being the simulation domain that contained in the meridian half-plane of each domain. For both geometries, the domain extends from the minimum radius r_{min} to the maximum radius r_{max} by a distance $H = 2$ m. The domain is $L = 5$ m long in the z direction. Two different roughly uniform unstructured mesh batches are created, one for each geometry. The mesh batches span in number of elements with characteristic element size $h \in (10^{-2}, 1)$. The mesh batch with no symmetry axis within the simulation domain is named \mathcal{M}_1 and accounts for 15 meshes. A second mesh batch including the symmetry axis is called \mathcal{M}_2 and is formed by 10 meshes. For all cases considered, second order Nédélec and Lagrange elements are used.

A series of tests have been implemented for ATHAMES by applying the MMS, which are classified depending on the mesh batches used as:

- Annular geometry tests MMS-1 and MMS-2.
- Cylindrical geometry tests MM-3 and MMS-4.

The tests are:

- Test MMS-1: a simulation domain without symmetry axis (using \mathcal{M}_1) and PEC walls is excited with a source term resulting from assuming an azimuthal manufactured field $\vec{E}_\theta^{mms} = \sin(k_r(r - r_{min})) \sin(k_z(z - z_{min}))$, being $k_r = 2$ and $k_z = 2$. A constant overdense plasma is assumed in the entire domain, with $n_e = n_0 = 5 \times 10^{17} \text{ m}^{-3}$. The test verifies convergence of the terms coupling real and imaginary parts of the azimuthal fields. Additionally, the terms from the dielectric tensor coupling the tangential components with the azimuthal components are also verified. The test also covers the influence of the applied magnetic field intensity (also assumed constant within the simulation domain) on the solution of both the tangential and the azimuthal fields. For regions where the \mathcal{R} mode is resonant, the effects of including an electron collisionality are evaluated.

- Test MMS-2: the same conditions and geometry as Test MMS-1 are evaluated, but in this case exciting the problem with a source term resulting from a manufactured electric field with both azimuthal and tangential components. The form of the manufactured field is shown in Eq. (4.4-5). The test is performed to verify that all the different bilinear forms in the block-matrix system are correctly implemented. Test MMS-2 is designed to verify that the convergence behavior of all the components of the wave equation solution is adequate. Additionally, an assessment of the importance of electron collisionality ν_e in the solution of the wave equation in magnetized plasmas with $B_0 > B_{res}$ is carried out.
- Test MMS-3: the same manufactured solution of test MMS-2 is used, for a simulation domain with $r_{min} = 0$ (using mesh batch \mathcal{M}_2). The test case represents a coaxial element with infinitely thin inner rod.
- Test MMS-4: using the cylindrical mesh batch \mathcal{M}_2 , the axisymmetric boundary conditions for mode $m = 0$ are verified (see Eq. (4.2-26)). The manufactured solution fulfilling these conditions is shown in Eq. (4.4-8).

4.4.1.3 Annular geometry tests

Convergence of the numerical solutions to the manufactured solutions for all the cases considered in test MMS-1 are shown in Figs. 4.11a and 4.11b. Starting with the unmagnetized case, the error only appears in the azimuthal component as the equations involving tangential field degrees of freedom have uniquely trivial solutions and thus no tangential field error appears. The azimuthal fields convergence rate is that of second order Lagrange nodal elements (i.e. $p = 3$). When including magnetization, the coupling between in-plane and out-of-plane degrees of freedom increases with B_0 and so does the error for both components. The convergence rate of azimuthal fields is in this case dominated by the truncation errors of the azimuthal fields, as the tangential ones are not excited.

The above-mentioned convergence rates are maintained for $B_0 < B_{res}$ or $\nu_e \neq 0$. For the excitation frequency chosen, $f = 2.45$ GHz, the ECR takes place at $B_0 = B_{res} = 0.0875$ T. At this value, the refractive index of the \mathcal{R} mode, defined in equation (2.3-32), diverges in absence of no collisionality. As a result, part of the dielectric tensor becomes singular. Above this magnetic field intensity, \mathcal{R} mode features a resonant cone for which a specific propagation angle features resonant absorption. As ATHAMES obtains full-wave solutions, and the solution is still resonant for some mode in a specific propagating direction, the convergence is jeopardized for $B_0 > B_{res}$. The inclusion of wave damping in terms of electron collisionality eliminates the singularity in \mathcal{R} and allows for the stabilization of the solution method, even for $B_0 > B_{res}$.

The difference between Test MMS-2 w.r.t. Test MMS-1 is that Test MMS-1 only validated the method to solve the normal component of the wave equation as well as its coupling by the dielectric tensor with the tangential components. This test is performed to validate and verify that all the different blocks in the block-matrix are correctly implemented, for the purely axisymmetric case. For all cases run here we will use $k_1 = k_2 = k_3 = k_4 = 4$. The components of the manufactured electric field solution ($\tilde{\mathbf{E}}^{mms}$) used for this test are

$$\tilde{E}_z^{mms} = \sin(k_1(r - r_{min})) + i \sin(k_2(r - r_{min})) , \quad (4.4-3)$$

$$\tilde{E}_r^{mms} = \sin(k_1(z - z_{min})) + i \sin(k_2(z - z_{min})) , \quad (4.4-4)$$

$$\tilde{E}_\theta^{mms} = \sin(k_3(r - r_{min})) \sin(k_3(z - z_{min})) + i \sin(k_4(r - r_{min})) \sin(k_4(z - z_{min})) . \quad (4.4-5)$$

The convergence of the errors obtained in test MMS-2 are shown in Figs. 4.11c and 4.11d. As all electric field components are now excited, the order of the method is now that of second order Nédélec elements for the tangential fields (i.e. $p = 2$). For the azimuthal fields the convergence rate is slightly worse than order $p = 3$ since the coupling between the two functions is present. This effect is more severe the higher the magnetization. The general trends observed regarding the influence of magnetic field and the convergence stability for $B_0 > B_{res}$ are maintained.

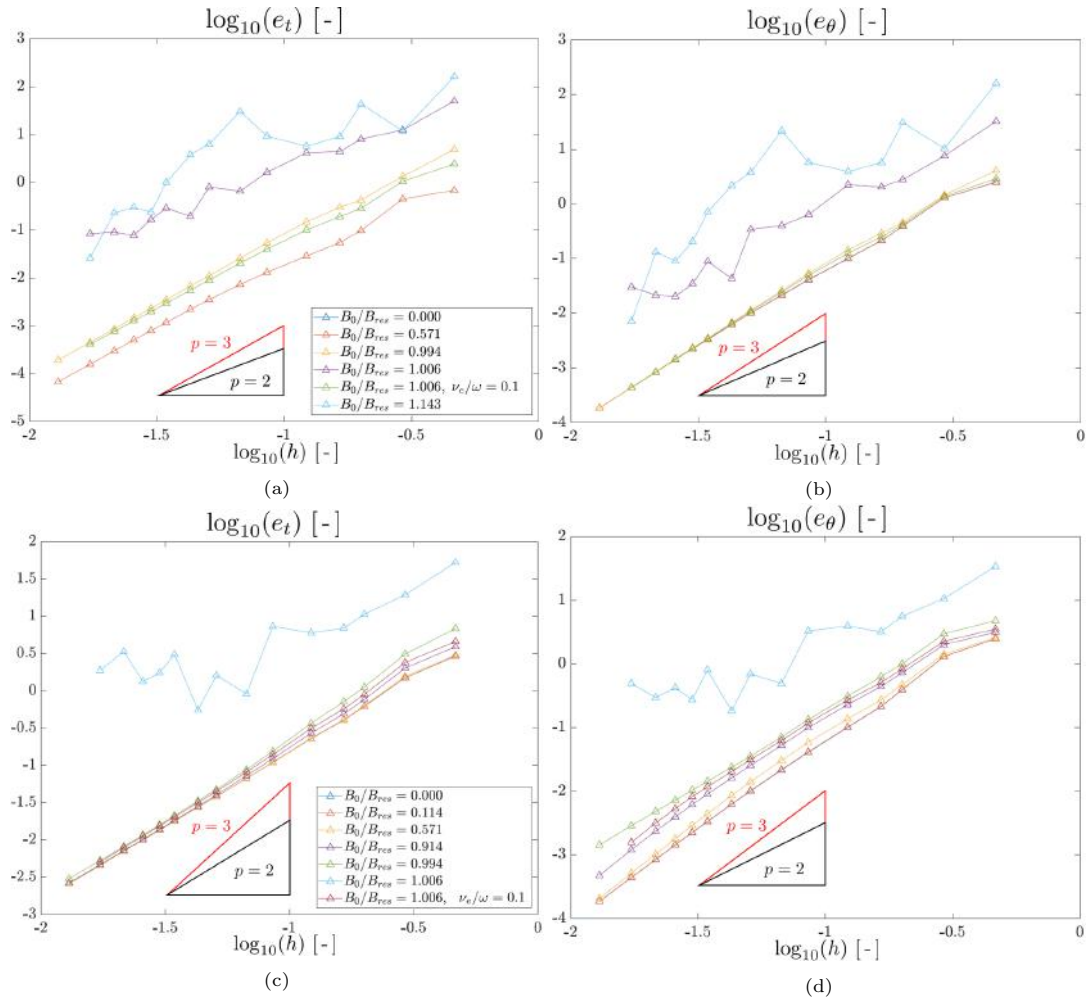


Figure 4.11: Convergence of the L^2 -norm errors of the in-plane and out-of-plane components of the electric field complex amplitude for tests (a)-(b) MMS-1 and (c)-(d) MMS-2 with mesh refinement for different intensities of the applied magnetic field.

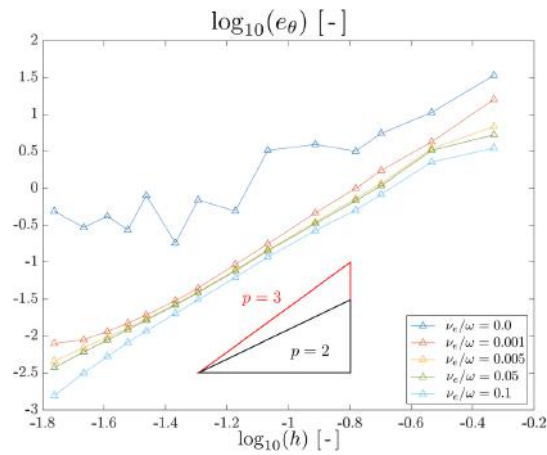


Figure 4.12: Convergence of the L^2 -norm errors of the out-of-plane electric field component of test MMS-2 with mesh refinement for different values of the electron collisionality.

A sensitivity analysis to electron collisionality ν_e on the solution of the wave equation in magnetized plasmas with $B_0 > B_{res}$ has been performed. The plasma studied is that of the region where the method convergence is unstable, so that the magnetic field is assumed to be $B_0 = 0.088$ T. The plasma density utilized is $n_e = n_0$. Observing the results shown in Fig. 4.12, a collisional damping three orders of magnitude smaller than the excitation frequency is already capable of stabilizing the convergence rate to the one expected from the method and similar to those obtained for Fig. 4.11d. The error decreases with increasing collisionality while maintaining the convergence rate. This indicates that even a small dissipation will and is sufficient to enhance the convergence of the method.

4.4.1.4 Cylindrical geometry tests

Test MMS-3 proves that the inclusion of nodes at the symmetry axis do not lead to errors in the solution. This verification test focuses on the terms with coefficients inversely proportional to r , and on the behavior of the entire method with nodes at $r = 0$. The convergence of this test is shown in Figs. 4.13a-4.13b.

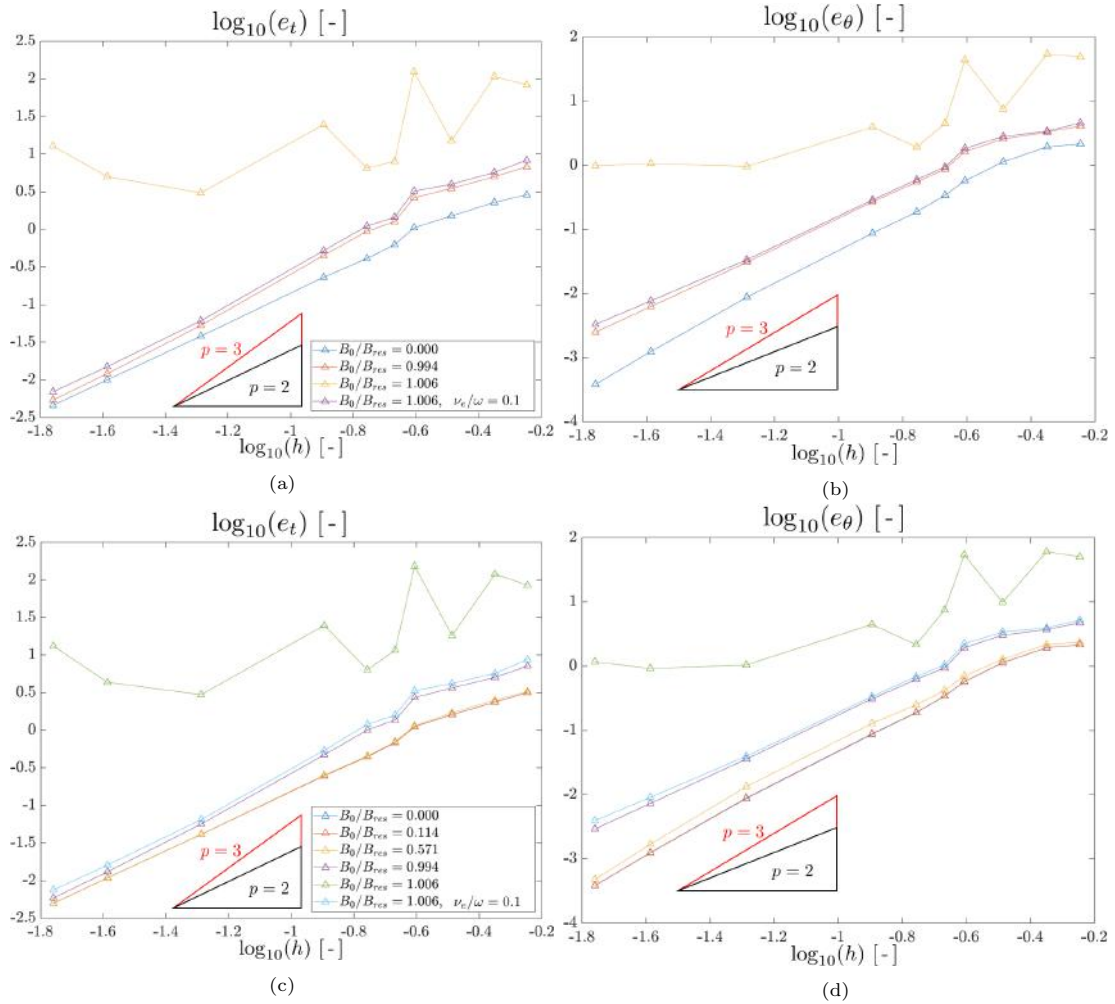


Figure 4.13: Convergence of the L_2 -norm errors of the in-plane and out-of-plane components of the electric field complex amplitude of tests (a)-(b) MMS-3 and (c)-(d) MMS-4 with mesh refinement for different applied magnetic field intensities.

The same trends as the ones predicted in test MMS-2 are observed, with tangential degrees of freedom showing a convergence rate of the second order Nédélec elements whilst the errors in the azimuthal degrees of freedom converge at order $p = 3$ for the unmagnetized case and tend to the tangential order $p = 2$ for increasing magnetization.

Test MMS-4 is used to verify that ATHAMES can impose axisymmetric boundary conditions at $r = 0$. The axisymmetric boundary conditions force the fields perpendicular to the symmetry axis (i.e. $\tilde{E}_r = \tilde{E}_\theta = 0$ at $r = 0$) if no inhomogeneous term (excitation current) is applied at the symmetry axis.

Satisfying these conditions, the manufactured solution for the electric field ($\tilde{\mathbf{E}}^{mms}$) used for this test is then the following:

$$\tilde{E}_z^{mms} = \sin(k_1(r - r_{min})) + i \sin(k_2(r - r_{min})) , \quad (4.4-6)$$

$$\tilde{E}_r^{mms} = r [\sin(k_1(z - z_{min})) + i \sin(k_2(z - z_{min}))] , \quad (4.4-7)$$

$$\tilde{E}_\theta^{mms} = \sin(k_3(r - r_{min})) \sin(k_3(z - z_{min})) + i \sin(k_4(r - r_{min})) \sin(k_4(z - z_{min})) . \quad (4.4-8)$$

As can be seen from Figs. 4.13c-4.13d both the tangential and azimuthal degrees of freedom converge as expected, verifying the fulfillment of the axisymmetric boundary conditions.

4.4.2 Mesh refinement sensitivity analysis

After showing the verification of the assembly method and boundary conditions for arbitrary test geometries using MMS, a sensitivity analysis to mesh refinement in a reference simulation of an ECRT is carried out to analyze the convergence of the method for problems of interest for the Thesis. In this subsection, the effects of refinement on the EM wave solutions in a coaxial ECRT prototype geometry are shown. The plasma properties and applied magnetic field data are shown in Fig. 4.14. The plasma properties are outputs of a simulation of the prototype using HYPHEN simulation platform [60] assuming an isothermal electron population with $T_e = 20$ eV. The magnetic field data is provided by the FPA-unit from the French Aerospace Laboratory (ONERA), and it is that of one of their prototype versions.

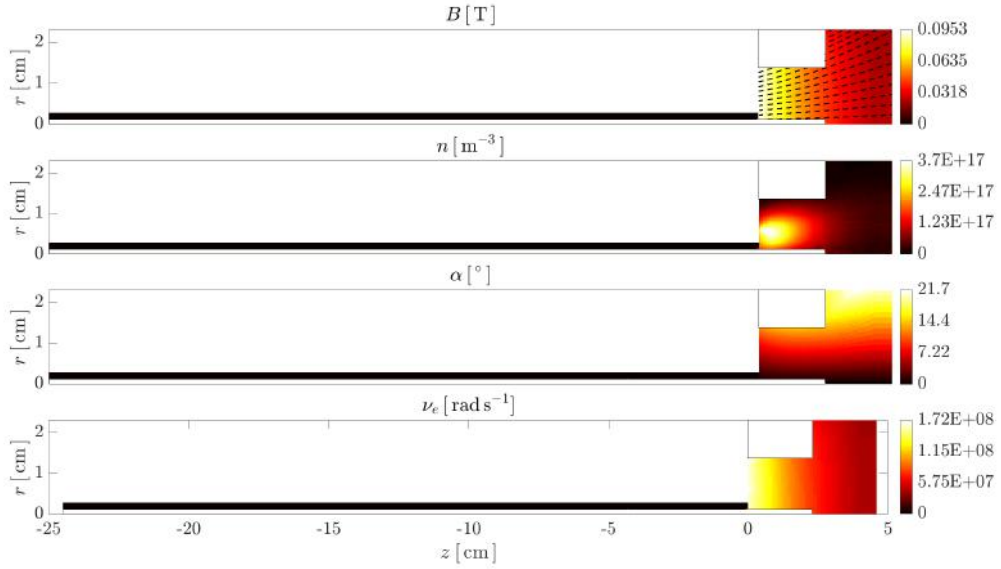


Figure 4.14: ATHAMES inputs for the mesh refinement sensitivity analysis.

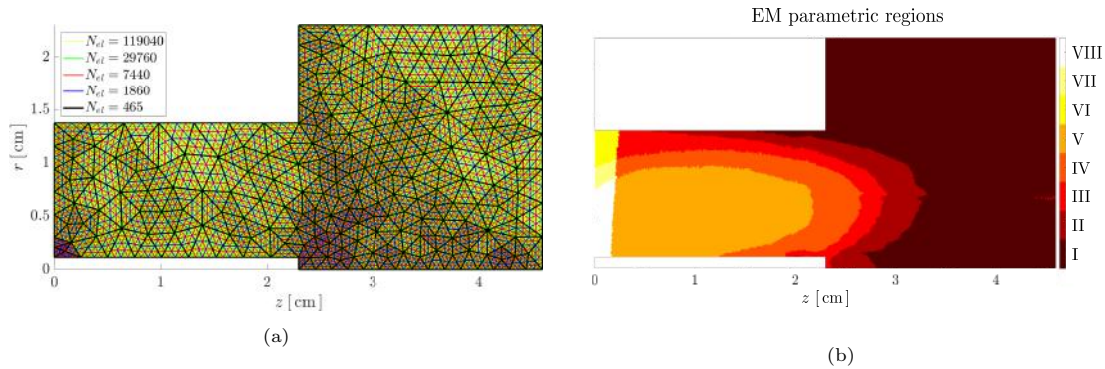


Figure 4.15: (a) Meshes used for the sensitivity analysis of refinement in the convergence of solutions in a ECRT geometry with a plasma featuring (b) map of the different electromagnetic propagation regions.

The mesh refinement strategy selected for this analysis is a consecutive mesh refinement. Starting with a roughly uniform mesh with 465 elements, a number of mesh refinements (N_{ref}) are applied by gradually splitting each initial triangular cell into four partition elements. Here, a total of four mesh refinements are analyzed with meshes featuring a total number of elements $N_{el} = 1860, 7440, 29760,$ and 119040 , respectively. All the meshes are represented in Fig. 4.15. This refinement is performed utilizing GMSH capabilities.

First of all, all electric field components are observed to fulfill the boundary conditions including the axisymmetric boundary conditions. The radial electric field \tilde{E}_r is the most relevant electric field component within coaxial ECRTs as it drives most of the power absorbed, as it will be explained in Chapter 5. Additionally it is the only field present within the coaxial, as the electric field in a coaxial waveguide is a TEM mode. The evolution of its complex amplitude and phase with consecutive refinements are shown respectively in Figs. 4.16a and Fig. 4.16b.

The maximum electric field amplitude appears close to the ECR and the inner rod prior to the ECR and at region III of the CMA, in which the previously mentioned high frequency oscillations appear. Part of these solutions are physical and another part is clearly driven by mesh element size, and mitigated by refinement. Consequently, a specific local refinement to this region and its adjacents (i.e. in the CMA diagram II and IV) is recommended. In order to analyze convergence the error estimates for all the fields are provided.

The errors e have been computed as a the difference between the simulation with different number of refinements N_{ref} and the reference case which is chosen to be the one with the finest mesh (i.e. in this case $N_{ref} = 4$). The values are compared at the nodes shared between both simulations. The amplitude errors are shown in absolute value and normalized with respect to the maximum magnitude of each component. Phase absolute error values are shown as signed values in degrees between -180 and 180 .

Figure 4.17 shows the convergence of the mean value of the errors for each field component amplitude and phase. The blue bars represent the mean error while the error bars represent the standard deviation of the error values. While the mean error represents a mean value of the error obtained in the whole simulation domain, where maximum errors gain importance, the standard deviation gives us an estimate of widespread of errors obtained. Namely, that the standard deviation represents the level of inhomogeneity of the errors achieved in the simulation. The higher the standard deviation the more inhomogeneous the error is and the larger the difference in errors achieved in the simulation. Thus, this provides key information when analyzing convergence of simulations, specially dealing with inhomogeneous plasmas. The method converges in the values of the amplitude for both real and imaginary parts, that explains why mean errors are higher for the phases than for the amplitude, being the latter computed taking the arc-tangent of the ratio between imaginary and real parts of the complex amplitude. These errors are localized in the regions where the abovementioned high frequency oscillations appear. Specific local refinement is

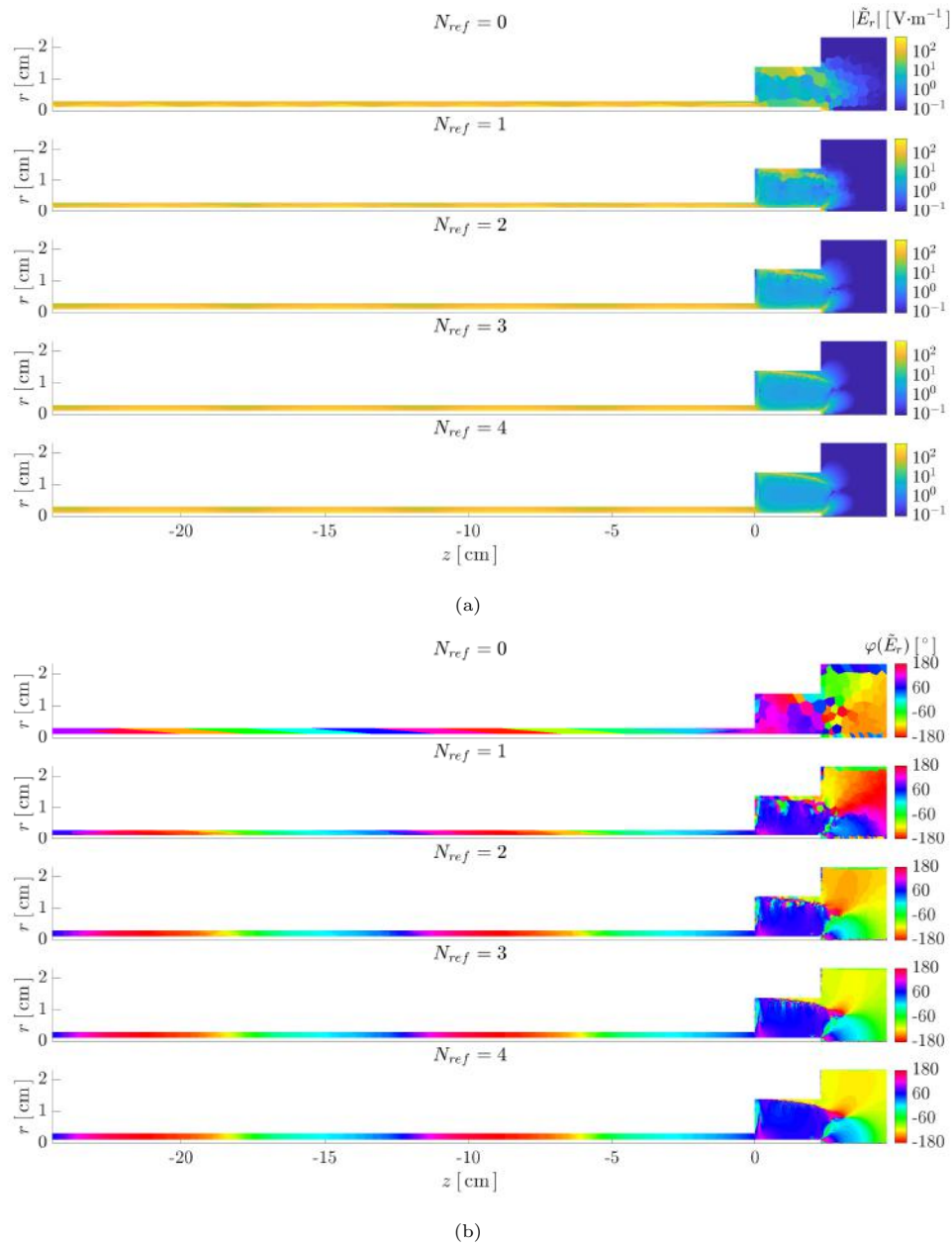


Figure 4.16: Evolution of the radial electric field complex amplitude (a) magnitude and (b) phase for different consecutive refinements.

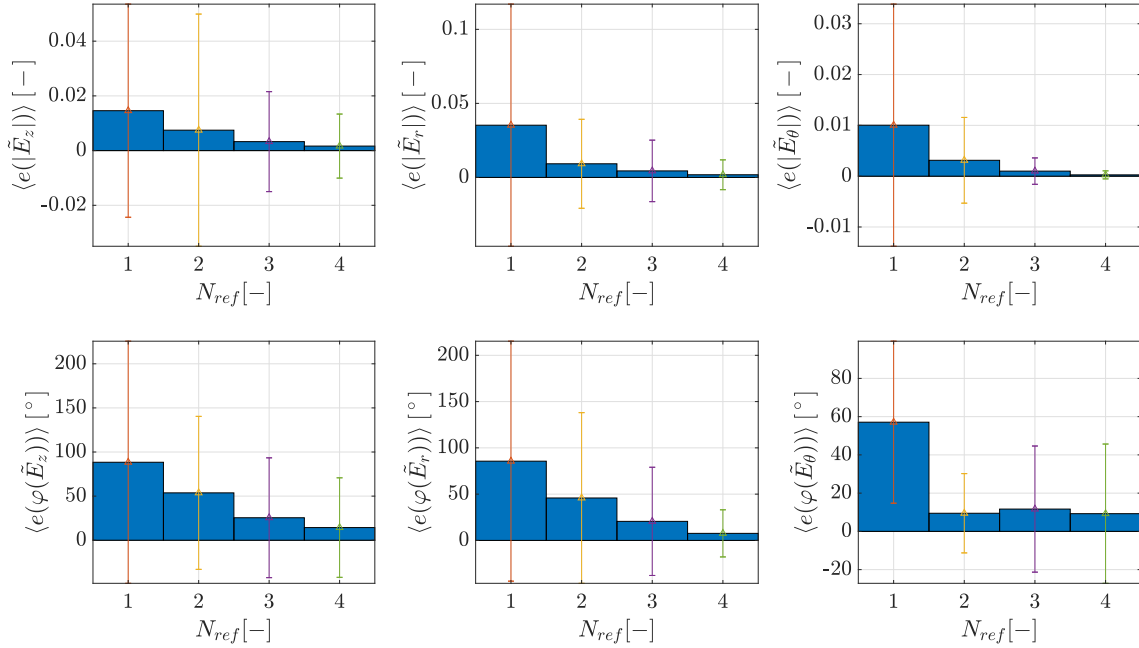


Figure 4.17: Evolution of error mean and standard deviation of each complex field component amplitude and phase with the number of refinements.

N_{ref} [-]	N_{el} [-]	t_c [s]
0	465	0.2
1	1860	0.9
2	7440	4.7
3	29760	36.4
4	119040	670.5

Table 4.7: Information on the number of elements, refinement steps and computational time for each mesh used in the convergence test. Workstation specifications: 16Gb RAM, Intel Core™i7-6700 CPU @ 3.40GHz x 8.

then required in these regions to mitigate and eliminate such spurious noise, sometimes even finer refinement than that required at the ECR region.

Apart from the EM fields, the main outputs of ATHAMES are the power absorption distribution Q_a , the power reflection coefficient $|R|^2$ and the integrated absorbed power P_a . The power absorption evolution with the number of consecutive refinements is shown in Fig. 4.18. It can be noticed that the power absorption converges to a profile where the major part of the absorption is focused at the ECR region and close to the inner rod (further details are provided in §5.3.2). Although the electric fields still feature noise at region III after 1 or 2 refinement steps, as the power absorption is not highly influenced by the fields in this region, it features faster convergence than that of the fields.

The influence of refinement on the overall performance parameters as the power absorbed and the power reflection coefficient are shown to converge with refinement in Fig. 4.19, being the former the fastest to converge. The convergence of the power reflection coefficient is more restrictive in terms of refinement requirements than that of the power absorbed, as it depends considerably on the accuracy to describe the fields within the source and, specially within the coaxial waveguide. If the scenario only requires an accurate description of the power absorption maps and absorbed power, a coarser mesh would result in sufficient accuracy. Therefore, the mesh accuracy required by the simulation will depend on which parameter is critical for the scenario investigated.

Table 4.7 shows the evolution of computational time required for each mesh of the study. The level of computational time required by a standard coaxial ECRT simulation having around 50-100

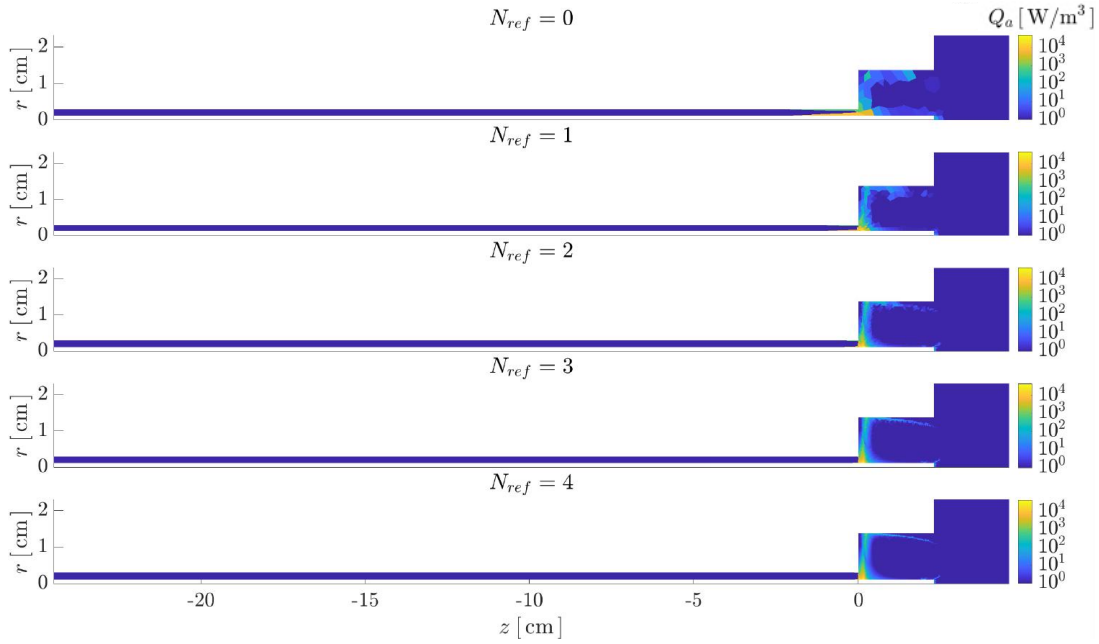


Figure 4.18: Absorbed power for different number of refinement steps.

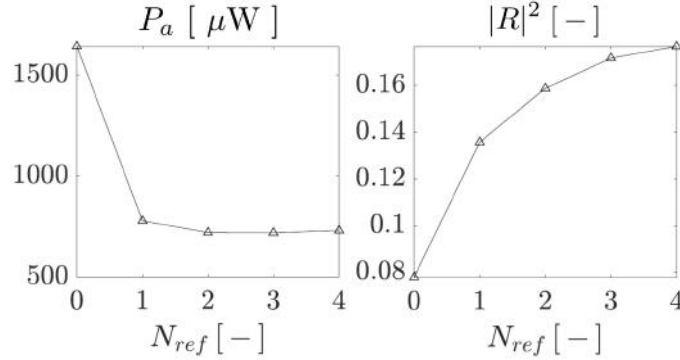


Figure 4.19: Convergence of the absorbed power and power reflection ratio.

thousand elements is between 1-10 minutes. Regarding its scalability, the computational cost of these simulations is only a function of the number of elements, where a linear regression results in a law $t_c \sim 1.44N_{el}^2$ with only a R-squared value of 0.981. In fact, the computational cost of this simulation could be improved with the use of complex number formulation and solvers as well as a parallelized version.

As a result of this investigation the behavior of the solutions with mesh refinement has been analyzed, highlighting the capabilities of the model and providing know-how on the refinement strategy to be selected when solving similar problems.

4.5 Sensitivity analysis on the electron collisionality

As it was revisited in Chapter 3, a nonzero wave damping is required for the use of the models presented in this Thesis. In absence of further refined methods to estimate its value (i.e. kinetic codes), the effective electron collisionality obtained by HYPHEN is used as electron damping frequency also for the electron momentum equation used in the collisional cold-plasma model (see §2.3.1).

This section shows the principal effects of electron collisionality on the solutions obtained by ATHAMES. The analysis is carried out taking as reference the mesh of 119040 elements used in §4.4.2. The results are obtained for different scaling factors applied on the effective collisionality map shown in Fig. 4.14.

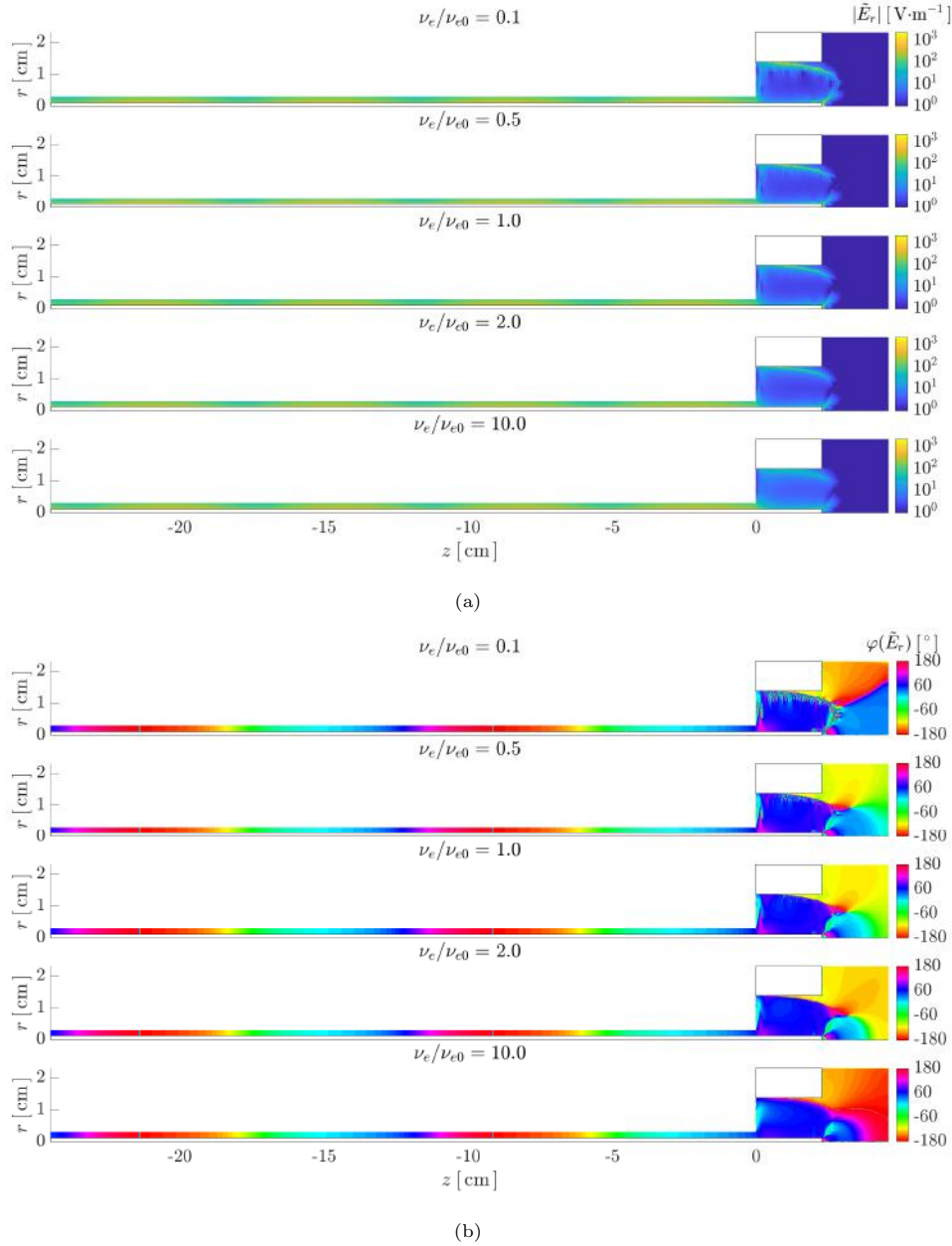


Figure 4.20: Evolution of the radial electric field complex amplitude (a) magnitude and (b) phase for different scaling factors on the electron collisionality.

The radial electric field solutions for different collisionalities are shown in Fig. 4.20. The first and most apparent effect of electron collisionality is the smoothing obtained on the high frequency oscillations found in EM parametric regions III and IV. The oscillations in both magnitude and phase are damped out, as can be observed in Figs. 4.20a and 4.20b. The peak electric fields resulting from this oscillatory behavior are also considerably reduced.

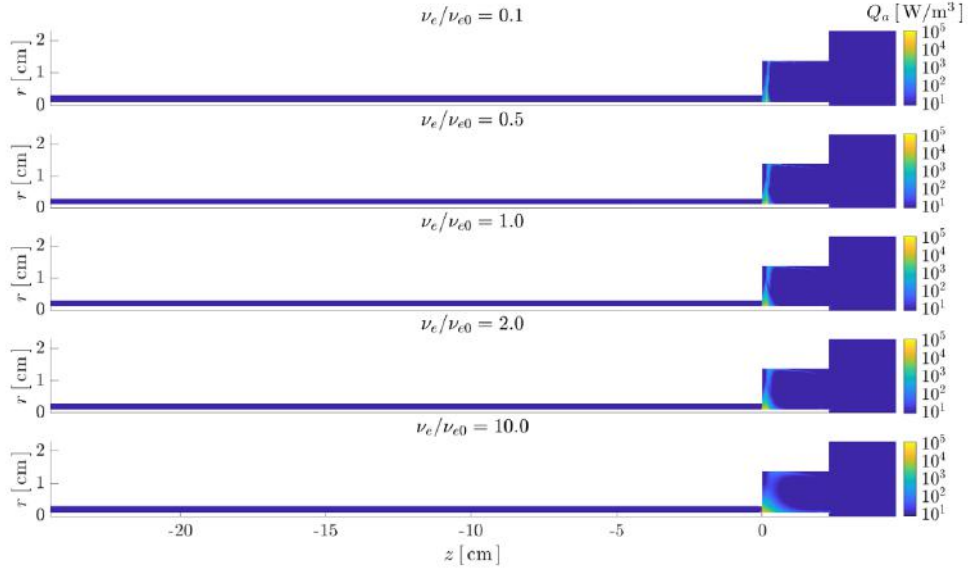


Figure 4.21: Absorbed power for different electron collisionalities.

The evolution of EM power absorption maps is shown in Fig. 4.21. As observed in section 3.1.4 for the 1D model, the main effect of the collisionality is to increase the thickness of the ECR region. For a change in ν_e of two orders of magnitude, the absorption region changes from being located exactly at the ECR, to a widespread region in the vicinity of the resonance.

The coupled simulations with HYPHEN use uniquely (up to this date) the EM power absorption map obtained by the code. This variable is shown here to maintain its overall topology whenever the collisionality is modified, apart from the widespread of lower electromagnetic power contributions. Moreover, the variations in the power absorption maps are mitigated by the fact that both codes use different mesh resolutions, being that of the EM solutions one or two orders of magnitude finer. As a result, the effects of the electron collisionality model selected are minor in the coupled solutions that are shown starting from Chapter 5.

ν_e/ν_{e0} [-]	t_c [s]
0.1	963.8
0.2	736.2
0.5	696.9
1	670.5
2	643.6
5	420.2
10	479.9

Table 4.8: Influence of the electron collisionality used on the simulation computational time.

The effect of collisionality on the computational time (t_c) is shown in Tab. 4.8. Although the computational time does not vary fully monotonically with the electron collisionality, it can be observed that it is reduced by collisionality. This result may be explained by the increase of the spatial frequency band filtered when increasing wave damping. Note that in this case, an increase of two orders of magnitude in the collisionality can lead to halving the computational time.

4.6 Concluding remarks

In this section the physical and mathematical model of the electromagnetic wave simulation code developed during this thesis has been shown, together with its associated numerical implementation details. An introduction to a generalized formulation is shown and then it is particularized to both planar (THAMES) and axisymmetric (ATHAMES) geometries, focusing in the latter since it is of greater interest for ECRT simulation. ATHAMES utilizes an axisymmetric mathematical variational formulation based on Galerkin's finite element method that fulfills the axisymmetric boundary conditions using a mixed finite element basis to discretize the electric field.

A cold-plasma collisional approach is used to model the plasma response to electromagnetic fields. The code solves for the electric field in presence of ECR plasmas with highly inhomogeneous EM propagation and absorption properties, featuring several cutoffs and resonances. The finite element method allows to use an unstructured mesh which provides several advantages, including the description of complex geometries and the application of predictive refinement. The latter consists on performing local refinement based on the mesh resolution requirements given by the principal EM wavelengths estimated locally. Additionally, predictive refinement is shown capable to mitigate spurious noise found around EM parametric regions III and IV. Similar numerical noise is found in other applications as in fusion reactors, and it is a subject of future research. The application of local refinement not only excels at refining closer to resonances but also to apply dedicated refinement to critical locations as the coaxial to thruster chamber transition, or perfect electric conductor corners.

The code verification has been shown with the multiple test cases used in both the planar geometry and the axisymmetric geometry. Incremental verification of features with increasing complexity is shown by the obtention of the convergence rates expected by the discretization choice (i.e. the finite element order used). Additional verification shows the effect of mesh refinement on the convergence of numerical solutions.

Finally, an investigation on the effects of electron collisionality on the 2D electromagnetic solutions is carried out. Increasing electron collisionality is shown to decrease the computational cost of the simulations. This increase in damping expands the wave number band filtered to lower wave numbers, damping out lower wave number solutions and thus decreasing computational time. This results in decreasing fundamentally spurious noise as can be seen in the electric field phase convergence. Regarding the magnitude of the radial electric field, while keeping its topology, increasing collisionality resulted in smoother magnitudes and decreased maxima. Moreover, as it was found in chapter 3, the main effect of collisionality is to control the thickness of the EM absorption region.

Future upgrades and extensions of the code include (i) the other azimuthal modes (i.e. $m > \pm 1$ and $m \geq 1$), (ii) absorbing boundary conditions including a perfectly matched layer and (iii) port boundary conditions .

Chapter 5

Coupled plasma transport and electromagnetic wave simulation of an ECR thruster

*An electron-cyclotron resonance thruster (ECRT) prototype is simulated numerically, using two coupled models: a hybrid particle-in-cell/fluid model (HYPHEN) for the integration of the plasma transport and a frequency-domain full-wave finite-element model (ATHAMES) for the computation of the fast electromagnetic fields. The quasi-stationary plasma response, fast electromagnetic fields, power deposition, particle and energy fluxes to the walls, and thruster performance figures at the nominal operating point are discussed, showing good agreement with the available experimental data. The ECRT plasma discharge contains multiple electromagnetic field propagation/evanescence regimes that depend on the plasma density and applied magnetic field that determine the flow and absorption of power in the device. The power absorption is found to be mainly driven by radial fast electric fields at the ECR region, and specifically close to the inner rod. Large cross-field electron temperature gradients are observed, with maxima close to the inner rod. This, in turn, results in large localized particle and energy fluxes to this component. The contents of this chapter have been published in the peer-reviewed journal *Plasma Sources Science and Technology* [57]. The contents of this chapter are part of EP2's contributions to MINOTOR project.*

5.1 Introduction

The electron cyclotron resonance thruster (ECRT) [5–10] belongs to the category of electrodeless plasma thrusters. Another example of this family of devices is the Helicon plasma thruster (HPT) [17, 92]. These thrusters use electromagnetic (EM) heating to generate and energize the plasma, and thus allow eliminating exposed electrodes from their design, which are often lifetime-limiting components. The ECRT relies on the localized absorption of EM power at an electron-cyclotron resonance (ECR) region, whereas the HPT is based on non-resonant heating. Both concepts utilize a cylindrical ionization source and an external magnetic nozzle (MN) to expand the plasma contactlessly and create magnetic thrust. The ECRT, which is the object of the present work, should not be mistaken with the gridded ion thrusters based on ECR heating [4].

The first investigation of this propulsion concept began in 1962 [5], using a waveguide to deliver the power into a cylindrical discharge chamber with an externally-applied magnetic field that ensured resonance conditions and configured the external magnetic nozzle. In [6], a 2% efficiency thruster with 22% energy and 80-90% coupling efficiencies were reported for a 320W argon proto-

type without performing any optimization of the device. In [7, 8], devices up to 15% thrust efficiency were built and tested. Similar performance was obtained recently as well [11, 12, 26, 50, 51, 53, 93–95].

A successful model of the ECRT must take into account the plasma transport problem and the plasma-wave problem, which are intimately coupled together. Existing ECRT transport models are (quasi) one-dimensional and either take a fluid quasineutral approach [10] or a particle-in-cell (PIC) approach [96]. More recent models focus on the HPT [97–99], but these models are in general applicable for the ECRT as these two thrusters share most characteristics in terms of transport phenomena.

On the other hand, plasma-wave interaction models in ECR plasmas have different requirements than those used for the HPT [54, 100] due to the presence of a resonance and highly inhomogeneous EM properties. Models for ECR heating have been developed for other applications as for fusion tokamaks [101, 102], ECR ion source plasmas [103] or plasma etching [37]. The physical phenomena governing plasma-wave interaction, wave propagation and absorption in ECR plasmas have been investigated in the past [32, 34, 36, 104, 105], mainly with 1D models. Methods used for wave simulation as beam/ray tracing algorithms [38, 39], while useful to obtain a first insight on propagation and absorption characteristics, are not adequate for an accurate assessment of the ECRT since the device characteristic length is comparable to the wavelength. A full-wave approach, that obtains solutions of Maxwell's equations directly in the simulation, either in time domain [40, 41] or frequency domain [42, 43], becomes necessary.

Despite these advances, the simultaneous and self-consistent computation of the plasma transport and the fast electromagnetic fields in the ECRT has not been achieved so far. As the power deposition can affect the plasma response and vice-versa, this coupling becomes necessary to understand the physics and the operation of the device and properly estimate its performance. Indeed, existing comparisons between experimental and theoretical results [10] of an argon tested device report large differences between the measured and expected, jet efficiency (e.g. 41% compared to a 2%) and coupling efficiency (e.g. 98% compared to a 30%). Further contemporary comparisons for the ECRT [51] accomplished a fairer agreement between measurements and theoretical estimations using an HPT model [99]. However, that model not only underestimates the steady-state electron temperature, but also does not describe the plasma cross-field diffusion and antenna/plasma power coupling. As a result, that model cannot reproduce radial profiles in plasma density, nor the power transfer efficiencies.

Recently, the European H2020 MINOTOR project [49] was funded to investigate and continue the development of the ECRT concept, with the purpose of demonstrating its feasibility for space propulsion. In the context of this project, a two-dimensional, axisymmetric model of the ECRT discharge has been developed to enable parametric investigations of the operation of this device, both to improve the current understanding of the complex phenomena within the thruster as well as to support the development of the prototype. The model is composed of two main components which are coupled together to obtain the plasma and electromagnetic field response in the thruster:

(i) a hybrid PIC/fluid model to solve for the internal and near-plume plasma transport, and (ii) a full-wave, finite element (FE) model of the electromagnetic field-plasma problem in the frequency domain to solve the electromagnetic fields and the power absorption in the device. An initial version of the former has been reported independently in [60, 73, 106, 107], while the latter was introduced in [58, 59].

In this work, we use this approach to simulate numerically the ECRT prototype developed by ONERA as part of the MINOTOR project in its nominal operating point [12, 53, 95], solving the coupled plasma transport problem and the electromagnetic problem. The maps of the different plasma properties and electromagnetic fields are discussed, together with the particle and energy wall fluxes. Finally, the performance parameters of the thruster are compared against the available experimental data, to provide a partial validation of the model.

The rest of the paper is structured as follows. The physical and numerical models used in each module and the simulation setup are described in section 5.2. Section 5.3 presents and discusses the simulation results. Finally, conclusions and future work are listed in section 5.4.

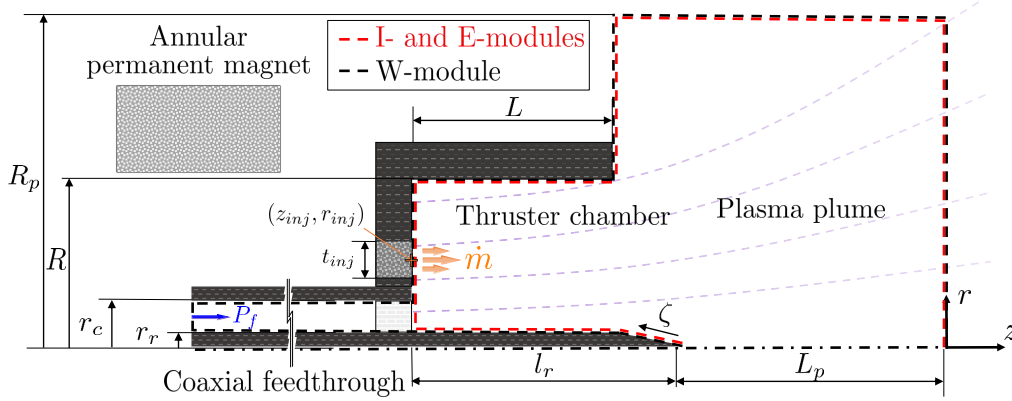


Figure 5.1: Sketch of the ECRT simulation domain. For geometrical dimensions refer to Tab. 5.1. The arc-length variable ζ covers the perimeter of the thruster wall meridian section.

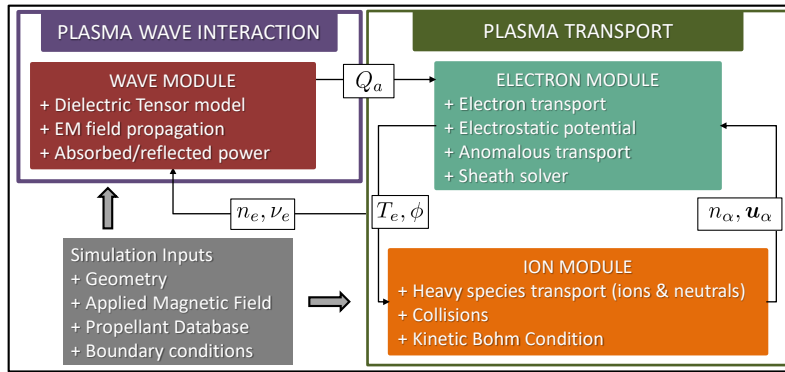


Figure 5.2: Overall code structure, composed of an ion/neutral module, an electron module, and a wave module.

5.2 Simulation model

The design of an ECRT (see Fig. 5.1) consists of a rear wall and a cylindrical lateral wall that form the thruster chamber. The chamber contains an inner rod element along its centerline. All these elements are metallic and covered by a thin boron nitride coating. Neutral xenon gas is fed into the chamber through injector holes on the rear wall. A coaxial cable feeds electromagnetic power to the thruster through a dielectric window located at the center of the rear wall. The core conductor of the coaxial cable is electrically connected to the metal of the inner rod element, and the shield of the coaxial cable is electrically connected to the metal of the rear and lateral walls. A divergent applied magnetic field creates a magnetic nozzle that is used to accelerate the plasma as shown in Fig. 5.1 and sets up the conditions for the electron cyclotron resonance inside the thruster chamber.

The model and code presented here have been tailored for the simulation of this coaxial ECRT, but are applicable to more general thruster types. The overall structure of the simulation model is shown in Fig. 5.2, and is based on the separation of two distinct time scales: that of the slow (up to a few MHz) plasma transport response, and that of the fast (GHz) applied electromagnetic field. The model is composed of three main modules: (i) The so-called Ion (I-) module, solving the slow response of the heavy species (i.e. ions and neutrals). (ii) The Electron (E-) module, solving the slow response of the electrons and the quasineutral, quasi-stationary electric potential map. The E-module also takes care of solving the thin non-neutral Debye sheaths that form on the (dielectric) thruster walls, the secondary electron emission (SEE), and the particle and energy fluxes to the walls. (iii) The Wave (W-) module, solving the fast time scale interaction

between the electromagnetic emission and the electrons. The I- and E-modules describe the quasi-stationary transport of the plasma. The features of these two modules have been described in Refs. [59, 60, 72, 73, 106–108]. Their main aspects are described briefly in the next subsections. The W-module [58, 59] is a new development and is thus described in detail afterwards.

Symbols \mathbf{E} and \mathbf{B} are reserved for the high frequency electromagnetic fields. The static magnetic field applied by the coils is called \mathbf{B}_0 , and the quasi-steady electric field is denoted as $-\nabla\phi$, with ϕ the electrostatic potential. Symbols n_s , T_s , \mathbf{u}_s , \mathbf{j}_s , refer to the quasi-steady density, temperature, macroscopic velocity and current density, respectively, of a generic plasma species s . The right-handed cylindrical vector basis, $\{\mathbf{1}_z, \mathbf{1}_r, \mathbf{1}_\theta\}$, and the unit vectors $\mathbf{1}_\parallel = \mathbf{B}_0/B_0$, $\mathbf{1}_\perp = \mathbf{1}_\theta \times \mathbf{1}_\parallel$, and $\mathbf{1}_n$ (outward unitary normal vector at the domain boundary) are used in the following. Without loss of generality, we take \mathbf{B}_0 pointing downstream.

As explained in more detail later, the four modules are run sequentially, in close loop, with different timesteps, communicating with each other to share the relevant variables. In particular, the E-module takes as inputs n_α and \mathbf{u}_α of all heavy species α from the I-module, and delivers ϕ and T_e to that module. In addition, the E-module takes the time-averaged absorbed power density Q_a as input from the W-module and delivers n_e and the electron total collision frequency ν_e to that module. Each module utilizes a different grid or mesh, optimized for its own requirements, and interpolation between the meshes is applied. The simulation domain for the I- and E-modules (in red in Fig. 5.1) consists of the thruster chamber and the magnetic nozzle region. The simulation domain for the W-module (in black in Fig. 5.1) adds a segment of the coaxial power feed cable.

5.2.1 The I-module

For the heavy species, a PIC formulation with Montecarlo collisions (MCC) is used [60]. Macroparticles evolve in an structured mesh subject to (i) a particle mover that propagates the trajectory of the macroparticles with a leap-frog scheme subject to the quasi-steady fields $-\nabla\phi$ and \mathbf{B}_0 ; (ii) various types of collisions, including ionization (e.g. single, double, and single to double) by electron bombardment and charge-exchange collisions among neutrals and ions [109], (iii) the interaction with the different channel walls and their Debye sheaths, which includes neutral accommodation at the walls and re-emission, ion recombination and re-emission as neutrals, and the fulfillment of the Bohm criterion at the sheath edge [110]. At the position of the injector, a prescribed mass flow rate \dot{m} of neutrals is injected into the domain. Heavy particles reaching the downstream open boundary are removed. Neutrals, singly-charged, and doubly-charged ions are treated as different heavy species and the corresponding macroparticles are kept in different computational lists, which are used for weighting their macroscopic properties onto the PIC mesh. Figure 5.3(a) plots the structured cylindrical-type mesh used in the I-module. The mesh is finer close to the walls to improve the characterization of gradients in the vicinity of walls. An statistical population control mechanism is implemented to each species looking for an optimal number and size of macroparticles in each cell [111]. A typical number of macroparticles per cell for this type of simulations is around 300. In order to improve the population control in the plume, the mesh cell-size is increased downstream.

5.2.2 The E-module

In their low-frequency response, electrons are treated as a magnetized diffusive fluid [72]. The set of fluid equations is the following:

$$\nabla \cdot \mathbf{j}_e = -\nabla \cdot \mathbf{j}_i, \quad (5.2-1)$$

$$0 = -\nabla p_e + en_e \nabla \phi + \mathbf{j}_e \times \mathbf{B}_0 + \mathbf{F}_{coll} + \mathbf{F}_{turb}, \quad (5.2-2)$$

$$\frac{\partial}{\partial t} \left(\frac{3}{2} p_e \right) + \nabla \cdot \left(\frac{5}{2} p_e \mathbf{u}_e + \mathbf{q}_e \right) = \mathbf{u}_e \cdot \nabla p_e - \mathbf{u}_e \cdot (\mathbf{F}_{coll} + \mathbf{F}_{turb}) + Q_a + Q_{coll}, \quad (5.2-3)$$

$$0 = -\frac{5}{2e} \nabla(p_e T_e) - (\mathbf{q}_e + \frac{5}{2} p_e \mathbf{u}_e) \times \mathbf{B}_0 + \frac{5p_e}{2} \nabla \phi - \frac{m_e \nu_e}{e} \mathbf{q}_e + \mathbf{Y}_{turb}. \quad (5.2-4)$$

Equation (5.2-1) states the conservation of electric current, with $\mathbf{j}_i = \sum_{s \neq e} Z_s e n_s \mathbf{u}_s$ the total positive current provided by the I-module. Equation (5.2-2) is the momentum equation, where electron inertia has been neglected; $p_e = n_e T_e$ is the (isotropic) electron pressure; and $\mathbf{F}_{coll} = -m_e n_e \sum_{s \neq e} \nu_{es} (\mathbf{u}_e - \mathbf{u}_s)$ is the resistive force due to collisions, with $\nu_{es} = \nu_{es}(T_e)$ the effective collision frequency of electrons at temperature T_e with species s , which includes ionization and excitation collisions and elastic electron collisions with neutrals and ions.

Finally, the term $\mathbf{F}_{turb} = \mathbf{1}_\theta \alpha_t j_{\theta e} B_0$ in equation (5.2-2) is a phenomenological turbulence model, with α_t an empirical parameter adjusted to match experimental results. Turbulence is believed to be the main source of anomalous transport in Hall thrusters, and this model (which results in a net enhancement of the electron transport perpendicular to the magnetic field) has been used successfully in the past to explain experimental measurements [112, 113]. Evidence of turbulence on electrodeless plasma thrusters like the ECRT is still very limited, but existing results [114] indicate that it is a pervasive element of these devices (and HPTs) as well. As the ECRT also features an $E \times B$ plasma like Hall thrusters, the same model is used here to introduce the effect of turbulent transport in the simulation. After a sensitivity analysis on α_t , which showed it affects substantially the peak electron temperature, but little the propulsive performance figures (such as thrust and specific impulse), a value $\alpha_t = 0.02$ was found to match well the experimentally available T_e measurements at the axis downstream [52].

Equation (5.2-3) is the internal energy equation, where: \mathbf{q}_e is the electron heat flux; $Q_{coll} = -n_e \sum_{s \neq e} \nu_{es} \varepsilon_{es}$, (with ε_{es} the energy yield of the collision) is the power sink due to collisions with heavy species, mainly ionization and excitation of neutrals. Equation (5.2-4) is a diffusive model for the electron heat flux, structurally similar to the momentum equation, with $\nu_e = \sum_{s \neq e} \nu_{es}$, and $\mathbf{Y}_{turb} = -\mathbf{1}_\theta \alpha_t q_{\theta e} B_0$ a turbulence-based contribution, here enhancing the perpendicular heat flux. Additionally, the quasineutrality condition

$$n_e = \sum_{s \neq e} Z_s n_s, \quad (5.2-5)$$

is imposed in the bulk of the simulation domain, i.e., except in the sheaths. In this expression, the right hand side is the positive charge density, provided by the I-module, with Z_s the charge number of each species.

Boundary conditions for the electron fluid equations depend on the type of surfaces. On the axis, symmetry conditions are imposed, implying that the radial electric current and electron heat flux are zero. On the current-free downstream boundaries, the net normal electric current, $j_n = \mathbf{j} \cdot \mathbf{1}_n$, is set to zero and the normal electron heat flux satisfies $q_{ne} = \mathbf{q}_e \cdot \mathbf{1}_n = 2T_e n_e u_{ne}$. At the thruster walls the normal electric current density j_n and the normal heat flux q_{ne} are computed by the sheath solver described next.

The Sheath solver relates the electron magnitudes at the sheath edge and the thruster wall. In the thruster simulated here, walls are covered by boron nitride, which has a high SEE yield, defined as the ratio of secondary-to-primary electron fluxes. The macroscopic SEE yield, $\delta_w(T_e)$ is modeled according to Ref. [115], which is based on the following parameters:

$$\delta_w = \delta_{ws} + \delta_{wr}, \quad \delta_{ws} = \frac{2T_e}{E_s}, \quad \delta_{wr} = \frac{\delta_{r0} E_r^2}{(T_e + E_r)^2}, \quad (5.2-6)$$

where $\delta_{ws}(T_e)$ and $\delta_{wr}(T_e)$ are yields for, respectively, (true) secondary electrons (emitted with a small temperature T_{se}), and elastically reflected primary electrons. For high electron temperatures δ_{ws} is limited to a maximum of 0.983, when charge saturation is expected to happen [116]. The energies E_s and E_r are δ_{r0} are material dependent. Additionally, the sheath model takes into account the partial depletion of the high-energy tail of primary electrons lost into the walls, with the replenishment parameter σ (equal to 100% for full replenishment). The net normal electric current to the dielectric wall, j_n , with contributions of ions and primary and secondary electrons, is zero. As a result the sheath local potential fall between sheath edge Q and (dielectric) wall W,

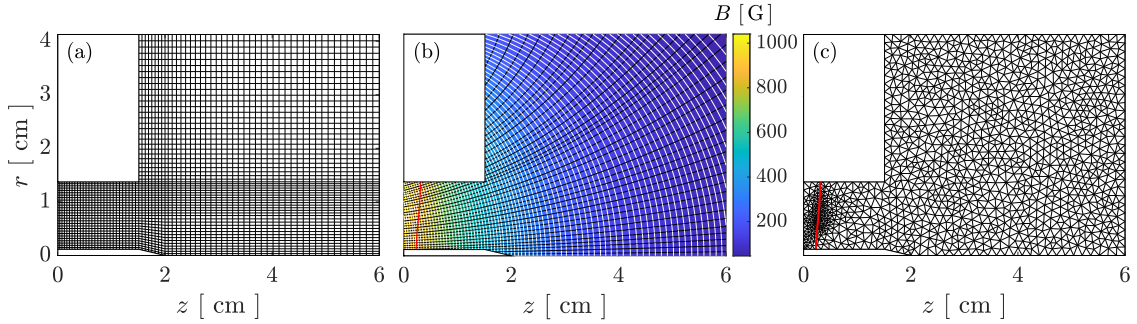


Figure 5.3: (a) PIC mesh, (b) MFAM and (c) representation of the W-module mesh. In (b), the colormap represents the applied magnetic field strength, magnetic streamlines are shown in black and their perpendicular in white. The red curve represents the ECR location.

fulfills the relation

$$e \frac{\phi_Q - \phi_W}{T_e} = \ln \left[\frac{en_e \bar{c}_e}{4j_{ni}} \Big|_Q (1 - \delta_{ws})(1 - \delta_{wr})\sigma \right]. \quad (5.2-7)$$

The normal heat flux to the wall, q_{ne} , is the difference of the normal flux of total electron energy, adding the contributions of primary and secondary electrons, minus the normal flux of convective energy of the electron fluid [115]. Settings here are for boron nitride: $E_s = 50$ eV, $E_r = 40$ eV, $\delta_{r0} = 0.4$, $T_{se} = 2$ eV and $\sigma = 0.3$ [112, 115, 117].

In order to avoid numerical diffusion caused by the large magnetic anisotropy, the electron fluid equations are solved in the magnetically-aligned mesh plotted in Fig. 5.3(b). Specific numerical algorithms have been developed for this [72]. For the conservation laws (5.2-1) and (5.2-3), these are based on finite volume schemes. For equations (5.2-2) and (5.2-4), which are actually state equations relating \mathbf{j}_e and \mathbf{q}_e with ϕ and T_e gradients respectively, the algorithms are based on finite difference schemes. Irregular cells, next to boundaries require special attention for their accurate solution.

5.2.3 The W-module

The electromagnetic wave theory used and the electromagnetic wave module (ATHAMES) are detailed in chapters 2 and 4, respectively.

5.2.3.1 W-module mesh refinement strategy

The different electromagnetic modes that exist in each region of figure 5.8 have widely varying characteristic wavelengths. Accurate simulation of the high-frequency electromagnetic fields demands a sufficient number of elements per wavelength, which calls for a specific W-module meshing strategy, driven by different requirements than the I-module and E-module meshes.

To illustrate the difficulty, Fig. 5.4 shows the complex phase of the fast electromagnetic fields \tilde{E}_z in a uniform mesh and a refined mesh. It also displays the characteristic number of mesh elements per local wavelength, this one computed from the dielectric tensor for each case. High wavenumber oscillations are observed in the neighborhood of the UHR surface in the uniform-mesh simulation results, which are only partially physical. Such oscillations do not correlate with waves as there is a mismatch between the expected wavelengths given by the local properties and the numerical solution. Furthermore, as the oscillations scale is of the order of the mesh-cell characteristic length, this suggests that such oscillations are in fact spurious noise. Indeed, progressive refinement of the mesh shows that the fields converge to those on the right of the figure, where most of this oscillations have disappeared and therefore are considered error noise. Only some of the oscillations remain in the low-density channel that occurs near the inner rod element in this simulation, as shown in the main text (Fig. 5.9). Noteworthy, while the noise affects the field phase, it was observed that it does not impact significantly the power absorption profile.

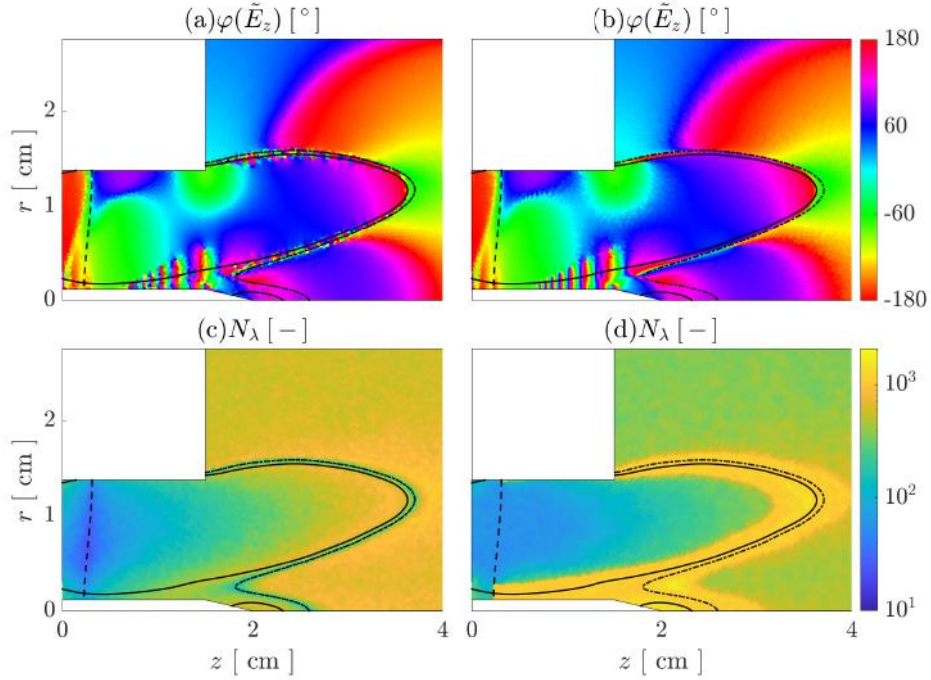


Figure 5.4: Complex phase of the \tilde{E}_z fast electromagnetic field and number of mesh elements per local wavelength for a uniform mesh (left) and for a refined mesh (right).

Therefore, in the present work the mesh is refined around the ECR and the UHR regions in the last iterations of the W-module only, a procedure that has proved successful in mitigating this spurious noise and speeding up convergence to the steady-state results.

As a final observation, it is noted that multiple plasma and magnetic field profiles were tested, reaching the conclusion that the location of this noise is in direct correlation with the location of the UHR surface. Similar spurious solutions near this resonance are reported near lower-hybrid resonances in other works [88], which show some mathematical analogy with the UHR. A regularization of the double-curl formulation of the finite elements scheme is suggested there as an alternative route to solve this issue [89, 90].

5.2.4 Simulation setup

The ECR thruster used for this simulation is that of the MINOTOR prototype being matured at ONERA, as shown in Fig. 5.1. The applied magnetic field generated by an annular permanent magnet is shown in Fig. 5.3(b), whose local unit vector points downstream, defining magnetic streamlines. The operational point is the nominal one for the device [12, 26]. The geometric, operational, and numerical parameters are listed in Tab. 5.1. The ECR surface is located approximately 3 mm downstream the backplate.

The instantaneous plasma properties computed in the coarser PIC mesh and the MFAM are smoothed using a Gaussian filter when interpolated to the electromagnetic mesh, and conversely, spatial anti-aliasing is applied when transporting Q_a from the W-mesh to the MFAM.

The I-module has a timestep of Δt_I , which ensures that the fastest ion particles do not cross more than half a cell of the PIC mesh per timestep. The E-module is run 40 times per I-module step. Since the electron density n_e and effective collisionality ν_e vary only slowly as the steady-state is approached, the W-module is only run every 5000 I-module steps.

To initialize the simulation, the I-module is run alone for a number of steps to fill the domain

Parameter	Name	Units	Value
l_r	Inner rod length	cm	2
r_r	Inner rod radius	cm	0.115
L	Lateral wall length	cm	1.51
R	Lateral wall radius	cm	1.375
L_p	Plume domain length	cm	2
R_p	Plume domain radius	cm	2.75
z_{inj}	Injection surface center z	cm	0.0
r_{inj}	Injection surface center r	cm	0.5735
t_{inj}	Injection surface width	cm	0.229
r_c	Coaxial shield radius	cm	0.3
f	Wave frequency	GHz	2.45
\dot{m}	Neutral mass flow rate	mg/s	0.2
P_a	Power deposited	W	30
Δt_I	I-module timestep	ns	10
Δt_E	E-module timestep	ns	0.25
Δt_W	W-module update timestep	μs	50
u_{inj}	Propellant injection velocity	m/s	300
T_{inj}	Propellant injection temperature	eV	0.02
α_t	Anomalous transport coefficient	-	0.02
$N_{el,I}$	PIC mesh's cell number	-	3360
$N_{el,E}$	MFAM's cell number	-	2550
$N_{el,W}$	Wave mesh's cell number	-	120782

Table 5.1: Geometrical, operational, simulation and mesh parameters.

with particles, using a simplified, Boltzmann-relation model to emulate the electron response. Then, the E-module is activated with a uniform Q_a map for an additional number of initialization steps. Finally, the coupled I-, E-, and W-modules are run together until steady state conditions are reached. Convergence of the plasma variables to steady state conditions is achieved already after 1.5 ms of simulation time. The simulation results of next section are shown at the end of the simulation, at 3.5 ms. Figure 5.5 illustrates the initialization and steady-state convergence of the simulation by plotting the computed thrust contributions of the different species. The updates of the power absorption profile are indicated by vertical dashed lines. In the following sections, all plasma variables shown have been averaged over 500 ion module time steps after reaching the converged state to reduce numerical noise.

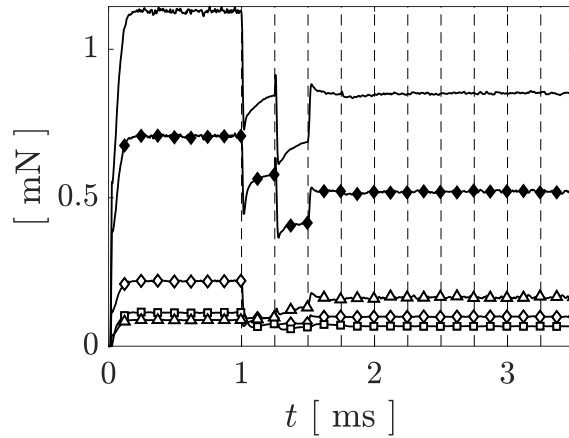


Figure 5.5: Evolution with simulation time of the thrust contributions of Xe^+ (filled diamond), Xe^{2+} (diamond), Xe (square), e^- (triangle) and the total (solid). After an initialization time of 1 ms, Q_a is updated every 250 μs (dashed).

5.3 Results and discussion

The steady-state solution arising from the three coupled modules is reported and discussed next for the nominal operating point of the ECRT. Firstly, the resulting plasma properties are presented, including the singly-charged ion velocity and streamlines and the main contributions to electron momentum balance. Secondly, we explain the high-frequency fields and the power absorption density profile, and its connection with the solution of the transport properties. Thirdly, the plasma fluxes to the device walls are analyzed. Fourthly, the thruster integral figures of merit are computed and compared against the available experimental data for this thruster.

5.3.1 Quasi-steady plasma transport properties

In the steady-state, the neutral propellant density n_n peaks at $6.5 \cdot 10^{19} \text{ m}^{-3}$ near the injection port (see Fig. 5.6(a)). Then, it decreases away from this location featuring a nearly homogeneous profile inside the thruster chamber, adding the contribution of ion recombination at the walls. Neutral density decreases as neutrals expand downstream and ionization takes place, falling more than two orders of magnitude downstream. This decrease is most evident close to the injector, where the ionization is dominant. Neutral density is lowest in the peripheral plume, essentially out of reach for the ballistic neutrals. The fraction of propellant mass flow rate leaving the discharge chamber as ions is roughly 50%.

The singly- and doubly-charged ion densities, n_{i1} and n_{i2} , are shown in Fig. 5.6(b) and (d). As it can be noted, n_{i1} is about one order of magnitude greater than n_{i2} , and both follow the same overall behavior. The maximum singly- and doubly-charged ion densities are of the order of $9.5 \times 10^{17} \text{ m}^{-3}$ and $9.6 \times 10^{16} \text{ m}^{-3}$, respectively. The peak densities are reached in the vicinity of the injector, where most of the ionization takes place. Ion densities decrease toward the thruster walls, and ions impacting there are recombined into neutrals. The ion densities drop noticeably around the inner rod element and in the magnetic tube that originates in this region, which coincides with the region of higher electron temperature as discussed further below. This feature of the plasma discharge was observed to be robust to a sensitivity analysis of the simulation. Consistently with $n_{i2} \ll n_{i1}$, the electron density n_e , shown in Fig. 5.6(c), is essentially equal to n_{i1} , peaking around $1.1 \times 10^{18} \text{ m}^{-3}$. The electron density decreases downstream along magnetic lines as the plasma expands, reaching values of $2.7 \times 10^{16} \text{ m}^{-3}$ at the symmetry axis at the end of the simulated magnetic nozzle domain. This value is consistent with estimations performed with other models as the quasi 1D model presented in Ref. [52].

The quasi-steady map of electron temperature T_e is shown in Fig. 5.6(e), with dashed lines indicating magnetic lines for reference. Due to the strong electron magnetization, effective energy transport rates of electrons along and across magnetic field lines are markedly different. While there exists large temperature gradients perpendicular to the applied magnetic field \mathbf{B}_0 , a near-isothermal behavior is observed in the parallel direction, at least in the finite domain simulated here. Gradual parallel cooling of electrons is expected further downstream, an aspect of the electron expansion that requires a kinetic treatment to be modeled consistently [118].

The maximum electron temperature is 43 eV and is found near the dielectric window that connects the thruster chamber with the coaxial cable, and in the magnetic tube that emanates from this location. As discussed later, the neighborhood of this window is also the location of the maximum power absorption. The electron temperature close to the symmetry axis is around 28 eV which is consistent with the experimental values reported by Lafleur et al. [119] and later by Corretero et al. [52] for 0.2 mg/s and, 20 and 30 W of absorbed power, respectively. T_e goes below 4.3 eV at the lateral wall of the thruster and close to 0.2 eV at the top of the external wall.

Further insight on the electron dynamics can be gained by inspecting the electron pressure $p_e = n_e T_e$, shown in Fig. 5.6(f). This variable is directly related to the thrust of the device, and with the quasi-steady electric field and azimuthal plasma currents, as discussed further below. While n_e displays a minimum in the neighborhood of the axis of symmetry and T_e presents a strong radial gradient, p_e shows a relatively smooth behavior in the whole discharge. Looking at

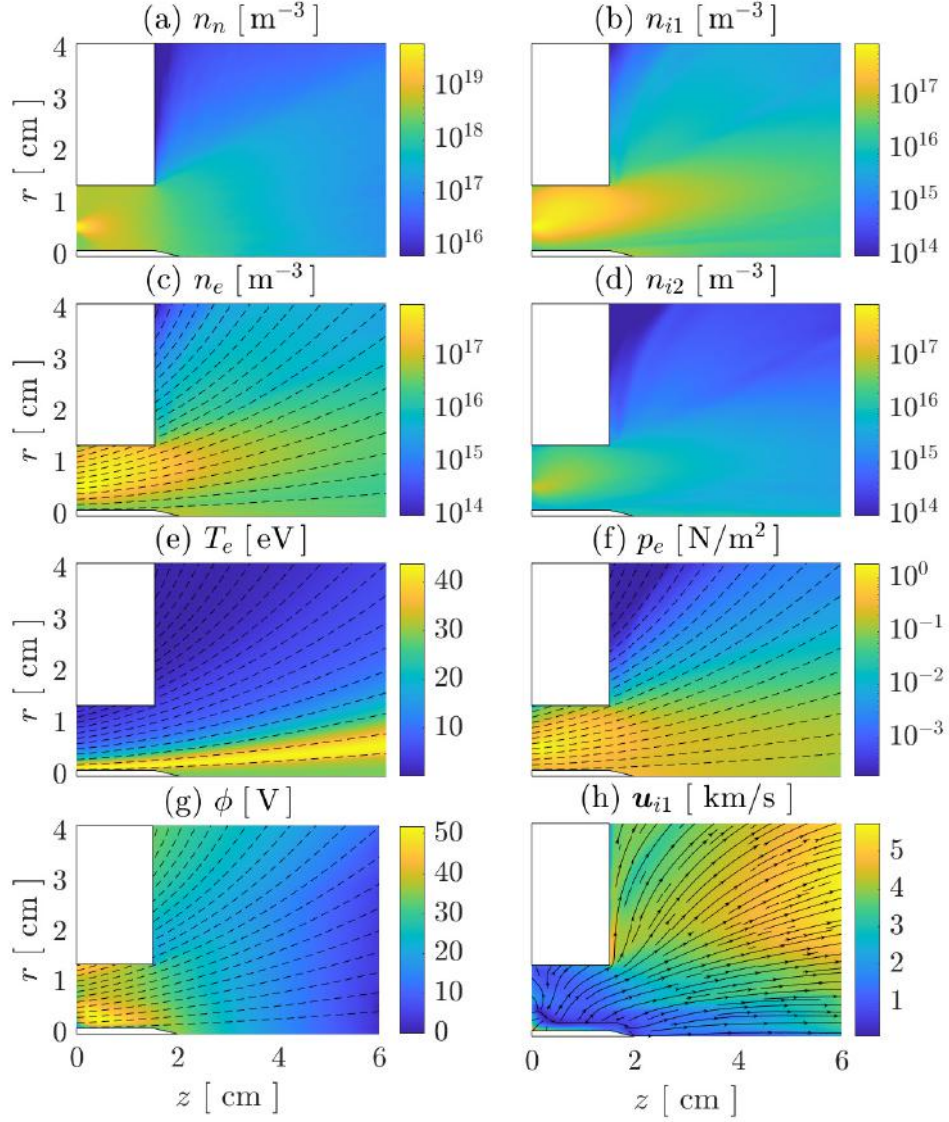


Figure 5.6: Quasisteady plasma transport results: (a), (b), (c) and (d) are neutrals, singly-charged ions, electrons and doubly-charged ions densities, respectively, (e) and (f) electron temperature and pressure, (g) electrostatic potential and (h) singly-charged ions meridional velocity.

$z = \text{const}$ sections of the thruster, the peak pressure takes place at a mid radius inside the annular chamber. Further downstream, in the MN, the maximum pressure is found closer to the axis of symmetry.

The quasi-steady plasma potential ϕ in Fig. 5.6(d) presents an axial fall of roughly 50 V within the simulation domain. It must be noted that the expansion will continue further downstream of this domain to infinity with collisionless electron cooling and further potential drop. The maximum value of ϕ is found inside the discharge chamber, close to the inner rod element of the thruster, right before the quasineutral pre-sheath decreases its magnitude toward the thin non-neutral wall sheaths. The potential decreases axially, along the MN. Note that the position of the maximum does not coincide with either the maximum of n_e , T_e , nor p_e . In the direction perpendicular to the magnetic lines, and always in the quasineutral domain, the potential is essentially flat, except close to the inner rod element where it drops several tens of volts. A minor, secondary maximum of ϕ can be seen close to the lateral inner corner of the discharge chamber, which is attributed to this corner region of being essentially magnetically isolated from the rest of the plasma by the applied field lines, which means that electron transport into this region is severely limited; the small potential rise in this part of the device enhances electron transport from the rest of the plasma toward this region. Similarly, the small increase of ϕ at the top-left corner of the plume domain is attributed to the lack of electrons in this second magnetically-isolated region, although in this case it is considered a numerical side-effect of the finite simulation domain and the presence of the lateral plume boundary.

Another aspect of interest of the ϕ -map is that the potential fall along each magnetic line is not proportional to the corresponding value of T_e , as could perhaps be expected. If this were true, a higher potential fall would be observed in the magnetic tube close to the inner rod element of the thruster. On the contrary, the potential fall is smooth and roughly the same across magnetic lines, indicating that the expansion is a global phenomenon for the whole plasma, despite electrons being well-magnetized. This behavior is consistent with the profiles of n_e and T_e of figures 5.6(c) and (e). Indeed, to leading order, the projection of equation (5.2-2) along $\mathbf{1}_{\parallel}$ yields a Boltzmann-like relation for each magnetic line within the simulated domain,

$$\frac{n_e}{n_{e0}} \simeq \exp \frac{e(\phi - \phi_0)}{T_e}, \quad (5.3-1)$$

where the subindex 0 represents values at a reference location for each line (e.g. upstream). As $\Delta\phi = \phi - \phi_0$ is roughly identical for all magnetic lines, the relative drop of n_e is smaller along the lines where T_e is larger.

The singly-charged ion meridian velocity \mathbf{u}_{i1} and their streamlines are shown in Fig. 5.6(h). While electrons are magnetized, the heavy ions are essentially unmagnetized and thus their dynamics is dominated mainly by the quasi-steady potential ϕ , which accelerates them downstream. Observe that ion streamlines (which roughly correspond to individual ion trajectories, since ions are relatively cold) do indeed not coincide with magnetic lines, and that the ion flow detaches inwardly from the magnetic field [120], resulting in less divergence than the expected one for fully-magnetized ions [121]. The resulting mean velocities at the last section of the simulation domain range from 3 km/s (at the axis) to 6 km/s (at the periphery). This difference is attributed to the location where the ions are created and the path they follow inside the ionization chamber before entering the MN region. For comparison, laser induced fluorescence measurements of the ECRT operating at nominal conditions [52] indicate ion velocities of about 7 km/s and 11 km/s at 4 and 12 cm downstream the thruster exit, respectively. In addition, LIF measurements obtained at U. Michigan [122] with a similar prototype report velocities around 9 km/s 4 cm downstream the thruster exit plane, at background pressure of 13 μTorr .

As a derived quantity, the meridian Mach number of singly-charged ions, based on the approximate local sound velocity, $M_{i1} = |\mathbf{u}_{i1}|/\sqrt{T_e/m_{i1}}$, features its maximal values (around $M_{i1} = 3$) in the peripheral region of the plume, while at its core M_{i1} is only slightly larger than 1. This radial variations are due to the differences in \mathbf{u}_{i1} , compounded with the variations in electron temperature T_e . Arguably, the supersonic expansion in the MN of the device is uneven. It seems

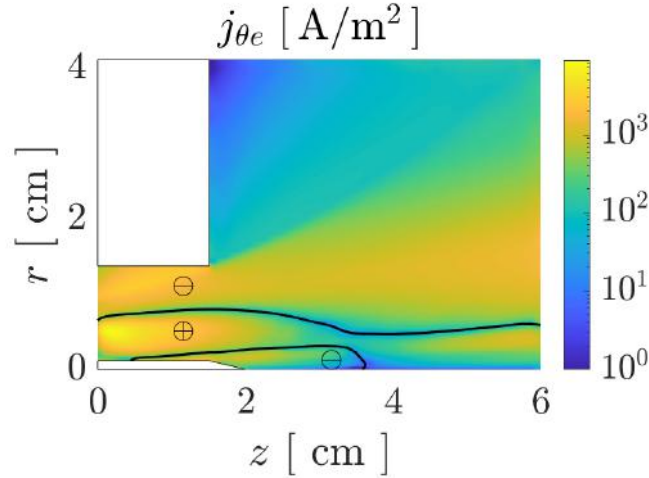


Figure 5.7: Electron azimuthal current density. The black contour line shows the location of the sign change. Icons \oplus and \ominus represent the regions of positive and negative currents, respectively.

plausible that the presence of the rod element in the ECRT discharge chamber induces a dip in the ion Mach number in its wake. This behavior was seen to be robust against the sensitivity analysis carried out, and will be subject of future studies.

Lastly, it can be observed that inside the discharge chamber part of the ion streamlines precipitate onto the walls of the thruster guided by the electrostatic potential fall near those surfaces, giving rise to wall losses, which are discussed in section 5.3.3.

The quasi-steady state azimuthal electron and ion currents are an essential aspect of the operation of the device, as their interaction with the applied magnetic field \mathbf{B}_0 is responsible for the generation of magnetic thrust and the cross-field confinement of the plasma. Figure 5.7 displays the azimuthal current of electrons $j_{\theta e} = -en_e u_{\theta e}$, which is more than two orders of magnitude greater than the azimuthal current of any ion species.

To leading order, in the perpendicular direction the electron pressure gradient $-\nabla p_e$ is compensated by the electrostatic force density $en_e \nabla \phi$ and the magnetic force, $j_{\theta e} B_0 \mathbf{1}_{\perp}$ (see equation (5.2-2)),

$$\frac{\partial p_e}{\partial \mathbf{1}_{\perp}} \simeq en_e \frac{\partial \phi}{\partial \mathbf{1}_{\perp}} + j_{\theta e} B_0. \quad (5.3-2)$$

Given that the quasi-steady electric potential is essentially flat across the magnetic field lines, the current $j_{\theta e}$ is responsible for most of the cross-field confinement of the electron pressure p_e . Consequently, the sign of $j_{\theta e}$ switches mid-radius, close to where the maximum p_e is found in the perpendicular direction, following the sign of $-\nabla p_e$.

The reaction to the axial magnetic force density, $j_{\theta e} B_{r0}$, is felt on the coils of the thruster, and is termed magnetic thrust. Since in the present simulation $B_{z0}, B_{r0} > 0$ in the domain, only negative $j_{\theta e}$ results in positive thrust generation. It can be seen that the outermost part of the plasma is the main contributor to magnetic thrust, while the electrons close to the inner rod element of the device cause some negative magnetic drag in order to confine the electron pressure away from this element. This is a consequence of the maximum electron pressure being located at an intermediate radius rather than the axis of symmetry, and is likely an effect of the presence of the inner rod element. Downstream of this rod element, a small localized region with $j_{\theta e} < 0$ is found.

5.3.2 Fast electromagnetic fields and power absorption

The solution to the high-frequency electromagnetic fields depends on the excitation frequency ω , the applied magnetic field \mathbf{B}_0 , the electron density n_e , and the collisionality ν_e . In particular,

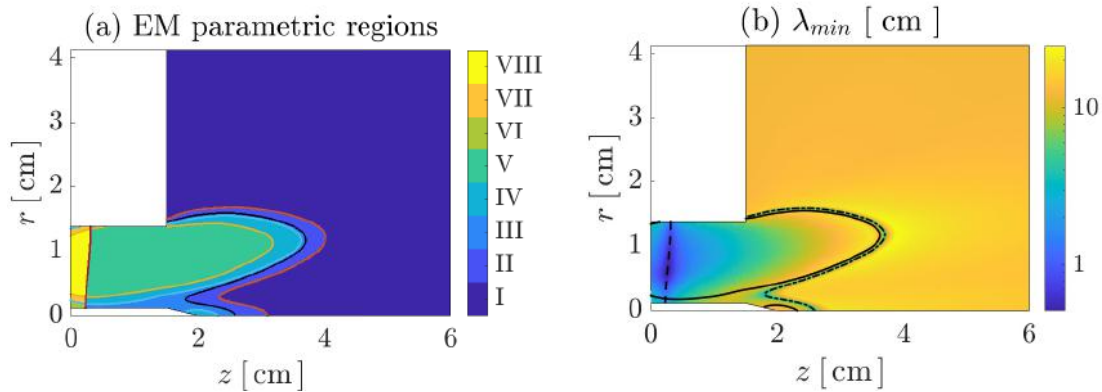


Figure 5.8: (a) Electromagnetic field propagation parametric regions with contours representing the boundary surfaces and (b) minimum principal wavelength, computed from the local dielectric tensor.

the first three variables determine the field propagation regimes, the cut-offs, and the resonances. The last variable, ν_e , which ranges from a maximum value of $4.5 \cdot 10^8$ Hz inside the source and decreases downstream, affects mainly to the homogeneity of the power absorption map. Notably, while \mathbf{B}_0 is an input to the simulation, n_e and ν_e depend dynamically on the plasma transport solution.

The different electromagnetic parametric regions in steady-state are shown in Fig. 5.8(a), following the numerical nomenclature (I to VIII) of Stix [27]. The right-hand circularly polarized wave (R) resonates when $\omega = eB_0/m_e$ which determines the critical value of B_0 (875 G) and the location of the ECR surface. This value separates regions I through V from regions VI through VIII. The plasma frequency cut-off occurs when $\omega = \omega_{pe}$, which determines the critical value of n_e ($= 7 \times 10^{16} \text{ m}^{-3}$). Regimes I, II, III, and VI take place below this value of n_e , and are considered underdense regimes. Regimes IV, V, VII and VIII are overdense regimes.

Region I (low B_0 , low n_e) is topologically equivalent to propagation in vacuum, with both R and L (i.e. left-hand circularly polarized) propagating modes. It is separated from region II by the R wave cut-off. In region II, only L waves propagate. As B_0 and n_e increase, eventually the upper-hybrid resonance (UHR) is crossed into region III, where two propagating solutions exist at directions other than \mathbf{B}_0 . Region IV (low B_0 , high n_e) exhibits propagating L waves only. In region V (separated from region IV by the L wave cut-off) no propagating solutions exist, and all electromagnetic fields are evanescent. Region VI (high B_0 , low n_e) features both R and L polarizations. Regions VII and VIII (high B_0 , high n_e) feature whistler R waves, which propagate in directions close to \mathbf{B}_0 ; additionally, region VII also has regular L-waves.

As it can be noticed in Fig. 5.8(a), in this ECRT simulation all these regions (i.e. I through VIII) are present within the simulation domain and in close proximity to each other. The contour lines detail the location of the different cutoffs and resonances, which act as the boundary surfaces of the different propagation regimes. In particular, the presence of the ECR and UHR stands out. Whereas the location of the ECR is fixed only by the magnetic field, the UHR is determined by a combination of both the magnetic field and the electron density.

As the electromagnetic power enters the discharge chamber through the coaxial line, it enters regions VI-VIII (upstream of the critical B_0), and soon reaches the ECR surface. Most of the discharge chamber is overdense ($\omega_{pe} > \omega$), and therefore downstream of this surface there is a region V where only evanescent fields are allowed. However, a thin low-density channel exists near the inner wall corresponding to regions III and IV. Power can propagate along this channel, and also tunnel through a short evanescent region. Further downstream, as both B_0 and n_e decrease, all other regions are crossed, until eventually region I is reached.

The existence of all these regions implies wide changes of the local wavelenghts in the domain. Figure 5.8(b) illustrates this by plotting the minimum wavelength in the perpendicular and parallel directions for all propagating modes. The smallest wavelenghts occur near the ECR and the UHR

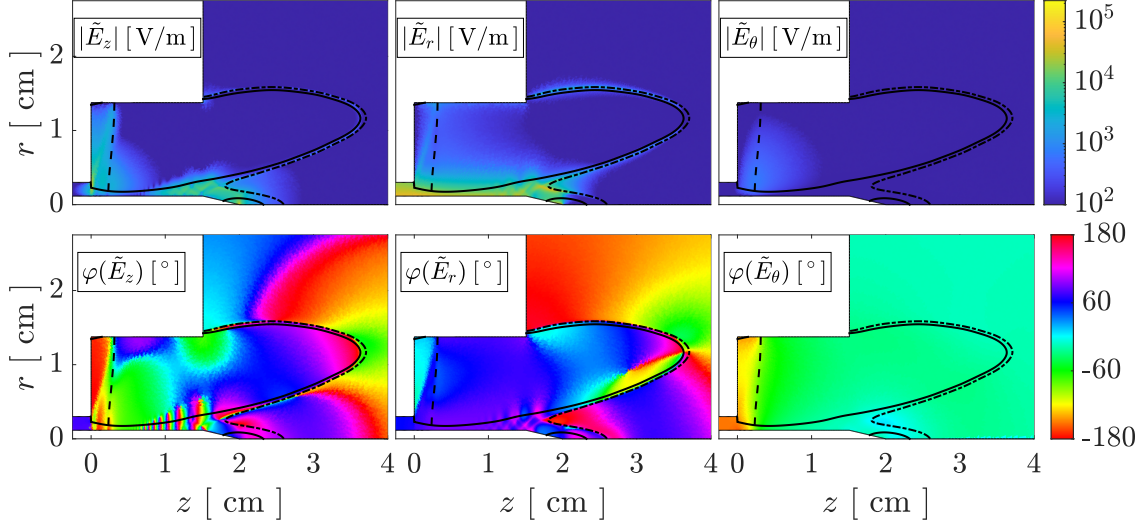


Figure 5.9: Electromagnetic wave electric field (complex magnitude and phase). The contour lines represent the cutoff $\omega = \omega_{pe}$, the ECR surface (dashed) and the UHR surface (dashed-dotted).

surfaces, and the W-module mesh has been refined accordingly, as described in chapter 4 and §5.2.3.1.

The amplitudes and complex phases of the three components of the fast electric field \mathbf{E} are shown in Fig. 5.9. The resulting electric field inside the coaxial cable is a strong radial field, characteristic of the TEM mode. As the power flows into the plasma, the radial component of the EM wave electric field \tilde{E}_r still dominates on both sides of the ECR surface, and continues to be large in the thin regions III and IV that exist around the rod element of the thruster. It can be observed that an axial electric field \tilde{E}_z also develops before the ECR surface and downstream from the rod element decaying after the resonance, and that the azimuthal field \tilde{E}_θ plays only a minor role. Small magnitude fields also exist downstream, around the UHR surface.

The phase plots in Fig. 5.9 indicate that no major wave structures exist in the domain, which would be evidenced by alternating phase structures, given its small size compared to the electric length in vacuum; the only exception is in the narrow propagation channel close to the inner rod element, where a short-wavelength mode is observed in \tilde{E}_z . No major standing-wave structures are observed within the simulation domain, indicating that reflection at the free surfaces downstream is small.

The power absorption density Q_a is shown in Fig. 5.10. Absorption occurs mainly at around the ECR surface, as expected. The power absorption has its maximum at the ECR, near the inner rod element of the thruster. Some power absorption also takes place around the inner rod, in the propagating channel. Overall, most of the power is deposited in the magnetic tubes close to the inner rod, which is also where electron temperature features its peak values. The absorption at the downstream UHR surface is non-zero, but orders of magnitude smaller.

The electromagnetic power absorption density Q_a , defined in Eq. (2.9–7), can be expressed in terms of the parallel, perpendicular and azimuthal components of the electric wave field as

$$Q_a = \frac{\omega\epsilon_0}{2} \left[\Im(\mathcal{S}) \left(|\tilde{E}_\perp|^2 + |\tilde{E}_\theta|^2 \right) + \Im(\mathcal{P}) |\tilde{E}_\parallel|^2 \right] + \omega\epsilon_0 \Im(\mathcal{D}) \Im(\tilde{E}_\perp^* \tilde{E}_\theta). \quad (5.3-3)$$

The absorption map can be explained by inspecting the magnitude of the different terms in equation (5.3–3). As the applied magnetic field is mostly axial in the device, $\tilde{E}_\parallel \simeq \tilde{E}_z$ and $\tilde{E}_\perp \simeq \tilde{E}_r$. At the ECR surface, the imaginary part of \mathcal{S} features its maximum and it is two orders of magnitude greater than the imaginary part of \mathcal{P} . As $|\tilde{E}_r| \gg |\tilde{E}_\theta|$, the power absorption density is therefore

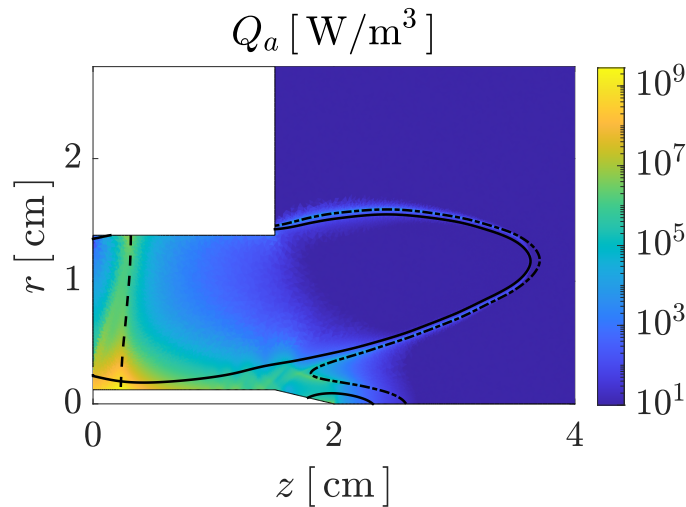


Figure 5.10: Electromagnetic power density absorbed by the electron species.

dominated by the term

$$Q_a \approx \frac{\omega \epsilon_0}{2} \Im(\mathcal{S}) |\tilde{\mathbf{E}}_r|^2. \quad (5.3-4)$$

This term reaches its peak value close to the exit of the coaxial line, where the radial electric field is larger and the ECR surface is found, and consequently this is where the higher Q_a occurs. Lastly, it is noted that while absorption at the resonance requires $\nu_e > 0$, the actual value of this parameter only influences the thickness of the resonance layer, while the integrated power deposited in it is essentially unaffected [56].

5.3.3 Particle and energy wall fluxes

Figure 5.11(a) displays the particle flux to the thruster walls for each species, as a function of arc-length variable ζ , introduced in Fig. 5.1. This variable starts at the tip of the inner rod, goes around clockwise along the thruster wall meridian section, finishing at the end of the external wall.

The internal thruster walls sustain a much larger particle flux than the external walls, differing in several orders of magnitude. Singly- and doubly-charged ion particle fluxes evolve similarly with ζ , being the former always greater than the latter. Singly-charge ion particle flux features values between 10^{19} and 10^{21} $\text{m}^{-2}\text{s}^{-1}$ flux, peaking around the middle of the rear wall, where the injector is located and ions density is maximum. Neutral flux to the walls is shown in the figure for comparison. Amongst all the regions inside the thruster chamber, the corner region between the rear and lateral wall collects the least amount of ions. All corners exhibit a discontinuity motivated by the change in normal vector but this corner region features enhanced magnetic shielding. As a result insufficient electron temperature in the vicinity of this region, ionization is poor there, and combined by the strong magnetization results in a repelling electrostatic field that limits the ion flux to the walls significantly. The primary electron flux follows a similar behavior to the singly-charged ions both at the lateral wall and backplate. Nevertheless, approaching the inner rod wall, the flux increases by more than an order of magnitude reaching values of about 10^{22} $\text{m}^{-2}\text{s}^{-1}$.

At each location along the (dielectric) walls, the net flux of negative and positive charges to the wall must be equal. The large difference between the fluxes of electrons and ions toward the inner rod wall is indicative of the large SEE that takes place there, where indeed the yield δ_{ws} , motivated by the considerable electron temperature, is close to unity. The difference of the fluxes decreases to near zero along the back, lateral, and external walls, where electrons are cooler and SEE becomes less important.

Figure 5.11(b) shows the total net energy flux to the walls of each species. This magnitude is relevant to understand the thermal loads endured by the exposed walls. The maximum energy

Parameter	Name	Units	UC3M	ONERA [26]
\dot{m}	Mass flow rate	mg/s	0.2	0.2
P_f	Input power	W	30	53.7*
F	Thrust	mN	0.840	0.850
F_p	Pressure thrust	mN	0.322	[-]
F_m	Magnetic thrust	mN	0.518	[-]
P_a	Absorbed power	W	26.9	27.9*
P_r	Reflected power	W	3.1	4.28*
I_{sp}	Specific impulse	s	428	429
I_i	Ion current	A	0.082	0.065
η_F	Thrust efficiency	%	6.6	6.5*
η_{prod}	Production efficiency	%	40.9	[-]
η_u	Utilization efficiency	%	50	45.1
η_e	Energy efficiency	%	25.3	[-]
η_c	Conversion efficiency	%	32.2	[-]
η_d	Divergence efficiency	%	91.2	[-]
ϵ_{exc}	Excitation losses	%	4.8	[-]
ϵ_{ion}	Ionization losses	%	7.0	[-]
ϵ_{wall}	Material wall losses	%	63.0	[-]
VSWR	Voltage ratio	-	1.8	2.15*
η_p	Power coupling eff.	%	91.8	86.7*

Table 5.2: Thruster performances. Values at the thruster (*) are computed from the data reported at Ref. [26] (before the vacuum chamber feedthrough) with the estimated 2 dB losses between that point and the thruster, as indicated in that reference.

load is exhibited at the inner rod. Electrons dominate the energy flux to this element, due to the high SEE, and are comparable to the ion energy flux in other walls. Singly-charged ions have a larger energy flux with respect to doubly-charged ions everywhere due to their significantly higher density. The maximum ion energy flux is 0.8 W/cm^2 , and occurs at the injector location, near the region where most ionization takes place. As could be expected, the corner region of the thruster is clearly well shielded magnetically, not only from a particle flux viewpoint as reported above, but also from an energy viewpoint.

Finally, Fig. 5.11(c) portrays the average impact energy per particle of each species. This variable is relevant in erosion studies, as the impact energy must be greater than a material dependent threshold energy for sputtering to take place. In this case, we see that doubly-charged ions are responsible for the highest per-particle energy deposition to the walls. This is due mainly to their double-charge acceleration in the wall sheaths; indeed, the sheath accounts for most of the impact energy for both singly- and doubly-charged ions everywhere. Energies ranging from roughly 10-20 eV to 200-300 eV are computed. The maximum impact energy takes place at the end part of the rod element, where experiments report the largest and fastest erosion under operation. Specific electron energy is small except on the inner rod element. Neutrals impact energy is negligible.

5.3.4 Propulsive performance

The thrust F of a MN-based thruster is generated partially inside the source, but mainly in the MN region, which extends to infinity. In the present simulation, F is computed by integration of the plasma momentum on the free boundaries of the domain $\partial\Omega_\infty$,

$$F = \sum_s \int_{\partial\Omega_\infty} (m_s n_s u_{zs} \mathbf{u}_s \cdot \mathbf{1}_n + n_s T_s \mathbf{1}_z \cdot \mathbf{1}_n) dS, \quad (5.3-5)$$

where the sum on s extends to all species. The thrust F can be divided in two contributions:

$$F_p = \sum_s \int_{\partial\Omega_w} (m_s n_s u_{zs} \mathbf{u}_s \cdot \mathbf{1}_n + n_s T_s \mathbf{1}_z \cdot \mathbf{1}_n) dS, \quad (5.3-6)$$

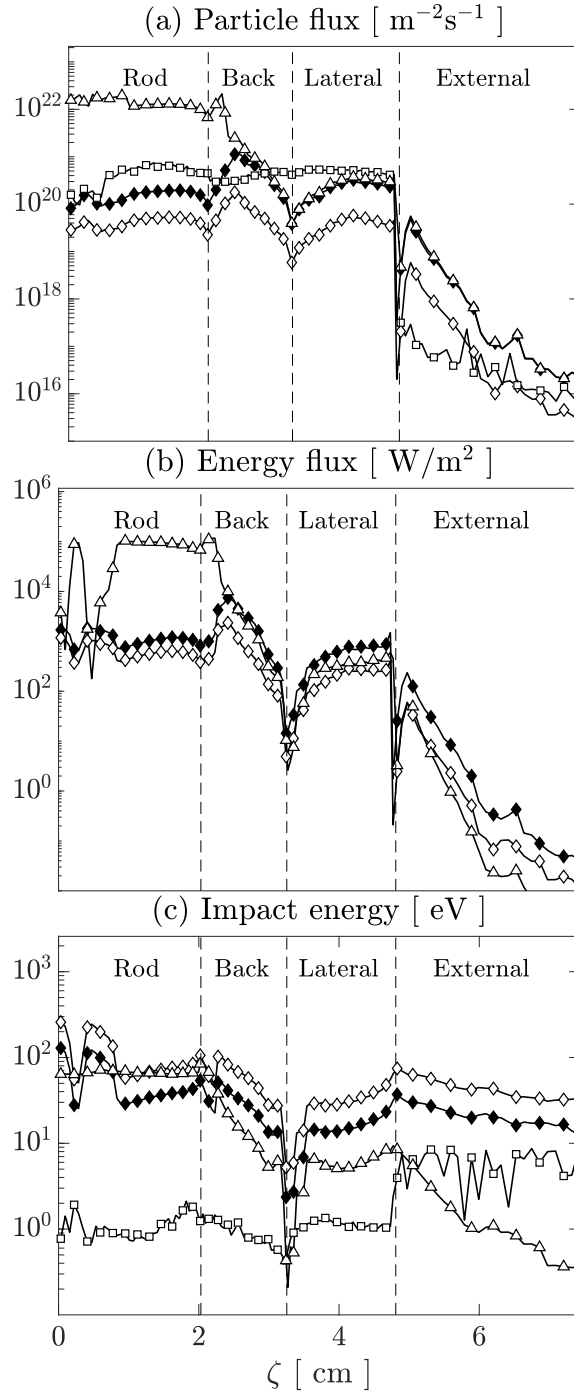


Figure 5.11: (a) Particle flux, (b) net energy flux and (c) average impact energy of the different species to the thruster walls: electrons (triangles), Xe^+ (filled diamonds), Xe^{2+} (diamonds), and Xe (squares).

and

$$F_m = \int_{\Omega} -j_{\theta} B_r dV, \quad (5.3-7)$$

which equal the sum of all the axial dynamic pressure force of each species s on the thruster walls $\partial\Omega_w$ and the axial magnetic force produced by the azimuthal plasma current on the thruster magnets, respectively [98]. It should be noted that the expansion continues further downstream, beyond the computational domain, and therefore a small part of the generated thrust is missed by the simulation. Indeed, the major part of ion acceleration in this thruster occurs in the first few cm after the thruster chamber exit [52], and therefore is captured here. The specific impulse is calculated from this magnitude as $I_{sp} = F/\dot{m}$.

The microwave power entering the thruster, P_f , is partially absorbed by the plasma, P_a , and partially reflected back through the coaxial cable, P_r , thus

$$P_f = P_a + P_r. \quad (5.3-8)$$

Notice that in the present simulations there are no free-space radiation losses; this is representative of the operation of the device inside a laboratory vacuum chamber, where the radiated power is confined.

The reflected power is obtained directly from the voltage standing wave ratio (VSWR), computed as the ratio of the maximum and minimum values of the radial electric field in the coaxial cable, and is directly related to the power coupling efficiency η_p as

$$\eta_p = 1 - \frac{P_r}{P_f} = 1 - \left(\frac{\text{VSWR} - 1}{\text{VSWR} + 1} \right)^2. \quad (5.3-9)$$

Observe that the reflected power cannot be considered a priori a loss mechanism, as this power can be recirculated back to the thruster quite efficiently by impedance matching in the microwave circuit design. Nevertheless, a large reflection ratio would be symptomatic of an inadequate power coupling to the plasma.

Following [72], the power balance for all plasma species can be expressed as

$$P_a = P_{exc} + P_{ion} + P_{wall} + P_p, \quad (5.3-10)$$

where P_{exc} and P_{ion} are the power spent in excitation and ionization of the propellant; P_{wall} is the kinetic, thermal, and heat flux power lost to the walls; and P_p is the power flux of all species through the free boundaries. Consequently, we can define the loss ratios $\epsilon_{exc} = P_{exc}/P_a$, $\epsilon_{ion} = P_{ion}/P_a$, and $\epsilon_{wall} = P_{wall}/P_a$.

The (overall) thruster efficiency is computed as

$$\eta_F = \frac{F^2}{2\dot{m}P_a}. \quad (5.3-11)$$

This efficiency can be approximately decomposed as

$$\eta_F \approx \eta_u \eta_e \eta_c \eta_d = \frac{\dot{m}_{i\infty}}{\dot{m}} \frac{P_p}{P_a} \frac{P_i}{P_p} \frac{P_{zi}}{P_i}, \quad (5.3-12)$$

where $\eta_u = \dot{m}_{i\infty}/\dot{m}$ is the utilization efficiency, i.e. the fraction of propellant mass flow rate that reaches the domain free boundaries as ions ($\dot{m}_{i\infty}$); $\eta_e = P_p/P_a$ refers to the energy efficiency, i.e. the fraction of absorbed power that becomes plume kinetic and thermal power (P_p); $\eta_c = P_i/P_p$ is the conversion efficiency, i.e. the portion of the plume power in the form of kinetic ion power (P_i); finally, $\eta_d = P_{zi}/P_i$ is the divergence efficiency, i.e. the fraction of ion kinetic power which in the axial direction (P_{zi}), thus generating thrust. The difference in equation (5.3-12) between η_F and the product $\eta_u \eta_e \eta_c \eta_d$ is due to the difference between F_i and F , which in a completely developed expansion is expected to be small. However, in the present simulation with finite domain, the

electron contribution to thrust accounts for up to a 25% (see Fig. 5.5) at the free downstream boundary. This suggests that the expansion is incomplete by $z = 4$ cm, and that additional thrust is to be gained further downstream as the magnetic nozzle continues to convert electron power into directed ion kinetic power.

In addition to these partial efficiencies, another relevant quantity is the production efficiency, defined as the ratio of ion flow rate at the free boundaries with respect to that at all the simulation boundaries including thruster walls,

$$\eta_{prod} = \frac{\dot{m}_{i\infty}}{\dot{m}_i}, \quad (5.3-13)$$

which is closely related to the number of times each atom undergoes reionization, and characterizes the plasma losses to the walls.

Table 5.2 displays the performance figures of the simulation. For comparison purposes, the available experimental data from ONERA thruster are also shown. The total thrust produced by the thruster in the simulation is 0.84 mN, and the specific impulse 428 s, which show a great agreement with the experimental measurements. The fraction of magnetic thrust to total thrust amounts to approximately 62%, which again agrees well with the available experimental data [123]: 60% for the device operating at 0.2 mg/s and 40 W.

In Ref. [26], efficiencies are computed with respect to the transmitted power (i.e. $\eta_p P_f$) and that this power includes the power losses in the cables, the feed-through, the DC block and the connectors/adapters, which are of the order of 2 dB. Table 7.2 shows the efficiencies and powers, taking into account the reported attenuation losses between the measurement location (prior to the tank) and the thruster. The thrust efficiency is very similar in the simulations and the experiments, around 6.6%.

The main inefficiency arises from plasma losses to the walls. First, the fraction of generated ions that become plume ions, given by η_{prod} , is quite low, about 41%, while the rest of them are recombined at the walls. Second, the energy efficiency is rather low, $\eta_e \approx 25\%$. While excitation and ionization losses (measured by ϵ_{exc} and ϵ_{ion}) are arguably small, about two-thirds of the absorbed power (ϵ_{wall}) is lost to the walls, transported by the ions and electrons that impact on them. In fact, the integrated energy fluxes (see §5.3.3) over the inner thruster walls areas adds up to 16.9W, where 51% is lost through the inner rod surface, 40% through the backplate, 9% through the lateral wall and 0.1% through the external wall. Large losses at the magnetically unshielded backwall are well-known from HPT analyses [98, 124] and the way to reduce them would be to shield that wall (without altering much the wave propagation). Magnetic shielding seems to operate rather well at the lateral wall; it does not behave well at the rod due to the large electron temperatures around it, leading to very large thermal loads in that thin element, which amounts for only a 6% of the total inner thruster walls area. To reduce this problem should be a central task of any design optimization of the thruster chamber.

The second main source of inefficiency is related to the meager utilization efficiency, a 50% in the simulation, and also in good agreement with the experimentally-obtained value. These values are also common in HPTs [125] and are likely due to the large wall recombination. The consequence is that a large fraction of the propellant is leaving the source as neutrals, generating essentially no thrust.

On a positive note, the divergence efficiency η_d of 91.2% shows that the kinetic power of ions leaving the domain is mainly axial and that good magnetic detachment takes place in the MN. On the other hand, and in line with the discussion above, the rather low conversion efficiency η_c evidences that the expansion is still incomplete in the simulation domain.

The experimentally-reported power coupling efficiency η_p is close to unity already in early designs [8] and in contemporary ones [53], where they report a 95%. These values are measured between the microwave generator and the microwave feedthrough on the tank, and therefore do not record the attenuation in the line from the tank feedthrough to the thruster. With the estimated power attenuation factor of 2dB given in [26], the actual coupling efficiency at the thruster entrance for the prototype simulated here is 87%. This value is close to the computed 92% coupling efficiency.

5.4 Concluding remarks

An axisymmetric model of the plasma discharge in an ECRT has been presented, which couples together the slow plasma transport and the fast electromagnetic fields. Self-consistent simulation results for a thruster of this type have been reported, discussed, and compared with existing experimental data from the MINOTOR ECRT prototype.

Results reveal the mutual dependency between the quasi-steady plasma properties and the high-frequency electromagnetic fields, as plasma density determines the propagation regimes and the location of cut-offs/resonances, while the power absorption map drives the electron temperature profile. Multiple electromagnetic propagation regimes coexist in the device. In most of the domain wave structures are not observed, which is expected due to the small dimensions of the thruster. The exception is the neighborhood of the inner rod element of the device, where a short wavelength mode has been found. The main contribution to electromagnetic power absorption is related to the radial electric fields at the ECR region, in particular those closest to the exit of the coaxial line. The ratio of reflected power is small. The field propagation beyond the ECR surface occurs along a low-density channel close to the inner rod element of the thruster. As the topology of these regions responds to the plasma density profile, varying the input mass flow rate or the input power is expected to alter them and consequently modify the electromagnetic power flow.

Large values of the electron temperature are observed in the magnetic tube that connects with the coaxial line exit. Electron temperature is almost uniform in the parallel direction to the magnetic field, but a large perpendicular gradient exists. The electron pressure profile, on the other hand, is smooth, not showing any pronounced peak. The plasma density profiles peak at an intermediate radius instead of at the axis of symmetry. This is likely a consequence of the presence of the inner rod, which makes the plasma density drop close to its surface.

The quasi-steady electric field developed by the plasma is similar along all magnetic lines in spite of the differences in electron temperature among them. This, combined with the observed ion velocity profile, results in a local ion Mach number that varies substantially among magnetic lines.

The particle and energy fluxes to the walls have been analyzed per species, showing that the inner rod of the thruster undergoes the largest particle and energy influx. This element has also shown to undergo the major part of the heat lost through the thruster walls. Thus, an alternative design choice for the geometry and the material of the inner rod element could lead to significant improvement of the overall thruster performances. Regarding the impact energy, the maximum is exhibited by doubly charged ions and overall it occurs at the inner rod element. Thus, this element will suffer from both thermal stress loads and the erosion provided by the impact of energetic ions.

The central part of the rear wall is essentially perpendicular to the magnetic field lines that expand into the MN region, and thus is connected to the bulk of the plasma discharge. Particle and energy fluxes to this part of the rear wall are large. On the contrary, the corner region between the rear and the lateral walls forms a nearly-isolated region which is well protected by the magnetic field, and this is reflected in the lower particle and energy flux to it.

The performance figures computed from the simulation results show a great agreement with existing experimental data, serving as a partial validation point for this numerical model. The main loss mechanisms are plasma losses to the walls, especially to the inner rod element, and a low propellant utilization. Given this agreement, and the difficulty of experimentally measuring detailed profiles as the ones obtained by the simulation, the present model could be used to propose novel designs that could optimize the overall thruster performance. Further work must continue to improve and validate the model, in particular running simulations in larger domains and using the available laboratory measurements of plasma properties.

Lastly, the numerical treatment of the fast electromagnetic fields near the ECR and UHR surfaces presents several difficulties, which have been addressed with a predictive local refinement strategy applied to the mesh of the W-module. Future work will seek for other schemes to reduce the need of refinement in these regions.

Chapter 6

Parametric investigation on the design and operation of the ECR30

This chapter analyzes on the impact of both the operating point and some design choices on ECRT performance. First, the effects of computational optimization of the reference simulation domain shown in Chapter 5 are analyzed. Second, the impact of the operating point on thruster performance and plasma properties is detailed. Third, an assessment of the influence of ECR location on thruster performance is provided, comparing its actual location with other alternatives. Fourth, multiple injector port configurations are tested. Finally, a sensitivity analysis on the anomalous transport coefficient is provided explaining its main effects and its influence of plasma properties and thruster operation. Part of the contents of this chapter have been published in a conference paper [61] and will be submitted for their publication to peer-reviewed journal Plasma Sources Science and Technology [62]. The simulation results are gathered in a simulation catalogue shown in appendix A. The contents of this chapter are part of EP2's contributions to MINOTOR project.

6.1 Reduced-domain simulation

In order to accelerate the multiple simulations of the parametric study, an optimized version with a reduced (RED) simulation domain compared to that of the reference (REF) simulation has been defined with the same thruster and nominal operating point. The thruster geometrical parameters are therefore the same of the reference case shown in Tab. 5.1, in chapter 5. Figures 6.1a and 6.1b show respectively the PIC-mesh elements and the MFAM cells of the RED simulation. In this section it is shown that the differences between the reference and reduced simulation domain results are minor, and that all major features of the plasma discharge are preserved. This optimization is applied to the rest of simulations in order to speed up the computational time required by the parametric analyses. The main simplifications utilized in RED simulation are:

- Decrease on the simulated plume size by a distance L axially, and R radially.
- The number of cells of the transport modules was decreased.
- The near top plume of the transport has been truncated to decrease computational cost since it required increasing the overall target number of particles per cell.
- Disregard charge exchange collisions (CEX) to save computational time as they do not play a major role in the plasma dynamics.

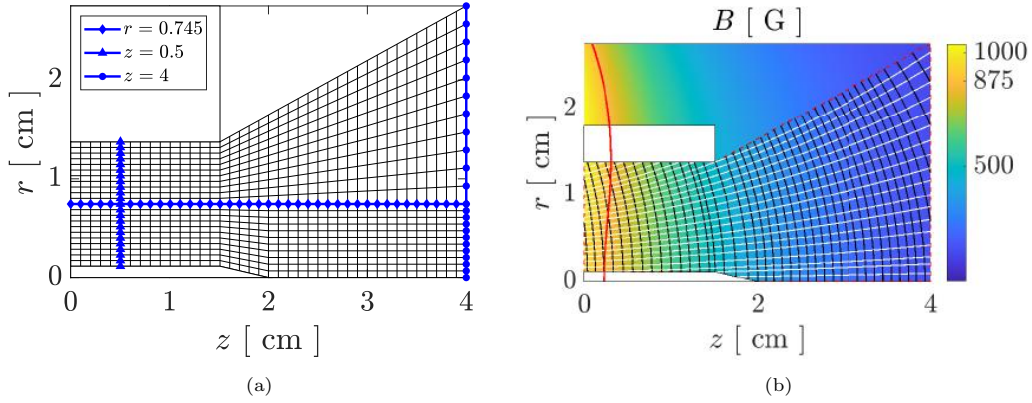


Figure 6.1: (a) PIC-mesh and (b) MFAM elements, with applied magnetic field in the colormap and the red curve representing the ECR location.

Name	Variable	Units	REF	RED
PIC-mesh elements	$N_{el,I}$	[-]	3360	880
MFAM elements	$N_{el,E}$	[-]	2550	807
EM-mesh elements	$N_{el,W}$	[-]	120782	96526
Computational time	t_c	[h]	150	15

Table 6.1: Comparison of mesh sizes and computational performance.

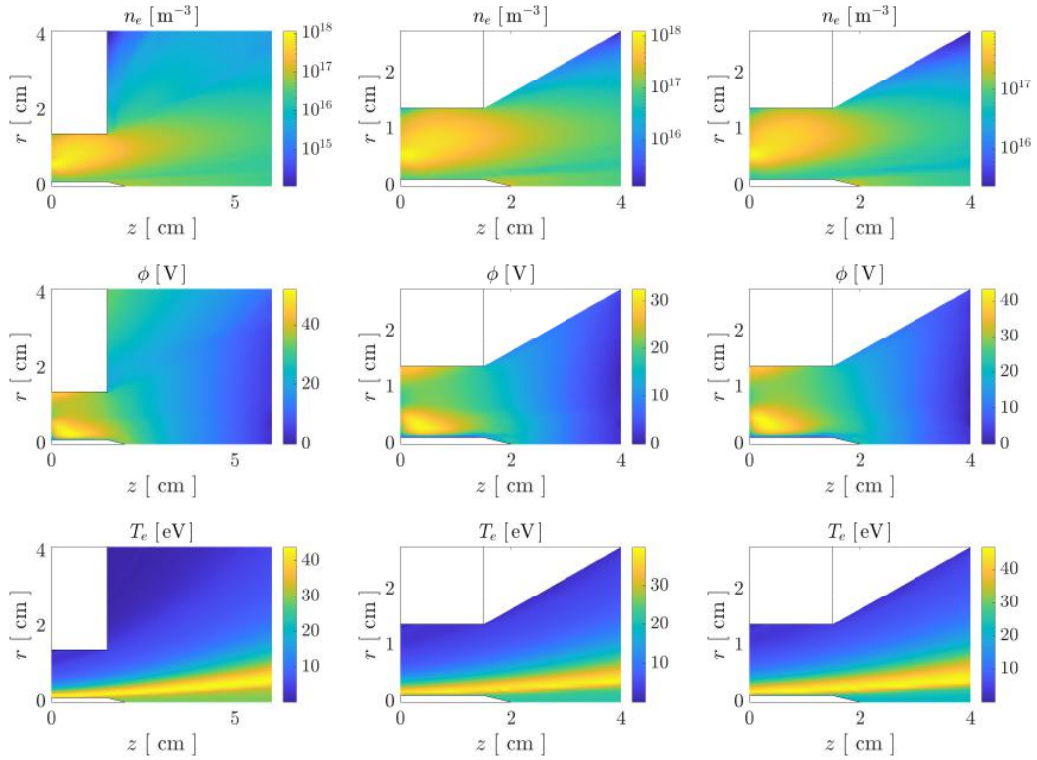


Figure 6.2: Results comparison for REF (left), I2 (center), and RED (right).

A first reduced simulation, I2, was performed and is illustrated in the appendix A after the reference case, REF. A second reduced simulation, RED, without double ions, was also carried out to assess the influence of this species. A sample of the comparison plots is shown in Fig. 6.2 for the three simulations.

As it can be observed in Fig. 6.2, simulations REF, I2, and RED present similar plasma properties. The performance figures for simulation RED are reported in Tab. A.1 alongside those of cases I2 and REF, and the other simulation cases considered in this study. The thrust, specific impulse, and thrust efficiency is lower than in simulation REF, in part due to the smaller plume domain, which means that less expansion and acceleration of the plasma is kept. This issue is partially mitigated by the fact that the simulation REF produced optimistic values for these quantities with respect to the experimentally measured ones, and the simulation RED is circumstantially closer to them. The values of the excitation losses, ionization losses, coupling efficiency, utilization efficiency are essentially the same in the two simulations. Mild differences exist in the plume divergence (which can again be attributed to the smaller domain) and also in the wall losses. The comparison amongst these simulations partially validates the simulation approach and code, and suggests that the smaller simulation domain and no double ions is sufficient to perform the parametric study.

6.2 Parametric investigation on the operating point

This section focuses on the effect of variations of the mass flow rate and the input power with respect to the nominal operating point (represented by simulation REF and RED of previous section). The new simulation cases are M0 and M2, which feature a 25% lower and higher mass flow rate with respect to the nominal case, respectively, and cases P0 and P2, which have half and double the nominal input power, respectively. All the other input parameters of the simulations are set to nominal. The reason behind of using the input power P_f rather than the absorbed power P_a in the analysis is to assess the changes in the power reflection ratio.

In order to support the study, the evolution of several variables along three distinct lines will be plotted in the following. Figure 6.1a shows these three lines. Firstly, a horizontal line located at the middle radius (i.e. $r = 0.745$ cm) of the thruster chamber, which allows to investigate trends in the axial direction. Secondly, a radial line of at $z = 0.5$ cm which provides with information of the radial dynamics inside the thruster chamber. Finally, a vertical line of nodes located at the end of the simulated plume.

Results show that the plasma transport maps exhibit no qualitative differences and thus similar topology with respect to the nominal case. Such feature reassures the robustness of the code. However quantitative differences are evident in the results. Variations in mass flow rate and input power modify the equilibrium state of the plasma discharge.

6.2.1 Neutral density

Figures 6.3a and 6.3b show the axial evolution of the neutral density for the different mass flow rates and input powers, respectively. Likewise Figures 6.4a and 6.4b show radial profiles of the neutral density.

The overall trend of neutral density is to increase with increasing mass flow rate, and to decrease with increasing input power. It seems evident that there is a direct correlation between the stationary neutral density and, as the crucial power to determine the plasma state is the absorbed power, the energy per particle P_a/\dot{m} . The proportionality is not direct since nonlinear mechanisms involving ionization, wall recombination and the plasma expansion play an important role. Nevertheless the main trend is observed in both axial and radial profiles.

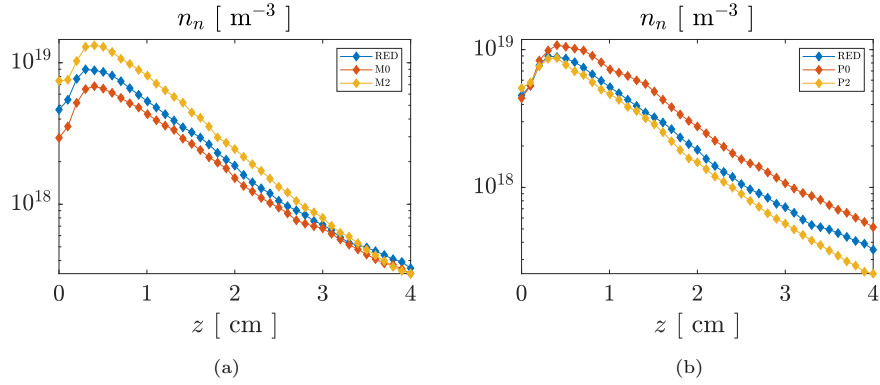


Figure 6.3: (a) and (b) show the axial evolution of neutrals density and for variation on the mass flow rate and input power respectively.

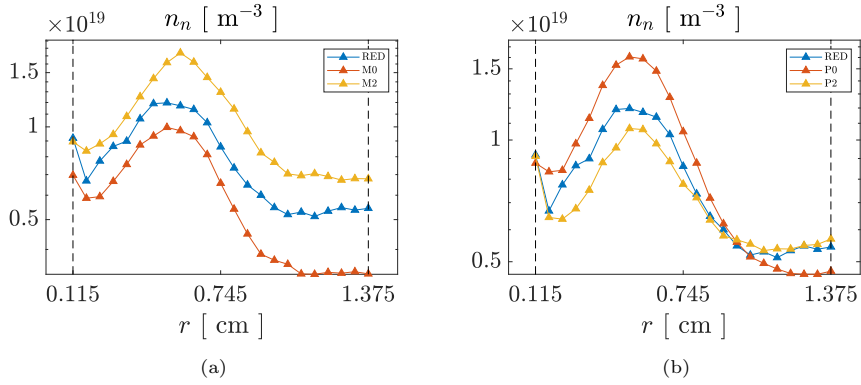


Figure 6.4: (a) and (b) show the radial evolution of neutrals density and for variation on the mass flow rate and input power respectively. Dashed lines represent the minimum and maximum radius of the thruster chamber.

6.2.2 Electron dynamics

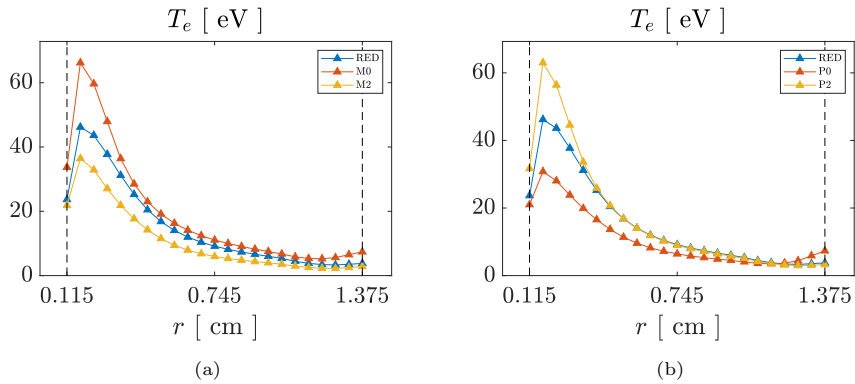


Figure 6.5: (a) and (b) show the radial evolution of electron temperature and for variation on the mass flow rate and input power respectively. Dashed lines represent the minimum and maximum radius of the thruster chamber.

In this section we analyze electron temperature, pressure, and density. Figures 6.5a and 6.5b show respectively the influence of mass flow rate and input power on the electron temperature along a radial section inside the thruster chamber. As can be noted in Fig. 6.5a, the electron temperature in stationary conditions decreases with increasing the mass flow rate, and this occurs in the whole domain but specially close to the inner rod surface, where the peak electron temperatures are found. For instance, the mean electron temperature in line $z = 0.5$ cm is 21.1, 18.2 and 12.5 eV for cases M0, RED and M2, respectively. Even in the lower temperature case, the electron temperature is sufficient to ionize well the propellant.

For mass flow rates much higher than those presented here, the electron temperature would eventually decrease enough to lead to a significant reduction of the ionization source rate, damaging the utilization efficiency η_u . This variable is useful in order to assess the quality of ionization, as it represents the ratio of ion mass flow rate at the plume boundaries with respect to the input neutral mass flow rate.

Conversely, increasing the input power leads to a significant increase of the electron temperature and its peak value. The increase is not proportional in the entire domain, it is enhanced close to the regions of maximum temperature. This is a result of the lack of changes in the relative power deposition map, which is quite robust to input power changes. Indeed, this map roughly scales with input power in the whole domain: the maximum power absorption for increasing input power is approximately 1, 2, and $4 \cdot 10^9$ W/m³. For further details on the power absorption maps for increasing power, see §6.2.5. Overall, it can be stated that the electron temperature response scales roughly with P_f/\dot{m} . In fact, since the input power is very similar to the absorbed power in the range of parameters simulated, this factor is again the energy per particle P_a/\dot{m} which determines the maximum electron temperature. For higher P_a/\dot{m} the maximum temperature increases steepening the radial gradients, influencing the radial electron momentum balance.

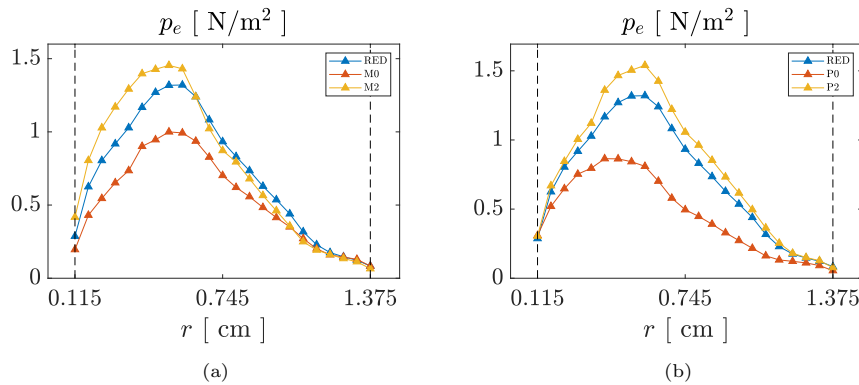


Figure 6.6: (a) and (b) show the radial evolution of electron pressure and for variation on the mass flow rate and input power respectively. Dashed lines represent the minimum and maximum radius of the thruster chamber.

Figure 6.6 shows the behavior of electron pressure in the radial section inside the thruster. Clearly, electron pressure increases everywhere with mass flow rate and input power. While increasing mass flow rate enhances electron pressure closer to the inner rod element, increasing the input power enhances the electron pressure mainly in the center of the annular chamber away from the either wall. The pressure value at the walls is essentially unaffected by these variations, and as a consequence, increasing either the mass flow rate or the power results in steeper radial gradients.

Lastly, figure 6.7 shows variations experienced by electron density. While these variations can be inferred directly from those of the electron temperature and pressure, it is worth discussing electron density due to its more complex behavior. An increase in any of the two variables clearly results in an increase of the electron density. This is related to ionization being the primary factor affecting the electron density in stationary conditions, and ionization is driven by mass flow rate and input power. While increasing mass flow rate enhances electron density everywhere, increasing the input

power enhances the electron density mainly at higher radii, away from the inner rod element of the thruster. In fact, the electron density close to the inner element is seen to decrease slightly with the input power. A steeper radial gradient arises as a consequence of this behavior.

The changing plasma density map also leads to significant changes in EM power propagation and absorption inside the thruster, and can be understood as a channel or “tube” for EM power propagation, as detailed in §6.2.5.

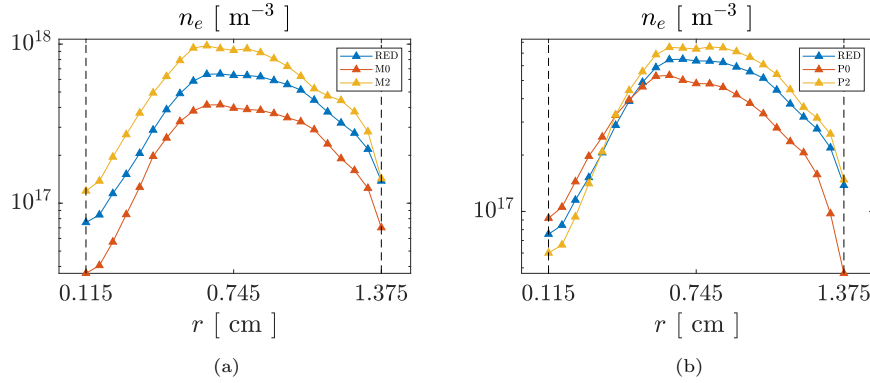


Figure 6.7: (a) and (b) show the radial evolution of electron density and for variation on the mass flow rate and input power respectively. Dashed lines represent the minimum and maximum radius of the thruster chamber.

To better understand electron dynamics, figure 6.8 focuses on the variation with input power P_f of the main terms in the electron radial momentum balance equation,

$$0 = -\frac{\partial p_e}{\partial r} + en_e \frac{\partial \phi}{\partial r} + en_e u_{\theta e} B_{z0} + F_{coll,r}, \quad (6.2-1)$$

where the resistive force $F_{coll,r}$ is in general negligible. Therefore, the principal force densities balancing Eq. (6.2-1) are the electron pressure, the electrostatic, and the magnetic ones.

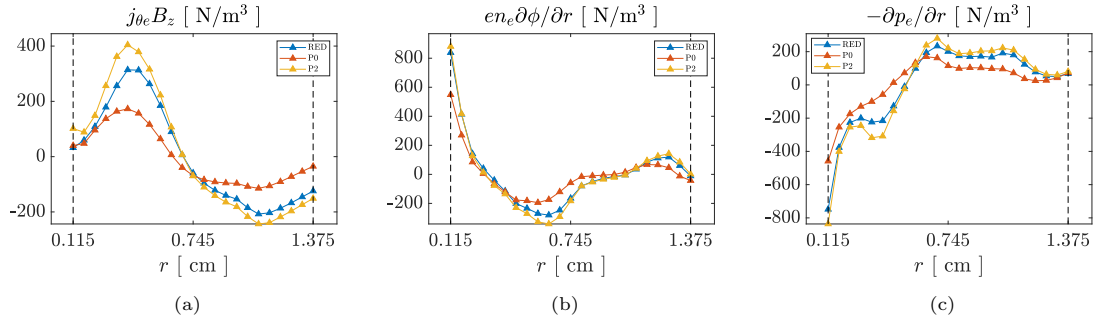


Figure 6.8: (a), (b), (c) show the radial evolution of the radial magnetic, electrostatic and pressure forces for variations on the input power. Dashed lines represent the minimum and maximum radius of the thruster chamber.

The electron pressure is the main driver of the electron dynamics. Figure 6.8 shows that there are two different regions radially: one where the pressure force pushes the electron radially outward (close to the lateral wall), and another where it pushes them inward (close to the inner rod element). It is seen that the radial derivative of the pressure becomes more pronounced as input power increases.

The magnetic force is the main force balancing the electron pressure, and also shows the two distinct regions (the outer one where it confines the electrons inward, and the inner one where it

pushes the electrons outward). The magnetic force responds readily to an increase of the input power. The magnetic force is essential for the correct operation of the device: while the $j_{\theta e} B_z$ component confines the plasma radially, the $j_{\theta e} B_r$ component (not shown here) is responsible of creating magnetic thrust.

The radial electrostatic force, however, is not negligible anywhere. On the other hand, it dominates close to the inner rod element in all cases, and becomes the leading confining force there. The electrostatic force varies only mildly with input power.

6.2.3 Ionization and ion-wall recombination

The ionization cost is directly measured by the ratio ϵ_{ion} . This value details the amount of power spent in ionization collisions and quantifies the amount of ionized propellant in the simulation domain, including the cost of reionization of plasma that is neutralized at the walls. In Tab. A.1 it can be seen that ϵ_{ion} increases from 5.0 to 7.7 and then to 10.1 with mass flow rate, and it decreases with input power from 10.6 to 7.7 and 5.9.

First ionization can be understood in terms of the behavior of neutral density, electron density and electron temperature previously reported. The rate of ionization $R_{ion}(T_e)$ is a function of the electron temperature that grows rapidly while $T_e \sim E_{ion}$, the ionization energy, which for Xe is 12.1 eV. Nevertheless, $R_{ion}(T_e)$ starts to saturate as $T_e \ll E_{ion}$.

Figure 6.9(a)-(c) shows the maps for ionization source rate $S_{ion} = n_e \nu_{ion}$ for the different mass flow rates (note the different scales in each plot). Ionization is highest close to the injector port, coinciding with the maximum in neutral density. We can notice that ionization is enhanced as mass flow rate increases, following the trend of ϵ_{ion} . For increasing mass flow rate we note that ionization occurs closer to the inner rod surface. Lastly, the rate of ionization decreases towards the lateral wall with increasing mass flow rate.

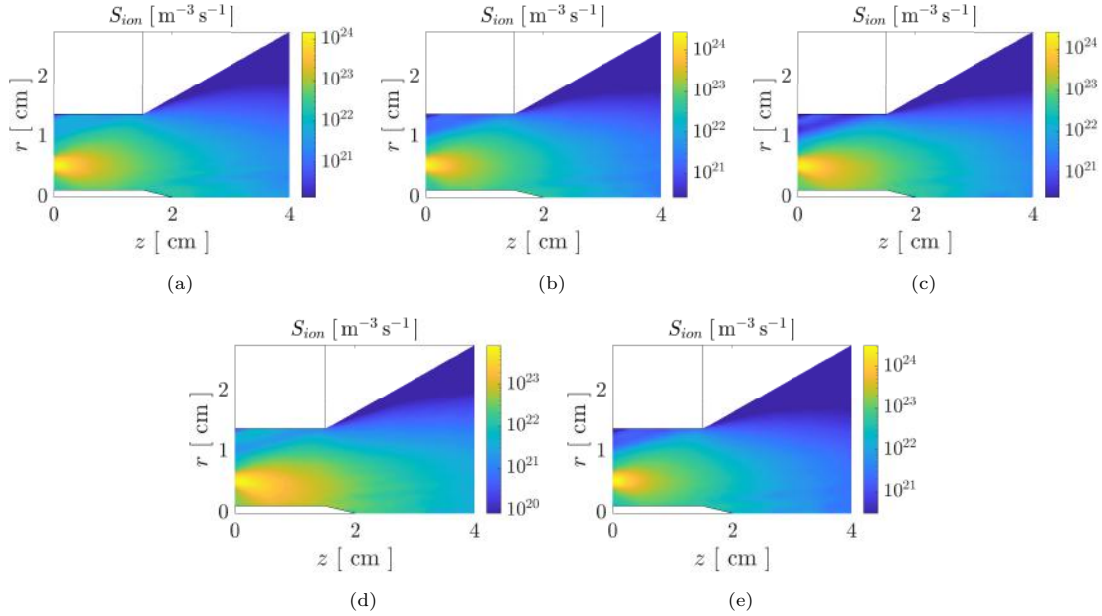


Figure 6.9: Ionization rate of (a) M0, (b) RED, (c) M2, (d) P0 and (e) P2 cases.

Figure 6.9(d) and (e) shows the different maps of ionization source rates for increasing input power, being from left to right, cases P0, RED and P2. In general, the ionization source rate obtained for all the simulations level of ionization increases considerably with input power, exhibiting maximum values of approximately 0.8, 2.5 and $3 \times 10^{24} \text{ m}^{-3} \text{ s}^{-1}$.

The rapid decrease of electronic temperature (see Fig. 6.5a) close to the lateral wall surface for increased mass flow rates also explains the decrease in ionization in that region. A slight decrease in electron temperature there results in a lower R_{ion} . However, the proportion of volume where electron temperature is greater than E_{ion} is of 80%, 68%, and 46%, for M0, RED and M2 case, respectively. This implies that although case M2 may seem more efficient in terms of usage of electron internal energy for ionization, only 46% of the volume is above the ionization energy.

The effect of mass flow rate and input power on wall fluxes, which are related to recombination and erosion, is shown on figure 6.10 and 6.11. As a reminder, ions recombined at the walls are re-emitted diffusively as neutrals, which contributes to the neutral density reported before.

Figure 6.10a shows the impacting or primary flux of ions $g_{i1,w}$ to the thruster walls. Note that in the majority of the thruster chamber walls, $g_{i1,w}$ increases with mass flow rate, exhibiting the highest values in the higher mass flow rate case (i.e. M2). This effect slightly more evident at the rod surface, where the effect of recombination seems to be playing a more important role in ionization, leading to increased neutrals density (see Fig. 6.4a). However, the mass flow rate and the ion flux to the walls is not correlated by direct proportionality. Recalling $g_{i1,w} = n_{i1}u_{r,i1} = n_e u_{r,i1}$, these two variables (see figs/Parametric. 6.7a and 6.10c) exhibit opposite dependence with mass flow rate and each of them does not follow a proportionality correlation, so nor does their product. Note that the density of plasma has been explained in §6.2.2 and the radial velocity of ions is directly related to the plasma potential, reviewed in section §6.2.4.

Ion-wall recombination is affected differently by input power depending on the region investigated. For instance, at the backplate and the lateral wall, as the general density of ions increases and so does the electric field towards the walls, resulting in a monotonic increase of the flux of primary ions to the backplate, thus increasing wall recombination effects there. However, at the lateral wall, the ionization source rate is significantly decreased for the same reason as with increasing mass flow rate, as the electron temperature there decreases (see Fig. 6.5b). Since the characteristic value of the electron temperature there is below the ionization source rate, the result is that ionization is reduced there. Close to the inner rod surface, the effect of ion-wall recombination on the ionization source rate is stronger (see Fig. 6.9d), relative to its maximum value than in the other two cases. However, this does not imply directly a higher primary ion flux to the walls for decreasing input power. This is due general increases exhibited in the ionization source rate with increasing input power. For increasing input power, both the plasma density and electron temperature with input power. Moreover, the dependence is non monotonic as we note that an intermediate input power provides with the maximum ion flux to the walls.

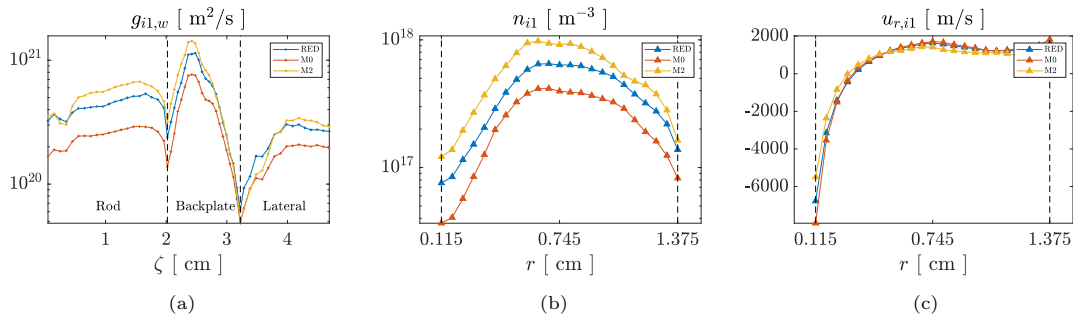


Figure 6.10: Plots for different mass flow rates of : (a) the impacting flux of ions with respect to the arc-length parameter ζ used to describe the location along the thruster chamber walls (see Fig. 5.1) and (b) and (c) show radial profiles of the electron density and radial ion velocity, respectively.

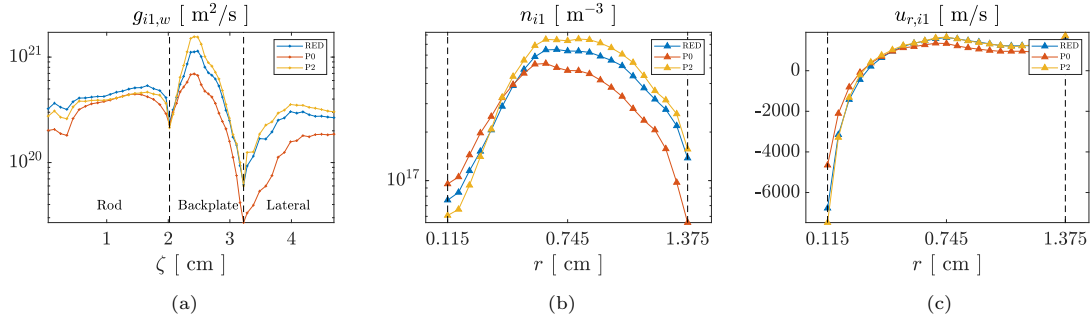


Figure 6.11: Plots for different input power of : (a) the impacting flux of ions with respect to the arc-length parameter ζ used to describe the location along the thruster chamber walls (see Fig. 5.1) and (b) and (c) show radial profiles of the electron density and radial ion velocity, respectively.

To summarize, mass flow rate affects strongly ionization and wall recombination. This leads to a modification of the equilibrium state of the plasma. The dependence of mass utilization efficiency on mass flow rate is not monotonic. For an electron population with temperatures well above E_{ion} in a low neutral density discharge, an increase in mass flow rate leads to a significant improvement of the amount of ionized propellant since it increases the neutrals density, thus increasing the electron density in stationary conditions and the mass utilization efficiency. Nonetheless, these improvements do not continue indefinitely. If the mass flow rate is further increased the level of propellant utilization saturates, and the discharge “extinguishes”. Increases in mass flow rate decrease the electron temperature. Whenever a further increase leads to $T_e < E_{ion}$, ionization is seriously hindered and the level of plasma density starts to saturate. Overall, in terms of ionization and propellant utilization we can conclude case M0 is the least efficient amongst all operation points and cases M2 and RED exhibit similar performances.

6.2.4 Acceleration

The expanding electrons create a quasi-static electric field ϕ in the plasma that accelerates the ions downstream, which due to their high mass, are essentially demagnetized. The electrostatic field $-\nabla\phi$ couples the motion of ions and electrons, and plays a crucial role in the dynamics of both species.

Figure 6.12 shows the effect of increasing mass flow rate on the map of electrostatic potential (note the different color scale of each plot). For smaller mass flow rates we note that the axial potential drop is higher, given the higher characteristic electron temperature of the discharge. Likewise, Figure 6.13 shows the evolution of the plasma potential maps with increasing input power, from left to right. We note that for increasing input power, the maximum potential drop in the domain is increased, as a result again of the increase of electron temperature.

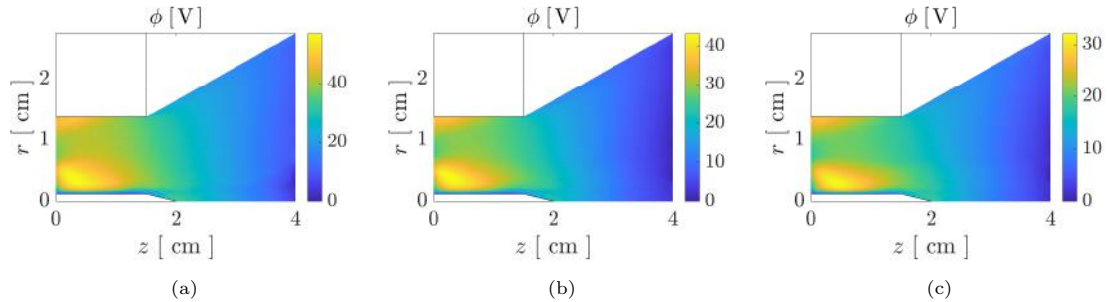


Figure 6.12: Electrostatic potential of (a) M0, (b) RED, and (c) M2 cases.

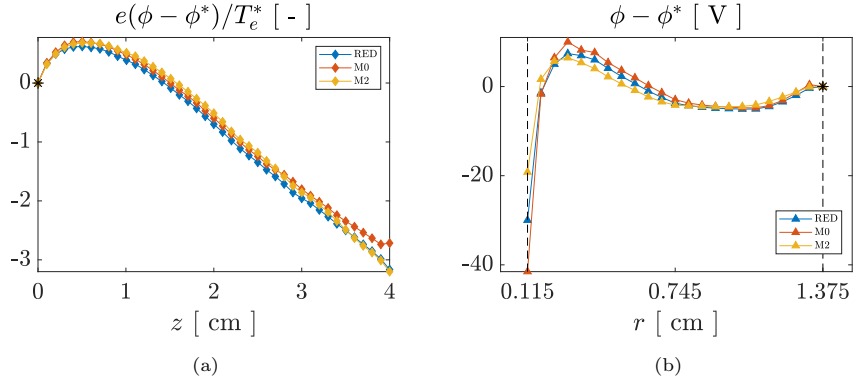


Figure 6.14: Effect of mass flow rate on (a) the axial and (b) the radial evolution of electrostatic potential. Axial values are normalized taking the backplate as reference, being T_e^* 9.6, 7.9, and 5.1 eV for cases M0, RED and M2, respectively. Radial potential takes as reference the potential at the lateral wall.

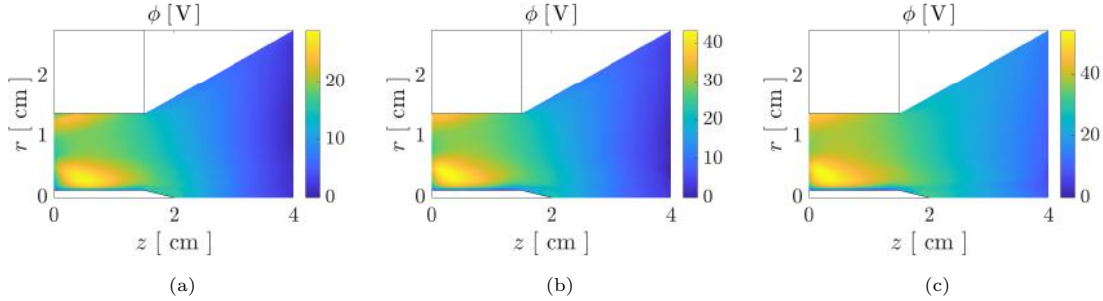


Figure 6.13: Electrostatic potential of (a) P0, (b) RED, and (c) P2 cases.

Figure 6.14a shows the axial evolution of the plasma potential along z (i.e., essentially in the parallel direction) on the mid-radius of the thruster chamber normalized with a reference potential and electron temperature, taken as the node indicated by the marker * to facilitate line comparison. For increasing mass flow rates the effect of the potential is to scale with the electron temperature almost linearly, as evidenced by the corresponding normalized curves.

Figure 6.14b shows the effect of mass flow rate on the radial evolution of the potential drop, taking as reference the potential at the lateral wall. Note that for increasing mass flow rate, the radial evolution of the potential, and thus the radial electric fields are almost unaffected in the bulk of the plasma. The main difference is the increase in the potential drop at the inner rod surface, explained by the increase in electron temperature there with decreasing mass flow rate.

Figure 6.15a shows the axial potential drop normalized with the potential and the electron temperature at the back plate for different input powers. Note that the axial electric field exhibited at case P0 is slightly smaller than for the other two cases, implying a lower normalized ion acceleration. Figure 6.15b shows the effect of input power on the radial potential fall, taking as above as reference the potential at the lateral wall. The behavior of the radial electric fields is again very similar for different input powers. The main differences are that the potential is higher close to the lateral wall for lower input powers as there the electron temperature is greater, and the higher radial electric field at the inner rod surface for higher input powers. The latter effect is again linked to a higher electron temperature near the inner wall, the higher the input power.

The secondary peak of the electric potential close to the lateral-back corner of the thruster chamber seems to be a robust feature of the discharge, as evidenced in figures 6.12 and 6.13. A slight difference between case P0 and the other two power cases is that the potential decrease towards the lateral wall close to the backplate is more evident (see top left corner of Fig. 6.13a).

Having reviewed the effects of both input power and mass flow rate in the electric potential,

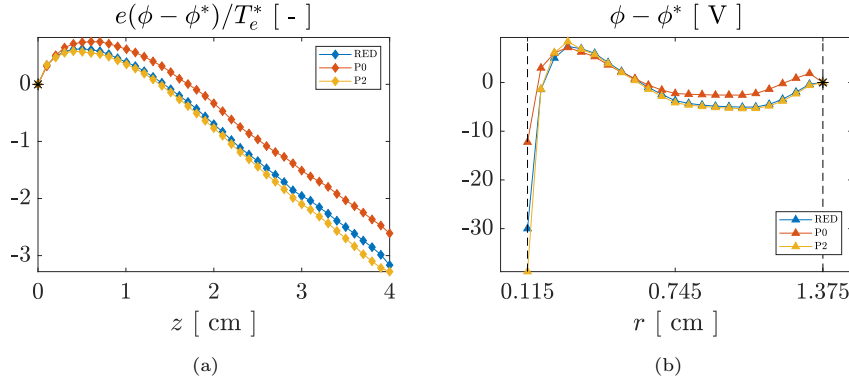


Figure 6.15: Effect of input power on (a) the axial and (b) the radial evolution of electrostatic potential. Axial values are normalized taking the backplate as reference, being T_e^* 5.1, 7.9, and 7.6 eV for cases P0, RED and P2, respectively. Radial potential takes as reference the potential at the lateral wall.

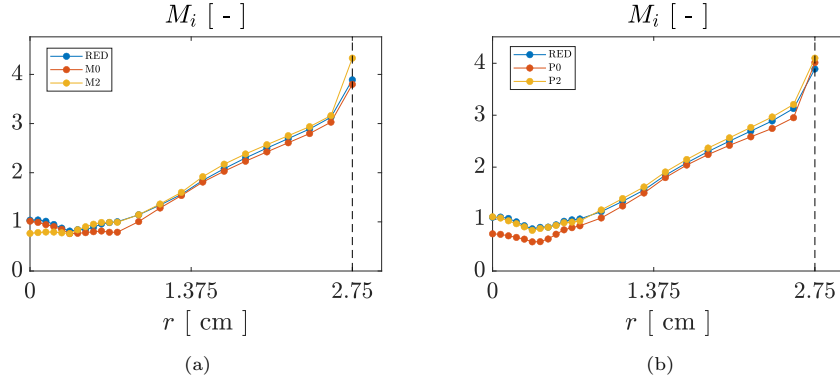


Figure 6.16: Plots of the radial evolution of the total local ion Mach number for different (a) mass flow rates and (b) input powers, respectively, at the plume end. The dashed vertical line indicates the end radius of the simulated plume.

we can directly deduce the behavior of ion acceleration. The local Mach number of ions M_i at the downstream boundary, defined as the ratio of the ions velocity with respect to the ion sonic velocity $c_s = \sqrt{T_e/m_i}$, is shown in Figures 6.16a and 6.16b. The behavior of this variable is essentially universal for all the simulations shown, as expected. As the kinetic energy gained by the ions is mostly determined by the axial potential drop, and this is proportional to the electron temperature, all maps should exhibit similar local Mach numbers for different mass flow rates and powers. Remarkably, the ion Mach number remains close to 1 near the axis of symmetry. This could suggest that this region is less accelerated than the periphery, which reaches Mach 3–4. The reason behind this behavior is still unknown and requires further exploration, but it could be related to the presence of the inner rod element, whose “shadow” downstream could impact the plasma acceleration profile.

6.2.5 Propagation and absorption of electromagnetic waves

Both the mass flow rate and the input power, by affecting the equilibrium state of the plasma transport properties, alter significantly the propagation regimes present in the thruster. This modifies the paths through which the electromagnetic power flows and reflects and even the resonant surfaces where these are absorbed.

In the nominal case, the EM power fed through the coaxial line enters an overdense plasma, regions VI and VII of the CMA diagram following the nomenclature of Stix [27]. The electron density decreases in the vicinity of the inner rod surface leads to the appearance of regions IV

and even III (underdense plasma). Contrary to region V (which only supports evanescent fields), regions IV and III admit propagation of electromagnetic power. Figure 6.17 contains all the relevant information about wave propagation and absorption as a function of mass flow ratio. Figures 6.17a, 6.17b and 6.17c show the different regions of electromagnetic wave propagation, including resonant and cut-off surfaces. Figures 6.17d, 6.17e and 6.17f display the radial wave electric field. Finally, figures 6.17a, 6.17b and 6.17c present the resulting power absorption maps. Please note the different color scales of each plot.

Within the range explored in this work, an increasing mass flow rate increases the electron density in the chamber. This leads to several changes in the propagation of waves in the thruster. An important effect is the increase in the size of the non-propagation region V. In all three cases, close to the lateral wall, no electromagnetic wave propagates downstream the ECR region, as region V dominates there. As a result the power absorption close to the lateral wall is negligible beyond the ECR region. On the contrary, density is sufficiently low close to the inner rod element of the thruster to enable wave propagation along a narrow channel in cases M0 and RED, and there is some field magnitude and power deposition in this region. The effect of increasing mass flow rate is to further close this channel.

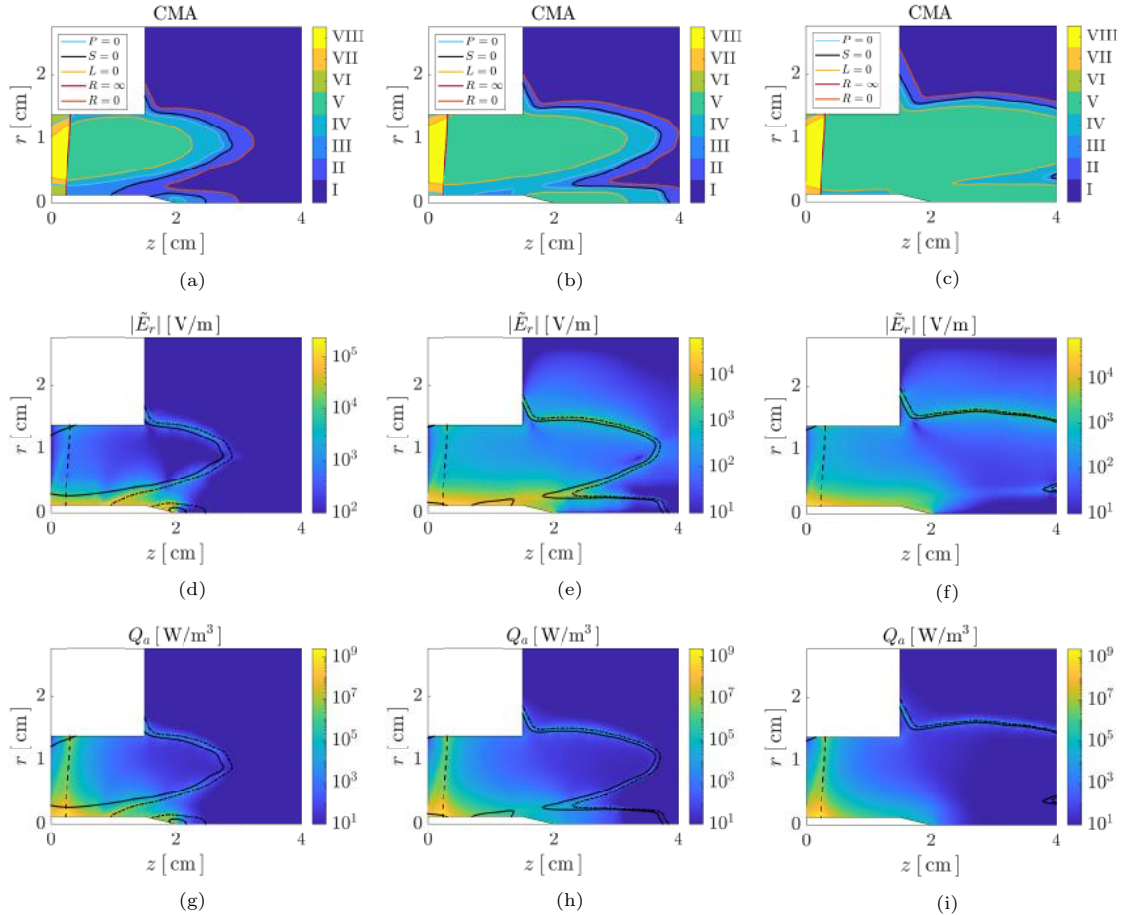


Figure 6.17: Figures (a), (b) and (c) show the CMA regions in the plasma; (d), (e) and (f) show the norm of the radial component of the EM wave electric field; (g), (h) and (i) power absorption density maps. From left to right increasing mass flow rate (M0, RED, and M2). Figures (a)-(c) include boundary surfaces as cutoffs (i.e. $P = 0$ (cyan), $R = 0$ (red), and $L = 0$ (ocher)) and resonances (i.e. $R = \infty$ (maroon) and $S = 0$ (black)). From (d)-(i) the ECR (dashed), the critical density loci (solid), and the UHR (dash-dotted).

The radial electric field is largest close to the ECR and UHR resonances, and close to the coaxial port and the inner rod element in all cases. For the lowest mass flow rate case, M0, the UHR surface is broken down in two parts: a main bow arc along and across the channel, and a small section that appears close to the rod tip. There, the radial electric fields intensify again, and also deposit considerable amount of EM power, as can be noticed in Figure 6.17g.

In the case of high mass flow rate, M2, the UHR surface is pushed farther downstream than in cases M0 and RED due to the higher plasma density. This effect results in “closing” the propagation channel to electromagnetic power, so that most electromagnetic power is now deposited just in the ECR zone. Note however that electromagnetic power still can and indeed does tunnel through the evanescent region, where some collisional absorption takes place, and reaches the UHR.

Regarding the coupling efficiency η_c , for increasing mass flow rates it decreases from 96.1% to 91.1% and to 80.0%. This is likely a consequence of the increased plasma density that enlarges the impedance mismatch between the plasma and the coaxial. As a consequence, the amount of reflected through the coaxial increases.

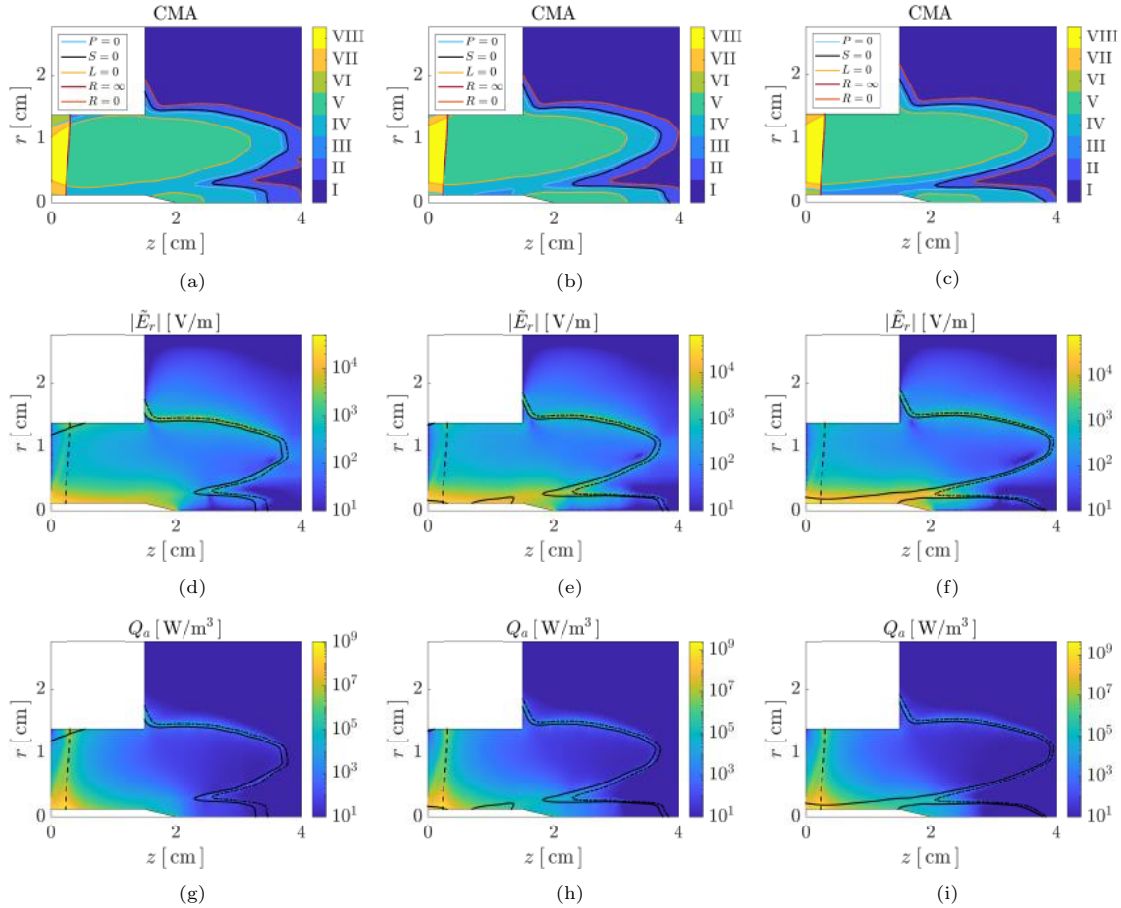


Figure 6.18: Figures (a), (b) and (c) show the CMA regions in the plasma; (d), (e) and (f) show the norm of the radial component of the EM wave electric field; (g), (h) and (i) power absorption density maps. From left to right increasing input power (P0, RED, and P2). Figures (a)-(c) include boundary surfaces as cutoffs (i.e. $P = 0$ (cyan), $R = 0$ (red), and $L = 0$ (other)) and resonances (i.e. $R = \infty$ (maroon) and $S = 0$ (black)). From (d)-(i) the ECR (dashed), the critical density loci (solid), and the UHR (dash-dotted).

Conversely, Figure 6.18 shows the influence of increasing input power from left to right in. In this case, the regions of the CMA map are essentially unaffected, and retain their overall shape and

size. The only noticeable change lies in the growth of the inner region V and a slight variation of the position of the UHR resonance, but much less significant than for increases in mass flow rate, linked to the variations in the plasma density. Additionally, the narrow propagation channel close to the inner rod segment acquires a small sized region of type III, similarly to a decreasing mass flow rate, but in a more prolonged shape (see Fig. 6.18c). This leads to stronger radial wavefields in this region a more power being deposited all along region III as can be seen in Figure 6.18i.

Concerning the maximum power density for each case, we note that for increasing input power the peak absorbed power, typically located at intersection of the inner rod surface with the ECR, rises from approximately 1.0 to 2.0 to 4.0 GW/m³ (note the different scales of the plots). This is the main effect of increasing power in the explored range, and is linked to the increase in electron temperature in the magnetic tube that passes by this peak.

As a result of the lower plasma density encountered at the plasma right after the dielectric window (i.e. coaxial to thruster chamber transition), for higher input power the coupling efficiency of the thruster η_c increases from 87.6, to 91.1 and to 91.6 %.

6.2.6 Thruster performances

Table A.1 shows that amongst all the species, the one contributing the most to thrust is the ions in all simulation cases as expected. For increasing mass flow rate, the ion thrust (i.e. F_i) increases a 40% from M0 to RED, and only a 6% from RED to M2. This trend can also be seen also in the energy efficiency which also saturates around \dot{m} of 0.2-0.25 mg/s. This implies that case REF is close to a local optimal in the performance of this thruster. Regarding the effect of input power on the thrust, we notice that F_i increases a 65% from P0 to RED, and a 15% from RED to P2, also denoting some saturation.

As discussed in §5.3.4 we define the propellant utilization efficiency $\eta_u = \dot{m}_{i\infty}/\dot{m}$ as the ratio of ions leaving the domain through the plume boundaries, $\dot{m}_{i\infty} = m_i \int_{\Sigma_p} n_{i1} \mathbf{u}_i \cdot d\mathbf{S}$, with respect to the input propellant mass flow rate, \dot{m} . In table A.1 one can find the values of η_u for the three different cases of mass flow rate (i.e. M0, RED and M2). The variation of the propellant utilization efficiency with mass flow rate does not exhibit a monotonic behavior, suggesting the existence of an optimum. This is due to the interplay between ionization and wall losses. An increase in mass flow rate generally leads to an increase in neutral density, increasing the amount of neutrals being ionized, increasing the amount of energy used for ionization which is extracted from the internal energy of electrons. Eventually, too much mass flow rate reduces the electron temperature, and ionization source rates drop. Despite an increase in mass flow leads to an enhancement of ionization initially, when the electron temperature starts to decrease below the ionization temperature, the propellant utilization saturates and even decreases. After this point of operation further increase in mass flow rate would significantly reduce the propellant utilization of the discharge.

Regarding the effects on input power on η_u , we note that increasing input power results overall in an increase of η_u . It is noted that the power fraction spent in ionization ϵ_{ion} decreases with input power, while the wall losses ϵ_{wall} increase at least in the explored range. The utilization efficiency is expected to saturate with input power at some point.

The specific impulse I_{sp} is a crucial figure of merit in the analysis of the performance of a thruster. Thruster designs with high I_{sp} are capable of both accomplishing missions with higher Δv requirement and reducing the propellant consumption for a specific mission, but result in lower thrust for the same input power and thrust efficiency. The specific impulse of electric propulsion devices is seen to scale roughly with the amount of energy provided to the propellant per unit mass, following $I_{sp}^2 \propto P_a/\dot{m}$, being P_a the power absorbed. Figure 6.19a shows the correlation between the specific impulse of the coaxial ECRT model presented here and the ratio of mass flow rate and available power, using as the latter the absorbed power (i.e. P_a). A linear regression shows a fit with goodness $R = 0.9181$.

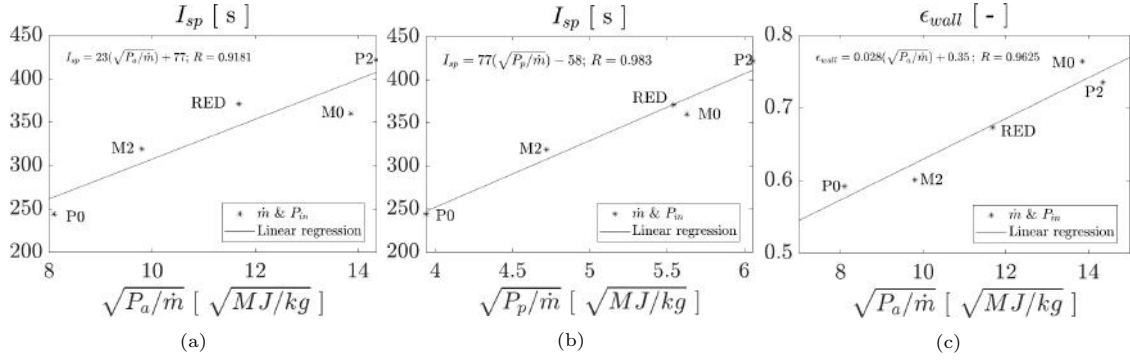


Figure 6.19: (a) and (b) show the specific impulse with respect to the square root of the ratio absorbed and plume power, respectively. Figure (c) shows the power ratio lost to the walls as a function of the square root of the ratio absorbed.

A more accurate description is obtained by plotting I_{sp} versus the *plume* power ($P_p = P_a \eta_e$) per unit mass. Since part of the absorbed power by the thruster is spent in losses such as ionization, excitation, and wall losses, P_p represents the amount of actually useful power for propulsion. Table A.1 shows that the amount of power used for energizing the particles in the plume (i.e. η_e) is not constant for different mass flow rates or input powers. Thus, $I_{sp}^2 \propto P_p/\dot{m}$ is a better description of the behavior of the specific impulse, with $R = 0.983$. Nevertheless, although the use of P_p for this regression is far more reliable, it can be rather difficult to estimate this power amount in a laboratory. Therefore, the law shown in Fig. 6.19a can be useful for a first approximation to estimate the specific impulse of the coaxial ECRT.

Lastly, figure 6.19c shows the wall losses exhibited for different mass flow rates and input powers. As can be noticed, they roughly scale with $\sqrt{P_a/\dot{m}}$ with a linear regression coefficient of $R = 0.9625$, which is a representative of the energy per particle. The energy per particle is directly related to the temperature and it is found to drive the temperature maximum, and as a result the wall losses, mainly driven by SEE emission.

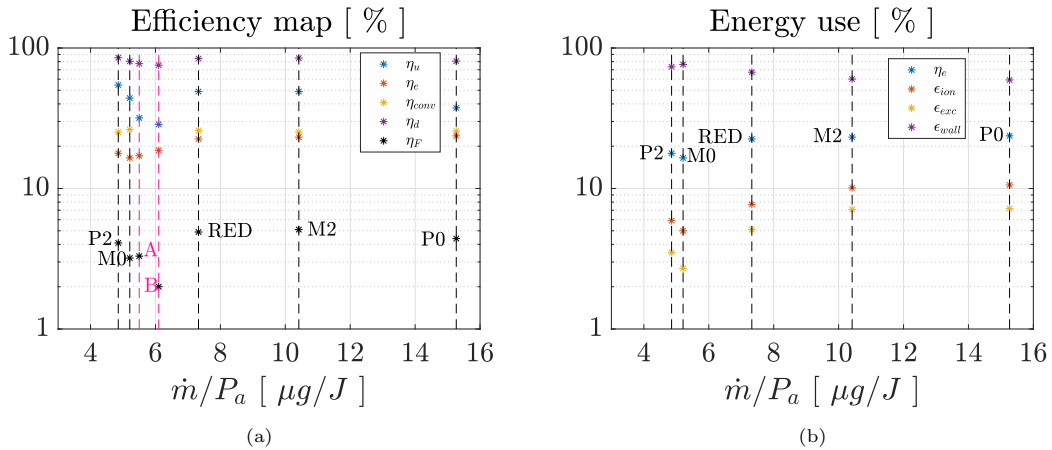


Figure 6.20: Map of efficiencies and energy use for the cases shown in the parametric investigation of input power and mass flow rate. For the sake of comparison, in (a) we show cases A and B (magenta), which are two operational points from the experimental investigation reported in Ref. [12].

Figures 6.20a and 6.20b show the variation of the different thruster efficiencies with the ratio of mass flow rate to absorbed power. In Fig. 6.20a we show two operational points measured in an experimental campaign reported in Ref. [12]. Comparing the experimental values with the estimated values obtained in this investigation we note that cases M0 and A denote fairly

comparable performances in overall thruster, utilization, energy and divergence efficiencies, for similar operational points. However the simulations overestimate the utilization efficiency. Note that the experimental cases provide no information about their conversion efficiencies.

We note that case B exhibits a significant decrease in performance with the ratio \dot{m}/P_a which is not estimated by the envelop of cases run in this investigation. This suggests either an overestimation of the optimal ratio \dot{m}/P_a for the coaxial ECRT model presented here with respect to the experimental thruster or a flawed experimental measurement.

Focusing on the simulation results, we note that only the energy efficiency and the utilization efficiency follow a trend with this ratio, the former increasing and the latter decreasing with it, similarly to the measurements given in Ref. [12]. The overall thruster efficiency exhibits a maximum relatively close to the nominal case.

Concerning the energy use, and as mentioned before, the energy lost to the wall decreases with the amount of mass flow rate per unit absorbed power. Furthermore, both ionization, excitation and energy ratios increase with increasing \dot{m}/P_a . However, the curves saturate at values between case M2 P0, where no significant changes can be noticed. This implies that there is an optimum in power input in this type of thruster and it is slightly to higher mass flow rates and lower input powers than the nominal operation point. Beyond that point, increasing the input power or reducing mass flow rate would result in larger wall losses, and more inefficient operation.

6.3 Effects of ECR location

The operation of the ECRT relies in the electromagnetic power deposition that takes place mainly in the ECR region. As was seen in chapter 5 and in section §6.2.5, the propagation and absorption of the wavefields in the plasma are determined by the plasma variables which, together with the magnetic properties, define the CMA regions. Understanding of the variables driving the appearance and switch between regions allows to predict not only the propagation but also the absorption of electromagnetic power based on plasma variables. In this section, an investigation on the influence of the location of the ECR region is carried out. Using the reduced nominal case (i.e. RED) as reference, we have scaled down and up the strength of the applied magnetic field B_0 to displace the ECR in the original device.

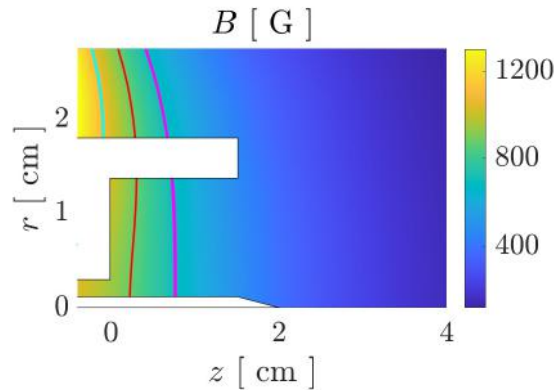


Figure 6.21: Resonance locations analyzed in the study. The applied magnetic field intensity of the reference case is shown in the colorbar. The contour lines represent the three ECR locations investigated: red (RED), cyan (ECR0) and magenta (ECR2).

This section shows cases for two alternative locations of the ECR region to the nominal:

- **ECR0**: decrease the applied magnetic field intensity by a 20%, thus moving the ECR upstream and outside of the discharge chamber. In this case we have forced the thruster to operate

without ECR to check whether its operation is feasible and to understand the mechanisms of power deposition in this case.

- **ECR2:** increase the magnetic field intensity by a 25%. This case enables studying the effects of moving the ECR region further downstream.

Figure 6.21 shows the location of the ECR regions for the two alternative cases and the nominal case, representing in the background color the nominal applied magnetic field. The different ECR locations investigated are shown in Fig. 6.21, being the cyan curve that for case ECR0, the red curve for the nominal case (RED) and the magenta that of case ECR2. As the excitation frequency is fixed, $B_{res} = 875$ G for all cases, modification of the magnetic field intensity results in displacement of the ECR location upstream (ECR0) or downstream (ECR2). This also affects the charged particles magnetization level, and thus the transport coefficients vary among simulations. Notwithstanding this, the main change in the plasma response is due to the effect of the shift in the ECR position on both wave propagation and absorption.

6.3.1 Propagation and absorption of electromagnetic waves

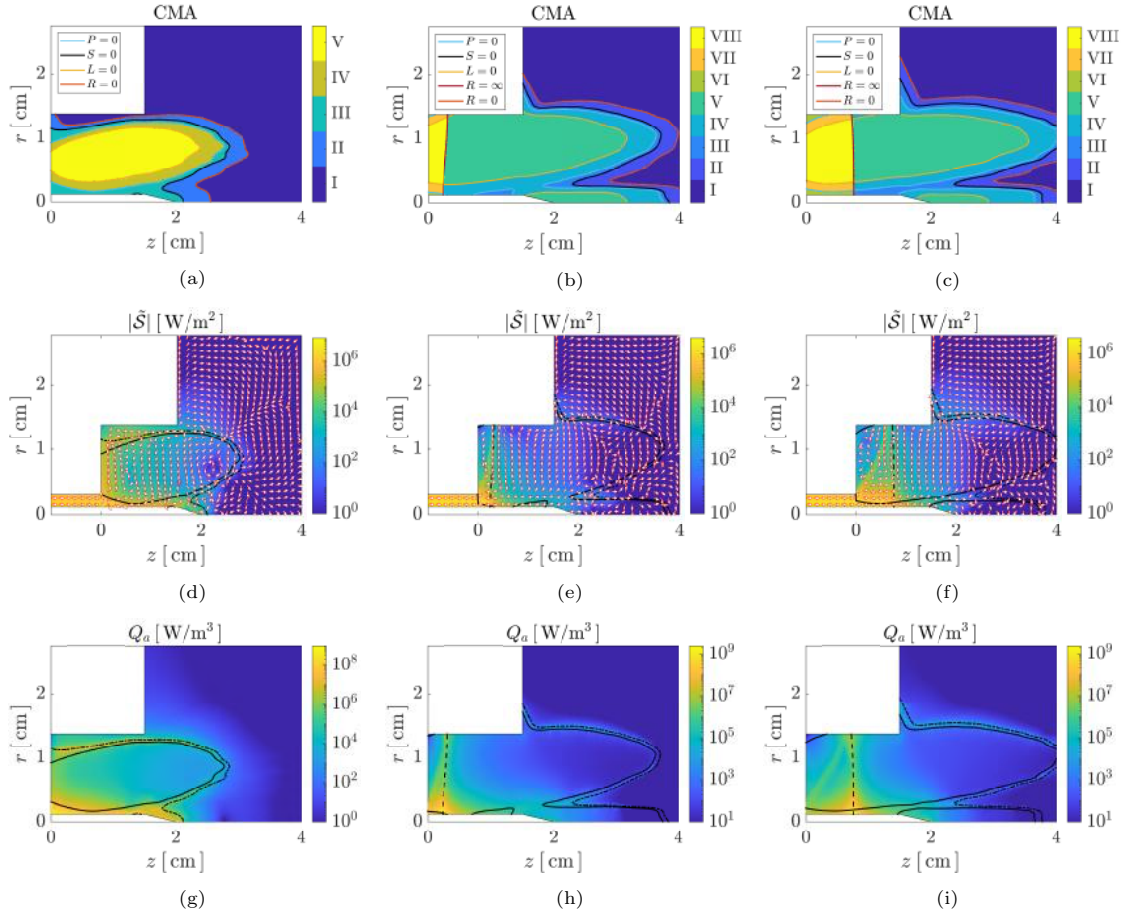


Figure 6.22: Figures (a), (b) and (c) show the CMA regions in the plasma; (d), (e) and (f) show the Poynting vector magnitude and direction and (g), (h) and (i) the corresponding power absorption density maps. From left to right, we show cases ECR0, RED, and ECR2. Figures (a)-(c) include boundary surfaces as cutoffs (i.e. $P = 0$ (cyan), $R = 0$ (red), and $L = 0$ (other)) and resonances (i.e. $R = \infty$ (maroon) and $S = 0$ (black)). From (d)-(i) the ECR (dashed), the critical density loci (solid), and the UHR (dash-dotted).

Figure 6.22 shows that the results for the propagation and absorption of electromagnetic waves in the coaxial ECRT with variations in the applied magnetic field intensity.

6.3.1.1 CMA regions

Varying the magnetic field strength in the domain affects the dielectric tensor κ of the plasma, which modifies its wave propagation and absorption properties. This is evidenced in the new CMA regions diagrams, presented in figures 6.22a, 6.22b and 6.22c. As detailed in section §6.2.5, the CMA regions diagram is a fundamental tool to understand both the paths of propagation and absorption of power in an electromagnetic thruster with a variety of cutoffs and resonances in its domain, as it is the case for ECRTs.

The ECR surface is not present inside the plasma domain in simulation ECR0. The wave power first enters the discharge chamber through regions of type III, IV and V. The type V region is a non-propagating region with evanescent fields. The absence of a principal resonance means that the wave power can only be reflected back to the coaxial cable, be weakly absorbed by electron collisionality, or be propagated further downstream to the UHR surface ($S = 0$).

The CMA regions diagram of simulation ECR2 is qualitatively similar to that of the reference simulation RED. It features a larger propagating region before the resonance, and still has a propagating channel close to the inner rod element of the thruster that can deliver power to the downstream UHR resonance region.

Comparing the three diagrams we note the resemblance between case RED. Only five regions (I-V) are present in case ECR0, as the plasma is always below line $R = \infty$ in the CMA parametric plane [27]. This leads to significant changes in the propagation of waves through the plasma and the regions of power deposition. As will be explained in §6.3.2.1, the plasma density decreases considerably faster towards the lateral wall for case ECR0. Such is the decrease in plasma density that even regions II and I are able to access and extend along the vicinity of the lateral wall. This allows the propagation of electromagnetic waves all along.

However, the three cases exhibit the narrow propagation channel of low density plasma close inner rod and the dielectric window. In cases RED and ECR2, the power accesses through regions VI, VII and VIII while in case ECR0 it does it through regions III and IV.

6.3.1.2 Poynting flux vector

In order to further analyze the EM wave propagation within the thruster, the Poynting vector becomes a useful tool, as it represents the flux of EM energy through the domain. Note that this represents the net flow of (resistive) power in steady state conditions, including any reflected power.

Figures 6.22d, 6.22e and 6.22f show the Poynting flux magnitude in the colorbar and the direction in arrows. These figures detail the different paths of propagation of the electromagnetic power through the thruster for different ECR locations. In all cases the power accesses through the coaxial cable, where Poynting intensity is largest. From this point on, the EM power flows mainly close to the inner rod surface. It propagates through region III in case ECR0 and through regions VI and VII in cases RED and ECR2, crossing the ECR region and continuing flowing along region III.

In cases RED and ECR2, the majority of the electromagnetic power flows into the regions upstream the ECR location and is absorbed there. This is denoted by the significant decrease in Poynting vector amplitude after crossing the ECR region. The Poynting vector bends and becomes essentially parallel to the ECR surface. This is also true near the UHR resonance.

Case ECR0, on the other hand, lacks the ECR and behaves differently. In absence of ECR, the power flows freely through region III, only limited by the $L = 0$ cut-off (interface between regions IV and V) and the UHR resonance. In this case it is the UHR that absorbs much of the power. In the nominal case RED, the coaxial ECRT allows the EM power to flow into the plasma and spread over most radii upstream the ECR. In case ECR0 we note that this is not the case and the

power is forced to flow in region III which can be understood as a layer around the plasma core. In this case the power cannot penetrate the denser plasma.

Additionally, in case ECR0, the electromagnetic energy is capable of tunneling through region V close to the back plate. This is motivated by the presence of collisions in the dielectric tensor, which makes the decay factor of the waves finite and allows waves to propagate through the evanescent region V.

6.3.1.3 Power absorption density

In cases RED and ECR2 and in agreement with the behavior of the Poynting flux vector, the power absorption is concentrated at the location of the ECR, featuring its maximum at the intersection between the ECR surface and the inner rod surface. Additionally, in both cases, some power is still absorbed along region III close to the inner rod surface, and also a small amount out of the thruster chamber, at the UHR location. The power absorption beyond the UHR is negligible.

In case ECR0, the absence of the ECR region forces the power to be absorbed in the other two regions mentioned for cases RED and ECR2. Note that since region III occupies more domain, the maximum power absorption density decreases almost an order of magnitude with respect to cases RED and ECR2. Note also the different color scale for the power absorption plot of this case.

Comparing the three different scenarios we note that the coupling efficiency of case ECR2 is enhanced with respect to case RED, increasing from a 91.1% to a 98.2 %. However, case ECR0 exhibits a strong reflection and slow coupling efficiency, in this case of 18.1%, resulting in only 5.42 W of absorbed power. This indicates that the presence of the ECR is essential for an efficient power coupling with the plasma in the thruster.

6.3.1.4 EM wave electric fields

Figure 6.23 shows the radial and axial components of the EM wave electric field in the thruster for different ECR locations, being from left to right, cases ECR0, RED and ECR2. The complex phase of each component is also shown.

In order of importance, the EM wave fields present in the coaxial ECR thruster are fundamentally radial and then axial, with some marginal azimuthal electric fields. The latter component has been omitted from the report since its magnitude was 2 or 3 orders of magnitude smaller than the other two.

Comparing cases RED and ECR2 we note that there is significant similarity between the two, in the shapes of the fields both in amplitude and phase. Prior to the ECR most of the electric fields propagate close to the inner rod surface in the form of radial electric fields. Additionally, part of the electromagnetic fields propagate from the dielectric window to the lateral wall, right upstream the ECR location, for both cases. Downstream the ECR location, the fields propagate with a dominant radial component, through region III of the CMA diagram, and continue to do so through this region. Regarding the phase of the radial electric fields, we note that in the region close to the inner rod surface, the radial electric fields shares the same phase. Furthermore, the UHR region forces a sudden change in the phase, as can be seen in both figs/Parametric. 6.23e and 6.23f. Prior to the ECR location, the phase of the radial electric fields experiences a sudden change at the location of the filament of fields connecting the dielectric window with the outer lateral wall. Concerning case ECR0, we note that the radial electric fields vary significantly with respect to the other two cases. The complex amplitude of the electric fields is intensified by more than an order of magnitude with respect to cases RED and ECR2. Notwithstanding, the fundamental electric fields are still radial, with some axial component, and they extend all along region III and vanish propagating into the plasma core (i.e. region V), similarly to cases RED and ECR2.

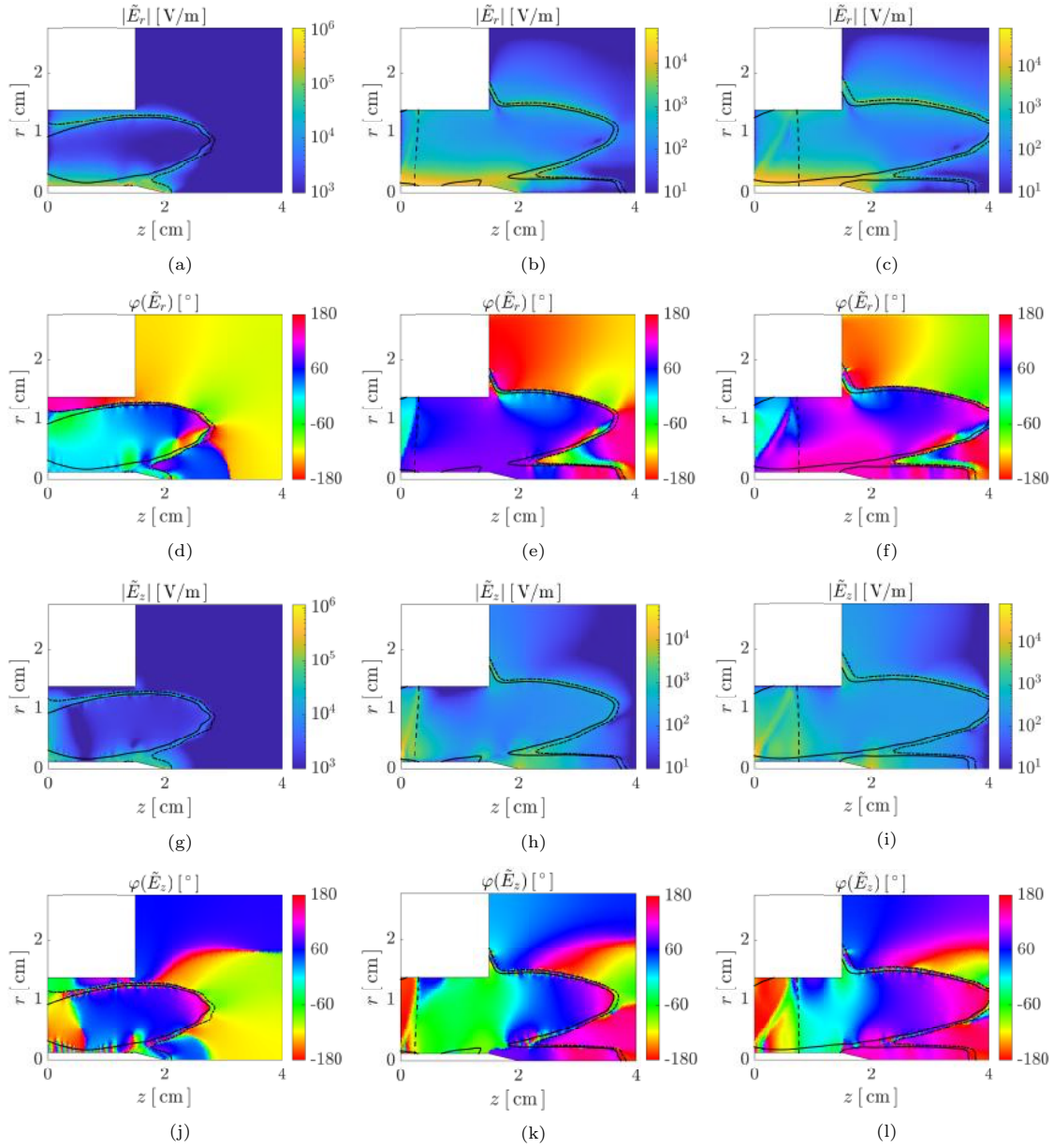


Figure 6.23: Influence of ECR location on the principal EM wave electric field components; (a)-(c) radial electric field norm and (d)-(f) respective phases, (g)-(i) axial electric field norm and (j)-(l) respective phases. Figures from left to right represent cases ECR0, RED, and ECR2. Boundary surfaces shown represented are the ECR (dashed), the critical density loci (solid), and the UHR (dash-dotted).

Regarding the phase of axial wave electric fields, we note that the three cases exhibit a fast frequency wavelike pattern in those fields populating region III. The fundamental nature of this fast frequency oscillations has been reported in other works close to the resonance $S = 0$ [88, 126] and will require further investigation. In Ref. [59] we showed that a local refinement applied on the region exhibiting this high frequency oscillations, not only reduced the oscillations but also showed that these arise in the vicinity of region $S = 0$. With increasing mesh refinement, the oscillations would localize in region III closer to the UHR and would propagate less into regions III and IV. This, however, was seen not to affect the power deposition maps.

Close to the inner rod surface, case ECR0 shows a coherent propagating axial wave, performing several cycles (red to red), from the dielectric window to the end of the inner rod. The presence of wave cycles is indicative of the presence of short wavelength waves. This is not seen in general in most of the device, where the characteristic wavelength is generally larger than the device size.

6.3.2 Neutral and plasma transport

The effect of varying the applied magnetic field strength is mainly to modify the EM power propagation and absorption map. This, however, also has an influence on the transport properties. Firstly, due to the modified power absorption map itself; secondly, due to the variation in the perpendicular transport coefficients that depend on the magnetic field strength.

6.3.2.1 Neutral and plasma density

Figures 6.24a and 6.24b show the radial evolution of the neutral and plasma density profiles along the radial section $z = 0.5$ (see Fig. 6.1a). Comparing the neutral densities of the three cases we note that the neutral density maps of case RED and ECR2 hold strong resemblance. This map was already discussed in previous sections. However, the neutral density of case ECR0 is significantly higher. This is mainly motivated by the lower ionization due to the lower electron temperature. The lack of ECR in the ECR0 case forces the EM power deposition out of the neutral core so that most power is absorbed both at the top and bottom corners of the thruster. Moreover, since close to the inner rod surface the power absorption is decreased by an order of magnitude, we note a significant increase of neutral density there for case ECR0.

The differences between cases RED and ECR2 in the both plasma and neutral density are mainly located close to the lateral wall, where both the plasma and neutral density are decreased in ECR2. This could partially be a result of the increased magnetization exhibited in the thruster for case ECR2 with respect to case RED, which limits perpendicular transport away from the plasma core, thus decreasing the plasma density there. As a consequence, the electric potential rises limiting the flux of ions to the dielectric wall to fulfill the condition of zero local net current density. This also decreases the amount of neutrals emitted by the lateral wall by ion-wall recombination.

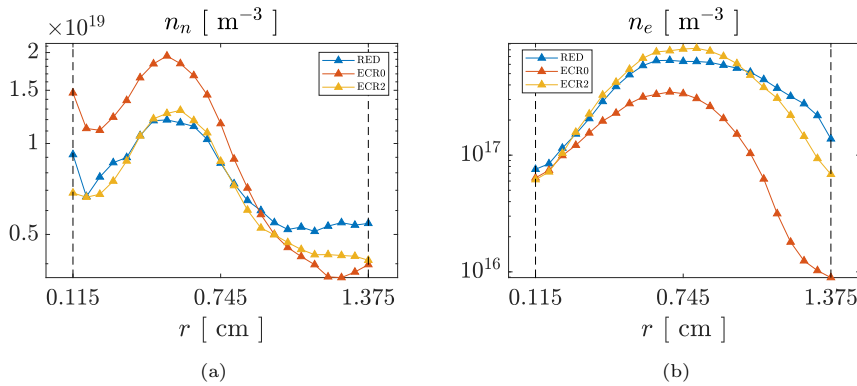


Figure 6.24: Effect of the ECR location on the radial profiles along PIC-mesh nodes located at $z = 0.5$ cm of (a) the neutral density and (b) electron density. Dashed lines represent the minimum and maximum radius of the thruster chamber.

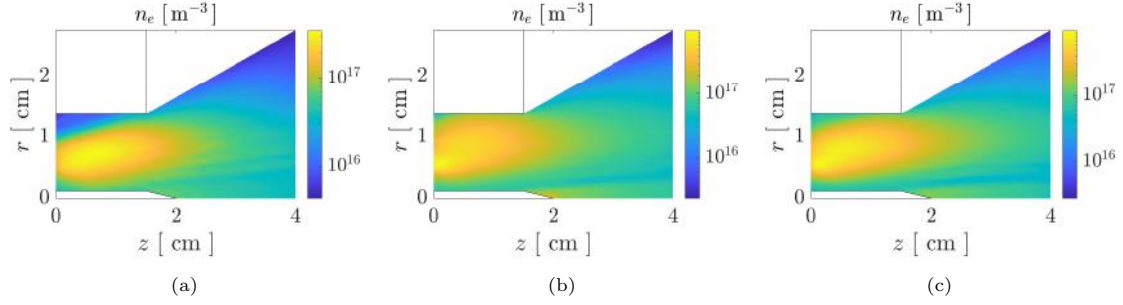


Figure 6.25: Electron density of (a) ECR0, (b) RED, and (c) ECR2 cases.

Figure 6.25 shows the different plasma density maps obtained for different ECR locations, being cases ECR0 (left), RED (center) and ECR2 (right). Case ECR0 exhibits a maximum plasma density of the order of $3.3 \times 10^{17} \text{ m}^{-3}$ while the other two achieve maxima of approximately 10^{18} m^{-3} . As can be seen comparing figures 6.25a, 6.25b and 6.25c, the plasma density decrease that occurs close to the lateral wall is accentuated in case ECR0. Contrary to cases RED and ECR2, case ECR0 presents some significant power absorption close to the lateral wall. Since the electron pressure has to decrease towards the wall, and the electron temperature is increased there due to the higher power absorption, the plasma density decreases faster towards the lateral wall.

6.3.2.2 Electron temperature and plasma potential

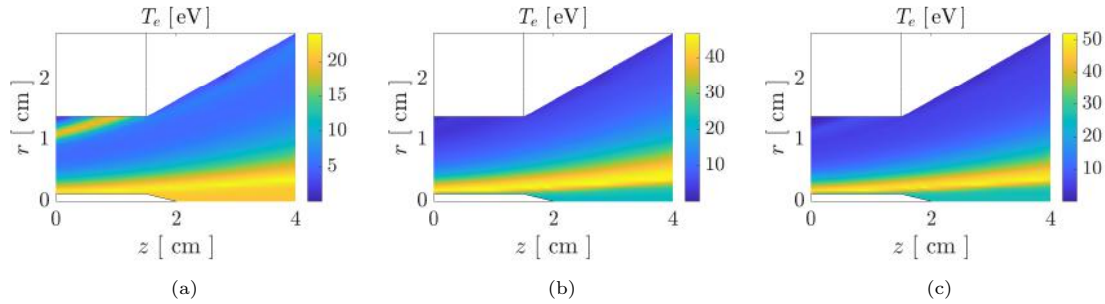


Figure 6.26: Figures (a), (b) and (c) show the electron temperature maps, for different locations of the ECR. From left to right we show cases ECR0, RED and ECR2.

The electron temperature is mainly determined by the power absorption, ionization and excitation losses, and fluxes to the walls. In the ECRT, for the level of magnetization, perpendicular electron transport is limited. As a result, the increase of the power absorption in certain regions generates a significant rise of internal energy in the magnetic tubes corresponding to higher absorption. The parallel heat conductivity is much higher than the perpendicular conductivity, and electrons remain isothermal along magnetic field lines. Comparing the electron temperature with the power absorption maps shown respectively in figures 6.26 and 6.22, we note this correlation between the locations of maximum power absorption and the regions of maximum temperature.

Figure 6.27a shows the radial evolution the electron temperature for the three alternative ECR locations at section $z = 0.5$ of the thruster chamber (see Fig. 6.1a). Both cases RED and ECR2 show that for a location downstream the backplate, the highly focused power absorption at the ECR close to the inner rod surface induces a dominant peak of temperature near it. However the power absorption decays moving to higher radius for both cases until for case ECR2 suffers a subtle rise close to the lateral wall, which is related with the small local peak of electron temperature close to the lateral wall for case ECR2 with respect to case RED that has no maximum.

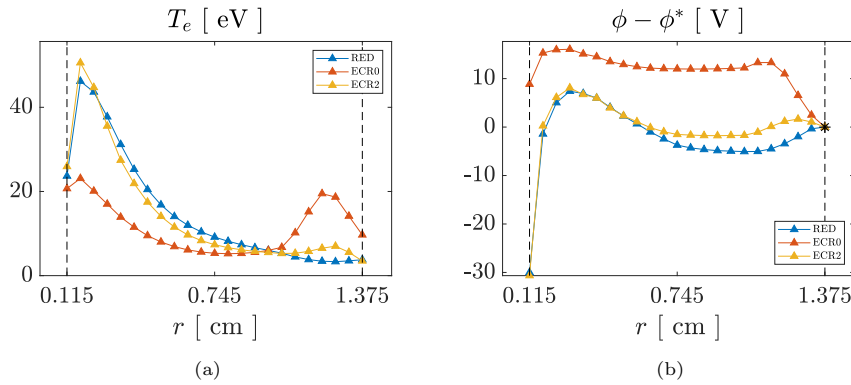


Figure 6.27: Effect of resonance location on the radial profiles along PIC-mesh nodes located at $z = 0.5$ cm of (a) the electron temperature and (b) plasma potential. Plasma potential is shown taking as reference the potential at the lateral wall. Dashed lines represent the minimum and maximum radius of the thruster chamber.

The electron temperature of case ECR0 behaves differently, fundamentally driven by the significant changes experienced in the power absorption maps. Since the plasma densities exhibited in region III are of the same order, and there in case ECR0 the power absorption density achieves similar levels of power absorption, and both regions have similar axial extension, we can deduce that there will be two peaks in electron temperature radially of more or less the same order, being the one close to the inner rod surface coarser as this region populates more magnetic field lines. This can be verified looking at Fig. 6.27a. Note that the second peak close to the lateral wall occurs in the magnetically-isolated corner of the discharge chamber, and that the temperature there exceeds the ionization energy threshold of Xenon.

Figure 6.27b shows the radial evolution along section $z = 0.5$ cm of the plasma potential, taking as reference the value at the lateral wall. Firstly, both cases RED and ECR2 again hold a high resemblance. The radial electric fields inside the thruster chamber are barely affected except that the electric field at case ECR2 shows a secondary peak in the electric potential before the lateral wall. The location of the maximum potential, similarly to the location of the maximum temperature are located at the same radius, and the radial electric field to the inner wall surface remains essentially unchanged. On the other hand, the behavior of case ECR0 is again completely different. A significant radial electric field appears towards the lateral wall for case ECR0 and the electric potential remains flat until close to the inner rod surface, where the electric field is much smaller than that for cases RED and ECR2 there. This can be a result of the difference in the gradients of temperature between simulations both close to the lateral wall and the inner rod surface.

Figure 6.28 shows the changes in plasma potential maps and the corresponding electrostatic field, with variations in the location ECR zone. Similarly to what was explained in §6.2.2, the potential drop in the axial direction is directly correlated with the electron temperature of the discharge. This can be noticed looking at the maximum values of the potential and that of the temperature for both cases. The former is approximately 25, 43, and 44 V and the latter 25, 44 and 51 eV, for cases ECR0, RED and ECR2, respectively.

The three simulations exhibit radial electric fields towards the inner wall surface, of the order of approximately 1, 5 and 7×10^4 V/m. Additionally the direction of the electric field at the lateral wall (before the plasma sheath) changes from case to case, pointing away from the wall in case RED, and to the wall slightly for case ECR2 and significantly for case ECR0. This will strongly affect the velocity of ions to the walls for the different cases, revisited in §6.3.2.3. Additionally, all cases experience a minimum electric field at an intermediate location. Furthermore, the radial component of the electric field is clearly positive for case ECR0 whilst for cases RED and ECR2 is slightly negative.

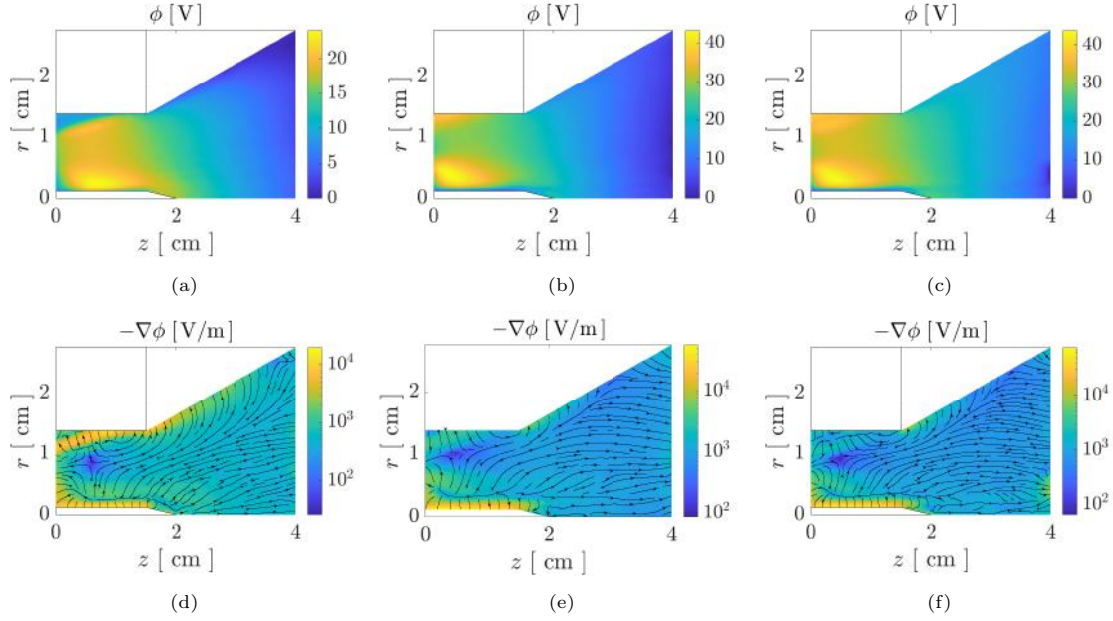


Figure 6.28: Figures (a), (b) and (c) show the plasma potential and (d), (e) and (f) the corresponding electrostatic field, for different locations of the ECR. From left to right we show cases ECR0, RED and ECR2.

6.3.2.3 Ion velocity

As ions are essentially unmagnetized their acceleration can be explained by the shape of the electric fields, shown in figs/Parametric. 6.28d, 6.28e and 6.28f. Figure 6.29 shows the variations in the velocity of ions with the variation of the ECR location. As detailed in §6.3.2.2, for case ECR0, the electric field close to the thruster walls, points towards each of them. As a result, ions accelerate, increasing their impact energy when reaching the walls. This is not the case for the lateral wall for cases RED and ECR2, where the electric field is negligible and in often points away from the wall before the sheath begins.

Regarding the acceleration of ions, we note that in case ECR0 it is much smaller than cases RED and ECR2. In fact, we can compute the local ion Mach number at the end of the simulated plume. This is shown in figure 6.30.

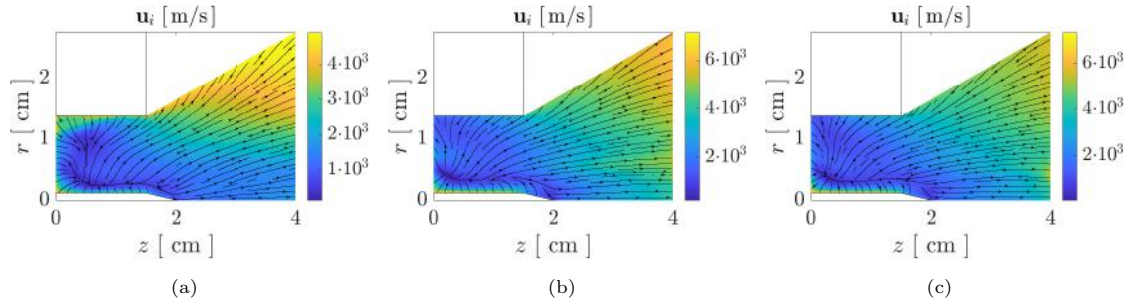


Figure 6.29: Figures (a), (b) and (c) show the velocity of ions for different locations of the ECR. From left to right we show cases ECR0, RED and ECR2.

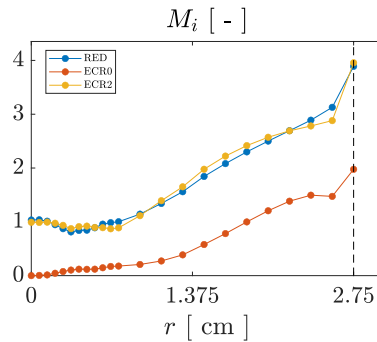


Figure 6.30: Effect of resonance location on the radial profiles of local ion Mach number at the end of the simulated plume. The dashed line represents the end radius of the simulated plume.

In this case we note that for case ECR0 the acceleration of ions drops significantly with respect to the other two. The acceleration obtained at the axis is rather inefficient, as there the velocity of ions is small and the electron population exhibits a considerably higher electron temperature at the axis. However, comparing cases RED and ECR2 we note no effective difference in terms ion Mach number.

6.3.2.4 Ionization rate

Figure 6.31 shows the influence of the ECR location in the ionization source rate. The results are consistent with those of the other variables, showing higher resemblance between cases RED and ECR2. The main difference between them is the region close to the lateral wall, where the ionization source rate increases significantly for case ECR2 (see Fig. 6.31c) with respect to case RED (see Fig. 6.31b). This is motivated by the higher electron temperature there (yellow curve in Fig. 6.27a). Although the difference is subtle, as the electron temperature there is below the ionization efficiency, the growth of ionization is exponential, so that in this region, case ECR2 presents an order of magnitude increase in S_{ion} .

Case ECR0 shows a significant rise in this region as well, coherent with the electron temperature peak exhibited prior to the lateral wall (see red curve in Fig. 6.27a). In general we note that case ECR0 ionization source rate is more homogeneous than the cases with ECR inside the thruster chamber. Notwithstanding, the ionization source rate is one order of magnitude smaller given the smaller overall electron temperature in the discharge of case ECR0 motivated by the lower amount of power absorbed by the plasma (5.42 against 27.3 and 29.5 for the other two). As the average electron temperature is below the ionization energy, the effects of ion wall recombination in the ionization source rate are more evident than for the other two cases (see Fig. 6.31a).

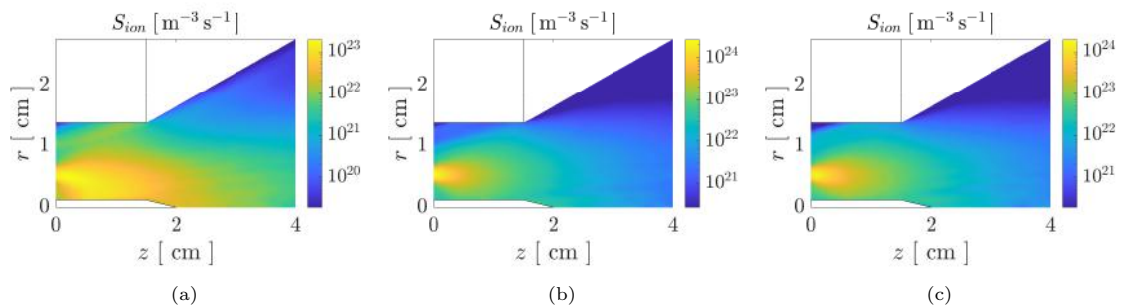


Figure 6.31: Figures (a), (b) and (c) show the ionization source rates for different locations of the ECR. From left to right we show cases ECR0, RED and ECR2.

6.3.3 Thruster performances and energy usage

Figure 6.32 shows the influence of the ECR location in both the thruster performances and the usage of the EM power absorbed by the electron population.

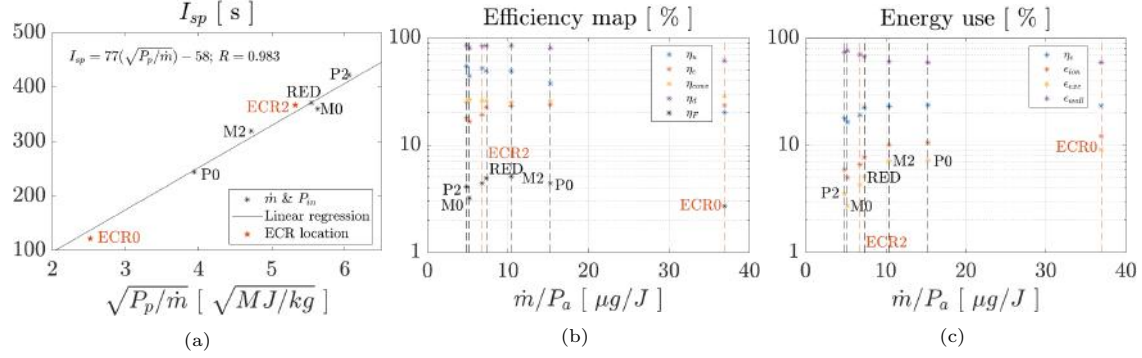


Figure 6.32: Maps of (a) specific impulse, (b) thruster efficiencies and (c) energy use, including cases of the parametric input power and mass flow rate. Cases with modified ECR location are highlighted.

Overall, displacing the ECR further downstream or upstream shows no significant effect in thruster performances. However some small modifications can be noticed. Both cases show similar convergence and divergence efficiencies. Notwithstanding that, despite the increase in the utilization efficiency for case ECR2 (from 49 to 52%), the decrease in η_e from 22.5 to 19.2% and the increase in P_a from 27.3 to 29.5 W, results in lower overall thruster efficiency of the thruster, that decreases from 4.9 to 4.4%. The main motivation in the decrease of η_e is the increase in the amount of losses to the walls, ϵ_{wall} , that is increased with respect to the reference case. This could be explained by an increased perpendicular transport modeled by both the turbulence-based force and heat flux, which is proportional to applied magnetic field intensity. Note that the latter is increased from case RED to ECR2 by a 25%.

Regarding case ECR0, the power reflection is too large, which decreases substantially the absorbed power (coupling efficiency 18.1% w.r.t the nominal 91.1%). While it is clear that this case has lower performance, the effect of removing the ECR is less deleterious than would be expected, reaching a thrust efficiency of 2.7%. The performance of case ECR0 is hindered by a poor utilization efficiency which can be a result of such a high \dot{m}/P_a ratio. Overall, the main inconvenience of this design is its low coupling efficiency.

6.4 Effects of variations on the injector geometry

In this section we show the effects of varying the injector geometry, as detailed in Table 6.2, with two alternatives:

- Case **INJZ0**: we displace the injector to lower radius at the backplate.
- Case **INJR**: we locate the injector at the lateral wall, close to the backplate, and inject the mass flow rate radially inwards. In this case we have increased the width of the injector port.

Parameter	Name	Units	REF	INJZ0	INJR
z_{inj}	Injection surface center z	cm	0.0	0.0	0.4
r_{inj}	Injection surface center r	cm	0.5735	0.35	1.375
t_{inj}	Injection surface width	cm	0.229	0.229	0.429
\mathbf{n}_{inj}	Injector surface normal	-	$\mathbf{1}_z$	$\mathbf{1}_z$	$-\mathbf{1}_r$

Table 6.2: Injector geometrical parameters.

6.4.1 Neutral and electron density

The injector affects mainly the distribution of neutral atoms inside the chamber. This, in turn, drives the dynamics of the plasma. The effect of the injector geometry on the neutral density is shown in Fig. 6.33.

Comparing the resulting stationary neutral density of cases RED and INJZ0, we notice that the main effect is to modify the radius of maximum n_n , following the injector location. The magnitude of this density is increased as the same mass flow rate is delivered at a lower radius.

Regarding case INJR, shown in Fig. 6.33c, we note that the behavior of n_n is completely modified. In this case, the maximum neutral density decreases (from 5 and 8×10^{19} to approximately $2 \times 10^{19} \text{ m}^{-3}$), provided the greater surface area of the injector now located at the lateral wall. Additionally, the resulting map of neutral density is much more homogeneous than the other two, and the average value is significantly higher than what could be expected from the increase in the injector area. The effect of the radial injector results in increasing the residence time of neutrals within the chamber. Figure 6.34a

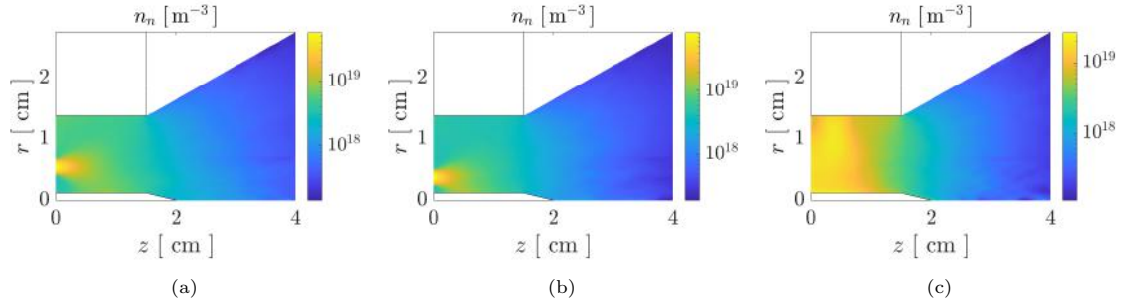


Figure 6.33: Figures (a), (b) and (c) show the neutral density maps for different injector geometries, being from left to right cases RED, INJZ0 and INJR.

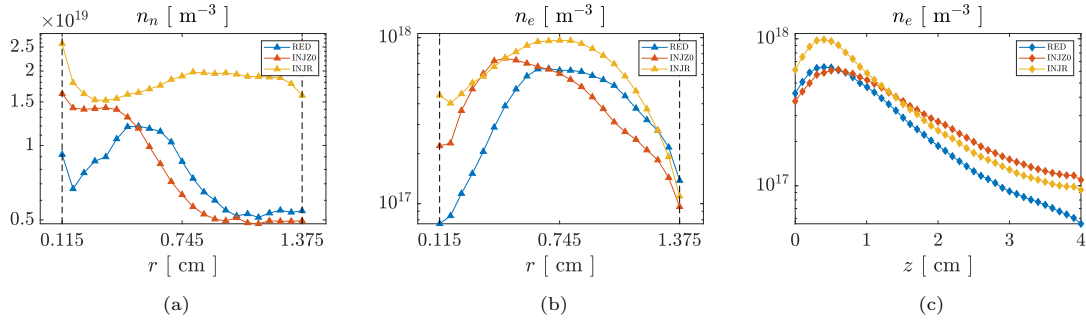


Figure 6.34: Effect of injector geometry on the neutral and electron densities. Figures (a) and (b) show the radial profiles of neutrals and electron density along PIC-mesh nodes located at $z = 0.5$ cm. Figure (c) shows the axial evolution of electron density along the line of PIC-mesh nodes located at radius $r = 0.745$ cm. Dashed lines in (a) and (b) represent the minimum and maximum radius of the thruster chamber.

In order to better appreciate the details inside the thruster chamber, in figure 6.34 we show the effect of the injector geometry in the radial profile of the neutral density at $z = 0.5$ cm. In fact, we notice that the average neutral density is much greater for case INJR than that of the other two cases, and that for case INJZ0, the density of neutrals is increased towards the inner rod surface with respect to case RED. Additionally we can notice the homogeneity previously mentioned for case INJR. And in all cases we note the effects of ion-wall recombination at the walls, being the effect the most significant for case INJR and the least for INJZ0.

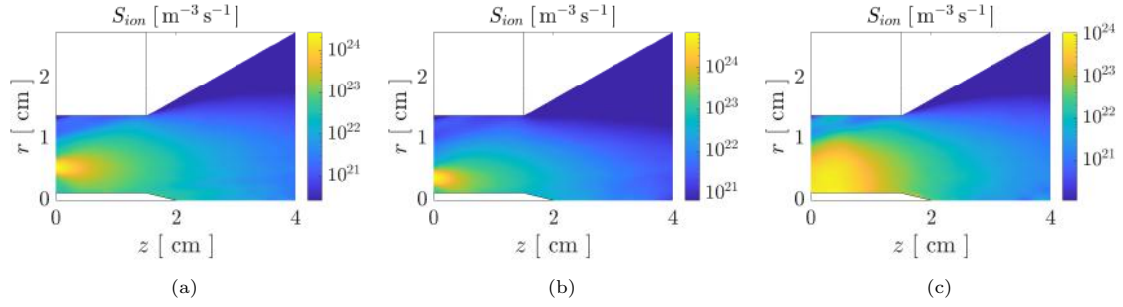


Figure 6.35: Figures (a), (b) and (c) show the ionization source rate for different injector geometries, being from left to right cases RED, INJZO and INJR.

Figures 6.34b and 6.34c show the influence of injector geometry in the radial (i.e. at $Z = 0.5$ cm) and axial (i.e. at $r = 0.745$ cm) evolution of electron density. We note that amongst all the parametric studies in this report, the injector location induces the most significant changes in electron density. Overall we note that the level of electron density achieved in case INJR is much greater than for the other two cases, being the lowest that of the nominal injection. The effect of moving the injector to lower radius along the backplate results in displacing the radius where the peak electron density is located in that same direction, reaching much greater electron densities close to the inner rod surface (from approximately 0.8 to $2 \times 10^{17} \text{ m}^{-3}$).

Regarding the axial profiles, we note that the peak electron density achieved with radial injection exceeds the other two cases. Furthermore we note that the expansion of the electron in the axial direction is the strongest for case RED, then for INJR and the least for case INJZO.

Figure 6.35c shows the effects of injector location in the ionization source rate. Ionization is strongly affected by the density of neutrals. Together with the more homogeneous character of the electron temperature, results in the homogeneous ionization source rate featured by case INJR (see Fig. 6.35c). Note that in this case the peak is not located right at the injector port but at the inner rod surface, and it features a lower gradient. The maximum ionization source rate varies in magnitude from case to case, being 2 , 6 and $1 \times 10^{24} \text{ m}^{-3}\text{s}^{-1}$ for cases RED, INJZO and INJR, respectively.

6.4.2 Electron pressure

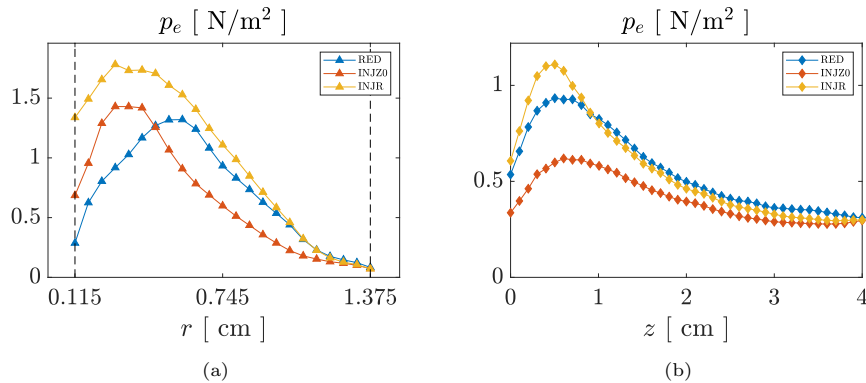


Figure 6.36: (a) and (b) show the radial and axial evolution of electron pressure and for variation on the injector geometry. Radial and axial evolution correspond to PIC-mesh nodes located that $Z = 0.5$ cm and $r = 0.745$ cm, respectively. Dashed lines represent the minimum and maximum radius of the thruster chamber.

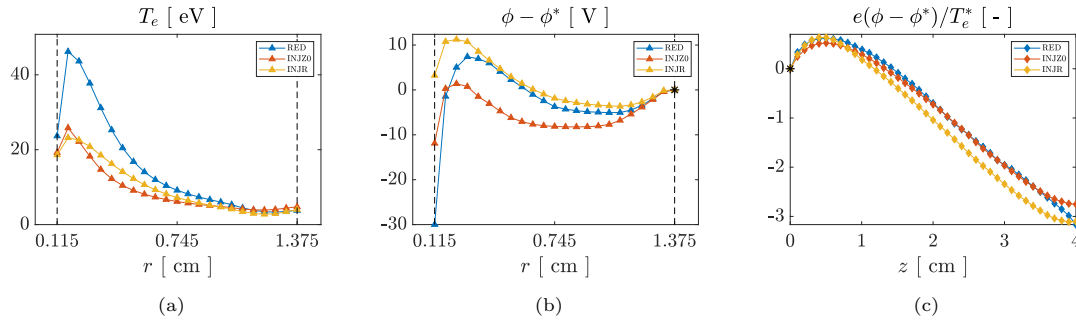


Figure 6.37: Effect of injector geometry on the electron temperature and plasma potential. Figures (a) and (b) show radial profiles along PIC-mesh nodes located at $z = 0.5$ cm of both the electron temperature and the electric potential, the latter taking as reference the value at the lateral wall. Figure (c) shows the axial evolution of plasma potential along the line of PIC-mesh nodes located at radius $r = 0.745$ cm, taking as reference the values at the backplate. Note that T_e^* is 7.9, 5.6 and 6.2 eV for cases RED, INJZ0 and INJR, respectively. Dashed lines in (a) and (b) represent the minimum and maximum radius of the thruster chamber.

Figure 6.36 shows the influence of injector location in the radial and axial profiles of the electron pressure. Both axial and radial profiles show that the overall level of pressure achieved in case INJR exceeds the other two. Comparing radial profiles we note that the pressure peak is moved towards the inner rod surface in both INJZ0 and INJR cases with respect to the location at the nominal case.

Additionally, we can notice that the stationary electron pressure close to the inner rod surface is much greater for the case with radial injection than for the other two.

Regarding the axial evolution, we note that the peak pressure axial location is rather similar for all cases. Nevertheless, the axial electron pressure drop is the highest for case INJR, which is coherent to the behavior shown in electron density.

6.4.3 Electron temperature and plasma potential

Figure 6.37 shows the effect of injector geometry in the electron temperature and plasma potential. Regarding the radial profile of the electron temperature, we note that the maximum temperature is achieved close to the inner rod surface for all the cases but that its magnitude is doubled for case RED with respect to the other two. Additionally case INJR exhibits a more homogeneous electron temperature than the other two close to this maximum. Moreover, all cases evolve similarly towards the lateral wall, reaching approximately the same T_e there.

Regarding the quasi-static electric potential, and similarly to what was mentioned in other parametric studies, its axial drop is proportional to the electron temperature (see Fig. 6.37c), which is not the case to the radial profile. Regarding the axial evolution we note that the potential drop is slightly greater than for the other two (in normalized values). In the case radial fields (see Fig. 6.37b) we note that there are significant changes between the cases. Although the electric field points towards the inner rod surface in all cases, there is a significant variation in their magnitude. This can be explained due to the differences in the electron temperature and density obtained. Figure 6.36a showed the radial profiles of electron pressure, in which we showed that the electron pressure drop towards the inner wall is greater than for the other two cases.

Close to the inner rod surface, electron pressure and electrostatic forces balance each other. As the temperature drop is much greater for case RED than for the other two, and the pressure drop is much greater for this case the electron density has to decrease faster towards the inner rod surface. However, in order to fulfill electron momentum balance, the increased electron pressure force has to be compensated with an increased electrostatic force. As the electron density decreases, the electric potential needs to drop significantly more for case RED than for the other two. Notwithstanding this difference, the radial electric fields are mild in the core of the thruster, and evolve similarly towards the lateral wall.

6.4.4 Ion acceleration

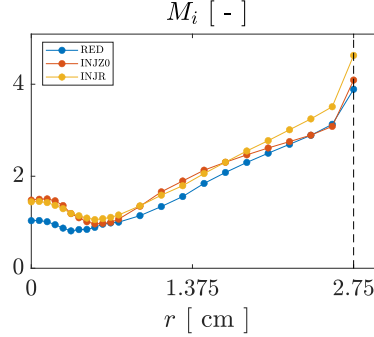


Figure 6.38: Effect of injector geometry in the radial profiles at the end section of the simulated plume. The dashed line represents the end radius of the simulated plume.

In order to compare ion velocities of the different injector geometries, figure 6.38 shows the radial profiles at the end of the simulated plume (i.e. PIC-mesh nodes $z = 4$ cm) of the local ion Mach number M_i .

Comparing the three simulations we note that the ion Mach number obtained for cases INJR and INJZ0, these are improved with respect to the nominal case, specially close to the symmetry axis, but also in the entire plume section. This typically indicates an improved thruster efficiency with respect to the nominal case, being the case with radial injection slightly more optimal.

6.4.5 Propagation and absorption of electromagnetic waves

As a consequence of the different plasma density map, injector location has also an effect in the electromagnetic propagation and absorption properties of the plasma, since it modifies significantly the electron density and collisionality. Figure 6.39 shows the influence of injector propagation in the CMA regions in the plasma, the Poynting vector and the power absorption density maps.

6.4.5.1 CMA regions

Given the enhanced electron densities featured by cases INJZ0 and INJR with respect to case RED, their corresponding CMA diagrams, shown in figures 6.39b and 6.39c, exhibit no propagating channel close to the inner rod surface. This is a major change in the topology of wave propagation. Upstream the ECR, this leads to the absence of regions VI and VII close to the inner rod surface in the vicinity of the dielectric window for cases INJZ0 and INJR and downstream the ECR region, it results in the disappearance of the low density “tube” for EM wave propagation close to the inner rod. The result is a dominant region V after the resonance until further downstream, extending in both cases until the end of the simulated plume.

6.4.5.2 EM wave radial electric fields and Poynting vector

As a result of this modification in the plasma density and thus the CMA diagram, the Poynting vector, shown in figures 6.39h and 6.39i, it cannot flow through that “tube” and its magnitude decreases rapidly after the ECR location for all the radius for cases INJZ0 and INJR. Consequently, the EM wave electric fields that are again dominated by its radial component, represented in figures 6.39e and 6.39f, exhibit a significant decrease close to the inner rod for these two cases. Following the trends described in all the other simulations, these fields intensify again at the propagating region III in the vicinity of the UHR. Additionally, the intensity of the Poynting flux increases for these cases in the path that goes from the dielectric window towards the intersection between the lateral wall and the ECR.

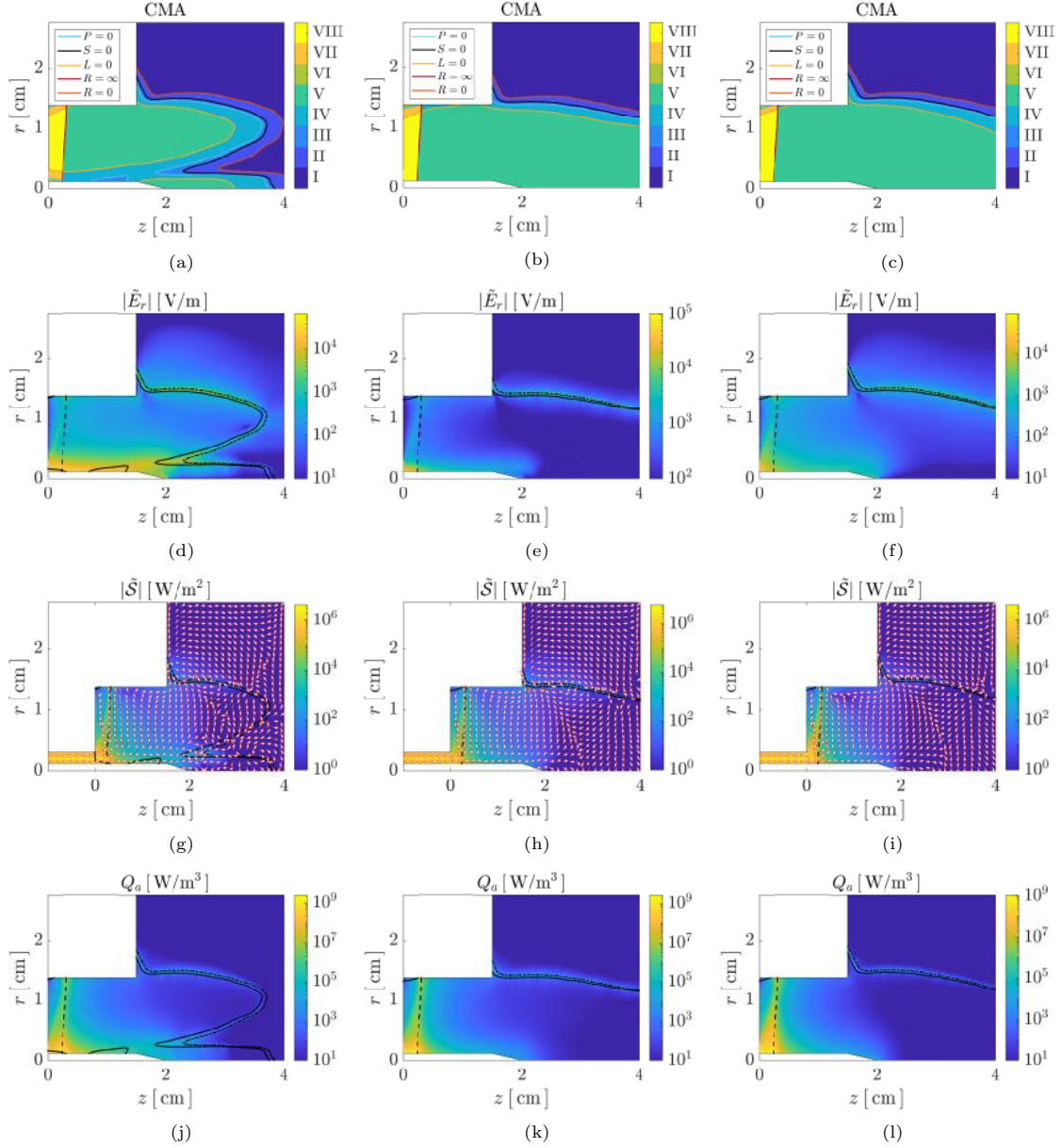


Figure 6.39: Figures (a), (b) and (c) show the CMA regions in the plasma; (d), (e) and (f) show the dominant component of the EM wave electric fields; (g), (h) and (i) show the Poynting vector magnitude and direction and (j), (k) and (l) show the corresponding power absorption density maps. From left to right, we show cases RED, INJZ0, and INJR. Figures (a)-(c) include boundary surfaces as cutoffs (i.e. $P=0$ (cyan), $R=0$ (red), and $L=0$ (ocher)) and resonances (i.e. $R=\infty$ (maroon) and $S=0$ (black)). From (d)-(l) the ECR (dashed), the critical density loci (solid), and the UHR (dash-dotted).

6.4.5.3 Power absorption

The behavior of power absorption density maps are consistent with the evolution of the Poynting flux vector in the domain. Note that the power absorption takes place in the regions where the Poynting flux flows through and there is sufficient electron density. Comparing the different cases, we note that apart for the extension of power absorption close to the inner rod surface of case RED, absent in cases INJZ0 and INJR, the main difference between the maps is the enhanced homogeneity obtained in the radial direction along the ECR for case INJR. This may explain the more homogeneous character of the radial electron temperature profile, shown in §6.4.3. Notwithstanding this, the profiles of power absorbed density are robust with different injector geometries, showing high resemblance between all cases with a dominant absorption taking place at the ECR region.

6.4.6 Thruster performances and energy usage

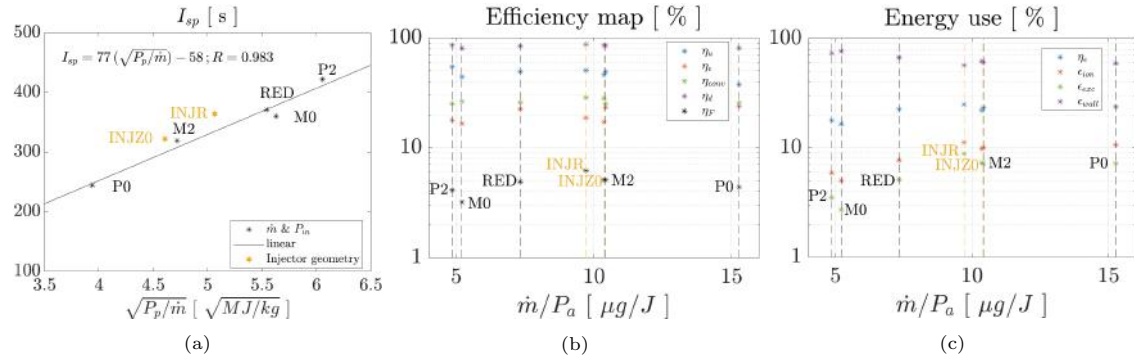


Figure 6.40: Maps of (a) specific impulse, (b) thruster efficiencies and (c) energy use as a function of absorbed power and mass flow rate, including cases of the parametric input power and mass flow rate. Cases with different injector geometry are highlighted.

Figure 6.40 shows the influence of injector location on (a) the specific impulse, (b) the thruster efficiencies and (c) the usage of power. The comparison is made with respect to the operational points of the nominal design discussed in the parametric investigation on mass flow rate and input power, highlighting in other the cases of modified injector geometry. We note that cases M2 and INJZ0 present almost the same ratio of absorbed power to mass flow rate. Comparing these two cases, there are no significant differences in terms of performances between the two injector locations, showing the same overall thruster efficiency (i.e. 5.1%) and similar partial efficiencies. This occurs even despite the fact that case INJZ0 shows a minor improvement in the specific impulse relative to the power used to accelerate the different species. Overall, case INJZ0 provides with no significant advantages in terms of performance, as an equivalent operational point of the nominal design (i.e. M2) provides with similar performances.

However, the case of radial injection is completely different. We note that a modification in the radial injector leads to improved overall thruster efficiency of a 20% relative to the nominal case, from 5.1% to 6.2%. This is a result of the improvements obtained with the use of a radial injection in the energy, utilization, divergence and conversion efficiencies. This improvement can also be visualized in Fig. 6.40a, where this case shows a significantly higher specific impulse for the amount of power used for acceleration purposes.

Figure 6.40c shows that for case INJR, the resulting wall losses are significantly decreased, from a 67.3% of case RED, to a 56.9%. This is a result of enhanced usage of energy, increasing the ionization and excitation losses and also that provided to accelerate the different species. As a result we can conclude that radial injection outperforms the axial injection alternatives.

6.5 Sensitivity analysis on the anomalous transport

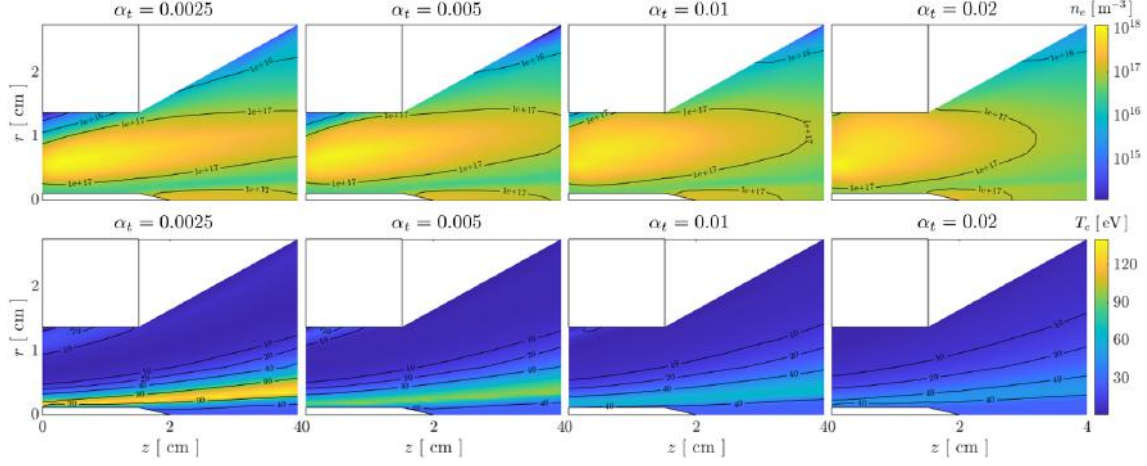


Figure 6.41: Effects of anomalous transport coefficient on the electron density and temperature.

A crucial model parameter, as explained in Chapter 5 is the anomalous transport coefficient α_t . In the electron fluid model used, this parameter has a contribution to the electron momentum equation, often denoted as α_{tm} and also a term contributing to the heat flux equation, denoted as α_{tq} . In principle, these two parameters are different. However, for the sake of simplifying the analysis, both parameters are taken to be equal to a single anomalous transport coefficient α_t .

Adequate selection of the value of α_t is still unascertained to this date, since there is no validated model capable explaining the anomalous cross-field diffusion featured in magnetized plasma discharges. Therefore, in order to understand the influence of anomalous transport on the estimated thruster performances and plasma properties, a sensitivity analysis to α_t was carried out with respect to simulation RED for fixed input power and mass flow rate. The analysis is performed for $\alpha_t \in [0.0025, 0.02]$ in order to observe the main effects on the solutions. Note that further details on the influence of the anomalous diffusion coefficient are provided in Chapter 9. Cases with no anomalous transport resulted in unphysical electron temperatures and therefore have been disregarded from this study.

In Fig. 6.41 the evolution of the electron density and temperature for increasing anomalous transport coefficient is shown. In general, the increase in anomalous transport coefficient enhances cross-field diffusion, increasing perpendicular mass and energy transport and smoothing the perpendicular gradients of plasma properties and variables as the electron density and temperature or the plasma electrostatic potential. As can be seen, the effect on the electron temperature is greater than that on the electron density in the range investigated. The maximum electron temperature decreases from 140 eV to 49 eV by increasing α_t one order of magnitude. However, the influence of modifications of the anomalous transport saturated for the maximum electron temperature whilst some effects in the plasma density could still be identified, as comparing n_e of cases $\alpha_t = 0.01$ to $\alpha = 0.02$. This suggests that in the regime of the reference simulation, for $\alpha_t \sim 10^{-3}$, variations lead to changes fundamentally in terms of T_e , while, for $\alpha_t \sim 10^{-2}$, start to become more evident in the electron density.

The main results of the sensitivity analysis in terms of thruster performance figures, discharge temperature and the different contributions to the total energy balance in the thruster are summarized in Tab. 6.3.

In terms of overall thruster performances (overall thruster efficiency, specific impulse, and thrust produced) the behavior is non-monotonic with α_t without exhibiting significant changes. The increase in plasma density close to the region of maximum power absorption (i.e. close to the

α_t [-]	0.0025	0.005	0.01	0.02
I_{sp} [s]	386	379	377	385
F [mN]	0.7567	0.7425	0.7389	0.7559
F_e [mN]	0.3045	0.2497	0.2123	0.1801
F_i [mN]	0.4034	0.4433	0.4732	0.5115
F_n [mN]	0.0488	0.0494	0.0534	0.0644
$I_{i,\infty}$ [A]	0.0707	0.0734	0.0759	0.0765
$T_{e,max}$ [eV]	140.7	101.4	67.7	49.2
P_a [W]	29.26	28.84	28.00	27.15
η_F [-]	0.0489	0.0478	0.0488	0.0526
η_{prod} [-]	0.6811	0.6210	0.5340	0.4114
η_u [-]	0.4813	0.4998	0.5168	0.5207
η_e [-]	0.2337	0.2243	0.2162	0.2316
η_d [-]	0.8645	0.9098	0.8995	0.8519
η_c [-]	0.1598	0.1782	0.2143	0.2549
ϵ_{ex} [-]	0.0250	0.0301	0.0382	0.0505
ϵ_{ion} [-]	0.0400	0.0476	0.0601	0.0820
ϵ_{wall} [-]	0.7099	0.7060	0.6917	0.6453

Table 6.3: Thruster performances and energy usage distribution for different values of both momentum and heat flux anomalous transport coefficients.

inner rod) has another effect and it is to increase power reflection as the impedance jump between coaxial and plasma is increased. This leads to an increased reflection ratio, and a slightly lower absorbed power.

As mentioned before, for higher α_t values, the electron temperature is smoother in the perpendicular direction. This leads to a larger volume of electrons with $T_e > 15.2$ eV (i.e. the ionization energy for singly charged xenon ions). As a consequence, the utilization efficiency of the thruster is improved. This can be observed also in the power used for ionization (i.e. ϵ_{ion}).

The increase cross-field transport leads to an increase on the number of ions reaching the walls, and thus, being recombined. As a result, the production efficiency decreases.

6.6 Concluding remarks

In this chapter the ECRT simulation model shown in chapter 9 has been utilized to analyze the effects on thruster performance and the plasma discharge of both the thruster operating point and modifications on thruster design such as the ECR location or the injector geometry. The main findings regarding neutral and plasma dynamics and EM wave propagation and absorption in the thruster chamber and the near plume have been discussed.

Regarding the operating point, the energy per particle (P_a/\dot{m}) is observed to be a key parameter driving thruster performance. It determines the temperature of the electrons which affects considerably the ionization rate, acceleration, but also the wall losses. In [57] two principal factors were identified in the reference case undermining thruster performance: (i) the large heat losses at the walls (around 65%) and (ii) the poor utilization values. Out of these factors, both are highly influenced by the energy per particle, the former being the most limiting for this thruster. Here, it was shown that the wall losses cannot be decreased by changing the thruster operating point since these are mainly driven by SEE emission, whose yield saturates almost completely for all the operating points explored. This occurs as a result of the electron temperature near the wall being greater or equal than half the crossover energy of the material. This losses result in limitation of the power used to ionize the propellant, as well as to energize the plasma constituents for efficient expansion. As a result, the operating point is not capable of improving thruster performances

as the reference point is close to the optimal operating point of the model. Note that this point occurs for greater mass flow rates than those found experimentally. Design modifications may be required for thruster optimization, as the substitution of the wall material by one with a greater crossover energy, specially at the inner rod and at the backplate. This will lead to decreased SEE and reduced losses, thus increasing the energy efficiency of the thruster.

Modifications in the operating point resulted only in minor variations in the electromagnetic propagation and absorption properties of the thruster. The most significant effect found was the appearance of EM propagation regions III and IV close to the inner rod due to electron density depletion occurring for high energy per particle cases (i.e. M0 and P2).

Regarding the investigations carried out on the ECR location, two major findings were found. Firstly, displacing the ECR location downstream would move the principal absorption region downstream accordingly, while roughly maintaining the overall thruster performances. Only a 0.5% absolute decrease in the thrust efficiency is found in case ECR2 with respect to case REF, which is a result of the anomalous heat transport losses to the walls driven by the rise in applied magnetic field intensity. Second, that the case ECR0 can still absorb EM power in the vicinity of the UHR, with a different absorption mechanism and less robust, since the UHR location is determined by the plasma density (a plasma state dependent variable) contrary to the ECR, which is completely determined by the applied magnetic field and the excitation frequency. This case results in low plasma density and meager coupling efficiency of 18.1% with respect to the nominal 91.1% and a less deleterious than expected 2.7% overall thruster efficiency.

Concerning the propellant injection configuration, it was found that the radial injection alternative outperformed the axial ones. A 20% relative overall thrust efficiency improvement was found between both cases. The main factor driving this improvement was found to be the decrease in wall losses. A more homogeneous neutral density within the chamber caused higher density close to the absorption region. As a result, the increased neutral density results in enhanced ionization close to the inner rod, and higher plasma density is found in this region. For a fixed power absorption profile, this leads to a significant decrease of the electron temperature and thus SEE yield, which results in decreased wall losses.

The analysis on the anomalous transport coefficient performed for values of $\alpha_t \in [0.0025, 0.02]$ showed that at this level of anomalous transport no significant changes can be noticed in the overall thruster efficiencies. The main effect of increasing α_t is to smooth the electron temperature profile, and decrease the maximum electron temperature obtained in the discharge.

Chapter 7

Alternative propellants

This chapter covers an investigation carried out on the influence of the propellant species utilized in the operation of the ECR30 thruster. Coupled electromagnetic and plasma transport simulations obtained utilizing the nominal species (i.e. xenon) are compared to the two other alternative species: krypton and argon. The contents of this chapter are part of EP2's contributions to MINOTOR project.

7.1 Alternative propellant properties

Since the 1980s, electric propulsion (EP) has relied mainly on xenon as propellant for in-flight applications. While the propellant mass savings are significant, thus decreasing the cost of launch compared to chemical propulsion, the cost of the required high-purity xenon is too high (currently around 3 k€/kg). Furthermore, the demand of xenon for in-space applications has increased in the last 20 years and will continue to increase with the generalization of the use of EP. Altogether this has led to a significant rise in the price of xenon. This justifies the growing interest in the investigation of possible replacements.

In Tab. 7.1, we show the different properties of each propellant considered. The alternatives are listed based on their effect on different domains as thruster performance (e.g. atomic mass, ionization cross-section), propulsion subsystem performance (e.g. density, critical pressure) and industrial suitability (e.g. cost, abundance). The toxicity of these three gases is null, and that makes them all suitable for ground testing. The main motivation leading the extensive use of xenon in EP lies on its outstanding properties in these different domains. Its high molecular mass and low ionization energy makes this species an excellent candidate in terms of thruster efficiency. Furthermore, the propellant is suitable for ambient storage and it is not toxic. Additionally, in the case of ECRT, it is acceptable that the level of purity of xenon is not as high, thus leading to a lower cost.

The main competitor to xenon is krypton due to its similar properties regarding thruster performance and its lower cost compared to that of xenon (from 2500 €/kg to 500 €/kg). However, as there is no natural krypton source: the extraction is performed by separation from liquid oxygen, and the cost remains relatively high. Krypton was identified by the MINOTOR consortium as the alternative propellant of highest interest for the project. Another alternative propellant is argon, which is expected to provide poorer performances compared to xenon but its abundance makes its cost almost three orders of magnitude smaller (from 2500 €/kg to 4 €/kg).

Based on the activities of the MINOTOR project partners (SAFRAN, ONERA), it was decided by the Consortium that propellants with high chemical activity were undesirable, as it is the case

for iodine, air (N₂, O₂, and derived compounds), etc. Based on the poor performances reported by other groups [127] on water based ECRTs, water was also eliminated from the list of alternatives.

Consequently, the following candidates are considered as alternative propellants in the present analysis:

Propellant	Molecular mass [amu]	Ionization energy [eV]	Scarcity	Cost
Xenon (nominal)	131.3	12.1	High	High
Krypton	83.3	13.9	Medium	Medium
Argon	39.9	15.8	Very low	Very low

Table 7.1: List of alternative propellants and their main characteristics.

The simulations shown and discussed in this document take into account the mass/charge ratio of each propellant for the particles in the PIC algorithm, and the ionization energy and excitation cost (not shown in the table) in the electron energy equation.

7.1.1 Collisions and interaction rates

There are different types of collisions to take into account when simulating the plasma of a EP thruster with Particle-in-Cell/fluid hybrid numerical schemes. It is necessary to distinguish between collisions occurring between electrons and heavy species and between heavy species. Besides intra-species collisions, we can classify the collisions modeled into:

1. Electron-heavy species collisions
 - (a) Elastic collision: $e + A \rightarrow e + A$
 - (b) Coulomb (elastic) collision: $e + A^+ \rightarrow e + A^+$
 - (c) Ionization: $e + A \rightarrow e + A^+$
 - (d) Excitation: $e + A \rightarrow e + A^*$
2. Heavy species - heavy species collisions
 - (a) CEX collision: $A + A^+ \rightarrow A^+ + A$

Every collision has an associated cross-section σ . The data for these σ can be found by quantum mechanics computations and/or experiments, and are recorded in existing data collections and databases as LXCAT¹ or published articles as ‘Atomic Data and Nuclear Data Tables’ and ‘Journal of Physical and Chemical Reference Data’. In the present work, the cross section information for the above propellants from LXCAT has been used.

Whilst for PIC models we can use directly the values of σ , for fluid models we need to compute the volume rates $R_{\chi,ij}$ of collisions ξ between species (i and j). The computation of this rates is performed as:

$$R_{\chi,ij} = \frac{1}{n_i} \int f_i \sigma |\mathbf{v}_i - \mathbf{v}_j| d\mathbf{v}_i, [m^3/s] \quad (7.1-1)$$

where the f_i are the species distribution functions, $\mathbf{v}_i, \mathbf{v}_j$ are the velocity vectors for each species, the frequencies are obtained as:

$$\nu_{\chi,ij} = n_i R_{\chi,ij} [N \text{ collisions}/s]. \quad (7.1-2)$$

After gathering the cross-section data from available resources, the models benchmark for the electron-heavy species rates has been performed assuming a Maxwellian distribution for electrons

¹<https://us.lxcat.net/>

(f_e) and negligible neutrals velocity. Thus,

$$R = \frac{1}{n_e} \int f_e(T_e) \sigma(|\mathbf{v}_e|) |\mathbf{v}_e| d\mathbf{v}_e. \quad (7.1-3)$$

As a result, integrating on the velocity, we obtain the rates as a function of the electronic temperature.

For xenon, krypton and argon, the essential collisions that need to be taken into account to formulate a relevant model are only electron-neutral collisions, ionization, excitation and Coulomb collisions. The integrated rates, using the cross section information from the LXCAT database, are plotted in Fig. 7.1.

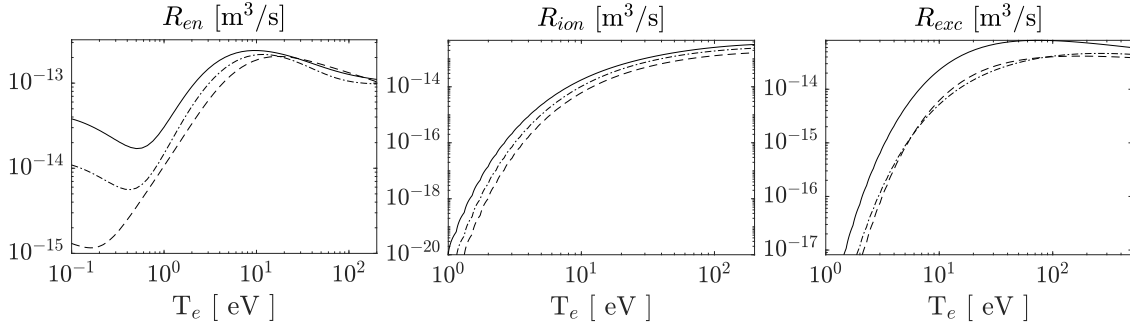


Figure 7.1: Collisional rates for xenon (solid), krypton (dashed-dotted) and argon (dashed).

For the case of Coulomb collisions, the collective electron to ion frequency for Maxwellian electrons is used so that

$$\nu_{ei} = n_e R_{ei}, \quad (7.1-4)$$

where

$$R_{ei}(T_e, n_e) = \left(\frac{T_e}{1\text{eV}} \right)^{-3/2} \left(9 + \frac{1}{2} \ln \left[\left(\frac{10^{18} \text{m}^{-3}}{n_e} \right) \left(\frac{T_e}{1\text{eV}} \right)^3 \right] \right) \cdot 2.9 \cdot 10^{-12} \text{m}^3 \text{s}^{-1}. \quad (7.1-5)$$

The collisional cross sections and the energy cost of inelastic collisions are structured and stored in a database system for its usage in HYPHEN. To maximize the accessibility by the user to the data, the propellant database is organized into folders and plain text files in json/yml format as follows:

1. “Species” data folder. This folder contains the elementary data related to each species, mass and inelastic processes and energy thresholds (ionization, electronic excitation, vibrational excitation, dissociation...). The data are separated by sections for each species and are contained in txt files.
2. “Binary collision” data folder. This folder contains the cross sections of the collisions between two particles of the considered species. and is structured as follows. Each species (Xe, Ar, Kr, as well as their ionized and excited versions, Xe^+ , Ar^+ , Kr^* , etc, as well as electrons e^-) has a dedicated folder. This species is considered as the first partner for a binary collision. Inside this folder, a full directory tree containing again all species exists. This second-level folders are considered as the second partner in the binary collision. Finally, inside this second-level folders, there are text documents for each type of collision between these two partners, which list their cross sectional data as a function of impact energy. This information is adapted from LXCAT and semi-empirical models found in the literature.

Currently, the database is functional for Xe, Kr, Ar, O_2 , N_2 , O and N and partial data for some reactions involving Ne and CO_2 . The present report is focused on the most promising candidates for alternative propellants of the ECRT, as identified above: Xe, Kr, Ar.

7.2 Simulations results

Using the model described in chapter 5 we have obtained coupled solutions of the coaxial ‘Big-Magnet’ ECRT developed by ONERA [26]. The case of xenon, published Ref. [57] is taken as the reference simulation of this study. The results shown are for stationary conditions, reached after several power absorption updates performed by the electromagnetic wave module.

7.2.1 Simulation setup

An sketch of the thruster is shown in Fig. 5.1 whose dimensions are described in Tab. 5.1. The applied magnetic field of this thruster (see Fig. 6.1b) creates a divergent magnetic nozzle. The location of the electron cyclotron resonance region is close to the back-plate, where the intensity of the magnetic field is 875 G, and is denoted in red. The electromagnetic domain is excited through a lumped port at the beginning of the coaxial, where the electromagnetic power is fed into the cavity through a dielectric window. The power accesses the thruster chamber and generates plasma currents that deposit power into the plasma, which are then used to ionize and energize the plasma. Then the plasma is accelerated throughout the plasma plume in the MN region.

Note the two domains used for these simulations shown in red for the hybrid module and in black for the electromagnetic module. The reason behind this choice relies on a numerical motivation. As can be noticed from the magnetic configuration of the thruster, shown in Fig. 6.1b, magnetic field lines are closely aligned with the thruster walls. In the simulations, perpendicular transport is insufficient to fill up with plasma the corner region above the last magnetic field line exiting the thruster chamber. This produces results with increased numerical noise in this region. Truncating the hybrid domain using a line nearly parallel to the last magnetic field line exiting the thruster chamber results in a significant improvement of PIC-related noise at the thruster exit.

As in previous chapters, the thruster walls are considered made of a perfect electric conductor (for the purposes of the wave module) covered by a thin layer of dielectric boron nitride (BN), taken into account in the plasma transport modules (PIC + electron fluid) as a dielectric material. The properties of BN regarding secondary electron emission are considered in the simulation. The outer boundaries of the domain are “free loss” surfaces where particles are simply removed.

Figure 6.1b also displays the magnetic field aligned mesh used by the electron fluid module, where white lines are magnetic streamlines and their perpendiculars are shown in black. A second mesh, of the structured type, is used for the heavy species PIC module.

Finally, the mesh requirements for the wave module are different than for the other two, requiring a higher concentration of elements close to the resonance regions. As a consequence, the EM-wave module requires interpolation to the other two meshes as well.

7.2.1.1 Geometry, applied magnetic field and operating parameters

The geometrical, applied magnetic field and operating parameters are those shown in Tab. 5.1. A fixed propellant mass flow rate \dot{m} is injected through an injection port as in figure 5.1 for all three simulations. A total input or forwarded power P_f electromagnetic power of 30 W is injected through the coaxial. The simulations prescribe the input power to the coaxial, so the total power deposited for the three simulations may vary (input minus reflected power; see Tab. 7.2).

7.2.2 Results

The following sections contain, in several plots, a summary of the steady-state simulations for each of the three chosen propellants, allowing the direct comparison from page to page. Each set of results corresponds to the self-consistent, converged simulation involving the PIC, fluid, and wave modules. The discussion of results is presented in Section 7.3.

7.2.2.1 Xenon

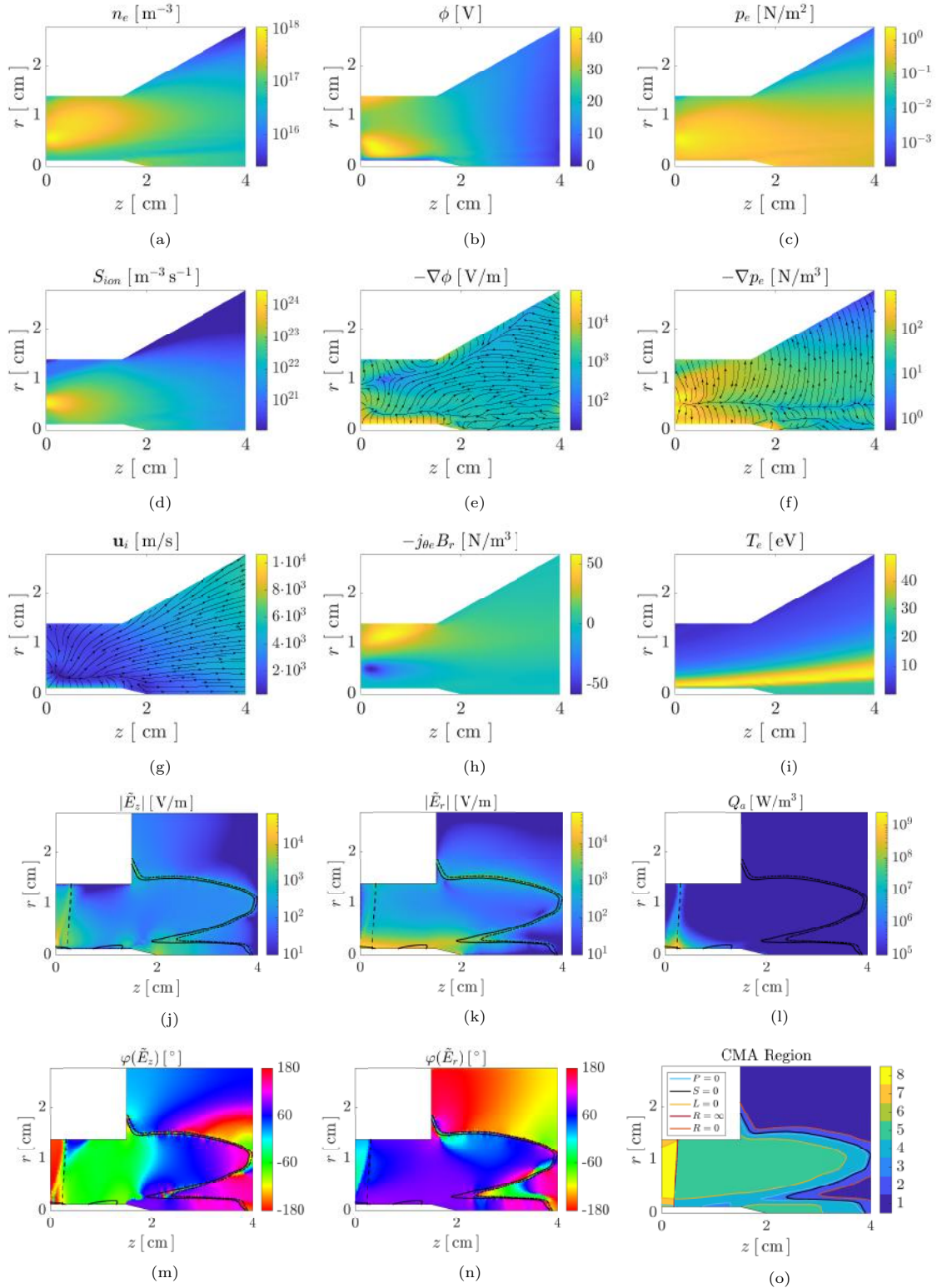


Figure 7.2: Principal simulation results using xenon as propellant.

7.2.2.2 Krypton

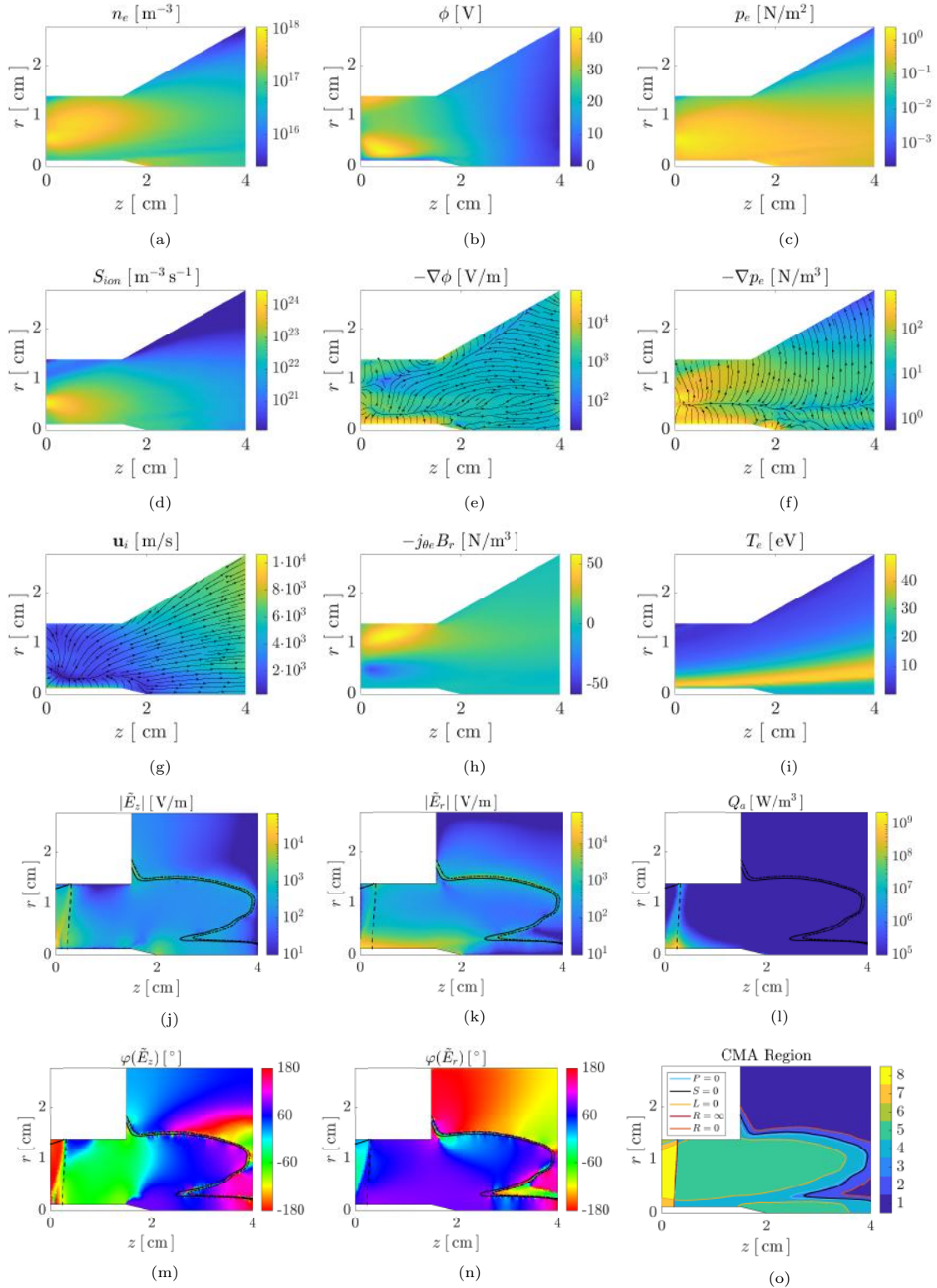


Figure 7.3: Principal simulation results using krypton as propellant.

7.2.2.3 Argon

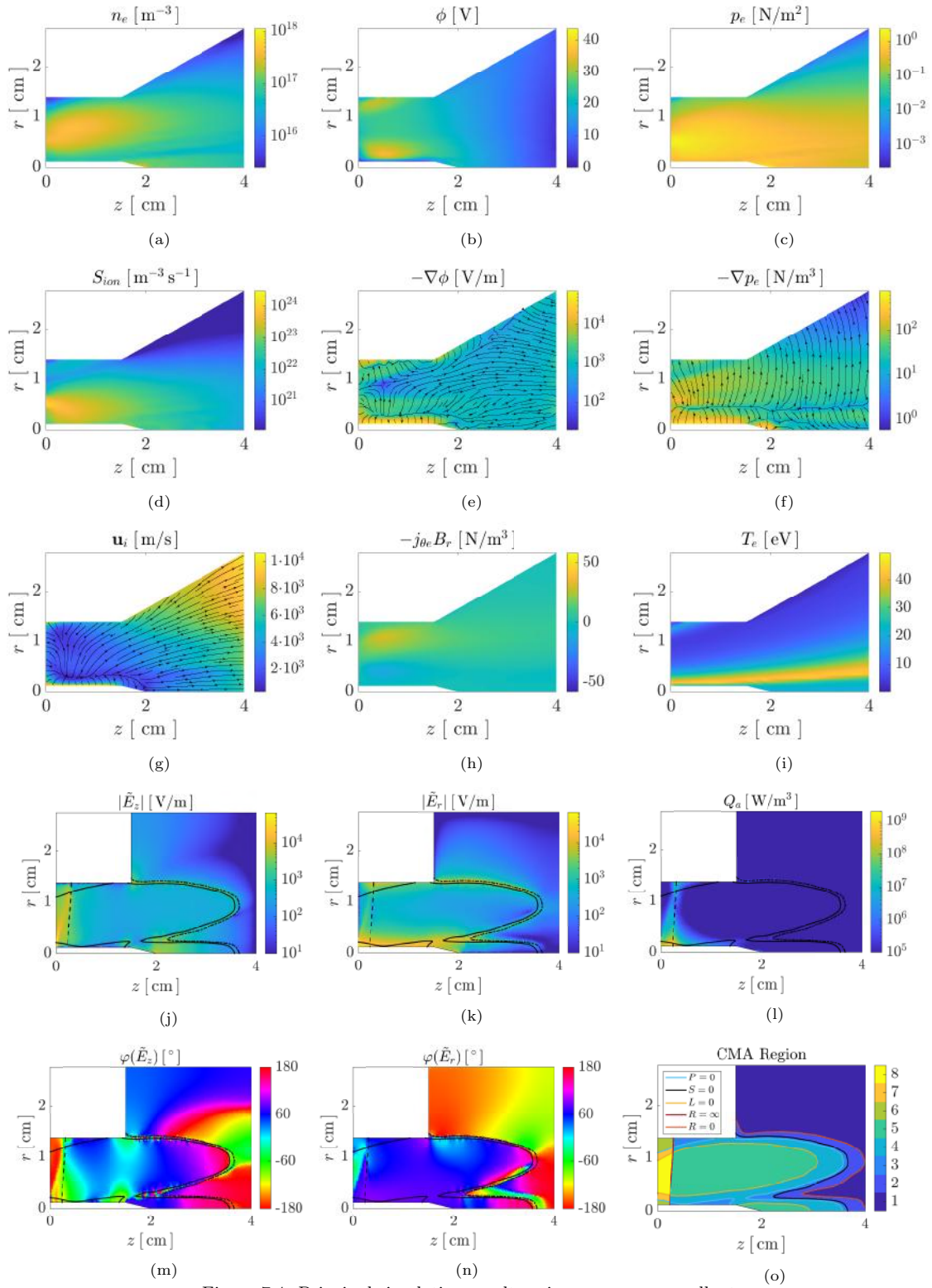


Figure 7.4: Principal simulation results using argon as propellant.

7.2.3 Thruster performances

The integrated thruster performances for the simulations using the different propellants are shown in Tab. 7.2.

Parameter	Name	Units	Xe	Kr	Ar
F	Thrust	mN	0.756	0.790	0.536
P_a	Absorbed power	W	27.1	26.5	27.5
I_{sp}	Specific impulse	s	385	403	274
I_i	Ion current	A	0.077	0.096	0.094
η_F	Thrust efficiency	%	5.1	5.9	2.6
η_u	Utilization efficiency	%	52.1	41.7	19.39
η_e	Energy efficiency	%	23.2	30.7	24.29
η_c	Conversion efficiency	%	25.5	25.3	23.74
η_d	Divergence efficiency	%	85.2	85.4	85.0
ϵ_{exc}	Excitation losses	%	5.1	2.8	4.9
ϵ_{ion}	Ionization losses	%	8.2	11.14	9.8
ϵ_{wall}	Wall losses	%	64.5	56.6	62.3
η_p	Coupling efficiency	%	90.7	88.3	91.8

Table 7.2: Thruster performances for different propellant species.

7.3 Discussion

The panels in the figures of previous sections show the similarities and differences between the three simulations with Xe, Kr, and Ar.

First and foremost, the similarity between the simulations with the different propellants is striking. As it can be observed, there are few qualitative differences in plasma density, electric potential, electron pressure and temperature, ionization rate, and ion velocity. Additionally, the absorbed power and the wave fields shows small variations among the three simulations. This suggests that the simulation procedure and the code are robust, and that the overall plasma response is quite independent on variations in quantities such as the mass/charge ratio, the cross sections, and the ionization and excitation costs. Notwithstanding this, some quantitative differences do exist, which are consistent with the expectations due to the variations in the defining characteristics of the propellants. These are discussed next:

1. The plasma density maximum is higher in the case of Xe than in the case of Kr than in the case of Ar. This is motivated by two effects. Firstly, the higher ionization cost of the latter drives the density down. Secondly, the lighter mass of the latter means a faster acceleration out of the thruster, again decreasing the plasma density. Note that, although Kr is much lighter than Xe, the plasma density is nearly as high as that of Xe. Contrary of what would be expected due to its higher ionization rate, this shows that the use of Kr does not harm the plasma production of this thruster. The Xe discharge exhibits a greater magnetic confinement (i.e. Hall parameter) as the electron collisional frequency is smaller than the other two cases. Thus, in this magnetic field configuration as the magnetic field increases transport to the top wall, a smaller magnetization due to lighter mass allows a more efficient acceleration and less losses to this wall (see Tab.7.2).
2. The electric potential drop in the thruster discharge chamber and in the simulated part of the plume region is larger in the Xe and Kr cases, where it is larger than in the case of Ar. The electric potential drop is responsible for the ion acceleration, and scales with the electron temperature, which is similar for the three cases albeit slightly larger in the Xe case. A higher potential drop is desirable, in principle, to increase the velocity of the generated plasma jet. The potential features two maxima, one near the central radius of the simulated

meridian section, and another close to the inner corner of the discharge chamber. The proposed explanation for this second maximum is the efficient electron confinement created by the applied magnetic field lines, which hinder electron transport from the central part of the discharge to this corner region. As ions are not similarly hindered by the magnetic field due to their larger mass, the electric potential responds creating this maximum to enhance electron transport to this region and maintain quasineutrality.

3. The differences in electron pressure are comparable to and related with the differences in plasma density. Noteworthy is that the location of the maximum electron pressure does not coincide with the maximum of electron temperature nor plasma density.
4. The ionization source S_{ion} displays a maximum roughly where the neutral injection port is located, i.e., where the neutral density is maximal. It should be noted that the particle density differs substantially for the neutrals, as the same mass flow rate in mg/s is injected for the three cases, but the atomic mass is different for each propellant. While not shown in the plots, the maximum neutral density is 1.5×10^{20} , 8.5×10^{19} , $5.5 \times 10^{19} \text{ m}^{-3}$ for Ar, Kr and Xe, respectively. Furthermore, due to the plasma magnetization decreasing in the sequence $\text{Xe} \rightarrow \text{Kr} \rightarrow \text{Ar}$, the ionization rate increases close to the coaxial core surface, where there is a higher neutral density enhanced by ion recombination. Additionally, it can be observed that in the sequence $\text{Xe} \rightarrow \text{Kr} \rightarrow \text{Ar}$, a second region of mild ionization appears near the top corner of the discharge chamber. This region appears due to the decreased plasma density there so that for a similar absorbed power provokes an increased electron temperature. The increase in the electron temperature rises the ionization rate in this region.
5. The electrostatic field appears as a result of the imbalance between the magnetic force and the pressure gradient in the momentum balance of electrons, which neglecting the small electron inertia and collisions is approximately:

$$\mathbf{0} \simeq -\nabla p_e + en_e \nabla \phi - en_e \mathbf{u}_e \times \mathbf{B} \quad (7.3-1)$$

The pressure gradient drives electron transport towards the walls as the pressure decreases in this direction due to ion recombination. At the coaxial core, the pressure gradient dominates the momentum balance in all three cases, so that the electric field has to compensate for this force. However, due to magnetic confinement of electrons, the plasma potential increases perpendicular to the magnetic field lines, away of the plasma bulk. This electrostatic field appears to decrease the flux of ions towards the regions of lower plasma density, in order to fulfill quasineutrality. The former effect is stronger close to the top corner of the thruster chamber the lower the atomic mass, thus giving rise to an electric field away from the wall, as happens for all simulations close to the coaxial core.

6. The ion velocity plot shows that the overall acceleration of the plasma produced by the thruster increases as the propellant mass is decreased as expected, reaching velocities of roughly 6, 8 and 10 km/s for Xe, Kr and Ar respectively, in the simulated region of the plume. It is relevant that this increase is due to the lower propellant mass and in spite of the lower potential drop developed by the plasma in the Ar and Kr cases.

Observe also that close to the antenna there is a high ion velocity directed against the antenna wall. This is a consequence of the large electric potential drop toward this surface, and is expected to drive the erosion of the antenna element that has been reported experimentally. Note that the appearance of electric field towards the top corner in Ar simulation results in an increased ion acceleration towards this region.

7. The magnetic axial force density $-j_\theta B_r$ is a relevant figure in the dynamics of the plasma in the thruster. It is indicative of the magnetic thrust force being generated by the device, as the thrust is essentially the reaction force to this force. Two major aspects are observed in these simulations. First, the overall strength of this axial force is similar for Xe and Kr, and

much lower for Ar. Secondly, the sign of this force depends on the sign of j_θ , which is mainly driven by the electron azimuthal current and in turn depends on the imbalance between electron pressure and electric field shown in the equation above. As a result, a positive axial force (i.e., accelerating) appears in the periphery of the plasma, which pushes the plasma out of the discharge chamber, and a negative axial force (i.e. decelerating) appears close to the antenna. This is inevitable, as the electron pressure decreases toward this inner wall, and is related with the maximum of the electric potential and electron pressure not being located at the axis ($r = 0$). In this regard, the presence of the antenna constitutes a major difference with respect to other electrodeless plasma thrusters which do not feature this obstacle for the plasma, such as the Helicon plasma thruster, and forces the displacement of the maximum to higher radii as indicated above. Comparing the simulations between Xe and Kr it is evident that although the maximum positive volumetric thrust generated is similar for both cases, the negative is more intense in the case of Xe. This implies a more efficient magnetic thrust is generated in the case of Kr. This is supported by the energy efficiency figure (see Tab. 7.2) .

8. Electron temperature is nearly constant along the magnetic field lines, indicating that an efficient along-field electron transport is taking place, and a less effective cross-field transport. A major peak of electron temperature appears in the magnetic lines that intersect the wave injection port (i.e., the coaxial channel). The suggested explanation for this observed behavior is the higher deposition of wave power in this region (as inferred from the Q_a plot), which raises the electron thermal energy in these magnetic lines. This leads to an efficient ionization in this part, but as the plasma is strongly confined from the coaxial core, the heating is excessive for the low plasma density in the region. As a result, the electron temperature rises significantly. It is noteworthy that this feature of the plasma discharge is present and consistent in all three simulations, with Xe, then Kr, then Ar showing the highest T_e peak.

Additionally, a small temperature increase can be observed near the inner corner of the discharge chamber in the Kr and more notably in the Ar case. This a consequence of the same principle as explained in previous paragraph, added to an increase of the power deposition in this area from the case of Xe to that of Kr and specially to that of Ar.

9. Finally, the last set of plots regarding the wave fields are discussed simultaneously. This set of plots contains the magnitude and phase of the axial and radial wave electric fields, \tilde{E}_z and \tilde{E}_r , the absorbed power Q_a , and the CMA diagram. The fields superscript comes from the modal decomposition both in time and azimuth as:

$$\mathbf{E} = \Re[\tilde{\mathbf{E}} \exp(-i\omega t + im\theta)], \quad (7.3-2)$$

so that they correspond to the mode of temporal frequency ω and azimuthal wave number m (in this case $m = 0$, the case relevant for ECRT's). The azimuthal component of the electric fields are not shown here, since they are negligible compared to the components in the zr plane.

The plot showing CMA regions explains the different propagating regions that exist in the plasma domain, following the nomenclature of Stix [27]. The different regions are separated either by resonance surfaces ($S = 0$, $R = \infty$) or by cutoff ($P = 0$, $L = 0$, $R = 0$) surfaces. The location of these lines depends on the applied magnetic field strength, B , which is identical for all three simulations, but also on the plasma density n , which is part of the dynamic plasma response. The ECR resonance (denoted as $R = \infty$ or the dashed black line) is clearly identifiable near the thruster chamber back-plate. It can be observed that the peak of Q_a corresponds to this line, as expected, and concentrates close to the coaxial port from where the power is input into the domain. Furthermore, in this simulations it can be noticed that the power absorption major contribution is due to the radial wave electric fields that appear in the vicinity of the ECR. The location of the maximum power absorption being at the ECR

is due to the increase in the refractive index there, maximizing absorption. However, the fact that the location is close to the coaxial core is motivated by a decrease of plasma density in the vicinity of the coaxial core. This decrease is such that the plasma is underdense (i.e. $\omega_p = e^2 n_e / \epsilon_0 m_e < \omega$) so electromagnetic waves with intense radial electric field component can propagate downstream the ECR resonance, as can be noticed in Figs. 7.2k, 7.3k and 7.4k. However, note that for the major part of the plasma bulk after the resonance, the propagating region is 5, where all electromagnetic waves are evanescent. This results in the absence of electromagnetic fields there and thus no power absorption. Close to the top wall for the case of Ar, the plasma density decreases (see Fig. 7.4a) so that a region of propagation appears (see Fig. 7.4o, resulting in radial electric fields appearing there (see Fig. 7.4k) and thus power absorption (see Fig. 7.4l).

The transitions $S = 0$ and $P = 0$, associated to the upper hybrid resonance and the electrostatic cutoff, can be identified by dashed-dotted and solid black lines, correspondingly. Note that the axial and radial electric fields exhibit maxim also at regions of propagation between these secondary surfaces, where the waves are allowed to propagate. A major difficulty in the simulation of the wave fields corresponds to regions close these lines, where it is necessary to refine the underlying mesh to resolve the fine structure close to $S = 0$ and $P = 0$, specially for the electric fields phase (compare Figs. 7.2m, 7.3m and 7.4m).

Overall, the differences between the three simulation regarding the wavefields and the absorbed power are very mild. At these excitation frequency, the wave response depends mainly on the electron population, whose differences are shown main in terms of the plasma density exhibited. Due to the slight variations in plasma density, the results are extremely similar independently on the propellant type.

Regarding overall performances of Tab. 7.2, it is noted that the figures of merit are expectedly larger for Xe and Kr, and lower for Ar. This is evident in the thrust efficiency, thrust force and specific impulse. In these simulations, Kr has a slightly larger value for these three parameters than Xe. The propellant utilization increases the lower the ionization energy required, showing that Xe has the better plasma production efficiency. Still, only about 50% of the mass flow rate leaves the thruster as ions. This is one of the major contributors to thrust efficiency loss. However, although other figures as the conversion efficiency or the divergence are very similar for all three cases given the similar electron pressures and magnetic fields for all cases, the explanation of Kr being more efficient than Xe lies in the energy efficiency. The energy efficiency is significantly greater for Kr than for Xe. Furthermore, note that the excitation losses are higher for xenon, then for Ar and the lowest for Kr, as could be expected from the excitation rates shown in Fig. 7.1 for electron temperatures in the order of 10-40 eV.

In the case of Ar it can be noticed that a poor utilization efficiency is achieved due to the high ionization energy and the low residence time resulting from its light mass. This, added to the high excitation losses, results in an inefficient propellant for these purposes. However, for a mission limited in cost-budget, the performances may still be considered acceptable, as they are half those of Xe.

Kinetic and thermal power fluxes to the material walls of the thruster are the dominant loss mechanism in the device. With this variable, however, there is not a clear trend with propellant mass, with higher wall losses in the case of Xe then Ar then Kr. Ion current is higher for Kr than for Xe as ions accelerate faster in shorter distances as they are lighter. It is also slightly greater than that of Ar due to the greater thrust exhibited by Kr, and despite the much lower mass of Ar.

Likewise, in terms of power reflection there is a slight change comparing Xe and Ar to Kr, but there is not a clear trend with propellant mass. It should be noted that power reflection is not a loss mechanism *per se*, as the reflected power can be managed by a matching network to be returned to the plasma.

Overall, based on the simulation results, Kr has shown the best performance among all propellants, slightly greater than that of Xe, in terms of thrust efficiency η_F , while for Ar, the efficiency is almost 50% of that of Xe.

7.3.1 Thruster modifications

The simulations and the analyses carried out in this work provide information on the response of the baseline thruster design to different propellants. As it has been shown, the differences in the operation with each propellant are quite mild, with the plasma and electromagnetic field being only quantitatively different from each other.

The main conclusion that can be extracted is that Xe and Kr offer similar propulsive performance figures. Contrary to what could be expected in terms of smaller residence time and higher ionization cost (and thus a less efficient plasma production), Kr has shown a better balance of the physical mechanisms driving the thruster performance. This is a combination of several facts. Firstly, a more adequate balance between magnetization and atomic mass resulted in decreasing plasma transport and losses to the top wall. Secondly, a more effective magnetic thrust with a lower “negative” maxima, lead to a greater power flux at the plume boundaries and thus a significantly greater energy efficiency. Last but not least, a lower excitation loss has allowed for a more efficient use of the deposited power. Altogether, has resulted in defining Kr as a clear competitor to Xe when used in this configuration of ECRTs.

Determining the thruster design changes necessary to optimize it to run with Kr or Ar in the face of changes that are seen to depend directly on propellant properties that cannot be modified is nevertheless a difficult task from the information available. There is, however, one aspect that can be partially controlled with the thruster design: the propellant utilization. This is one of the efficiency parameters that suffers a greater and more consistent variation with the propellant type. It is evident from the results that the lighter propellants display a lower propellant utilization, and this is in part due to the larger ionization mean free path of the lighter (and faster) neutrals that are injected in the chamber. Two design changes are therefore recommended to mitigate this problem and therefore raise the propellant utilization:

1. Improve the injector of neutrals, to promote a longer residence time in the chamber, e.g. by injecting radially or even towards the rear wall. This measure will likely also improve the performance with Xe.
2. Extend the length of the thruster to allow more neutrals to be ionized within the discharge chamber. This, however, comes at the cost of increasing the wall losses in the device, so a trade-off must find the optimal thruster length for each propellant type.

7.4 Concluding remarks

The simulations show that differences in the plasma response are only mild between the xenon, krypton and argon cases. Xe and Kr outperform Ar in terms of thruster efficiencies. Notwithstanding this, the differences in performance are not large, and neither of these propellants are ruled out as candidates for propulsion with the ECRT. Krypton has shown slightly better performances than Xe for this configuration. This added to other advantages in terms of cost and availability, makes krypton a great alternative candidate propellant. Suggested adaptations of the thruster to the alternative propellants include enlarging the ionization chamber and relocating/re-engineering the neutral injector to maximize the neutral residence time in the chamber.

Further work must compare and validate these simulation results against experimental data. Additionally, the values of cross-sections and species modeling should always be revisited to improve and add complexity and detail to the model.

Chapter 8

ECRT Scale-up study

This chapter covers an investigation on the scaling of the thruster, comparing the thruster performances of a scaled-up high power ECRT prototype developed by ONERA to that of the reference thruster investigated in previous chapters. The objective is then to analyze the influence of scale on the prototype plasma properties and performances utilizing the coupled model developed during this thesis. The contents of this chapter are part of EP2's contributions to MINOTOR project.

8.1 Thruster scale-up configurations

The low power coaxial ECRT prototype ECR30 [11, 12, 51, 52, 56–59, 61, 95, 123, 128] investigated up to this point is utilized as the reference configuration in this study, and as the baseline for the comparison and discussion of the scaled-up 200 W ECRT. The latter version design and geometry is chosen by ONERA. The next section details the simulation setup, and section §8.1.2 presents the simulation results.

8.1.1 Simulation setup

The parametric sketch applicable to the two coaxial ECR thrusters is shown in Chapter 5, Fig. 5.1; the dimensions for each thruster configuration are described in Tab. 8.1. The applied magnetic field of the 30 W and 200 W thrusters, shown in Fig. 8.1a and 8.1b respectively, creates a nearly axial high-field region inside the discharge chamber and a divergent magnetic nozzle outside of it (i.e. magnetic beach). The ECR location for the nominal operation frequency of 2.45 GHz is close to the backplate, where the intensity of the magnetic field is 875 G, and is denoted in red. Neutral Xe gas is injected through an injector port, located inside the discharge chamber. The injector location is different for the 30 W and 200 W thrusters. In both cases, the electromagnetic power is fed via a coaxial line and through a dielectric window. In the simulations, the excitation of the electromagnetic fields is carried out with a lumped port located upstream of the coaxial cable. The power accesses the thruster chamber and induces high-frequency plasma currents that interact with the fields and eventually result in power absorption in the plasma. The plasma transport inside and outside of the device are essential processes to understand thruster performance and plasma acceleration.

Figures 8.1a and 8.1b display the simulation domain of HYPHEN modules for each thruster. The simulation domain in the 200 W thruster is larger and features a longer plume domain, including the lateral plume region right outside of the thruster chamber. Results show that in these low-density regions the number of macroparticles per cell decreases substantially, as expected. However, it was

deemed still sufficient for a proper description in the cases of the ECRT 200 W. The reference 30 W simulation has a shorter plume domain and leaves out of the transport simulation domain the corner region outside of the thruster domain.

The thruster walls are metallic walls covered by a thin layer of dielectric boron nitride (BN). In the transport modules, these walls are correspondingly modeled as dielectric walls with secondary electron emission yield. In the wave module, these walls are considered perfect electric conductors. The outer boundaries of the domain are “free loss” surfaces where particles are simply removed, and natural boundary conditions are used for the wave module.

Figures 8.1a and 8.1b also display the magnetic field aligned mesh (MFAM) used by the electron fluid module, where white lines are magnetic streamlines and their perpendiculars are shown in black. A second, structured mesh is used in the heavy species PIC module. Finally, the mesh requirements for the wave module are different than for the other two, requiring a higher concentration of elements close to the resonance regions. As a consequence, a third, finer unstructured mesh is used in the EM module.

Parameter	Name	Units	ECRT 30 W	ECRT 200 W
l_r	Coaxial core length	cm	2	4
r_r	Coaxial core radius	cm	0.115	0.2
L	Outer conductor length	cm	1.51	4
R	Outer conductor radius	cm	1.375	3.5
L_p	Plume length	cm	2	8
R_p	Plume length	cm	2.75	10
z_{inj}	Injection surface center z	cm	0.0	0.4
r_{inj}	Injection surface center r	cm	0.5735	3.5
t_{inj}	Injection surface width	cm	0.229	0.8
\mathbf{n}_{inj}	Injector surface normal	-	$\mathbf{1}_z$	$-\mathbf{1}_r$
r_{coax}	Coaxial cable outer radius	cm	0.3	0.59
$L\omega/c$	Thruster electric length	λ	0.1633	0.3267
A/V	Area-volume ratio	m^{-1}	228.6	85.6
L/R	Aspect ratio	-	1.455	1.143

Table 8.1: Geometric parameters for the 30 W and 200 W thrusters.

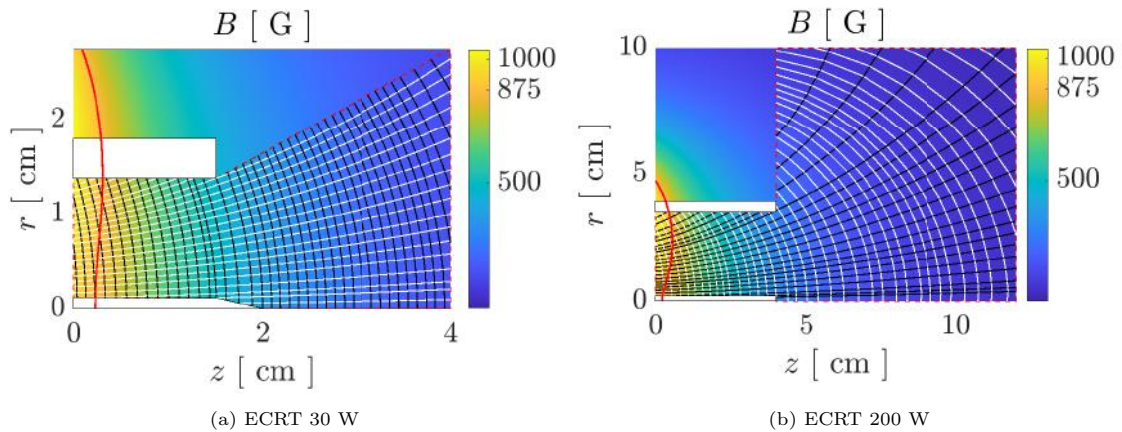


Figure 8.1: Applied magnetic field geometry together with MFAMs of the 30 W and 200 W thruster simulations. Magnetic streamlines are shown in white and their perpendicular in black compose the MFAM.

As stated above, the injector ports for the 30 W and 200 W thrusters are different. The

main difference is their location in the chamber. Table 8.1 shows generalized injector geometrical parameters z_{inj} , r_{inj} , t_{inj} , and \mathbf{n}_{inj} . The center injection port of width t_{inj} is located at (z_{inj}, r_{inj}) coordinates, being $z_{inj} = 0$ the backplate location. The normal vector \mathbf{n}_{inj} to the injector surface points in the direction of the propellant injection. The injection in the 200 W ECRT is performed radially inwards at the outer conductor close to the top of the backplate. This configuration is not shown exactly Fig. 5.1, which represents the reference injection configuration (i.e. that of the 30 W prototype).

A consequence of this thruster scale-up is that the area-to-volume ratio of the thruster differs by a factor three between the two thruster models. This ratio is expected to affect to a large extent the wall losses and the efficiency of the device. The electric length (i.e. the number of wavelengths in vacuum per length of thruster) has been doubled with the new thruster, since the operating frequency is the same. However the value is still smaller than unity. The influence of this parameter is not straightforward to analyze, as the wavelength in vacuum and in the plasma can differ by orders of magnitude. Finally, observe that the aspect ratio L/R is also different in the two thruster models. This ratio is expected to influence the propellant utilization efficiency, by enabling more or less propellant to be ionized within the discharge chamber before the neutral atoms escape from it. Another, minor difference between the thrusters is that both coaxial core and outer wall extend for the same length in the 200 W version, while the former is larger than the latter in the 30 W thruster.

Parameter	Name	Units	ECRT 30 W	ECRT 200 W
\dot{m}	Xe mass flow rate	mg/s	0.2	0.6881
P_f	Power input	W	30	200
P_f/V	Input power to volume ratio	W/cm ³	3.37	1.30
P_f/\dot{m}	Input power to mass flow ratio	J/mg	150	290.7

Table 8.2: Operational parameters for the 30 W and 200 W thrusters.

The operational parameters of the thruster for the two thruster simulations are shown in Tab. 8.2. The input electromagnetic power injected through the coaxial cable is used to label the two thruster configurations. In the simulations, the input power is fixed to this value, and the deposited power is computed as a part of the solution. The power that is not deposited in the plasma is reflected power that comes back through the coaxial cable. Both thrusters use an excitation frequency of 2.45 GHz. The propellant mass flow rate increases by a factor 3.5 approximately in the ECRT 200 W thruster. In all cases, we fix the neutral injection to a Maxwellian distribution of 0.02 eV temperature and 300 m/s velocity. The injected power to volume ratio is smaller in the ECRT 200 W thruster. However the power to mass flow rate ratio is roughly doubled. Regarding the anomalous transport coefficient used, in absence of more information about the 200 W thruster experimental data to carry out a fitting of the coefficient, it was decided to fix $\alpha_t = 0.02$ for all simulations.

8.1.2 Simulation results

The following pages contain the simulation results. Figures for the various plasma profiles are included for each simulation case described next. Results are shown for stationary conditions, reached after sufficient simulation time with all modules coupled together. The coupled solution of the ECR30, the 30 W ECRT developed by ONERA is shown as the **Case 1** simulation. The first simulations of this 30 W ECRT were shown in Ref. [59]. This is used as the reference for the comparison of the scaled up, 200 W thruster. **Cases 2 to 4** correspond to the 200 W scaled-up thruster. **Case 2** simulates the nominal proposed configuration described above, with the nominal operating parameters. The other two cases feature variations with respect to the nominal 200 W case, to explore certain aspects of the scale-up process. **Case 3** increases the coaxial cable outer radius by a factor of 3. **Case 4** (plots not shown; only performances in table 8.3) is similar to

simulation Case 3, but fixes the power deposited to be the same as the one of **Case 2** to enable the comparison between both coaxial designs for the same power deposited.

Thruster performances defined in Chapter 5 and summarized in Tab. 8.3. The ionization length is computed as

$$L_{ion} = \frac{u_n}{\nu_{ion}}, \quad (8.1-1)$$

where u_n and ν_{ion} are, respectively, characteristic neutral velocity and ionization frequency of the plasma located inside the thruster chamber. The former is taken to be that of the injection as the neutrals within the chamber do not accelerate to much larger velocities. For the latter, we have taken an average of the properties inside the chamber for a fixed axial position located right after the resonance. A comparison between the ionization length and the thruster length allows to infer the level of propellant ionization in the thruster. A modification of any parameter affecting the ionization frequency (or the electron temperature or the neutral density) inside the thruster chamber will have a direct correlation with the utilization efficiency and thus thruster performance.

Parameter	Name	Units	Case 1	Case 2	Case 3	Case 4
\dot{m}	Mass flow rate	mg/s	0.2	0.6881	0.6881	0.6881
P_f	Power input	W	30	200	200	242
F	Thrust	mN	0.756	5.021	4.442	5.054
P_a	Absorbed power	W	27.1	171.5	129.4	171.0
I_{sp}	Specific impulse	s	385	744	654	749
I_i	Ion current	A	0.077	0.350	0.346	0.349
η_F	Thrust efficiency	%	5.1	10.7	11.0	10.9
η_u	Utilization efficiency	%	52.1	69.3	68.5	69.1
η_e	Energy efficiency	%	23.2	35.6	35.5	36.3
η_c	Conversion efficiency	%	25.5	28.6	28.8	28.8
η_d	Divergence efficiency	%	85.2	86.9	88.7	86.6
ϵ_{exc}	Excitation losses	%	5.1	3.5	4.4	3.6
ϵ_{ion}	Ionization losses	%	8.2	5.8	6.9	5.9
ϵ_{wall}	Wall losses	%	64.5	57.1	60.1	56.5
η_p	Coupling efficiency	%	90.7	85.7	64.7	70.6
L/L_{ion}	Thruster to ionization length ratio	-	36	75	59	70

Table 8.3: Thruster performance results of the cases considered in the scale-up study.

8.1.2.1 Case 1: ECRT 30 W reference simulation

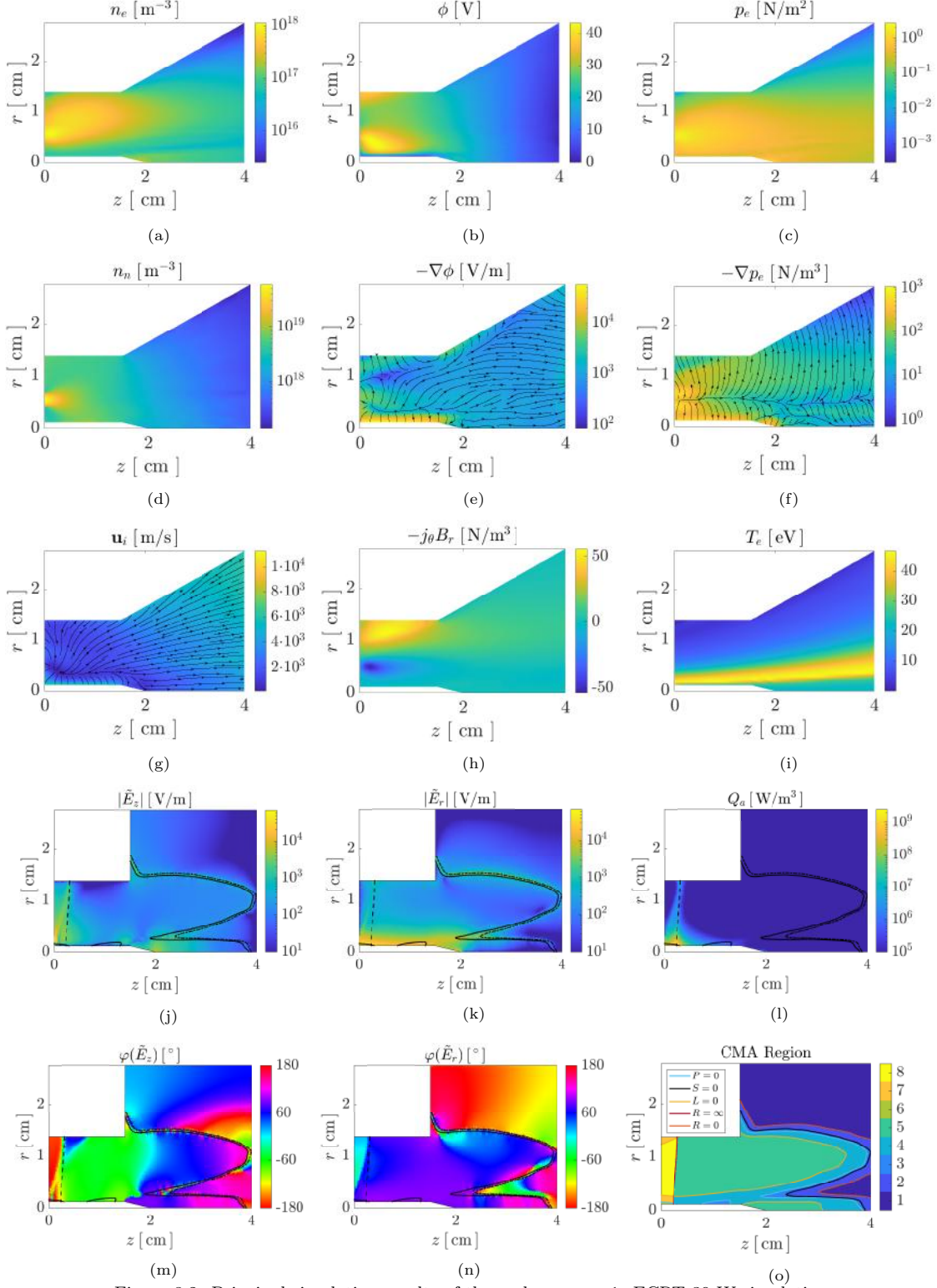


Figure 8.2: Principal simulation results of the scale-up case 1: ECRT 30 W simulation.

8.1.2.2 Case 2: ECRT 200 W simulation

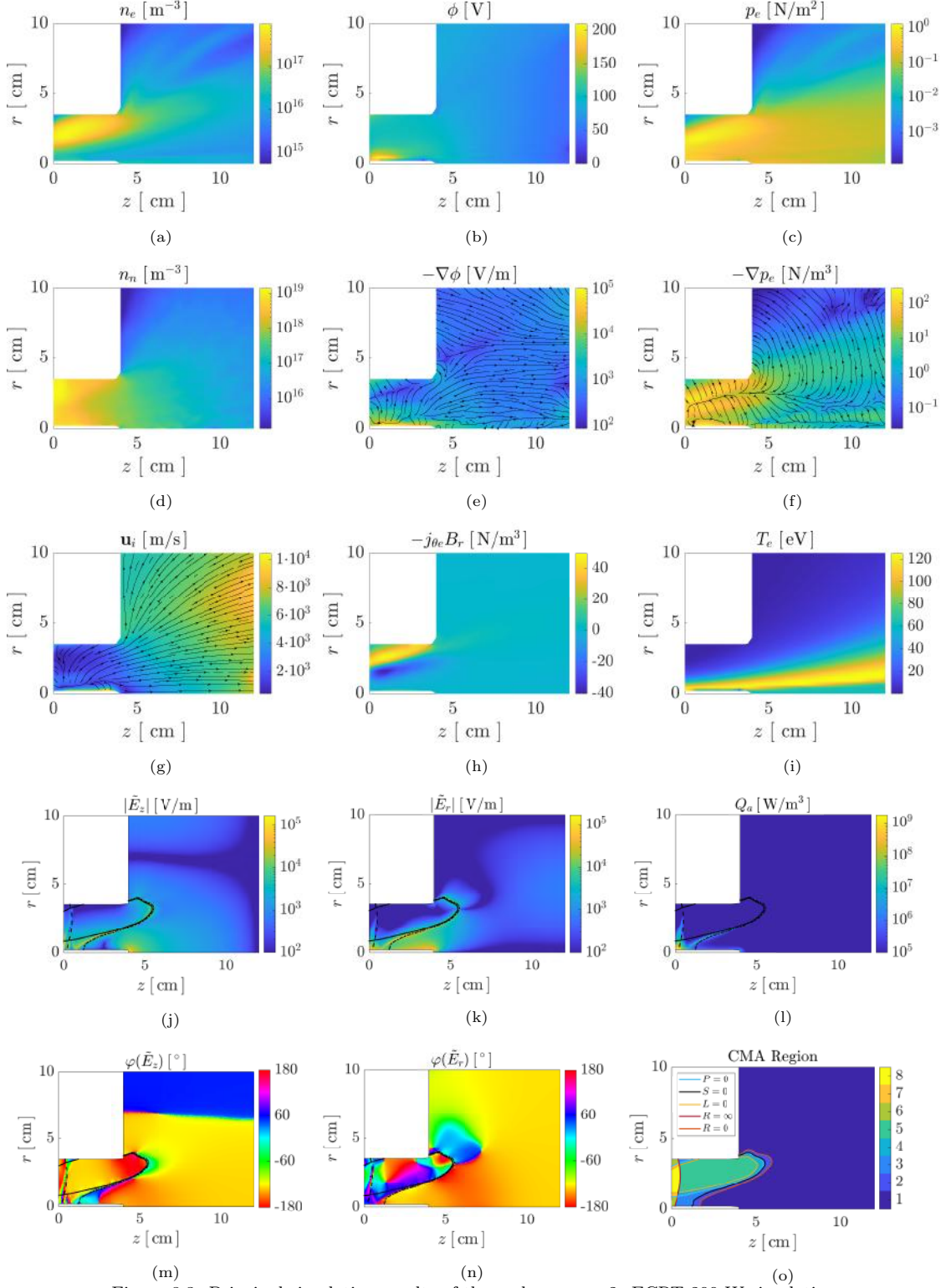


Figure 8.3: Principal simulation results of the scale-up case 2: ECRT 200 W simulation.

8.1.2.3 Case 3: ECRT 200 W with larger coaxial cable outer radius

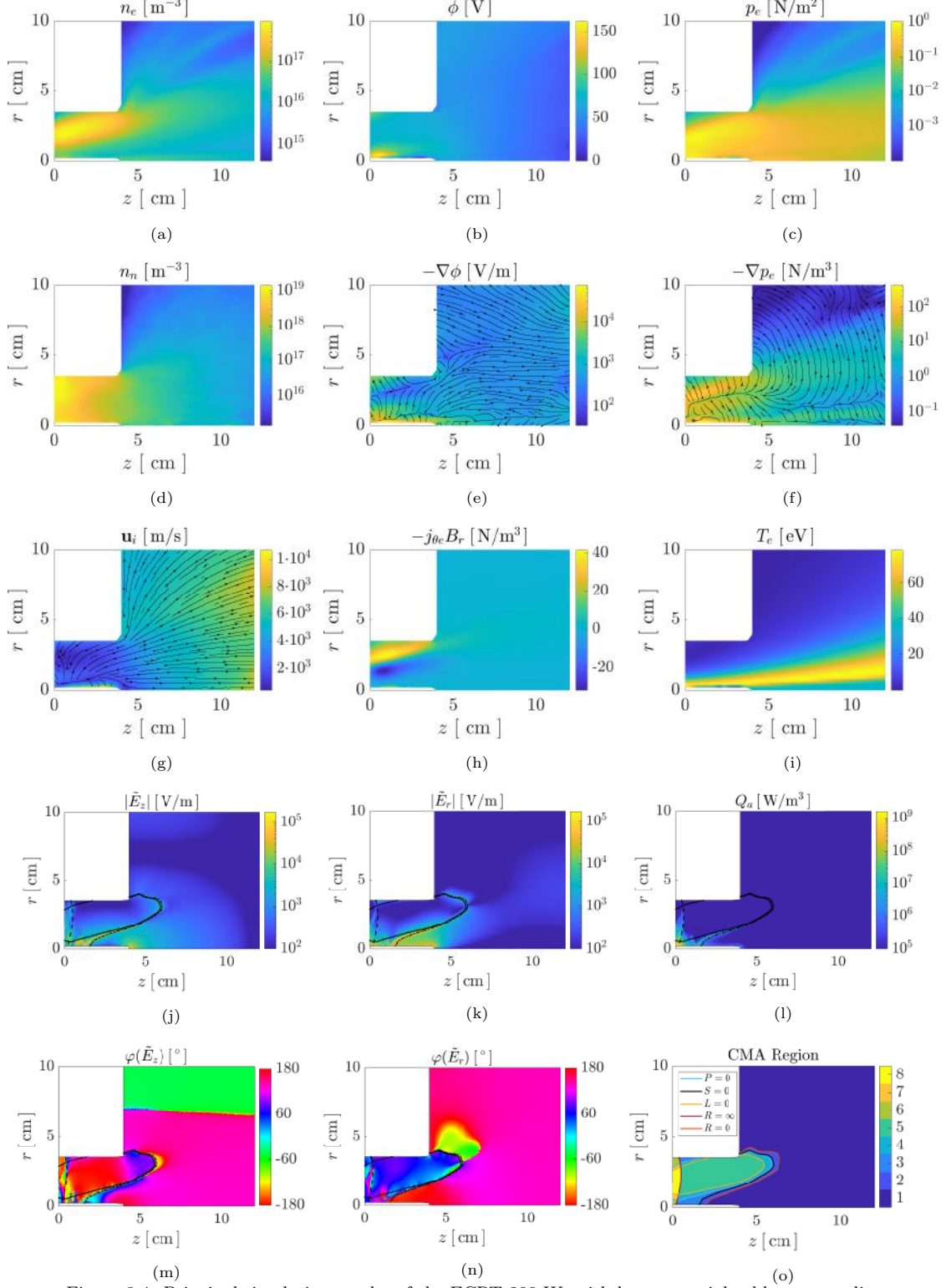


Figure 8.4: Principal simulation results of the ECRT 200 W, with larger coaxial cable outer radius.

8.2 Discussion

Both thrusters feature considerable differences in all variables and many commonalities. The following points identify and discuss the commonalities that can be observed between the thrusters:

1. The plasma density is larger in an intermediate radius within the thruster chamber. This is mainly motivated by the plasma recombination at the antenna core (density decays toward all walls) and the divergence of the magnetic field lines (plasma expansion takes place in the direction of the magnetic nozzle).
2. The electron pressure ($p_e = n_e T_e$) is maximum at an intermediate radius too, thus leading to a change in the radial pressure gradient. The electron pressure gradient is balanced mainly by the magnetic force and the electric force, and lastly by all other terms in the electron momentum equation (collisions, anomalous transport, etc). Keeping only the first two terms we have

$$\mathbf{0} \simeq -\nabla p_e + en_e \nabla \phi - en_e \mathbf{u}_e \times \mathbf{B}.$$

Since the electron pressure peaks at an intermediate radius, the magnetic force exhibits a sign change. This leads to two distinct regions in the plasma domain, one with diamagnetic currents with respect to the applied field (the peripheral part of the plasma), which generates *positive thrust*, and a region with paramagnetic currents with respect to the applied field (the part of the plasma closer to the axis of symmetry), with a negative magnetic thrust contribution (see Figs. 8.2h, 8.3h and 8.4h).

3. The electron population is nearly isothermal along magnetic field lines as can be seen in Figs. 8.2i, 8.3i and 8.4i. This behavior is a result of the high thermal conductivity exhibited in the direction parallel to magnetic field lines compared to their perpendicular counterpart.
4. The maximum electron temperature takes place at the magnetic field line where the maximum power deposited is located. This is generally at a magnetic field line close to the coaxial core. Note that temperatures above several tens of eV are reached in both thrusters, even exceeding the 100 eV in many operation points. The electron temperature on each magnetic tube is related to the amount of electromagnetic power absorbed by the plasma in that tube and the losses to the walls and to the free boundaries downstream. As the pressure profile is smooth, this peak of electron temperature is accompanied by a dip in electron density, which is also prevalent in the two thruster configurations.
5. The location of the maximum power absorption is found to be directly correlated to two main features. Firstly the location of the ECR region determines in this magnetic configuration the axial location of the power deposition [56]. Secondly, the power is not distributed uniformly along the resonance (i.e. ECR). Instead, it is determined by the radial location of electromagnetic fields along the resonance [59]. This location in this type of thrusters is the vicinity of the coaxial core, where the radial electric fields are larger. Additionally, a non-negligible fraction of the power absorbed takes place at the upper-hybrid resonance region, further downstream, in the two thrusters. This aspect, however, varies substantially from the 30 W configuration to the 200 W configuration.
6. The steep gradients of plasma density towards the coaxial core also induce strong electrostatic fields towards the antenna wall. This is motivated by the strong temperature gradient exhibited radially away from the coaxial core. As a result, high velocity ions reach this surface, which can lead to erosion.
7. Concerning the magnetic thrust (see Figs. 8.2h, 8.3h and 8.4h), the results show that the positive thrust is generated close to the upper part of the thruster chamber in both thrusters. A major part of the magnetic thrust production, consequently, takes place at larger radii.

On the other hand, both designs feature many differences:

1. The injection is performed axially for the 30 W whilst it is done radially for the 200 W thruster. This affects considerably the profile of the neutral density, and has its impact on the thruster performances. Note that the neutral density within the thruster chamber is around 50% higher for the 30 W thruster. This implies that possibly a higher mass flow rate would increase the characteristic plasma density of the discharge for the 200 W thruster. This increase would lead to an increase in the ionization frequency of the propellant and thus could result in an increase of the utilization and thus, its thrust efficiency.
2. The plasma density achieved in the 200 W thruster is less than in the 30 W thruster. The beam of plasma is thinner and the decrease towards the antenna core is steeper, reaching densities of the order of 10^{16} m^{-3} .
3. The electric potential features a main maximum close to the core wall, but the peak is much greater for the 200 W cases. The potential difference between the maximum inside the thruster chamber and the plume is greater for the 200 W case. The maximum is also more focused and closer to the core wall. This is motivated by the smaller density and higher temperature there for the 200 W thruster, which requires a steeper electrostatic field to compensate the pressure gradient close to the coaxial core (see Figs. 8.2e, 8.3e and 8.4e). As a consequence of the larger electric field, ions undergo more acceleration toward the coaxial core wall (see Figs. 8.2g, 8.3g and 8.4g). A small, secondary ϕ increase is seen toward the magnetically-isolated region of the upper left corner of the thruster discharge chamber in the 30 W design. This potential rise is less noticeable in the 200 W cases, but still present.
4. The main difference between the pressure maps of **Cases 2 & 3** with respect to **Case 1** is the pressure decrease towards the top wall, which is more pronounced in the 200 W thruster simulations, driving larger diamagnetic drift currents and thus larger magnetic thrust densities in this region.
5. The region of maximum pressure (or null pressure gradient) can be noticed to be closer to the axis in the 30 W thruster than for the simulations of the 200 W thruster. The location of this maximum is the location of the change in direction of the pressure gradient in Figs. 8.2f 8.3f 8.4f. This maximum defines the location of the change of sign in $j_{\theta e}$ and thus the zero of the magnetic thrust density. The pressure gradient features stronger gradients closer to this maximum since the density decreases faster away from the plasma beam core.
6. The neutral density profiles shown in Figs. 8.2d, 8.3d and 8.4d, are different due to the change in the injection strategy. Note that the location of the maximum density is always located in the vicinity of the injector.
7. The electron temperature reaches higher values for the 200 W thruster simulations, specially **Case 2**. One of the main differences between simulation **Case 2** and **Case 3** is the resulting maximum temperature, being approx. 125 eV and 75 eV, respectively. This is in line with the lower absorbed power of Case 3.
8. The wave propagation regions, cut-offs, and resonances vary largely between the 30 W and 200 W thrusters. Firstly, the location the upper hybrid resonance ($S = 0$) changes considerably, crossing the entire thruster chamber and reaching the backplate in **Cases 2 & 3**, while it was external in **Case 1**. This is a result of the much smaller density near the axis, which brings this resonance further upstream. Secondly the low density regions before the ECR resonance are larger and appear both near the top wall and the thruster core in the 200 W case. Thirdly, the evanescent region downstream of the ECR resonance (region 5 in the CMA diagrams) shrinks, and opens up a larger propagation channel close to the inner rod wall in **Cases 2 and 3** (Figs. 8.3o and 8.4o). This enables a larger amount of electromagnetic power to flow after the resonance through this channel.

9. Regarding the high-frequency electromagnetic fields themselves we notice several differences. The electromagnetic fields after the ECR can still propagate in regions 3 and 4 of the CMA diagrams, and feature maxima that follow these regions. Also while no standing-wave structures are identifiable in the 30 W thruster, the fields in the plume region of the 200 W thruster have lines of nodes (see Figs. 8.3m and 8.4m). This shows the effect of imposing a reflecting boundary condition in the plume for the electromagnetic problem and the need to implement an absorbing boundary condition or a perfectly matched layer.
10. Regarding the power absorption, we note that there is a significant contribution in the propagating regions 3 & 4, even downstream the ECR region. This shows that non-negligible absorption takes place in these regions and not in the ECR region (see Figs. 8.3l and 8.4l). This is one of the main differences with the reference 30 W thruster simulation.
11. Regarding the performances, the difference in energy efficiencies is the largest (a 60% greater for the 200 W thruster). Furthermore, the propellant utilization increases around a 40%. This is first related to the thruster to ionization length ratio which is improved in the 200 W thruster mainly by its increase in the thruster length. As a result, the resulting thrust efficiency is doubled with the 200 W thruster comparing with the 30 W thruster. This increase would be expected from the increase in the power level of the device.
12. Wall losses are slightly smaller for the 200 W thruster, as expected from the smaller A/V ratio. However, the losses are still comparable which means that a major part of the power is still lost to the walls. This inefficiency is likely the main area of work where the ECRT can be improved at this time.
13. Lastly, and in line with the change of wall losses, excitation and ionization, losses although still considerable, are smaller for the 200 W thruster.

When comparing **Cases 2** and **3** (nominal and x3 outer coaxial cable radius, respectively) we notice that there are not many major differences in terms of performances nor in the plasma variables. However, this does not discard the outer radius of the coaxial as an optimization parameter. The main differences found between the simulations are listed below:

1. The power absorption upstream the ECR region is slightly more distributed towards higher radius for **Case 3** than for **Case 2**. This is, indeed, the main motivation to explore this change in the coaxial cable design.
2. The maximum electron temperature found in the simulation domain is higher for **Case 2** than for **Case 3**. Although it could be thought that this is a result of previous point, it has been found that the key aspect driving this decrease is the lower amount of power deposited in the plasma exhibited for a fixed power input of 200W (i.e. **Case 3**). This is confirmed by analyzing the simulation results for **Case 4**, which is identical to Case 3 except for the power deposited, which is fixed to equal that of Case 2 (171 W), so that we can compare both coaxial designs for the same level of power deposited. Results not only showed the same maps for all variables including the same maximum electron temperature as Case 2, but also very similar performances as shown in Tab. 8.3. Therefore, it is inferred that the coaxial radius modification only changes the coupling efficiency of the transmission line, as a result of the change in the impedance of the line, but that the electron temperature maximum in the 200 W configuration is mainly driven by the total absorbed power.
3. Comparing the coupling efficiencies we note that there is an increase in the coupling of a 6% from **Case 3** to **Case 4**. This means that the impedance mismatch is smaller. For a fixed coaxial line impedance, this implies that the impedance of the plasma has been reduced.
4. The minimum in the thrust force is smaller in the coaxial thruster so that the profile is more efficient for acceleration, given the fact that the maxima are similar and so are the profiles.

8.2.1 Thruster optimization

The simulations and the analyses carried out provide information on the response of the baseline coaxial ECR thruster design to different scales and we have included an analysis of the effect of a different coaxial radius with two additional cases.

This work has shown that the differences in the operation with scale can be significant. The analysis has enriched our know-how about the factors driving the performance and operation of ECRT. The main conclusion that can be extracted in this regard is that the ECRT increases its efficiency for mid power and its scaling is adequate, mainly by improving its utilization and energy efficiencies. Furthermore, it has been noticed that the decrease of plasma density towards the inner core that allows the propagation of strong electromagnetic fields close to the coaxial core, which are responsible for the electron heating and plasma production. This results in the production of a discharge that features highly energetic electrons together with a dense plasma.

However the 200 W thruster has room for improvement since the plasma density is relatively lower and the plasma density decreases towards the coaxial core more than what it is desirable, since heating is still localized there. Additionally, the power deposited in the thruster is a major parameter driving thruster performance and optimal operating points have to be found for each geometric design. A parametric investigation on mass flow would provide more optimal operation points for the 200 W thruster. However, focus will be taken in the development of a thorough parametric analysis of the low power thruster.

Several design changes are suggested based on the results shown for the 200 W thruster, that should be explored experimentally and numerically to optimize the thruster design:

1. Increase the inner coaxial radius so that the recombination is brought closer to the plasma core and in order to bring the region of maximum heating closer to the core of the plasma beam obtained.
2. Design a permanent magnet configuration so that the ECR surface intersects with the backplate and not the coaxial core. This results in the maximum power absorption being away from the coaxial core surface, and thus increasing thruster performances.
3. Vary the length of the thruster's outer conductor wall. Probably a more optimal point can be found since the thruster operation seems to depend considerably on the variables in the region where magnetic field lines are closed by the backplate and the upper wall.
4. Change the propellant injection strategy so that we increase the amount of plasma generated close to the coaxial core. Maybe two different simultaneous injections, one at an intermediate location within the thruster chamber. Furthermore we suggest to increase the mass flow of the discharge as it was noticed that the plasma density level achieved was lower than the 30 W thruster, related to the lower propellant densities featured and the higher electron temperatures.
5. Rework the shape of the outer conductor wall to conform with the lines of the applied magnetic field. This can eliminate the magnetically-isolated corner region which drives plasma losses, as the plasma generated there does not connect with the accelerating magnetic nozzle region. Naturally, this must be done carefully not to spoil the propellant utilization efficiency.

8.3 Concluding remarks

The results shown in this chapter serve to analyze the main variables and performance figures of the scaled-up 200W ECRT design. This can enable improving our comprehension of the coaxial ECRT scaling. The simulations show that both designs share a lot of common-points which comprise our current understanding of ECRTs. Additionally, several differences have been noticed between both thrusters and have been analyzed.

Moreover the effect of increasing the coaxial radius (i.e. applying a x3 factor to the external radius of the coaxial) in this configuration has been investigated and has resulted to affect mainly the coupling efficiency since it changes the impedance of the coaxial line. However, for the same power deposited (i.e. comparing cases 2 and 4), it has been noticed that the thruster performances and operation remain unaffected by this modification. Nevertheless, this does not rule out this parameter as a possible parameter to improve thruster performances in different thruster configurations.

Notwithstanding this, the differences in ECRT performance from low power to medium power follow expectations as increasing the overall thrust efficiency by increasing the propellant utilization and energy efficiency. Furthermore wall losses are smaller than for the low power design which could be expected from geometrical parameters as the smaller area-to-volume ratio of the chamber. A parametric analysis could be performed to the higher power thruster in order to find optimal design point of operation.

Additionally, we have reported some suggestions for possible thruster modifications design. Amongst these suggested modifications, we have included increasing the inner coaxial radius, to bring the maximum power absorption towards the core of the plasma beam, change the magnetic field configuration to affect the power deposition, vary the length of the thruster chamber's outer wall and investigate multi-injection strategies to optimize the neutral distribution and residence time within the thruster chamber.

Future work would include extending the amount of scenarios considered regarding scaling parameters, as aspect ratio, area to volume ratio, and thruster electric length, in order to extend our knowledge regarding ECRT scaling laws. Additionally, it is expected that the anomalous coefficient may be an important parameter for the upscaled versions of the thruster. Anomalous transport quantitative fitting based on experimental data (as it is carried out in Chapter 9) would be useful to improve the estimations of both plasma properties and thruster performances in the upscaled thruster versions.

Chapter 9

Comparison of hybrid coaxial ECR thruster model to experimental measurements

Electrostatic probe and thrust balance measurements of an electron-cyclotron-resonance plasma thruster with magnetic nozzle are compared against numerical simulations of the device that solve self-consistently the plasma transport problem with a hybrid particle-in-cell/fluid approach and the microwave electromagnetic fields using vector finite elements. The comparison evidences that enhanced cross-field diffusion is present in the plasma, and a simple phenomenological anomalous transport model similar to those used in Hall thruster modeling is proposed. Reasonable agreement is found on the ion current density and plasma density profiles, ion energy distribution function downstream, and thruster performances. Differences in the experimental and numerical behavior of electron temperature and electrostatic potential highlight the areas of the model that need to be improved: the electron heat flux closure relation, which must correctly account for the longitudinal electron cooling observed, and the treatment of electrostatic boundary conditions. Part of these results will be submitted for their publication to peer-reviewed journal Plasma Sources Science and Technology [63].

9.1 Introduction

The Electron Cyclotron Resonance Thruster (ECRT) concept was conceived in the 1960s when it was first noted that plasma could be accelerated by electromagnetic (EM) fields, and extensive research was carried out to design them [8]. After the 1970s, the funding ceased and it was not until the late 1980s that the research was continued at JPL [24].

Amongst other electric propulsion (EP) technologies, the ECRT belongs to the family of electrodeless plasma thrusters, as the Helicon Plasma Thruster (HPT)[17, 92]. As implied by their classification name, these thrusters do not require the use of electrodes for their operation. Electrodes are electrically conducting components such as cathodes, anodes, or neutralizers which are typically considered thruster lifetime-limiting components [129], as they suffer increased erosion resulting from the substantial particle fluxes and heat loads they are subjected to. Instead, electrodeless plasma thrusters consist of two main elements: a radiofrequency (RF) source and an applied magnetic field. The former is in charge of heating and ionizing the propellant by plasma-wave interaction. The latter has multiple roles: first, it allows the EM propagation in overdense plasmas and, for the ECRT, it generates an Electron Cyclotron Resonance (ECR) region, key for

EM wave absorption in that technology. Second, the magnetic field confines the electrons, limiting the particle interaction with the thruster walls. Last, it generates a magnetic nozzle (MN) that accelerates the plasma plume, thus increasing thrust.

The first versions of the ECRT [8, 24, 130] were based on a waveguide coupling between the feeding microwave power and the plasma. Later works [11, 53] characterized the more efficient coaxial-coupled version of the thruster. This version generates high energy ion energy beams at low powers (around 200 eV for 30 W of absorbed power). Although still featuring meager thrust efficiencies, its simple design and high repeatability from one ignition to the other and the robustness of the wave absorption mode, have led to extensive research in Europe [12, 50, 52, 53, 119] and the USA [122, 131, 132].

Despite the extensive experimental work carried out on the ECRT, the modeling and simulation efforts are scarce. An analytical quasi-1D model designed for HPTs was adapted to the ECRT case and applied to estimate successfully the overall thruster performances [51]. However, the model underestimated the electron temperature and lacked modeling of both cross-field diffusion as well as antenna/plasma power coupling. A more complete two-dimensional axisymmetric model of the ECRT including these two last features has been developed and applied recently to obtain coupled simulations of the plasma wave interaction and the plasma transport [57]. The plasma transport is modeled with hybrid approach, using Particle-in-cell (PIC) method for the heavy species (i.e. neutrals and ions) and a fluid model for the electrons. The electromagnetic response of the plasma is modeled with Maxwell's inhomogeneous wave equation and a collisional cold plasma dielectric tensor formulation [27].

The model uses a description of electron cross-field anomalous diffusion based on a phenomenological turbulence model. The presence of anomalous diffusion in MN plasma thrusters is less ascertained than in other EP prototypes, as in Hall effect thrusters (HET), where near-wall conductivity (NWC) [133] and turbulent transport are theorized to be the principal mechanisms driving anomalous transport. NWC is enhanced by high secondary electron emission (SEE) yields, which replace the magnetized electrons, and effectively increase the wall conductivity. Dielectric wall ECRTs, as boron nitride (BN) sources, are expected to feature saturated SEE yields given that characteristic electron temperatures T_e 25 eV are similar to the half cross-over energy of BN [134]. Turbulent transport is known to be correlated to plasma instabilities. Recent research [132] measured wave dispersion in the magnetic nozzle of an ECRT, consistent with the lower hybrid drift instability (LHDI), with a dominant effective electron collision frequency over classical collisions. Anomalous diffusion in ECRTs is most likely a combination of multiple local phenomena.

The main objective of this work is to test the capabilities of the coaxial ECR model shown in [57] to reproduce and interpret experimental measurements of a real ECRT prototype, not only in terms of thruster performances, but also plasma properties. The model assumptions are verified and its principal limitations are illustrated, specially related to the electron fluid module.

Section 9.2 gives an overview of the methodology employed to obtain a comparison between experimental ECRT measurements and model estimations. The model equations are discussed together with the effects of anomalous diffusion. Section 9.3 details the measured angular and axial plasma properties measured and a parametric investigation on the anomalous diffusion that allows to perform an empirical fit. Then, we discuss the impact of cross-field diffusion on the plasma discharge. Finally we compare thrust and ion energy measurements with simulation results, and discuss the principal discrepancies between experimental and model estimations.

9.2 Methodology

The comparison between experimental data and numerical simulations has been performed on a ECRT prototype (see Fig. 9.1a) developed at ONERA since 2010, notably in the framework of the MINOTOR project H2020 [51, 52, 119, 122, 135].

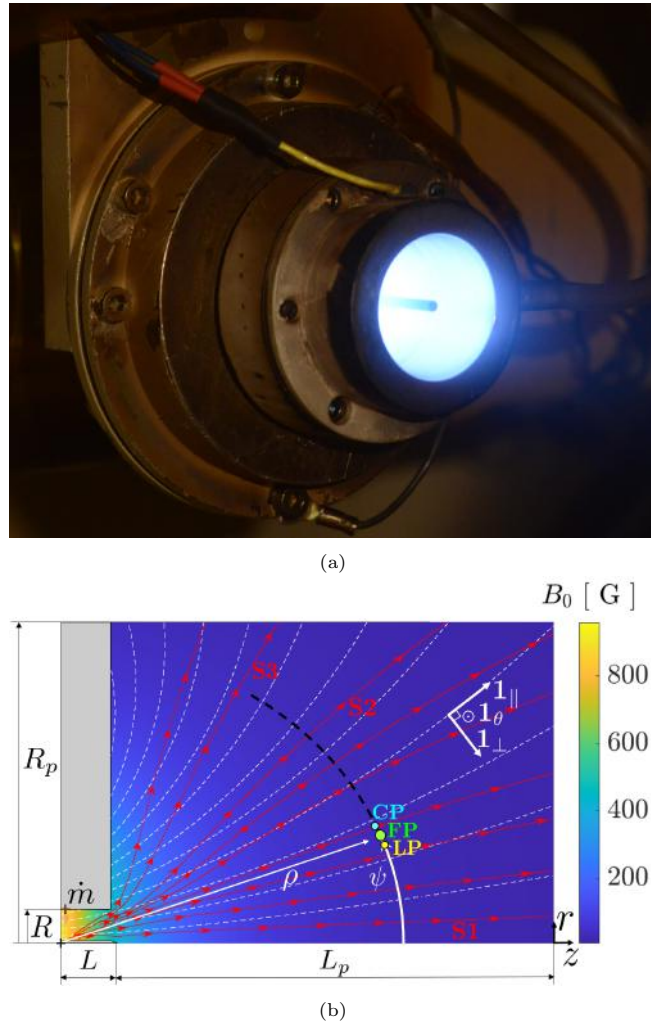


Figure 9.1: (a) ECRT prototype operating in the ONERA-B09 facility; (b) ECRT simulation domain showing: magnetic field intensity (colormap), magnetic field lines (white dashed), Xe⁺ streamlines for case $\alpha_t = 0.05$ (red), local magnetic coordinates (white). Additionally, the experimental setup detailed in §9.2.1 is sketched.

Figure 9.1b shows the simulation domain, where the prototype consists of a $L = 2$ cm long semi-open coaxial structure with $2R = 2.75$ cm in diameter and a backplate made of boron nitride (BN), located at $z = 0$. The BN backplate acts as a transparent window to microwave power forwarded through a coaxial line by a transverse electromagnetic (TEM) mode. The walls of the inner and outer conductor of the thruster source are made of metal and are coated with BN spray.

The magnetic field is provided by an annular permanent magnet placed at the back of the ECR source, so that at the ECR region the magnetic field intensity is 875 G, corresponding to an electron cyclotron frequency of 2.45 GHz. The thruster is powered by a microwave generator at a frequency of 2.45 GHz. The absorbed power (P_a) by the plasma is 30 W. The thruster is fed with xenon at 2 SCCM following a radial injection configuration.

Plasma properties are compared in the near plume of the thruster. Data points locations are chosen considering both experimental (plasma perturbation produced by the probes and probe damaging) and numerical (computational cost scaling with simulated plume size) limitations.

9.2.1 Experimental setup

Tests are carried out in the ONERA-B09 facility: a cylindrical vacuum chamber of 2 m in length and 0.8 m in diameter. The secondary pumping system consists of three turbomolecular pumps and one cryogenic pump, yielding a total pumping speed of 13,000 l/s for xenon, with a base pressure of 10^{-7} mbar. During thruster operation at 2 SCCM the typical pressure is of the order of 4×10^{-6} mbar.

The microwave power line consists of VAUNIX LMS-402D signal generator and a Microwave Amps Ltd power amplifier. The forward and reflected power to and from the thruster is measured with two LB478A (LadyBug Technologies) power sensors and directional couplers. Power losses through the feeding line are measured prior to the test campaigns so that the total absorbed power is known for every operating condition. Thrust measurements are performed with the thrust balance developed at ONERA [12], which is a pendulum balance with a quasi-frictionless pivot. The thruster is mounted at the end of the arm.

Plasma parameters are collected along angular and longitudinal profiles in the MN. Three measurements campaigns are carried out and are labeled experiment (Exp.) A, B and C in the forthcoming. Exps. A and B identify angular measurements, while Exp. C represents the axial measurements following the plasma expansion in the plume. The BN coating of the thruster inner and outer walls is applied prior to both Exp. A and Exp. B. For the angular profiles, plasma probes are mounted on a motorized rotational stage with the rotation axis centered with respect to the backplate of the thruster, as shown in Fig. 9.1b, following the (ρ, ψ) coordinates. They are taken 16 cm downstream from the backplate and the angle is varied between -45° and $+45^\circ$. Probes are oriented such that the collecting (or measuring) surface is normal to the ρ -direction for all ψ angles. For the longitudinal profiles, plasma probes are moved using motorized translational stages, allowing for two degrees of freedom along the z and r axis, defined in Fig. 9.1b. The longitudinal profiles are measured along the plume central axis, i.e. $r = 0$ cm. For the three experimental campaigns (A, B and C) the probes were mounted in order to minimize the perturbation induced from each other during a plasma measurement.

Plasma diagnostics are performed with three different probes constructed in-house and a commercial ion analyzer. The Faraday probe consists of a collector of 6 mm in diameter biased at -350 V. The collected ion current is measured through a 33 k Ω -shunt resistance. The curling probe, called CP700 in [136], consists of a 35 μm -thick spiral copper resonator of 106 mm in length, etched on a 0.5 mm-thick RO4003 sheet. It measures the local electron density following the plasma permittivity [136]. The Langmuir probe consists of a tungsten wire of 150 μm in diameter and 5 mm in length. The bias voltage at the probe tip is swept from -100 V to +100/+120 V (depending on the probe distance to the thruster). The collected current is measured through a 6 k Ω -shunt resistance and recorded on a National Instruments DAQ board (NI BNC-2110). Data are post-processed using the Druyvestein method [137] and OML theory in order to determine electron density and temperature. Low discrepancy is obtained from the two post-processing methods. Ion energy distribution function is measured with a PSM003 Hiden Analytical ion analyzer, which faces the thruster and is mounted at approximately 1.7 m from the thruster exit plane ($z = L$ in Fig. 9.1b).

9.2.2 ECRT model

The model used in this work was introduced in [57] and obtains coupled solutions of the plasma transport and electromagnetic plasma response in ECRTs. The reader is referred to that work for the details of the model and its numerical implementation. In the following, only aspects of the model directly relevant to this work are discussed, with a special emphasis on the electron response.

The electrons are modelled as a magnetized diffusive fluid, satisfying:

$$n_e = \sum_{s \neq e} Z_s n_s, \quad (9.2-1)$$

$$\nabla \cdot \mathbf{j}_e = -\nabla \cdot \mathbf{j}_i, \quad (9.2-2)$$

$$0 = -\nabla p_e + en_e \nabla \phi + \mathbf{j}_e \times \mathbf{B} + \mathbf{F}_{coll} + \mathbf{F}_{turb}, \quad (9.2-3)$$

$$\frac{\partial}{\partial t} \left(\frac{3}{2} p_e \right) + \nabla \cdot \left(\frac{5}{2} p_e \mathbf{u}_e + \mathbf{q}_e \right) = -\nabla \phi \cdot \mathbf{j}_e + Q_a + Q_{coll}, \quad (9.2-4)$$

$$0 = -\frac{5}{2e} \nabla (p_e T_e) - (\mathbf{q}_e + \frac{5}{2} p_e \mathbf{u}_e) \times \mathbf{B} + \frac{5p_e}{2} \nabla \phi - \frac{m_e \nu_e}{e} \mathbf{q}_e + \mathbf{Y}_{turb}. \quad (9.2-5)$$

Equation (9.2-1) is the quasineutrality condition that is imposed in the plasma bulk. Non-neutral plasma sheaths are treated separately, computing the local potential fall between the sheath edge and the dielectric wall, and the electron energy flux to the wall.

Equation (9.2-2) represents the electric charge conservation within the domain, where $\mathbf{j}_e = -en_e \mathbf{u}_e$ and $\mathbf{j}_i = \sum_{s \neq e} Z_s en_s \mathbf{u}_s$ are the electron and ion charge current densities.

Equation (9.2-3) represents the inertia-less electron momentum balance, where $p_e = n_e T_e$ is the isotropic electron pressure and ϕ is the electrostatic potential. The term $\mathbf{F}_{coll} = -m_e n_e \sum_{s \neq e} \nu_{es} (\mathbf{u}_e - \mathbf{u}_s)$ groups the different resistive forces due to collisions of electrons with species s , with $\nu_{es} = \nu_{es}(T_e)$ the corresponding effective collision frequency. This includes inelastic collisions as ionization and excitation, and elastic electron collisions with neutrals and ions.

Equation (9.2-4) is the energy balance for electrons in the inertia-less limit, where the term $5/2 p_e \mathbf{u}_e + \mathbf{q}_e$ is the electron internal energy flux, with \mathbf{q}_e is the electron heat flux. $Q_{coll} = -n_e \sum_{s \neq e} \nu_{es} \varepsilon_{es}$, with ε_{es} the energy yield of the collision, is the power sink from electron collisions with heavy species as ionization and excitation of neutrals.

Equation (9.2-5) is electron heat flux equation, structurally similar to the momentum equation, with $\nu_e = \sum_{s \neq e} \nu_{es}$, the electron collision frequency.

Equations (9.2-3)-(9.2-5) are projected in the local orthonormal magnetic basis $\{\mathbf{1}_\perp, \mathbf{1}_\parallel, \mathbf{1}_\theta\}$ shown in Fig. 9.1b, where $\mathbf{1}_\perp$ and $\mathbf{1}_\parallel$ represent the perpendicular and parallel directions to the local magnetic field vector \mathbf{B} in the meridional plane, $\mathbf{1}_\theta$ completing the orthonormal basis.

The model includes a phenomenological turbulence model for anomalous cross-field diffusion in the momentum and heat flux equations, $F_{turb} = -\mathbf{1}_\theta \alpha_t j_{\theta e} B_0$ and $Y_{turb} = -\mathbf{1}_\theta \alpha_t q_{\theta e} B_0$, with α_t a constant empirical parameter.

In order to discern the effects of anomalous transport, let us solve for \mathbf{j}_e in Eq. (9.2-3). The projection in $\mathbf{1}_\theta$ reads:

$$j_{\theta e} \approx -\chi' j_{\perp e} = -\sigma_e \frac{\chi'}{1 + \chi \chi'} \left[\frac{1}{en_e} \frac{\partial p_e}{\partial \mathbf{1}_\perp} - \frac{\partial \phi}{\partial \mathbf{1}_\perp} \right], \quad (9.2-6)$$

$$\approx -\frac{1}{B_0} \left[\frac{\partial p_e}{\partial \mathbf{1}_\perp} - en_e \frac{\partial \phi}{\partial \mathbf{1}_\perp} \right], \quad (9.2-7)$$

where $\sigma_e = e^2 n_e / m_e \nu_e$ is the parallel conductivity, e and m_e the electron charge and mass, and $\partial / \partial \mathbf{1}_\perp$ is the perpendicular directional derivative. Hall parameters are defined as:

$$\chi = \frac{\omega_{ce}}{\nu_e}, \quad \chi' = \frac{\omega_{ce}}{\nu'_e} = \frac{\omega_{ce}}{\nu_e + \alpha_t \omega_{ce}} = \frac{\chi}{1 + \alpha_t \chi} \approx \alpha_t^{-1}, \quad (9.2-8)$$

with $\omega_{ce} = eB_0/m_e$ being the electron gyro-frequency. The approximation in (9.2-6) assumes that the equivalent current density from electron collisions with heavy species $j_{\theta c} \ll \chi' j_{\theta e}$. The approximation in Eq. (9.2-7) holds as $\chi \chi' \gg 1$ for the cases considered, since $\chi > \mathcal{O}(10^3)$ and $\chi' > \mathcal{O}(10)$. The inclusion of anomalous diffusion increases the effective electron collisional rate to ν'_e , limiting magnetic confinement and decreasing the Hall parameter to χ' .

On one hand Eq. 9.2–7 shows that the azimuthal electron currents are determined directly by the balance of the electron diamagnetic and $E \times B$ drifts. On the other hand, the perpendicular electron current is determined not only by this balance of electron drifts but it scales with α_t . This is a result of perpendicular conductivity being inversely proportional to an effective Hall parameter χ_{eff} squared, defined as

$$\chi_{eff} = \sqrt{\chi\chi'} \approx \sqrt{\chi/\alpha_t}. \quad (9.2-9)$$

Analogously, one can repeat the analysis with the perpendicular electron heat flux

$$q_{\perp e} \approx -\frac{5 T_e}{2 e^2} \frac{\sigma_e}{1 + \chi\chi'} \cdot \frac{\partial T_e}{\partial \mathbf{1}_{\perp}} - \frac{5 T_e}{2 e} \frac{(1 - \chi\chi')j_{\perp e} - j_{\perp c}}{1 + \chi\chi'}, \quad (9.2-10)$$

showing that both, the “conductive” and “convective” terms can be shown to be proportional to α_t . Note that this does not imply that the perpendicular electron particle and heat fluxes will increase proportionally to α_t . Instead, the rise in perpendicular conductivity modifies the plasma balance, both increasing the perpendicular fluxes and smoothing the perpendicular ϕ , p_e , n_e and T_e gradients.

Heavy species as neutrals and ions are treated as macroparticles, and their dynamics are simulated using a particle-in-cell (PIC) approach. The PIC code considers (i) ionization collisions (e.g. single, double, and single to double) by electron bombardment, (ii) particle to wall interaction including their respective Debye sheaths, neutral accommodation and re-emission, ion recombination and re-emission as neutrals, and the fulfillment of Bohm criterion at the sheath edge, (iii) particle removal at open boundaries, (iv) macroparticle listing according to species type. A weighting algorithm computes the integrated macroscopic properties on the PIC mesh, which are combined with the electron properties obtained from the convergence of the electron fluid model. An iterative and time marching strategy is used to converge to steady state solutions.

Additionally, the plasma response to electromagnetic waves is simulated using a finite element code that solves the inhomogeneous Maxwell’s wave equation. The plasma currents appearing as a response to the electromagnetic excitation are obtained applying a cold-plasma collisional model [27]. The contributions of heavy charged species (singly- and doubly-charged ions) can be neglected at this frequency. A TEM mode is excited within the coaxial line, which accesses to the plasma source through the dielectric window. The model computes the electromagnetic power deposited in the plasma derived from the frequency response of the plasma to the EM excitation. The EM power absorption map (Q_a) is provided as an input to the electron fluid model, and acts as an energy source. The coupling between the EM and the transport problems is not required to be continuous (i.e. for every timestep) since the characteristic time of electromagnetic response currents is in the nanosecond range, compared to the transport which are in the microsecond range. Hence, the electromagnetic code is called only every 10000 transport code steps. Convergence to stationary conditions, reaching self-consistent solutions, is obtained after 3-4 updates of coupled iterations (i.e. after 1.5-2 ms).

The domain, shown in Fig. 9.1b, is composed by the thruster wall boundaries, the open boundaries, the injection port and the symmetry axis. The thruster walls are treated as a dielectric for the transport and as a perfect electric conductor for the electromagnetic wave module, given that the BN coating is transparent to EM wave propagation. In order to obtain a finer comparison, the simulated domain has been extended compared to previous results shown in [57]. As a result of a trade-off between experimental and numerical (or simulation) limitations, the simulated plume extension is set to be $L_p = 18$ cm long and $R_p = 13$ cm in radius.

9.3 Results and discussion

In this section, we present a comparison between the numerical and experimental results obtained in the near plume of the ECRT prototype shown in Fig. 9.1a.

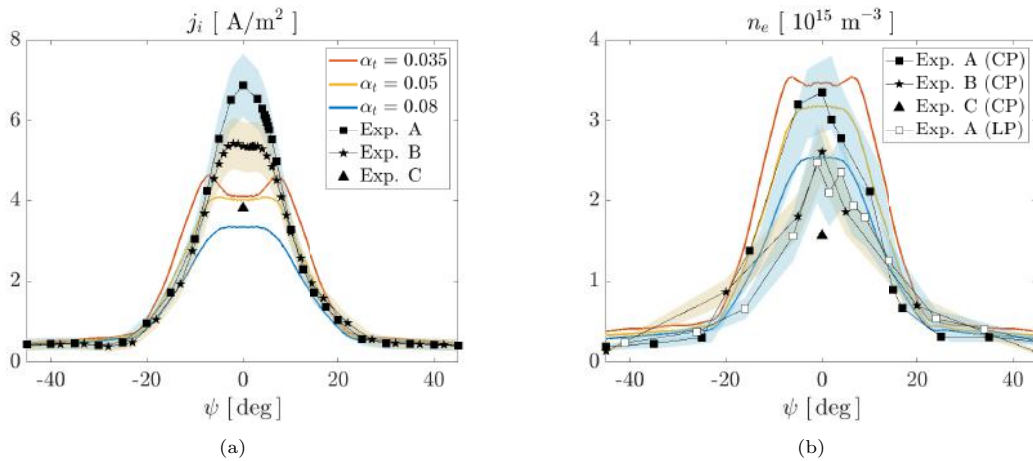


Figure 9.2: Angular profiles at $\rho = 16$ cm, for 2 SCCM - 30 W of (a) the ion current density and (b) the electron density. Numerical results (solid lines) for different anomalous transport coefficients are shown against experimental measurements (scatter symbols). Experiments A, B, and C are summarized in §9.2.1. LP data points are represented in hollow scatter points.

9.3.1 Angular profiles

Figure 9.2 shows angular measurements for both the total singly- and doubly-charged ion current and electron density at $\rho = 16$ cm from the thruster backplate, for Exps. A, B and C, detailed in §9.2.1. Error bars, accounting for measurements uncertainties for the Faraday probe, curling probe and the Langmuir probe are estimated as detailed in refs. [136, 138, 139], respectively. Systematic errors such as probe leakage current, DAQ system acquisition, and applied bias voltage are considered for the FP. Both systematic and statistical errors are considered for the CP. The presented error bars do not account for thruster variability from one experiment to the other.

Good qualitative agreement is obtained between the experimental results from Exp. A, B and C, although, some quantitative differences can be observed in the peak values of ion current and electron density. The differences from Exp. A to Exp. B may be attributed to slight variations in the application of the BN coating on the thruster walls. The coating process leads to non-uniform grains of coating that may feature irregularities on the thickness, therefore affecting the nature of the plasma discharge and the losses to the walls. From Exp. A and B to Exp. C the difference in the measured values may be associated to the change in the experimental setup and to the BN surface degradation during thruster operation. It is noteworthy to mention that the translational motorized stage (present in Exp. C) is immersed in the plasma plume, therefore perturbations in the plasma expansion may occur. Inversely, the rotational stage present in Exp. A and B does not interfere as much with the plasma plume.

Repeatability of Exp. A is shown in Fig. 9.3, whose electron density measurements are characterized by the same experimental setup and the same thruster coating. Exp. A exhibits fair repeatability characterized by maximum relative variations within 15% difference, and a mean standard deviation of $1.5 \times 10^{14} \text{ m}^{-3}$, for the measurements of the 22nd, 23rd and 27th of April. A decrease of the measured plasma density can be observed from April 22nd to April 29th. This effect may be explained by modification in the BN coating during thruster operation. Modifications on the deposited BN layer were observed at the end of the campaigns of Exp. A and C.

9.3.2 Cross-field diffusion

The model presented in §9.2.2 was tested on its estimation capabilities of the experimental measurements. The model includes a phenomenological turbulence model featuring an empirical anomalous diffusion parameter α_t to be adjusted based on experimental measurements. While reducing the parameter below $\alpha_t = 0.02$ resulted in no variations on the plasma density response neither on thruster performances for a similar ECRT [57], a sensitivity analysis for $\alpha > 0.02$

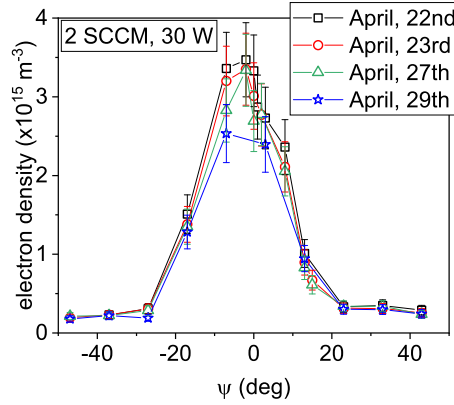


Figure 9.3: Repeatability of experiment A: the electron density angular measurements obtained with the CP at 2 SCCM, 30 W.

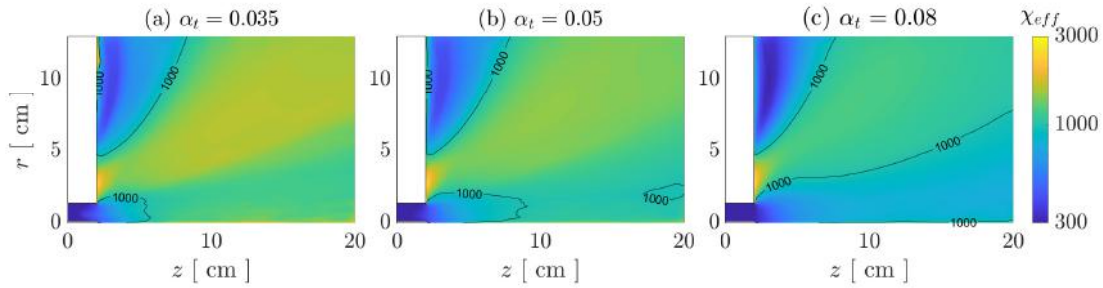


Figure 9.4: Comparison of the effective Hall parameter in the meridional plane for different anomalous diffusion coefficients at 2 SCCM - 30 W.

revealed plasma discharge variations due to significantly increased diffusion. A parametric investigation on α_t was performed to characterize the impact of enhanced cross-field diffusion on the stationary plasma discharge and overall thruster performances. In order to simplify the analysis, an homogeneous coefficient is considered in our simulation domain. This allows to provide a rough estimate of the anomalous diffusion within the plasma discharge, even though a more accurate analysis may require the use of an inhomogeneous coefficient, as it is expected to be dependent on local plasma phenomena.

The magnetic confinement is described by the Hall parameters defined in Eq. 9.2–8. In Fig. 9.4 we show the effective Hall parameter for the three cases of anomalous diffusion coefficient presented in this work. This parameter depends on both χ' and χ . On the one hand, in Eq.(9.2–8) it is shown χ' is constant and barely equal to α_t^{-1} . In fact it amounts for 28.05, 19.74, 12.39 for $\alpha_t = 0.035, 0.05, 0.08$, respectively. On the other hand, it depends on the Hall parameter χ which is inhomogeneous, and thus also χ_{eff} (see Fig 9.4). The Hall parameter depends on the total electron collision frequency ν_e , which is the sum of electron to heavy particle collision rates as: (i) inelastic ν_{inel} and (ii) elastic ν_{en} electron-neutral and (iii) Coulomb collisions ν_{ei} . The first two, scale with the neutral density which leads to significantly lower χ_{eff} at the source, that increases along the plume expansion as the density drops significantly faster than the applied magnetic field intensity. At the near lateral plume, low neutral density levels lead to enhanced electron magnetic confinement (i.e. higher χ_{eff}). For $r > 5$ cm, close to the thruster exit plane, a region of weak magnetic confinement appears due to rapid increase of ν_e there. It is motivated by the rise of the Coulomb collision frequency ν_{ei} up to values $\mathcal{O}(10^5$ Hz), sufficiently high to dominate ν_{eff} in this magnetically isolated region, and causing a rapid decline in the electron magnetic confinement. From Spitzer model [140] it is known that Coulomb collision frequency $\nu_{ei} \propto T_e^{-3/2}$, which decreases to values $\mathcal{O}(10^{-1}$ eV) due to limited perpendicular heat transport.

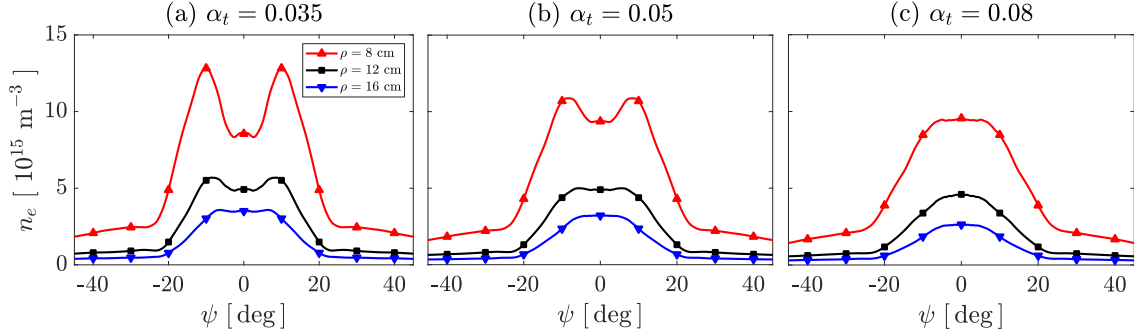


Figure 9.5: Angular electron density profiles at different ρ , for (a) $\alpha_t = 0.035$, (b) $\alpha_t = 0.05$ and (c) $\alpha_t = 0.08$ at 2 SCCM - 30 W.

As a result, the effect of increasing α_t on the effective Hall parameter can be subdivided in two. Firstly, as $\chi' \propto \alpha_t^{-1}$, the entire map of χ_{eff} decreases. Secondly, the effect on χ is related to the plasma properties resulting from the global changes in the plasma, which can be related to perpendicular gradients smoothing, lower electron temperatures, and greater axial gradients due to higher beam divergence.

Figure 9.5 displays the angular profiles of the electron density at $\rho = 8, 12,$ and 16 cm, for the different cases of α_t presented. The scale in the ordinate is kept constant for subplots (a)-(c) in Fig. 9.5 for the sake of comparison. For anomalous diffusion coefficients $\alpha_t \lesssim 0.035$ a doubly-peaked ion current and density is obtained by the simulations at $\rho = 16$ cm.

The double peak could be expected to appear naturally due to the boundary conditions imposed by the presence of the inner rod in the coaxial structure, provoking that the maximum plasma density is located at some radius within the source between the wall limits.

The cross-field diffusion allows to increase electron particle and energy perpendicular fluxes. In particular, the coaxial ECRT was shown [57] to provide with EM power absorption in a very specific location. This absorption region is not necessarily located at the region of ionization. Generally, it is located at higher radius than that of maximum radial EM fields at the ECR, and thus the region of maximum EM power absorption. Perpendicular fluxes are crucial to allow electrons to reach the absorption region and be energized. The EM heating leads to an increase in the electron pressure, but for low cross-field diffusion, magnetization limits perpendicular transport, and the electron density drops towards the absorption region. As a result, the EM energy is distributed amongst a smaller electron population, resulting in both higher electron temperature and perpendicular electron temperature gradients.

The enhanced perpendicular transport resulting from increased anomalous diffusion leads to mitigate this process, smoothing the perpendicular gradients, and replenishing the vicinity to the inner rod with electrons. The inclusion of α_t also contributes to this phenomenon by increasing the perpendicular heat conductivity and perpendicular heat transport. This readjusts the internal energy balance, allowing to distribute further cross-field wise. In Fig. 9.5 we can see this effect, where the presence of further accentuated peaks occurs for cases with lower anomalous diffusion. As a result the effect of insufficient anomalous transport is associated to the presence of singly or doubly-peaked angular electron density profiles and it is related to the dynamics within the source (i.e. $z \in [0, 2]$ cm) and the region of EM power absorption, which dominates the electron temperature in this type of thrusters. This effect extends to other variables as the the ion current (see Fig. 9.2a). However, the double peak in the ion current is also motivated by the presence of more significant ionization along acceleration streamlines closer to the symmetry axis. More details are given in §9.3.3.

A corresponding effect is observed along the plume. Moving downstream along the MN, the electrons demagnetize and enhanced cross-field diffusion leads to increase the electron perpendicular fluxes, which end up replenishing the low density region featured at $r = 0$. This mechanism can be noticed comparing Figs. 9.5(a), (b) and (c) where the double peaks appearing for upstream

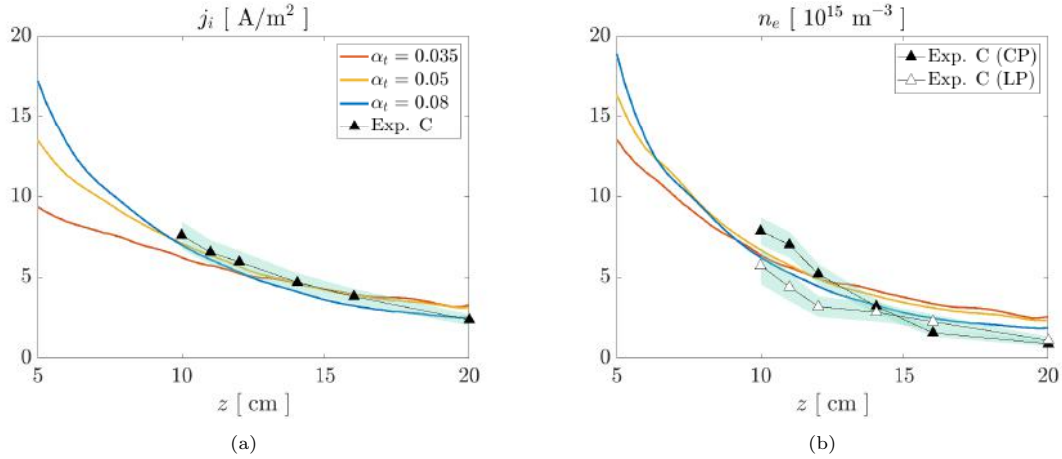


Figure 9.6: Comparison of the axial evolution of (a) the total ion current density and (b) the electron density at 2 SCCM - 30 W. The plasma potential is referenced with respect to the potential of the experiments at $z = 10$ cm.

for some cases are smoothed as the plasma expands along the MN.

Overall, the principal effect of increasing α_t is that both perpendicular electron current density and heat flux feature an increased perpendicular conductivity. This modifies the plasma balance and results in decreased perpendicular gradients, including those of the electrostatic potential. Thus, the ion confinement in the expansion is decreased, increase the beam divergence. As a consequence, as can be seen in Figs. 9.2a and 9.2b, the general trend is that both ion current and electron density decrease for α_t .

Figure 9.2 shows estimations of the angular profiles for several anomalous diffusion coefficients at the location of the measurements ($\rho = 16$ cm). The results obtained by the model predict that classical cross-field diffusion (i.e. $\alpha_t = 0$) cannot explain the profiles reported experimentally. For values below $\alpha_t \approx 0.035$, the qualitative angular profiles estimated by the simulation show a maximum current and electron density peaks at $\psi \neq 0$, denoting a “conical” beam shape. For $\alpha < 0.035$ the double peak increases and the maximum displaces to higher radius, creating a density depletion close to the thruster symmetry axis, i.e. $\psi = 0$. Therefore, the model estimates that the levels of anomalous diffusion are at least above $\alpha > 0.035$ for this ECRT at the investigated point of operation.

The comparison of experimental measurements and model estimations from Fig. 9.2 reveals that the model can capture quantitatively the angular profiles of both total ion current and electron density of the plasma discharge in a region of $|\psi| \in [7^\circ, 45^\circ]$. However, the simulated peak ion current is not seized by the model (Fig. 9.2a). For $\psi \in [-7^\circ, 7^\circ]$ the model underestimates the ion current, with a relative error between the case with $\alpha_t = 0.05$ and the measurements between 34% and 90%. Nonetheless, as we will show now, this difference is not as significant when comparing in terms of integrated ion beam current. An ion beam current $I_b(\psi_{max})$ can be obtained by integrating the charge density flux through a surface defined by maximum angle ψ_{max} as:

$$I_b(\psi_{max}) = \pi \rho^2 \int_{-\psi_{max}}^{\psi_{max}} j_i(\psi) \sin(|\psi|) d\psi, \quad (9.3-1)$$

where ρ is the distance of the probe with respect the center of rotation (i.e. the backplate, as shown in Fig. 9.1b). The total ion beam current is obtained for $\psi_{max} = \pi/2$ [138]. Here, a 45° ion beam current $I_b(\pi/4)$ is computed, due to limited availability of the experimental data (i.e. practical limitations related to the experimental setup and mounting). Yet, $I_b(\pi/4)$ allows to perform a representative comparison, as this angle span covers the beam core.

The 45° ion beam current $I_b(\pi/4)$ is 48.5, 42.9 and 37.1 mA for $\alpha_t = 0.035, 0.05$, and 0.08 , and 42.1 and 40.6 mA for Exp. A and B, respectively. Although the simulated-experimental difference close to the symmetry axis is significant, the $I_b(\pi/4)$ obtained in the case of $\alpha_t = 0.05$ highly agrees

α_t [-]	AD coefficient	Exp.	0.035	0.05	0.08
F [μN]	Thrust	601 ± 15	929	877	776
I_{sp} [s]	Specific impulse	318 ± 16	474	447	396
I_i [mA]	Total ion current	-	78	74	67
$I_b(\pi/4)$ [mA]	Ion current $\pm 45^\circ$	42.1 ± 5	48.5	42.9	37
η_F [%]	Thrust efficiency	3.1	7.2	6.4	5.0
η_u [%]	Utilization eff.	-	47.1	44.3	40.6
η_d [%]	Divergence eff.	-	80.1	72.0	63.1
$T_{e,max}$ [eV]	Maximum T_e	10.7*	23.5	20.0	16.0

Table 9.1: Thruster performances for simulations varying the anomalous diffusion coefficients compared to experimental measurements. Note that (*) measurement is taken at $z = 10$ cm.

with the experimental values.

Regarding the electron density shown in Fig. 9.2b, estimations from the model of the plasma density are more accurate, specially allowing to capture the peak electron density values, attained close to the symmetry axis. Although case with $\alpha_t = 0.08$ estimates Exp. B maximum density with a 2.5% relative error, case with $\alpha_t = 0.05$ captures as accurately, not only the maximum density value from Exp. A, but also its angular evolution.

Based on the above-mentioned criteria, the highest agreement between simulations and experiments is achieved for the case of $\alpha_t = 0.05$. Accordingly, this value is selected as the reference simulation case to continue the analysis in the rest of this work.

Figure 9.6 shows the comparison between measurements and simulations (with increasing α_t) for the axial evolution of both ion current and electron density. Simulation results are plotted between 5 and 20 cm; experimental data are obtained between 10 and 20 cm. The axial evolution of the total ion current density, shown in Fig. 9.6a, is properly captured by simulations with $\alpha_t = 0.05$ when compared to Exp. C. Indeed, the maximum relative error with respect to the measured value is below 6.5%. The higher the anomalous diffusion, the steeper the ion current axial gradient. This effect is explained by the increased beam divergence following the raise in perpendicular transport.

The axial density measurements are shown in Fig. 9.6b for the CP (solid black) and LP probe (hollow black). As can be noticed these two measurements feature the highest differences in the region closest to the thruster, approximately from 10 to 14 cm. It is in this region where the highest disagreement between numerical and experimental values is found.

The model underestimates the electron expansion along the plume, which denotes that the axial electron density gradient is not properly captured by the model, specially closer to the thruster. Further discussion on this disagreement is provided in §9.3.4.

9.3.3 Thruster performances and ion energy

In addition to the measurements performed on plasma properties, also direct thrust and power deposited in the plasma measurements were obtained. These results are shown in Table 9.1, compared against model estimations for the different cases considered.

The thruster performances are computed as shown in Chapter 9. The model overestimates the thrust measured by experiments and so do derived quantities as the specific impulse or the thrust efficiency. A 46% relative error is obtained between the measured and estimated thrust. It is known that background pressure can affect thrust measurements of EP devices. In particular, in the case of the ECR thruster, previous works [141] have reported a decrease in thrust measured from 800 to 400 μN for an increase in background pressure from 10^{-7} to 10^{-5} mbar-Xe. Wachs et al. [122] showed laser induced fluorescence measurements in a similar ECRT to the one analyzed in this work featuring a 37% ion energy drop for an increase in background pressure from 1.3×10^{-6} to 3.5×10^{-5} mbar-Xe. A background pressure of 4×10^{-6} mbar-Xe was measured in our experiments at the ONERA-B09 facility. This value lies within the range of values reported modifying ECR performances in the previous ECRT experiments mentioned. Thus, it can be expected that both

the thrust provided and mean ion energy in the plume when operating in total vacuum (i.e. free space), which represents the simulated conditions, would be greater than the one obtained in these experimental conditions. Moreover, the equivalent Xe neutrals density corresponding to the measured background pressure of 4×10^{-6} mbar-Xe is approximately 10^{17} m^{-3} . The reference simulation case used in this comparison estimates a xenon neutral density at the axis in the range of $10^{17} > n_n > 10^{16} \text{ m}^{-3}$ for $5.8 < z < 15.3$ cm. Therefore, the background pressure measured in this experiment is expected to alter the collisions in the plume and the expansion along the MN.

Two other figures influenced by anomalous diffusion are the utilization and divergence efficiencies. The utilization efficiency is the amount of ion mass flow rate per unit propellant flow rate used, that is propelled and accelerated along the plume. For increased cross-field diffusion the electron temperature in the discharge decreases as can be seen in Tab. 9.1. As a consequence, the level of ionization decreases, deteriorating the utilization efficiency of the discharge.

The drop in divergence efficiency noticed by increasing α_t is motivated by the enhanced perpendicular electron transport. Along the radial direction, the quasineutral plasma develops an electrostatic potential that confines the plasma, limiting radial ion currents. As electron magnetic confinement is deteriorated, the electrons can propagate further in the perpendicular direction and the radial electrostatic ion barrier is weakened, resulting in higher beam divergence. Overall, α_t increases the proportion of radial ion flux with respect to axial flux, which represents a drop in divergence efficiency.

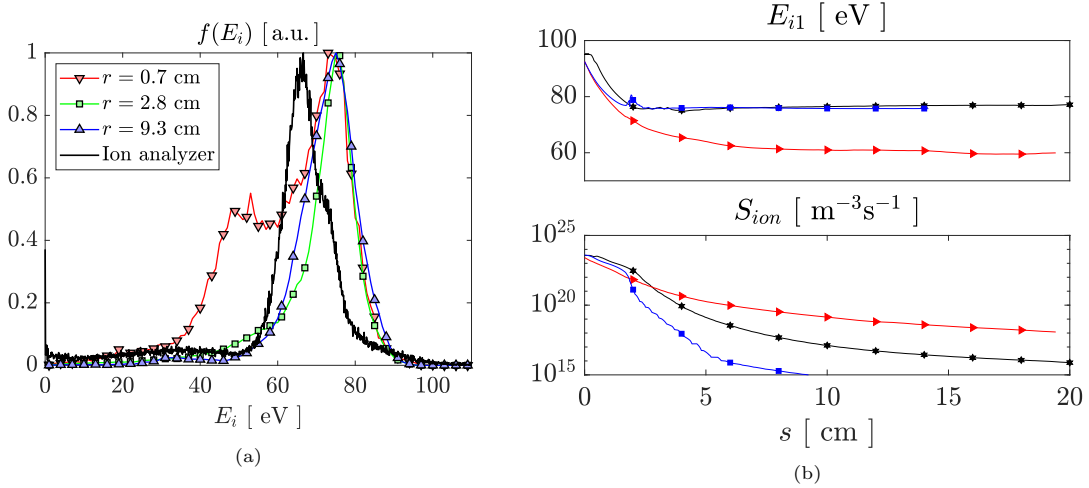


Figure 9.7: (a) Comparison of the ion energy distribution function of Xe^+ at the end of the simulated plume for different radii (scatter points) and the measured profile from the ion analyzer (solid black line); (b) Evolution along streamlines S1 (red), S2 (black), and S3 (blue) shown in Fig.9.1b of (a) Xe^+ total energy and (b) ionization source for simulation case with $\alpha_t = 0.05$.

The ion energy distribution function (IEDF) of singly-charged xenon ions is obtained for the reference simulation case at each surface element of the end of the simulated plume. These are compared to the distribution function measured with the ion analyzer. Note that the ion analyzer is located at the end of the chamber (i.e. $z \approx 1.7$ m from the thruster).

Figure 9.7a shows the averaged IEDF of the reference simulation case at different radii. The averaging has been computed over the adjacent elements considering a weighting factor proportional to the associated cell-volume, so that each cell's IEDF is representative of a cell's ion population. The distribution function is represented in arbitrary units.

As can be seen in Fig. 9.7a, the simulation reveals that the Xe^+ IEDF shape varies along the radial direction, featuring a low energy tail closer to the thruster axis. Nonetheless, the peak energies are not affected and are found at approximately 74 eV. The experimental mean ion energy are of the order of 65 eV. This difference may be attributed to background pressure effects, but there are other assumptions that could affect ion acceleration (e.g. dielectric boundary conditions).

In addition, it is noteworthy to mention that the ion analyzer and the thruster may not be perfectly aligned.

Figure 9.7b shows the evolution of the singly-charged ions average total energy and ionization source function along the arc-length parameter s of streamlines S1, S2 and S3, shown in Fig. 9.1b. The total energy takes into account the kinetic and potential energy. Along each streamline, ions exchange potential and kinetic energy, being the potential energy proportional to the total potential drop along the streamline. For an ideal expansion, ion total energy is conserved along every streamline. However, significant ionization along the acceleration results in newly generated ions with lower kinetic energy, that decreases the mean ion energy of the population accelerating along that streamline. Figures 9.7b(a) and (b) show that within the thruster chamber the ionization source is significant and consequently, the total energy of ions decreases. The ionization source function is proportional to the neutrals and electron density and is highly influenced by local electron temperature. The simulation ion source function is maximum at the thruster chamber, and decreases axially along the expansion. After exiting the thruster chamber ($s \gtrsim 2$ cm), the ionization source function features a clear-cut reduction in its derivative, for cases S2 and S3. These streamlines access the lateral near plume, where the ionization source decreases rapidly, following neutral density and electron density and temperature. Overall, streamlines with higher divergence angles feature smaller decrease in total energy as ionization becomes insignificant earlier in the acceleration. Ions accelerating along S1, the closest to the thruster symmetry axis, feature a 33% drop in total energy, and 26% compared to ions accelerating along S2 and S3. This is coherent to the low energy tail appearing in the IEDF shown Fig. 9.7a for lower radius (i.e. $r = 0.7$ cm). As expected, once the ionization is negligible, the ion energy stays constant along streamlines.

9.3.4 Electron cooling and other model limitations

The model used in this work, presented in §9.2.2, features a dominant parallel heat conductivity with respect to its perpendicular counterpart. As a result, after solving the energy balance, isothermal electrons are obtained along magnetic field lines. The symmetry axis, which is a magnetic field line, features isothermal electrons as can be noticed in Fig. 9.8. Along these lines, Boltzmann relation $\phi - \phi^* = \ln(n/n^*)T_e/e$ holds. It is known that the isothermal limit not only assumes that there is no electron cooling in the MN expansion, but also imposes that $\phi - \phi^* \rightarrow -\infty$ as $n/n^* \rightarrow 0$, which is inadequate for infinite expansion modeling. Results for the axial evolution of the electron temperature are shown in Figure 9.8b, where the plume of an ECRT is seen to exhibit electron cooling as was found in the past in Ref. [52]. Electron cooling is measured experimentally, as the electron temperature decreases with z from 10.7 to 5.2 eV between $z = 10$ and $z = 20$ cm.

Although not justified for a collisionless plasma plume, the polytropic state law

$$T_e = T_{e0} \left(\frac{n_e}{n_{e0}} \right)^{\gamma-1}, \quad (9.3-2)$$

where T_{e0}, n_{e0} are the electron temperature and density at the thruster exit plane (i.e. $z = 2$ cm), and γ the polytropic expansion coefficient, has been used in the past to model electron cooling and successfully provide estimations of the general characteristics of a plume expansion [142, 143]. For Exp. C, averaging the axial density measurements shown in Fig. 9.6b and combining them with the LP electron temperature measurements, an experimental polytropic coefficient $\gamma = 1.34 \pm 0.04$ is obtained. Merging the numerical values for $T_{e0}, n_e(r=0), n_{e0}$ with the experimental polytropic coefficient as in Eq. (9.3-2), an axial electron temperature evolution is obtained for each α_t case (shown in dashed diamond in Figure 9.8b). These profiles are compared to the experimental electron temperature measurements. The experimental temperature is best captured for $\alpha_t = 0.05$ case.

As in previous works [52], it was noticed that taking subsets of experimental data at different axial positions would result in different polytropic coefficients. As a consequence, we can conclude that the MN of an ECRT cannot be modeled by a polytropic law. The electron temperature is

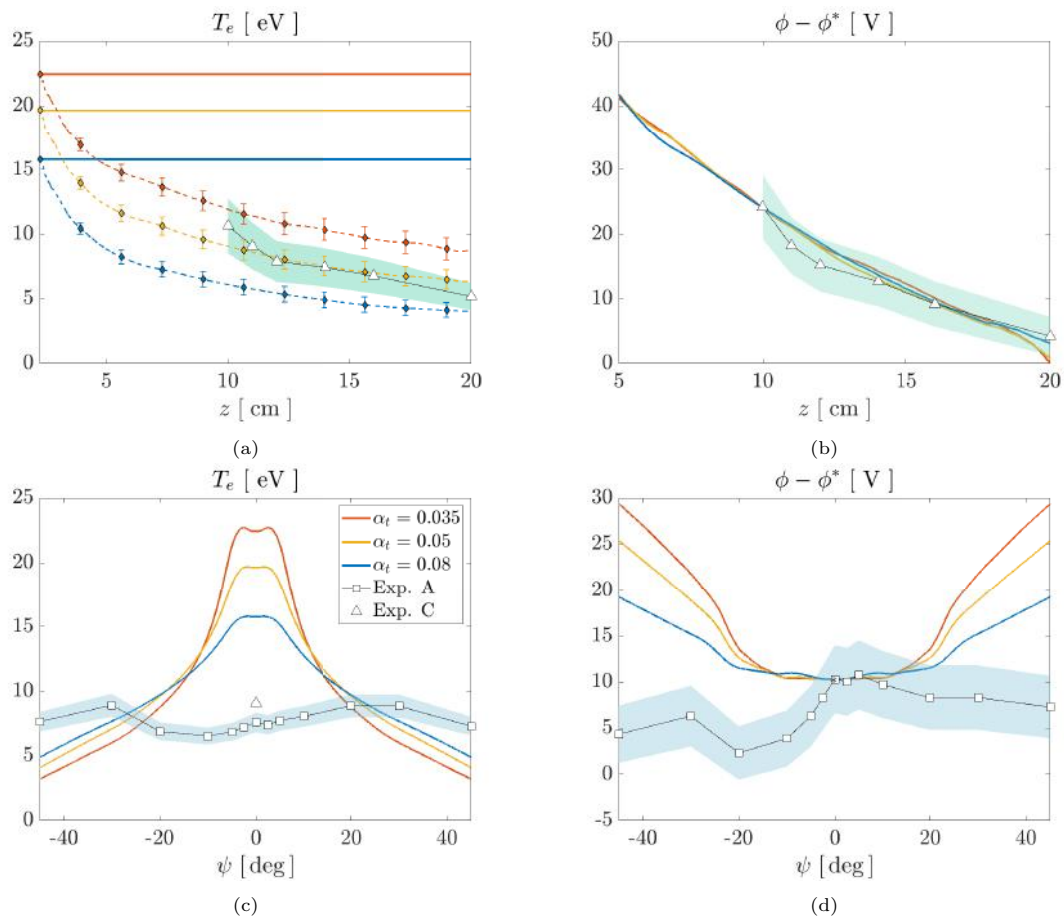


Figure 9.8: Comparison of Langmuir probe measurements of the electric potential and electron temperature to model results at 2 SCCM - 30 W. The reference plasma potential (ϕ^*) is taken with respect to the experimental values at $z = 10$ cm for the axial profile, and at $\psi = 0^\circ$ for the angular.

known to decrease along magnetic field lines even in a collisionless scenario, far away from local thermodynamic equilibrium, as a consequence of the kinetics of the electron population and further refined models are needed to model the plume expansion in a MN [118, 144, 145].

As the model considers a finite simulation domain, it requires the intuition and definition of adequate boundary conditions. In this model dielectric boundary conditions are used for the open boundaries. Although this boundary condition is simpler to implement as it is local, the definition of a null integrated current boundary condition is more realistic, which is another critical improvement to be carried out in the forthcoming model developments. In Fig. 9.8a it can be noticed that the estimated potential drop for all cases reproduces fairly that of experiments. However, the disagreement is expected to increase for longer simulated plumes, as electron cooling in the plume leads to finite electrostatic potential drop, opposite to the infinite drop estimated in the isothermal limit.

Another aspect not considered up to this point is that the diffusion coefficient for particle is not necessarily that for energy diffusion. Although the angular electron density profiles were captured for $\alpha_t = 0.05$, the electron temperature angular profiles shown in Figure 9.8c disagree. Despite the fact that the collisionless cooling, not considered in this model, may play a significant role, the disagreement could also be explained by insufficient energy anomalous diffusion at the thruster source. As can be seen, from $\alpha_t = 0.035$ to 0.08 the peak electron temperature decreases by 32% and, the angular profile is smoother the higher the anomalous transport. This effect can be also seen for the plasma potential shown in Figure 9.8d.

However, a single anomalous transport coefficient is unable to capture both electron temperature and density measurements simultaneously. In this work, the anomalous transport coefficient used in both momentum (i.e. \mathbf{F}_{turb}) and heat flux (i.e. \mathbf{Y}_{turb}) contributions is equal. Fixing the momentum contribution to that of $\alpha_t = 0.05$, a sensitivity analysis on the anomalous heat transport coefficient (i.e. in \mathbf{Y}_{turb}) showed that it has a dominant effect on the electron temperature while having minor impact on angular distributions of both electron density and ion current. In conclusion, the ECRT discharge is likely to feature greater levels of anomalous cross-field energy diffusion than particle diffusion.

9.4 Concluding remarks

In this work, angular and longitudinal probe measurements of thrust balance measurements, and self-consistent numerical simulations of an ECRT prototype that integrate the slow plasma dynamics and the fast electromagnetic fields, have been compared with the main goal of benchmarking the physical model of this device. This is part of the ongoing effort toward the improvement and validation of our current understanding of the phenomena involved in the operation of ECR thrusters, essential for the eventual optimization of the technology.

A thorough comparison is hindered by the inherent limitations of experimental measurements, namely (1) the error associated to probe measurements, (2) the inability to obtain measurements closer to the thruster exit or even inside the ionization chamber without introducing an excessive perturbation, (3) the influence of background pressure on the magnetic nozzle expansion, and (4) the effect of wall ageing on repeatability and thruster operation. Nevertheless, and taking all these caveats into account, the model shows reasonable to good agreement with the observed plasma density and ion current density angular and longitudinal profiles, downstream ion distribution function, and thruster performances.

It has been shown that the cross-field plasma transport is larger than the one predicted by classical models, and that some form of enhanced (anomalous) transport is needed to correctly reproduce the plasma and thrust measurements. The present work has explored this with a simple, phenomenological, uniparametric anomalous transport model, similar to those used in Hall effect thruster modeling, that lowers the effective Hall parameter in the plasma, finding that values of $\alpha_t \simeq 0.05 - 0.08$ adequately reproduce the behavior of the measurements. An annular-shaped plasma profile is seen to form in the source region due to the presence of the central antenna

pole, which gradually evolves into a single-peaked profile downstream. The distance in which this transition occurs is seen to depend on the anomalous transport parameter. To our knowledge, this is the first time that some form of anomalous transport has been suggested in ECRTs. More advanced models are likely needed to properly reproduce the complexities of their physics and constitute an open area of research.

The comparison has also enabled the identification of key areas of improvement of the model. Firstly, the electron heat flux closure relation presently employed must be corrected, and possibly incorporate the latest kinetic modeling results [145, 146], to accurately predict the observed electron cooling along the magnetic nozzle. Secondly, boundary conditions for the electrostatic potential must be designed carefully to better represent the expansion of a plasma plume to infinity. Additionally, background pressure effects could be included in the model, as this would lead to a better understanding of their influence on the measurements and facilitate the “translation” of vacuum-chamber data to in-flight conditions.

On the experimental side, any improvements to mitigate the drawbacks listed above would enable a deeper validation of the model. In particular, measurements of the plasma properties further upstream (perhaps using different plasma diagnostic techniques than the ones employed here to limit perturbation of the thruster operation) would be needed to elucidate the right physics of the plasma source region and near plume, the plausible existence of an annular-shaped, hollow plasma due to the presence of the antenna in this region, and better assess the magnitude of cross-field transport.

Chapter 10

Conclusions

In order to conclude this thesis, its major contributions have been summarized in §10.1, followed by the future research lines identified to continue this work, shown in §10.2.

10.1 Main thesis contributions

In this thesis we have developed, applied and partially validated an ECRT simulation model covering the main physical phenomena taking place in ECRT plasma discharges.

The one dimensional model of Williamson [34] for the propagation and absorption of RHP waves in ECR plasmas has been thoroughly revisited and its main details have been discussed, including the asymptotic solutions obtained by Budden [55]. The effects of the dimensionless electron density and collisionality on the propagation and absorption of RHP waves crossing a cutoff resonance system have been investigated for both, waves propagating in the (i) increasing and (ii) decreasing magnetic field direction. The collisionless estimations of the reflection, transmission and absorption coefficients obtained by Budden were captured by the simulations including wave damping. Only for both $\gamma \sim \eta$ or greater, and in the case of RHP waves propagating in the increasing magnetic field direction, the collisionless estimations have been observed to fail as the cutoff structure is sufficiently modified by such level of collisionality. As a result, the reflection coefficient decreases, and both the transmission and absorption coefficients increase. This level of electron collisionality is far from the one expected in ECRTs (i.e. $\eta \gg \gamma$). Instead, the main effect of including damping in the cold plasma tensor formulation, and thus, in the waves dispersion relation, is the thickness increase of the resonant region.

The collisionless electron individual response to RHP wave fields has been investigated and compared to the analytical solution obtained by Lieberman [30], based on the stationary phase method. The analytical solution has been revisited and the main conclusions on the heating mechanism for a uniformly distributed electron population in phase are found to be: (i) the mean energy gain of the electrons due to ECR is always positive; (ii) the higher both the gradient in the normalized magnetic field and electron parallel velocity at the ECR region, the lower the energy gain per electron; (iii) the energy gain is proportional to the RHP wave amplitude at the resonance squared, leading to the need of determining accurately the electric field wave to estimate absorption properly; (iv) the higher the initial perpendicular velocity of electrons, the higher the electric field required to produce an energy gain to all phases; (v) for an increasing ratio $\Delta A/A(-\infty)$, the electron phases approach to a single gyrophase, with a phase dispersion that decreases with that ratio; as a result, after a resonance crossing with significant heating, electrons “lose track” of their initial gyrophase and the resulting electron population features a phase synchronization or

coalescence. The analytical solutions based on the stationary phase method have been compared to the exact numerical solution utilizing (i) a stationary electric field which is that of the solution at the resonance, i.e. $\bar{E} = \bar{E}_-(0)$; (ii) the solution of the RHP wavefield including its axial evolution (i.e. $\bar{E} = \bar{E}_-(s)$). The results verify that case (i) recovers the analytical solution, and that for case (ii) it is shown that the analytical solution overestimates absorption, specially for cases with $\eta \geq 1$.

One of the principal outputs of this thesis is a two-dimensional axisymmetric full-wave model of the electromagnetic wave propagation and power absorption in ECRT plasma discharges. The development of the model followed a thorough literature review of the existing models of different phenomena involved in the propagation of electromagnetic waves in magnetized plasmas and also, in the absorption of electromagnetic waves in ECR plasmas. The two-dimensional axisymmetric model has been implemented in a computational code called ATHAMES. The code has been implemented in object oriented programming language C++, and its design has been simplified featuring a modular architecture that facilitates extending its capabilities with future model upgrades. The code uses the finite element method to solve Maxwell's inhomogeneous wave equation in the presence of ECR plasmas. The method allows obtaining numerical solutions taking advantage of the benefits of using unstructured meshes, including (i) the ability to solve in arbitrary and complex geometries, allowing to define curved geometries avoiding stair-stepping issues, and (ii) the capability of defining local refinement strategies based on the requirements of each region in the simulation domain. This latter feature is utilized to carry out a predictive mesh refinement, where the mesh element size distribution is defined by the estimated local minimum wavelength. This minimum wavelength is computed employing the dispersion relations for each propagating mode at each point using the collisional dielectric tensor formulation and the local plasma and magnetic properties. This feature allows to obtain accurate and efficient solutions at each node in the simulation domain. Specifically, predictive refinement has been proven to be relevant in the mitigation of high-frequency oscillations found in the electromagnetic field solutions in the vicinity of UHR and the \mathcal{P} cutoff surfaces. A thorough verification campaign of ATHAMES has been carried out using mainly the MMS to develop several integration tests. Other analyses, as the effect mesh refinement on the electromagnetic solutions have also been verified. Additionally, special attention has been devoted to the effects of using a collisional cold plasma tensor formulation. Similarly to what was found for the one-dimensional model, the results of the two-dimensional model showed that the fundamental effect of wave damping is to widen the thickness of the resonant absorption region, in general located at the ECR region for the plasmas investigated in this thesis.

The code ATHAMES has been coupled to the hybrid PIC/fluid plasma transport code HYPHEN to obtain coupled plasma transport and electromagnetic wave simulations approaching self-consistency. The codes have been utilized to characterize the plasma properties and thruster performances of an ECR thruster operating at 30 W input power and 0.2 mg/s xenon flow rate, and to understand its principal operational principles. Maximum electron density and pressure have been found to be located at an intermediate radius. Azimuthal electron current are found to shear at the radius of maximum electron pressure. Two differentiated regions of the plasma have been observed: one diamagnetic with respect to the applied magnetic field that generates positive thrust, and another one, paramagnetic, with a negative thrust contribution. An electron temperature of approximately 28 eV has been obtained at the symmetry axis, consistent with experimental values reported by Lafleur et al. [119] and later by Correyero et al. [52]. Results also revealed mutual dependency between the quasi-steady plasma properties and the fast electromagnetic fields. For instance, as could be expected, the plasma density has been seen to influence the electromagnetic propagation and absorption landscape within the thruster (i.e. the location of the different cutoffs and resonances as the UHR). The electron temperature has been observed to be driven mainly by the power absorption profile, suggesting its dominant character in the electron internal energy balance. It has been shown that multiple electromagnetic propagation regions coexist within these plasma discharges. Wave structures were not observed in the majority of the domain, which could be anticipated given the small thruster dimensions and the presence of a dominant evanescent region downstream the ECR (i.e. region V). The only exception found occurs in the vicinity of

the inner rod, where a short wavelength wave mode is observed. This wave mode appears as a result of the “opening” of an EM wave propagation channel close to the inner rod in the form of CMA regions III and IV. This channel is opened due to the plasma density depletion found in the vicinity of the inner rod which is mainly explained by wall recombination. Regarding power absorption, it has been verified that the estimated location of the principal part of electromagnetic power absorption is located at the ECR region. Interestingly, it has been shown that in the case of coaxial ECRTs, the power absorption takes place at the ECR region and close to the inner rod surface. The EM power absorption has also been demonstrated to be driven mainly by radial EM-wave electric fields close to the ECR. These fields exhibit their maximum magnitude in the vicinity of the inner rod, both due to the presence of this propagation channel and the natural topology of the TEM mode in a coaxial geometry. As a consequence of this power absorption shape, and its dominance in the electron internal energy balance, the location of the maximum electron temperature was also found close to the inner rod. The ratio of reflected power has been observed to be below 10%, denoting the good coupling efficiency obtained with this technology. Fair agreement with experimental measurements [26] of the ECRT simulated has been obtained, estimating a rather poor overall thruster efficiency around 6%. The thrust is also captured by the model, and a reasonably good agreement is found in the proportion of magnetic (62%) to total thrust reported by experiments [123]. The obtained meager utilization efficiency (around 50%), also in agreement with experimental measurements, has been identified previously in other electrodeless thrusters as the HPT [125]. Another hindering characteristic of this thruster is that 63% of the power fed to the thruster is lost through the walls in the means of heat, specially through the inner rod surface (32.1%) and the backplate (25.2%). The latter is characteristic of the magnetically unshielded backwalls [98, 124]. Nevertheless, the heat load at the inner rod is much greater due to its much smaller area compared to that of the backplate. This, combined to the considerable ion impact energies found at the inner rod, could explain the erosion observed experimentally in this component. Further efforts should be taken on modifying the thruster design to reduce the heat wall losses, specially at the inner rod, but also to a minor degree at the backplate.

A thorough parametric investigation has been carried out on both the ECRT operating point and its design, to firstly analyze its performances, and secondly, the evolution of the plasma variables, seeking for potential improvements on the thruster design. The energy per particle (P_a/m) has been observed to be a key parameter driving thruster performance. This parameter is strongly correlated to the electron temperature which affects considerably the utilization and also the wall losses. The former showed a major limitation due to an undesirably high level of ion recombination at the walls, which resulted in neutrals being ionized multiple times on average. The latter were found to be dominated by the electron contribution, as SEE saturation has been observed to occur in all thruster walls close to the inner rod, as the electron temperature close to these walls exceeded the half-crossover energy of boron nitride. As a result of this work it has been suggested to modify the material used for the thruster walls. No improvement has been found on the overall performances when modifying the operating point, being the nominal case close to the optimal in terms of overall thrust efficiency. Regarding the analysis performed on the thruster design two main design choices were analyzed for the ECR30 thruster: (i) the location of the ECR region and (ii) the injector location and orientation. The displacement of the ECR further downstream while still within the thruster chamber has been found to provide no significant performance variations. The main difference observed was the displacement of the fundamental power absorption region following the ECR location. The special case of an ECRT without ECR (i.e. located upstream the thruster backplate) resulted in EM power absorption located at the EM parametric region III, close to the UHR. As it could be expected, the ECR has been demonstrated to be a more effective method of electromagnetic power absorption than the UHR, and this case proved to have both lower performances and maximum plasma density achieved in the discharge. Regarding the injector location, it has been shown that radial injection results in improvements on thruster performance as it increases the homogeneity of the neutral density within the thruster chamber, increasing the ionization close to the inner wall, decreasing the local temperature there, and as a result, lowering wall losses with respect to axial injection configurations.

The analysis carried out on alternative propellants assessed the expected behavior of the thruster performances with the propellants used. Overall, differences among xenon, krypton and argon were minor. Argon exhibited the worst performances amongst all the alternatives, motivated by both its higher ionization cost and its lighter molecular mass (this latter increasing the acceleration of the propellant), driving down plasma density of the discharge. Surprisingly, this effect was compensated in the case of krypton, as it featured improved energy efficiency as a result of the decreased wall losses. In conclusion, krypton was suggested as a feasible cost-effective candidate given its lower commercial cost compared to xenon.

The investigation on upscaling the device showed that several features are characteristic of the ECR thruster technology, as, for instance, the maximum electron density and pressure being located at an intermediate radius, the shearing azimuthal electron currents, the differentiated diamagnetic and paramagnetic regions, the latter resulting in a negative thrust contribution, and also the electron density depletion close to the inner rod. Other features as the location of the region of maximum power absorption have been shown to be maintained when the thruster was scaled up. Amongst the fundamental differences, the 200W ECRT versions resulted in *(i)* increased utilization efficiencies (up to a 40%) due to the increase in the ionization length ratio obtained by the increase in thruster length, *(ii)* decreased wall losses expected since it decreased the area to volume ratio, *(iii)* increased energy efficiency and *(iv)* overall an increase of 100% in relative thruster efficiency.

As a final part of this thesis, in a joint collaboration with ONERA research center, a combined numerical and experimental campaign carried out at their facilities, has enabled the comparison of simulation and measurement data. The presented results show a reasonable to good agreement between the model and the experimental data. It has been shown that the cross-field plasma transport in the ECRT is larger than the one predicted by classical models, and that some form of enhanced (anomalous) transport is needed to correctly reproduce the plasma properties and thrust measured. This comparison has explored this matter with a simple, phenomenological, uniparametric anomalous transport model, which lowers the effective Hall parameter in the plasma, finding that values of $\alpha_t \simeq 0.05$ partially reproduce the behavior found in the measurements. An annular-shaped plasma profile has been seen to form in the source region in the model due to the presence of the inner rod, which gradually evolves into a single-peaked profile downstream. The distance in which this transition occurs is seen to depend on the anomalous transport parameter. The disagreements and a sensitivity analysis made on both anomalous diffusion coefficients (momentum and heat) suggested that the heat anomalous diffusion coefficient should be greater to reduce the differences between measurements and experiments. Further advanced models are needed to capture all the details of the complex phenomena taking place in ECRT discharges. Specifically, several potential improvements on the electron fluid were identified and are commented in §10.2. A thorough comparison is hindered by the inherent limitations of experimental measurements, namely (1) the error associated to probe measurements, (2) the inability to bring the electrostatic probes too close to the thruster ionization chamber without introducing an excessive perturbation, (3) the influence of background pressure on the magnetic nozzle expansion, and (4) the effect of wall ageing on repeatability and thruster operation. Nevertheless, and taking all these caveats into account, the model shows reasonable to good agreement between the observed plasma density and ion current density angular and longitudinal profiles, downstream ion distribution function and thruster performances.

10.2 Future research lines

Several improvements of the different models used in this thesis have been identified. Firstly, the current version of ATHAMES is ready to be extended to all possible axisymmetric modes which would allow to model other EP technologies utilizing electromagnetic power absorption as means of plasma generation and energization (e.g. the HPT). Other features that could be introduced are other boundary conditions as an absorbing boundary condition, the implementation of perfectly

matched layers for adequate simulation of electromagnetic problems with significant stray radiation.

Additionally, MPI parallelization of ATHAMES would be suggested if future simulations required scalability. Also, as the condition number of the linear systems to be solved would benefit from a complex variational formulation, the use of complex number solvers would also be recommended, being this feature available in a newer versions of MFEM library. Alternatively, the use of different preconditioners for accelerating the problem solution still using a real variational formulation could be investigated.

The collisional cold plasma model used in this thesis employs the effective electron collisionality obtained from the electron fluid model. Although the impact of this variable on the model solutions applied to the ECRT has been estimated to be minor, alternative methods for its estimation could be used, including kinetic effects utilizing an electron distribution function, and of ions if their susceptibility was not negligible for the application studied.

The validation campaign carried out with the real prototype revealed several improvements to be implemented in the electron fluid model of HYPHEN, among which three aspects are highlighted. Firstly, the electron heat flux closure relation presently employed must be corrected, and possibly incorporate the latest kinetic modeling results [145, 146], to accurately predict the observed electron cooling along the magnetic nozzle. Secondly, boundary conditions for the electrostatic potential must be designed carefully to better represent the expansion of a plasma plume to infinity. Thirdly, background pressure effects could be included in the model, as this would lead to a better understanding of their influence on the measurements. This will also be an interesting tool to facilitate the vacuum-chamber to in-flight data comparison and improve the understanding of the effect of the test facilities on the measured performances on ground, which is known to be relevant for these devices [141]. Finally, an additional area of further work is the investigation and the formulation of more advanced anomalous transport models for the ECRT, starting with non-uniform anomalous transport coefficient profiles.

Chapter A

Simulation list

This appendix gathers the simulation results of the parametric investigation (see Chapter 6).

Simulation outline

- CASE REF: reference simulation of the ECR thruster. The simulated domain extends 6 cm axially and 4.125 cm radially. The transport simulation domain includes the top plume that extends from the last applied magnetic field line exiting the thruster chamber to the maximum radius of the domain. Simulation includes both singly-charged and doubly-charged ionization.
- CASE I2: in this simulation the plume is truncated close to the thruster. Modifications are summarized in section §6.1. The simulation domain extends 4 cm axially and the top plume has been removed. CEX collisions have been deactivated. Both PIC-mesh and MFAM have been coarsened. The timestep of ions and electrons has also been increased.
- CASE RED: case I2 without double ions. It is the so-called “reduced” case and has been used as the nominal simulation to vary parameters to perform this parametric analyses.
- CASE M0: case RED with injected mass flow rated modified to 0.15 mg/s.
- CASE M2: case RED with injected mass flow rated modified to 0.25 mg/s.
- CASE P0: case RED with injected electromagnetic power modified to 15 W.
- CASE P2: case RED with injected electromagnetic power modified to 45 W.
- CASE ECR0: case RED with a scaling factor used in the applied magnetic field intensity, $B_{factor} = 0.8$ so that the ECR is located behind the thruster backplate (see Fig. 6.21).
- CASE ECR2: case RED with a scaling factor used in the applied magnetic field intensity, $B_{factor} = 1.25$, displacing the ECR slightly downstream (see Fig. 6.21).
- CASE INJZ0: case RED with injector port (still at the back plate) moved towards the inner rod and closer to the applied magnetic field line exhibiting maximum electron temperature in the thruster (see details at Tab. A.1).
- CASE INJR: case RED with injector port located at the lateral, close to the backplate (see details at Tab. A.1).

Parameter	Name	Units	REF.	I2.	RED.	M0	M2	P0	P2	ECR0	ECR2	INJZ0	INJR	ON.51W[26]	ON.29W[26]
\dot{m}	Mass flow rate	mg/s	0.2	0.2	0.2	0.15	0.25	0.2	0.2	0.2	0.2	0.2	0.2	0.2	0.2
P_f	Power input / forwarded	W	30	30	30	30	30	15	45	30	30	30	30	51 ¹	29 ¹
B_{factor}	Applied magnetic field scaling factor	[-]	1	1	1	1	1	1	1	0.8	1.25	1	1	1	1
z_{inj}	Injection surface center z	[cm]	0.0	0.0	0.0	0.0	0.0	0.0	0.0	0.0	0.0	0.0	0.4	-	-
r_{inj}	Injection surface center r	[cm]	0.5735	0.5735	0.5735	0.5735	0.5735	0.5735	0.5735	0.5735	0.5735	0.35	1.375	-	-
\mathbf{n}_{inj}	Injector surface normal	[-]	1 _z	-1 _r	1 _z	1 _z									
η_c	Coupling efficiency	%	91.8	92.6	91.1	96.1	80.0	87.6	91.6	18.1	98.2	64.5	68.5	-	-
P_a	Absorbed power	W	26.9	27.8	27.3	28.8	24.0	13.1	41.2	5.42	29.5	19.3	20.6	32.2 ¹	18.3 ¹
F	Thrust	mN	0.840	0.741	0.728	0.530	0.781	0.479	0.827	0.238	0.720	0.631	0.713	0.850	0.420
F_i	Ion thrust	mN	0.611	0.496	0.489	0.349	0.515	0.296	0.564	0.124	0.485	0.421	0.490	-	-
F_e	Electron thrust	mN	0.162	0.186	0.169	0.125	0.193	0.120	0.197	0.050	0.173	0.139	0.149	-	-
F_n	Neutral thrust	mN	0.067	0.059	0.070	0.056	0.073	0.063	0.066	0.064	0.062	0.070	0.073	-	-
I_{sp}	Specific impulse	s	428	378	371	360	319	244	422	122	367	322	364	429	214
I_i	Ion current	A	0.082	0.087	0.071	0.049	0.09	0.055	0.08	0.03	0.076	0.068	0.074	0.062	0.036
η_F	Thrust efficiency	%	6.6	5.3	4.9	3.2	5.1	4.4	4.1	2.7	4.4	5.1	6.2	5.6 ¹	2.4 ¹
η_u	Utilization efficiency	%	50.0	53.0	49.0	44.0	49.0	37.5	54.5	20.1	52.0	46.0	50.5	45.1	25
η_e	Energy efficiency	%	25.3	22.9	22.5	16.5	23.2	23.7	17.8	23.4	19.2	22.0	24.9	16	-
η_c	Conversion efficiency	%	32.2	25.1	25.9	26.3	25.2	25.6	25.3	28.4	26.0	28.2	28.6	-	-
η_d	Divergence efficiency	%	91.2	85.8	84.1	80.4	84.8	80.6	85.3	61.3	83.3	85.3	86.8	70	70
ϵ_{exc}	Excitation losses	%	4.8	4.9	5.1	2.7	7.1	7.2	3.5	9.1	4.3	7.3	8.8	-	-
ϵ_{ion}	Ionization losses	%	7.0	7.1	7.7	5.0	10.1	10.6	5.9	12.2	6.6	9.8	11.2	-	-
ϵ_{wall}	Wall losses	%	63.0	65.4	67.3	76.4	60.1	59.2	73.5	59.4	70.5	62.4	56.9	-	-

Table A.1: Outline of cases studied in the parametric investigation shown in chapter 6, including operational parameters, electromagnetic performances, thruster performances and losses conspectus. ONERA's experiments P_f includes the power losses in the cables, the feed-through, the DC block, and the connectors/adapters, which are estimated to be at least 2dB. The overall thruster efficiencies shown here use the estimated absorbed power for the experiments.

Case REF

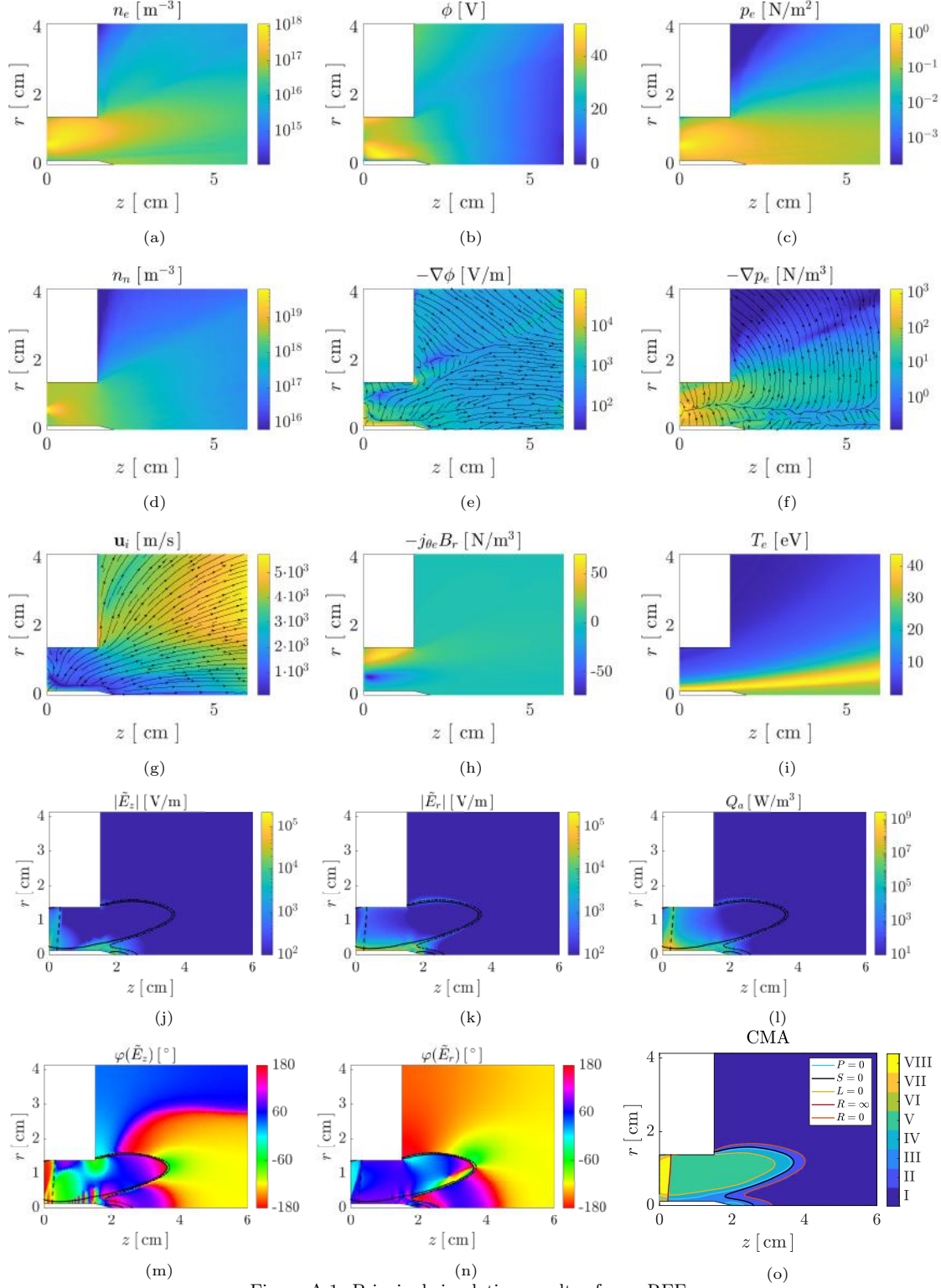


Figure A.1: Principal simulation results of case REF.

Case I2

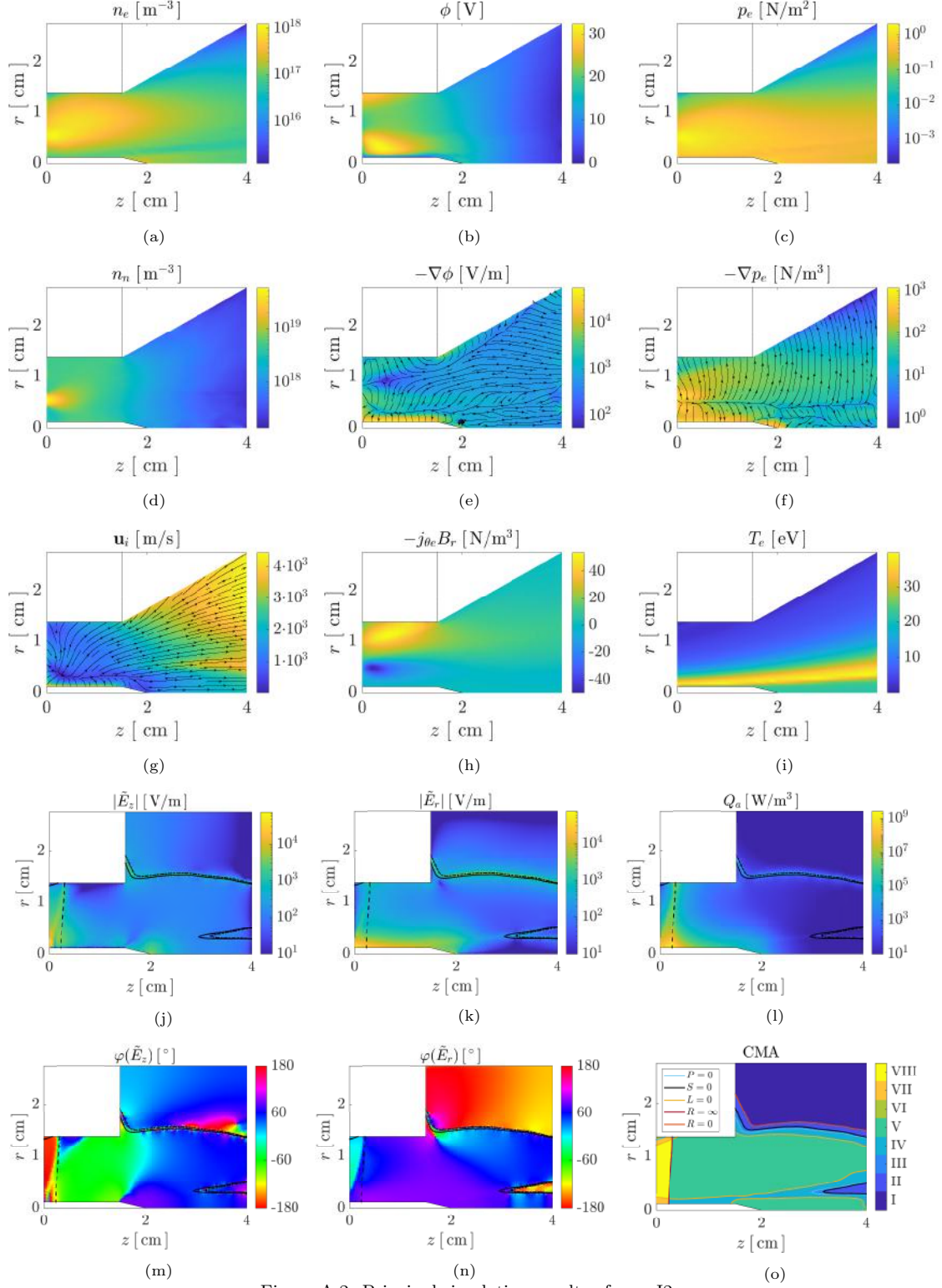


Figure A.2: Principal simulation results of case I2.

Case RED

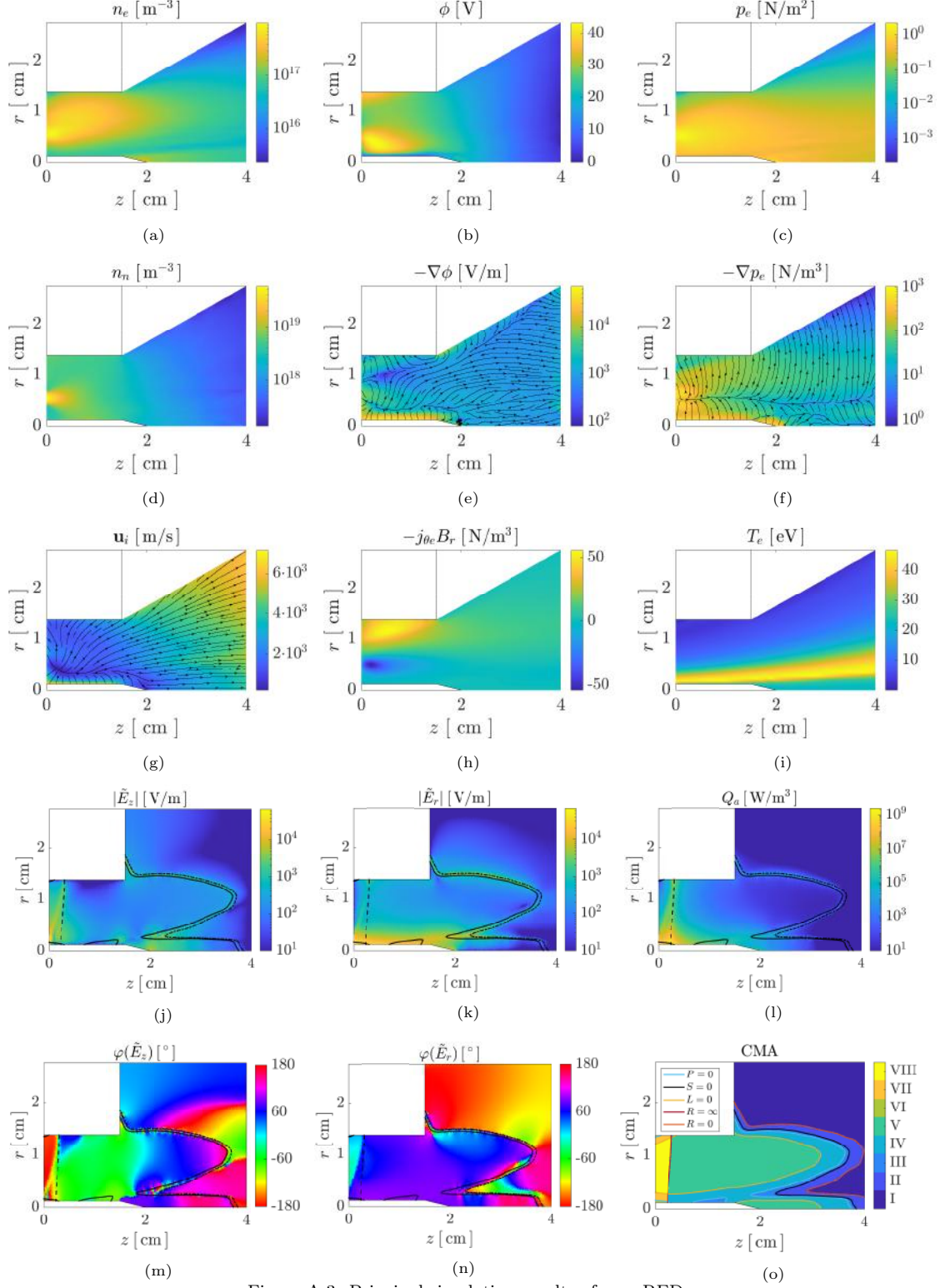


Figure A.3: Principal simulation results of case RED.

Case M0

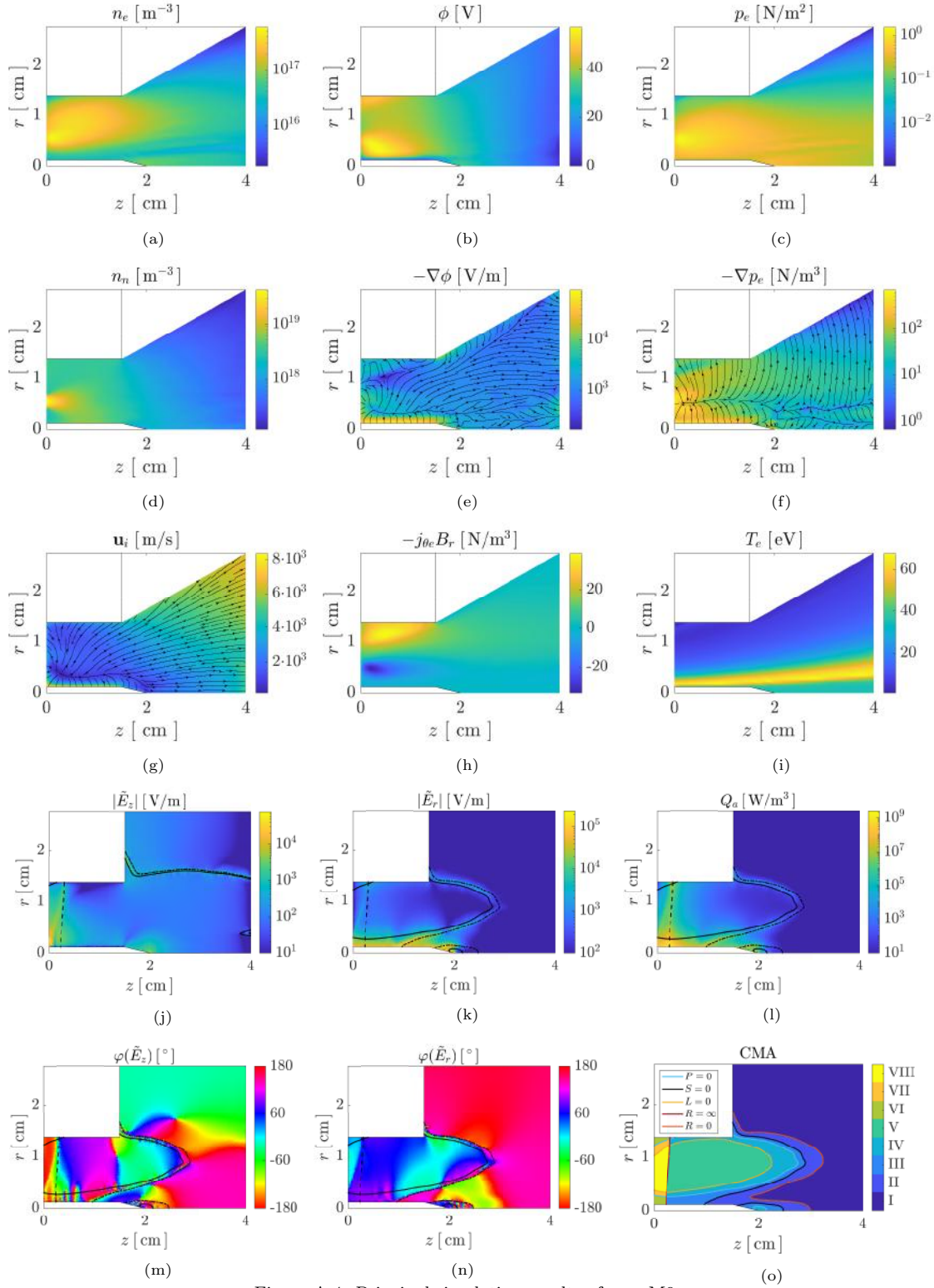


Figure A.4: Principal simulation results of case M0.

Case M2

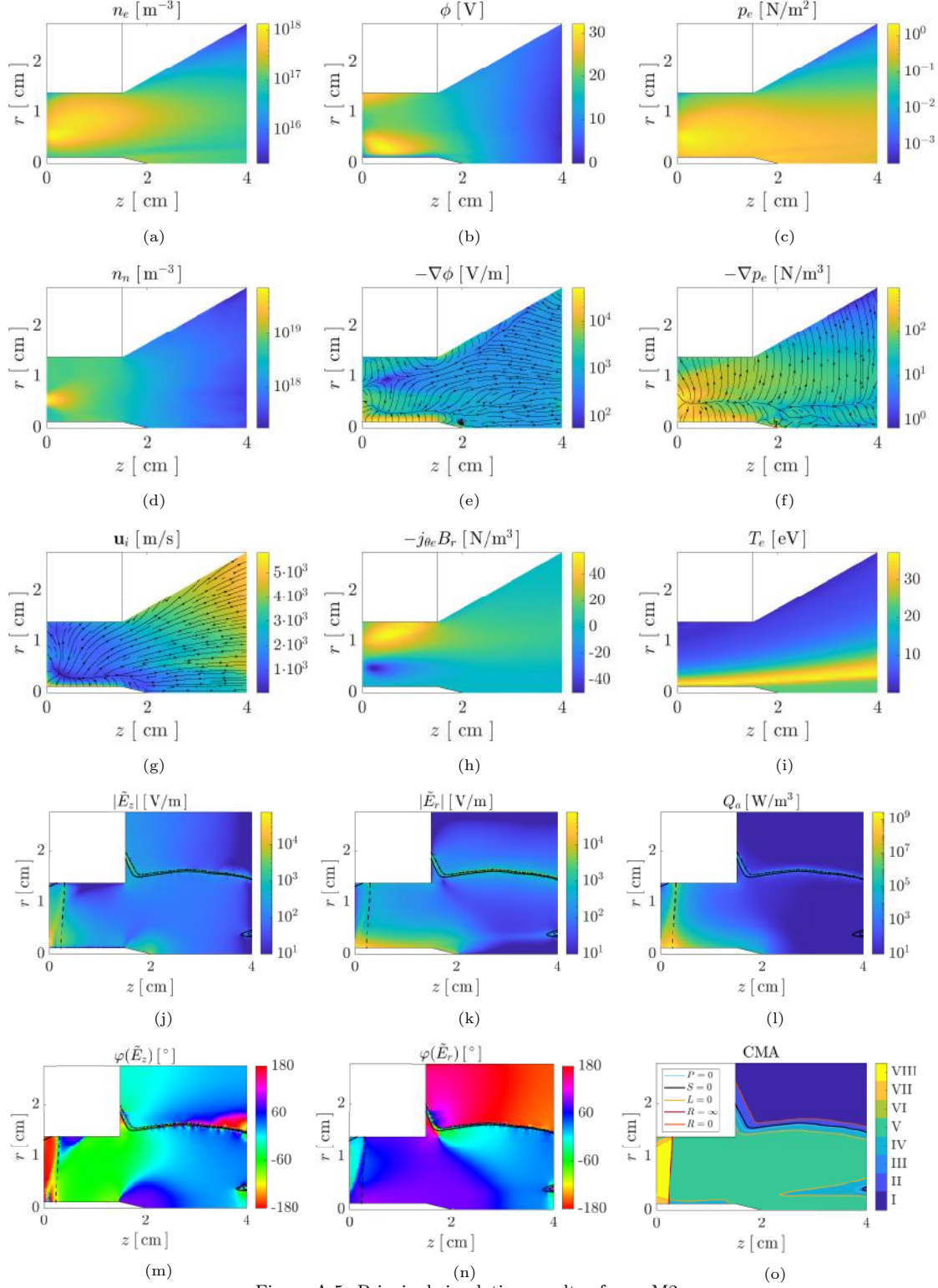


Figure A.5: Principal simulation results of case M2.

Case P0

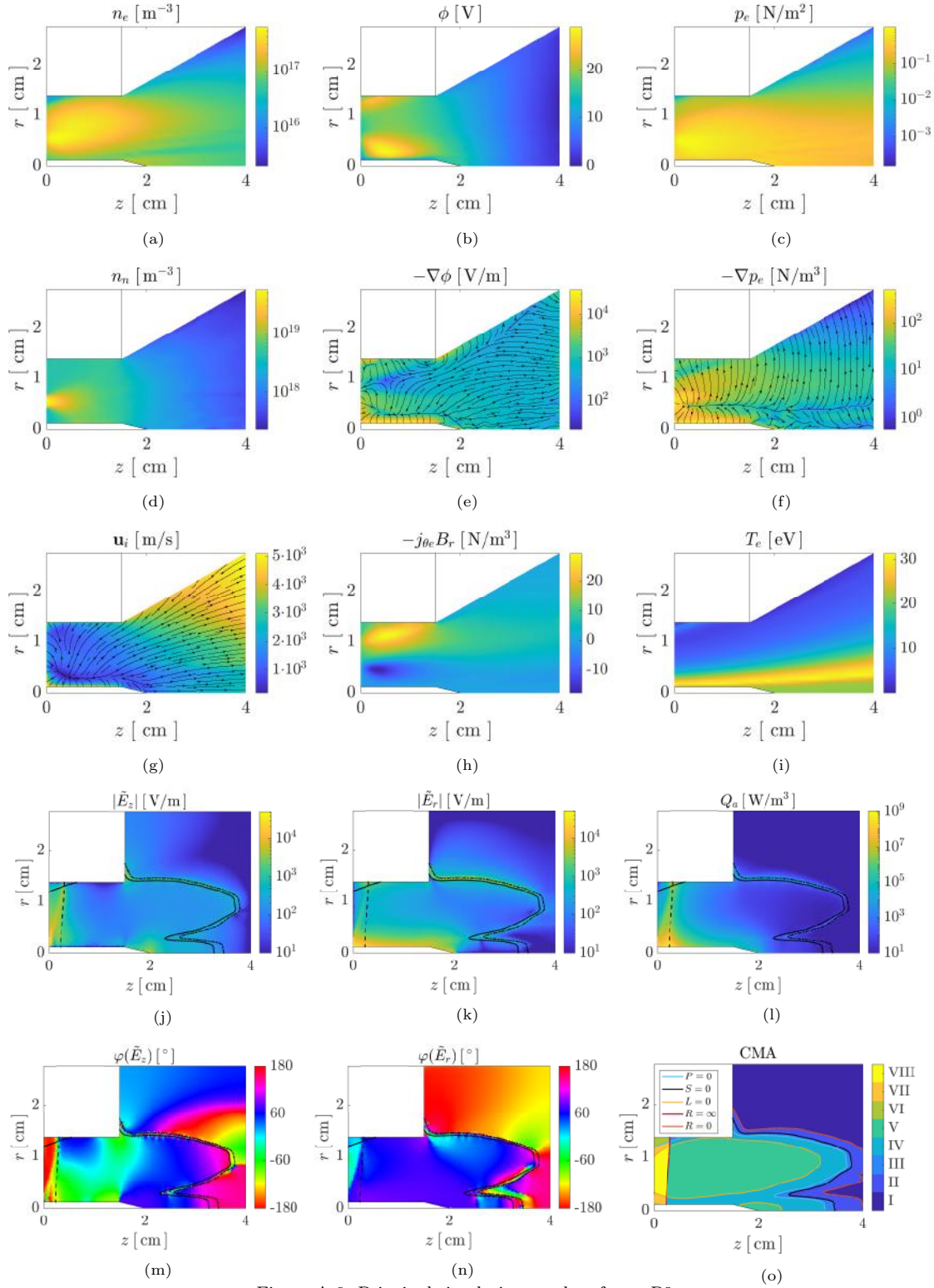


Figure A.6: Principal simulation results of case P0.

Case P2

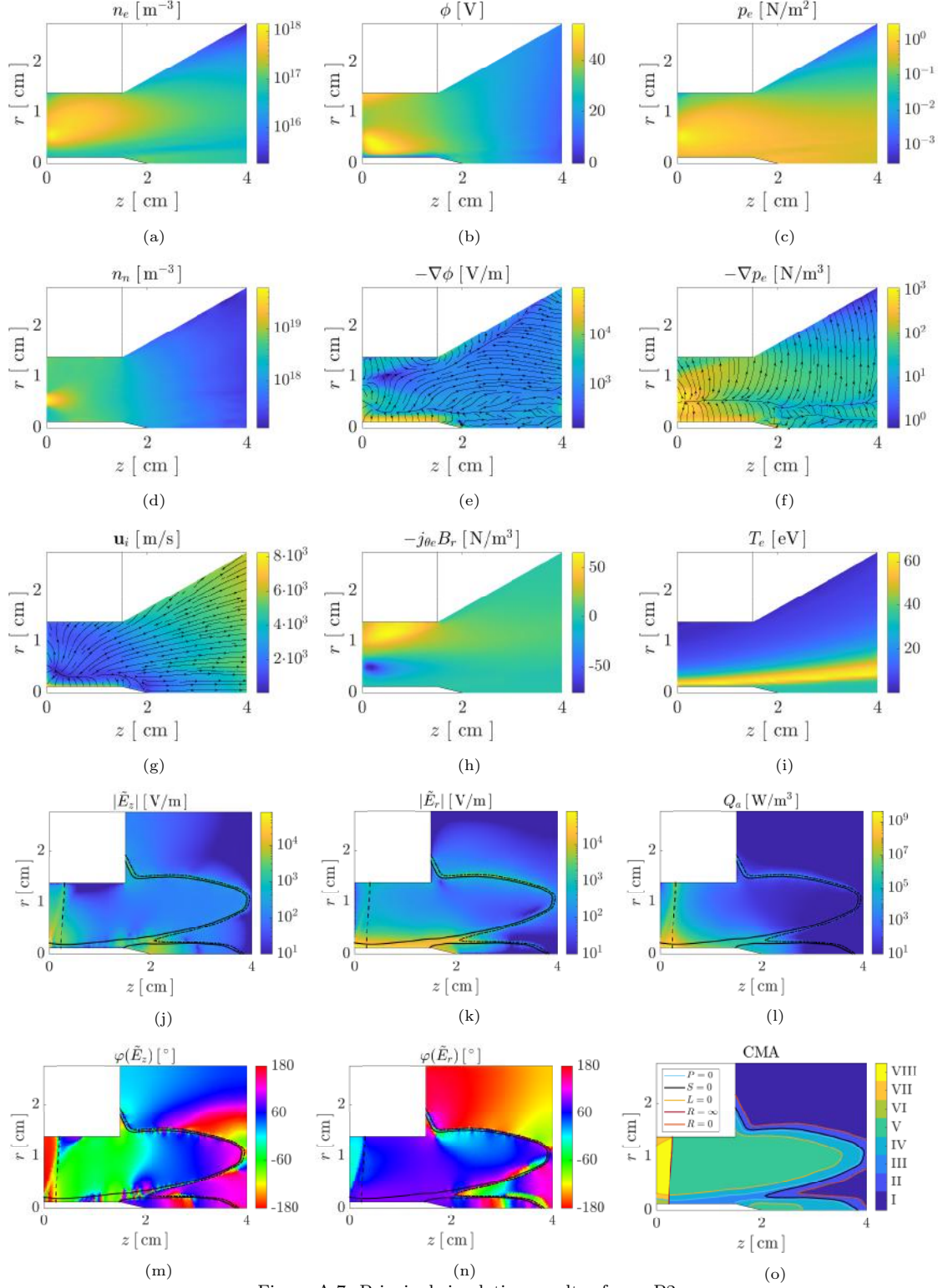


Figure A.7: Principal simulation results of case P2.

Case ECR0

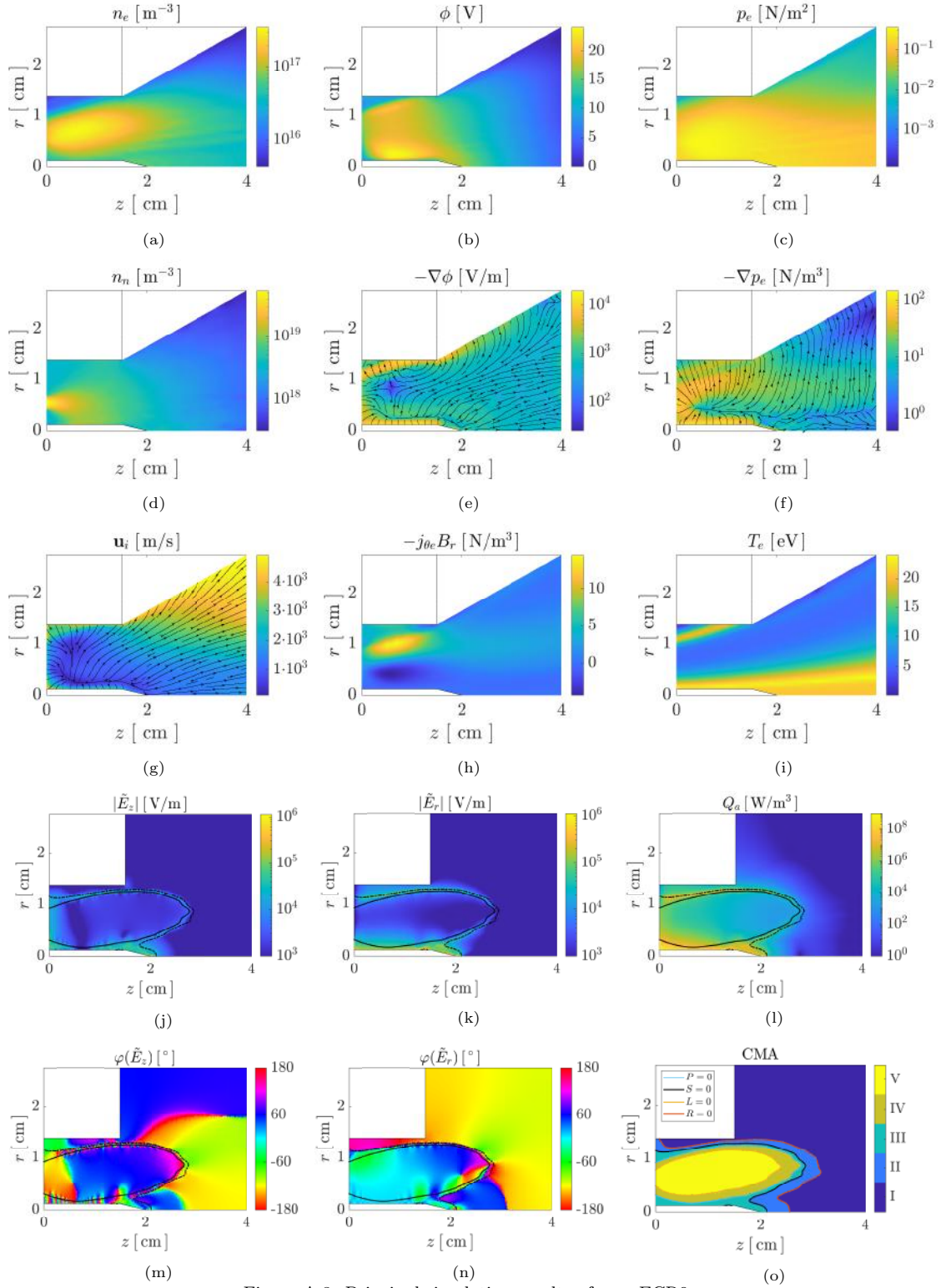


Figure A.8: Principal simulation results of case ECR0.

Case ECR2

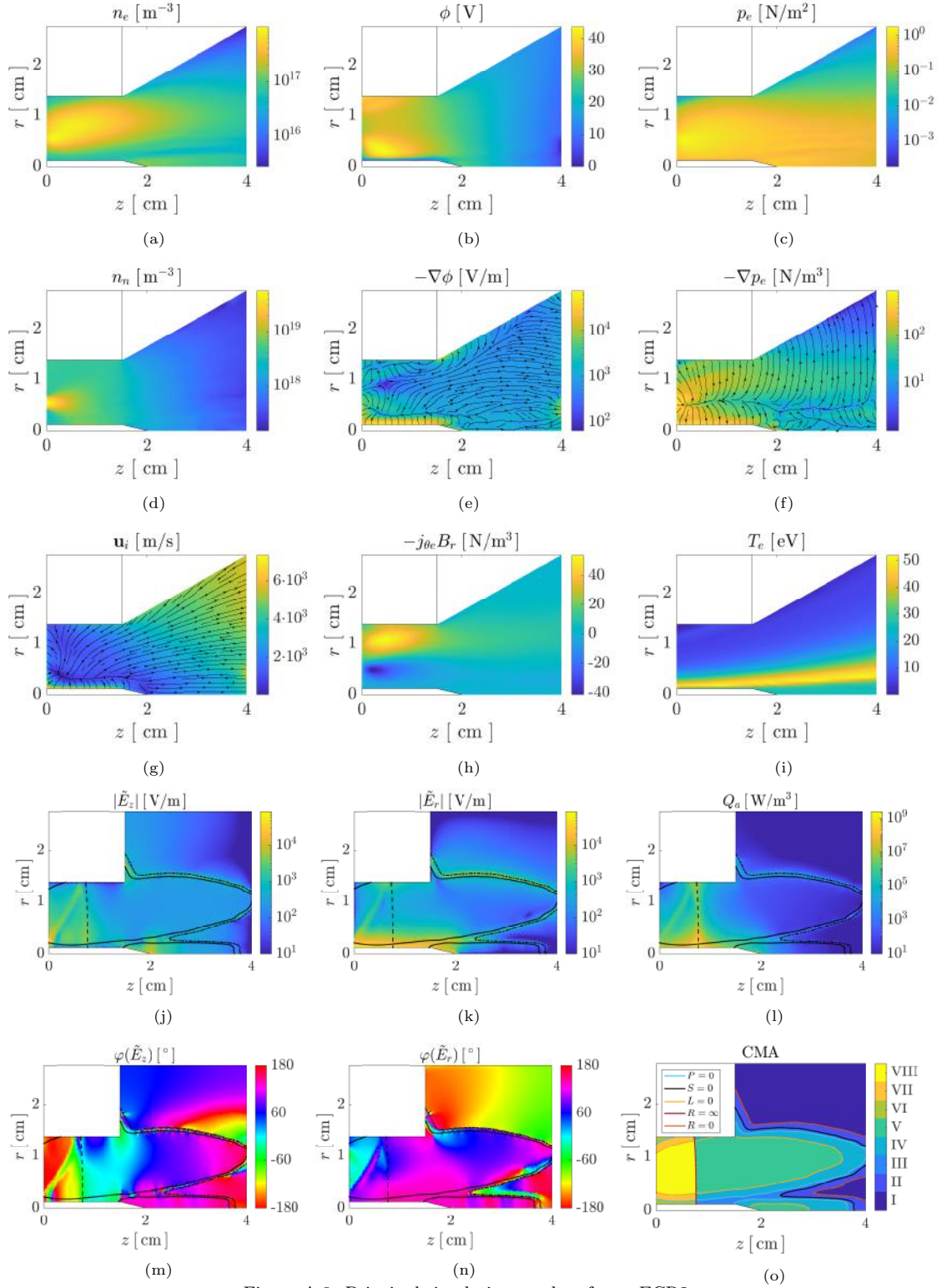


Figure A.9: Principal simulation results of case ECR2.

Case INJZ0

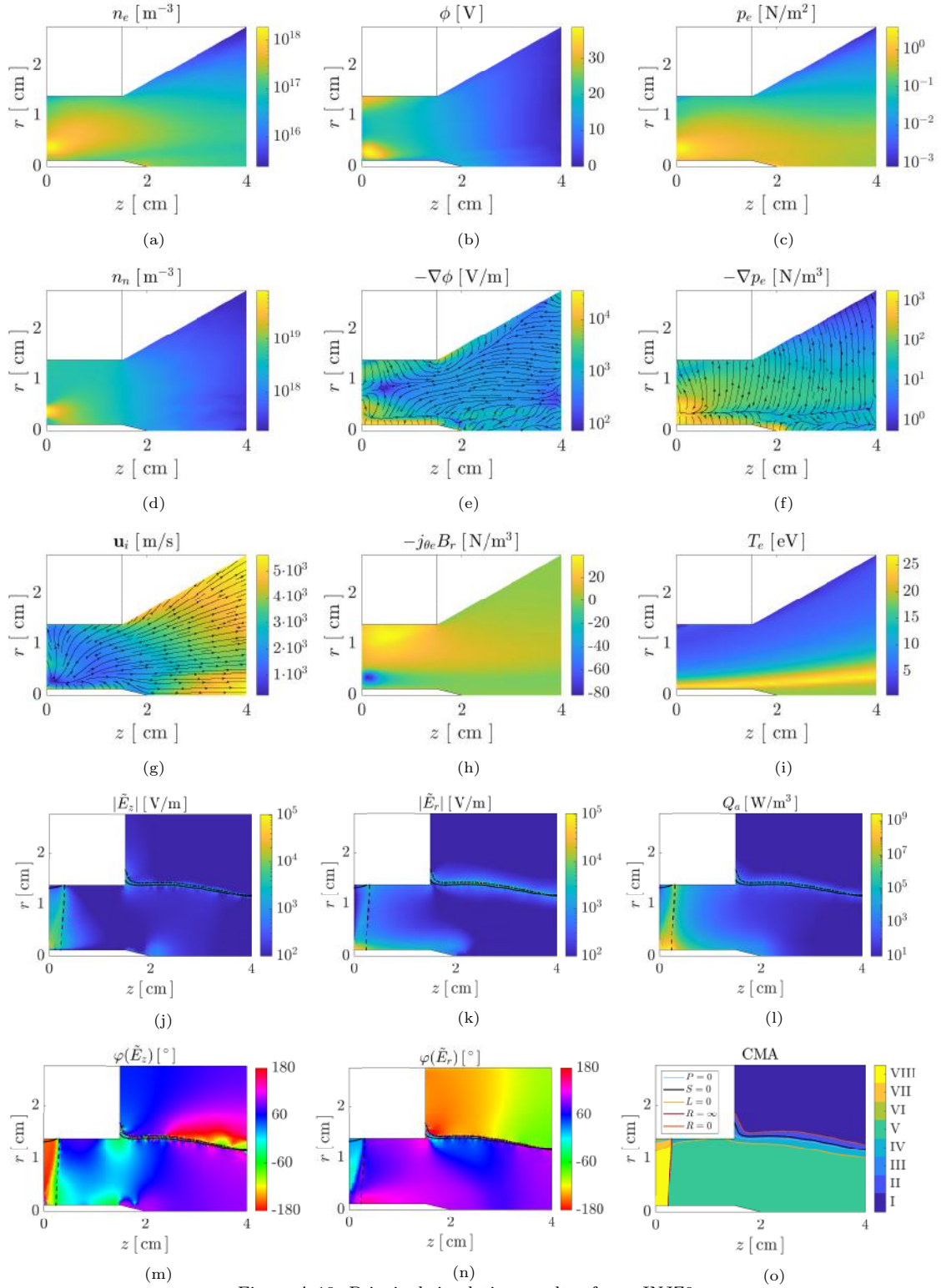


Figure A.10: Principal simulation results of case INJZ0.

Case INJR

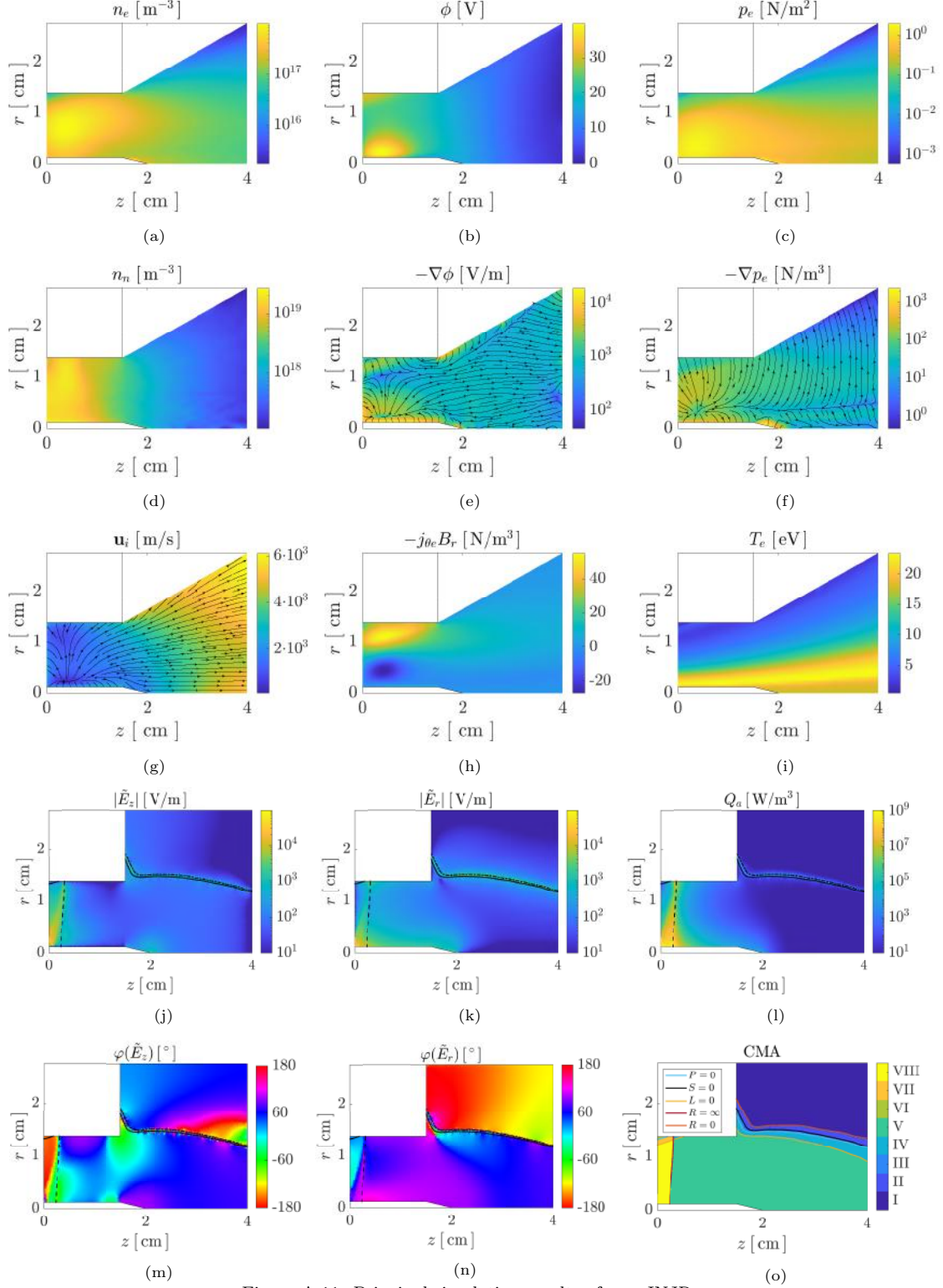


Figure A.11: Principal simulation results of case INJR.

Bibliography

- [1] R. G. Jahn. *Physics of Electric Propulsion*. Dover, 2006.
- [2] M. Martínez-Sánchez and J.E. Pollard. Spacecraft electric propulsion — an overview. *Journal of Propulsion and Power*, 14(5):688–699, September 1998.
- [3] E. Ahedo. Plasmas for space propulsion. *Plasma Physics and Controlled Fusion*, 53(12):124037, 2011.
- [4] H. Kuminaka, K. Nishiyama, I. Funaki, T. Yamada, Y. Shimizu, and J. Kawaguchi. Powered flight of electron cyclotron resonance ion engines on Hayabusa explorer. *Journal of Propulsion and Power*, 23(3):544–551, 2007.
- [5] D. B. Miller, E. F. Gibbons, and P. Gloersen. Cyclotron resonance propulsion system. In *Electric Propulsion Conference*, page 2, 1962.
- [6] D. B. Miller and E. F. Gibbons. Experiments with an electron cyclotron resonance plasma accelerator. *AIAA Journal*, 2(1):35–41, January 1964.
- [7] G. W. Bethke and D. B. Miller. Cyclotron resonance thruster design techniques. *AIAA Journal*, 4(5):835–840, 1966.
- [8] G. F. Crimi, A. C. Eckert, and D. B. Miller. Microwave driven magnetic plasma accelerator studies (Cyclops). Technical report, General Electric Company, Space Sciences Laboratory, Missile and Space Division, 1967.
- [9] J. C. Sercel. Electron-cyclotron-resonance (ECR) plasma thruster research. In *24th Joint Propulsion Conference*, page 2916, 1988.
- [10] J. C. Sercel. *An experimental and theoretical study of the ECR plasma engine*. PhD thesis, California Institute of Technology, 1993.
- [11] J. Jarrige, P. Q. Elias, F. Cannat, and D. Packan. Performance comparison of an ECR plasma thruster using argon and xenon as propellant gas. In *33rd International Electric Propulsion Conference*, Paper 2013-420, Washington D.C., October 7-10, 2013. Electric Rocket Propulsion Society, Fairview Park, OH.
- [12] T. Vialis, J. Jarrige, A. Aanesland, and D. Packan. Direct thrust measurement of an electron cyclotron resonance plasma thruster. *Journal of Propulsion and Power*, 34(5):1323–1333, 2018.
- [13] F. F. Chen. Plasma ionization by helicon waves. *Plasma Physics and Controlled Fusion*, 33(4):339, 1991.

- [14] F. N. Gesto, B. D. Blackwell, C. Charles, and R. W. Boswell. Ion detachment in the helicon double-layer thruster exhaust beam. *Journal of Propulsion and Power*, 22(1):24–30, 2006.
- [15] S. Pottinger, V. Lappas, C. Charles, and R. Boswell. Performance characterization of a helicon double layer thruster using direct thrust measurements. *Journal of Physics D: Applied Physics*, 44(23):235201, 2011.
- [16] J. Navarro-Cavallé, M. Merino, and E. Ahedo. The helicon plasma thruster: State-of-art prototypes and modeling. *Plasma Sources Science and Technology*.
- [17] J. Navarro-Cavallé, M. Wijnen, P. Fajardo, and E. Ahedo. Experimental characterization of a 1 kW helicon plasma thruster. *Vacuum*, 149:69–73, 2018.
- [18] F. Diaz and R. Chang. The VASIMR rocket. *Scientific American*, 283(5):90–97, 2000.
- [19] M. Bornatici, R. Cano, O. De Barbieri, and F. Engelmann. Electron cyclotron emission and absorption in fusion plasmas. *Nuclear Fusion*, 23(9):1153, 1983.
- [20] R. Geller. *Electron cyclotron resonance ion sources and ECR plasmas*. CRC Press, 1996.
- [21] J. Asmussen, T. A. Grotjohn, P. Mak, and M. A. Perrin. The design and application of electron cyclotron resonance discharges. *IEEE transactions on plasma science*, 25(6):1196–1221, 1997.
- [22] D. B. Miller, G. W. Bethke, and G. F. Crimi. Final report: Investigation of plasma accelerator (Cyclotron Resonance Propulsion System). Technical report, NASA Lewis Research Center, November 1, 1965.
- [23] D.B. Miller and G.W. Bethke. Cyclotron resonance thruster design techniques. *AIAA JOURNAL*, 4(5), 1966.
- [24] J. C. Sercel. Electron-cyclotron-resonance (ECR) plasma acceleration. In *AIAA 19th Fluid Dynamics, Plasma Dynamics and Lasers Conference*, 1987.
- [25] J. C. Sercel and D. J. Fitzgerald. ECR plasma thruster research: Preliminary theory and experiments. In *AIAA 25th Joint Propulsion Conference*, 1989.
- [26] J. Jarrige, P. Q. Elias, F. Cannat, and D. Paakan. Characterization of a coaxial ECR plasma thruster. In *44th AIAA Plasmadynamics and Lasers Conference, San Diego*, 2013.
- [27] T. H. Stix. *Waves in plasmas*. Springer Science & Business Media, 1992.
- [28] D. G. Swanson. *Theory of mode conversion and tunneling in inhomogeneous plasmas*. John Wiley & Sons, 1998.
- [29] D. G. Swanson. *Plasma Waves, 2nd Edition*. IOP Publishing, Bristol, UK, 2003.
- [30] M. A. Lieberman and A. J. Lichtenberg. *Principles of plasma discharges and materials processing*. John Wiley and Sons, Hoboken, NJ, 2005.
- [31] J. Musil and F. Zacek. Penetration of a strong electromagnetic wave in an inhomogeneous plasma generated by ECR using a magnetic beach. *Plasma Physics*, 13(6):471, 1971.
- [32] M. Brambilla. Self-consistent field and power absorption from electron cyclotron resonance in a high frequency plasma accelerator. *Plasma Physics*, 10(4):359, 1968.
- [33] A. F. Kuckes. Resonant absorption of electromagnetic waves in a non-uniformly magnetized plasma. *Plasma Physics*, 10(4):367, 1968.

- [34] M. C. Williamson, A. J. Lichtenberg, and M. A. Lieberman. Self-consistent electron cyclotron resonance absorption in a plasma with varying parameters. *Journal of applied physics*, 72(9):3924–3933, 1992.
- [35] H. Koivisto. The effect of microwave frequency and grad B on the energy of electrons in an electron cyclotron resonance ion source. *Review of scientific instruments*, 70(7):2979–2983, 1999.
- [36] B. P. Cluggish and J. S. Kim. Modeling of wave propagation and absorption in electron cyclotron resonance ion source plasmas. *Nuclear Instruments and Methods in Physics Research Section A: Accelerators, Spectrometers, Detectors and Associated Equipment*, 664(1):84–97, 2012.
- [37] J. E. Stevens and J. L. Cecchi. Wave propagation and plasma uniformity in an electron cyclotron resonance plasma etch reactor. *Japanese journal of applied physics*, 32(6S):3007, 1993.
- [38] W. M. Manheimer. A simple scheme for implementing wave absorption in quasi-neutral PIC simulations of ECR plasma. Technical report, Naval Research Lab Washington DC Fundamental Plasma Processes, 1998.
- [39] A. Cardinali, D. Melazzi, M. Manente, and D. Pavarin. Ray-tracing WKB analysis of whistler waves in non-uniform magnetic fields applied to space thrusters. *Plasma Sources Science and Technology*, 23(1):015013, 2014.
- [40] H. Muta, T. Sakoda, Y. Ueda, and Y. Kawai. One-dimensional simulation of microwave propagation in electron cyclotron resonance plasmas. *Japanese journal of applied physics*, 36(2R):872, 1997.
- [41] H. Muta, Y. Ueda, and Y. Kawai. Three-dimensional simulation of microwave propagation in an electron cyclotron resonance plasma. *Japanese journal of applied physics*, 36(7S):4773, 1997.
- [42] Y. Yasaka, A. Fukuyama, A. Hatta, and R. Itatani. Two-dimensional modeling of electron cyclotron resonance plasma production. *Journal of applied physics*, 72(7):2652–2658, 1992.
- [43] Y. Yasaka and N. Uda. Practical scheme for three-dimensional simulation of electron cyclotron resonance plasma reactors. *Journal of Applied Physics*, 89(7):3594–3601, 2001.
- [44] D. Melazzi, D. Curreli, M. Manente, J. Carlsson, and D. Pavarin. SPIRES: A Finite-Difference Frequency-Domain electromagnetic solver for inhomogeneous magnetized plasma cylinders. *Computer Physics Communications*, 183(6):1182–1191, 2012.
- [45] D. Melazzi and V. Lancellotti. ADAMANT: A surface and volume integral-equation solver for the analysis and design of helicon plasma sources. *Computer Physics Communications*, 185(7):1914–1925, 2014.
- [46] A. Taflove and S. C. Hagness. *Computational electrodynamics*. Artech house, 2005.
- [47] J. L. Volakis, K. Sertel, and B. C. Usner. *Frequency domain hybrid finite element methods for electromagnetics*. Morgan & Claypool Publishers, 2006.
- [48] J.M. Jin. *The finite element method in electromagnetics*. John Wiley & Sons, 2014.
- [49] D. Packan, P.Q. Elias, J. Jarrige, M. Merino, A. Sánchez-Villar, E. Ahedo, G. Peyresoubes, K. Holste, P. Klar, M. Bekemans, T. Scalais, E. Bourguignon, S. Zurbach, M. Mares, A. Hooque, and P. Favier. The MINOTOR H2020 project for ECR thruster development. In *35th International Electric Propulsion Conference*, number IEPC-2017-547. Electric Rocket Propulsion Society, 2017.

- [50] F. Cannat, J. Jarrige, T. Laffeur, P.Q. Elias, and D. Packan. Experimental geometry investigation of a coaxial ECR plasma thruster. In *Proc. of the 34th Int. Electric Propulsion Conf. (Kobe-Hyogo, Japan)*, pages 2015–242, 2015.
- [51] F. Cannat, T. Laffeur, J. Jarrige, P. Chabert, P.Q. Elias, and D. Packan. Optimization of a coaxial electron cyclotron resonance plasma thruster with an analytical model. *Physics of Plasmas*, 22(5):053503, 2015.
- [52] S. Correyero, J. Jarrige, D. Packan, and E. Ahedo. Plasma beam characterization along the magnetic nozzle of an ECR thruster. *Plasma Sources Science and Technology*, 28(9):095004, 2019.
- [53] S. Peterschmitt and D. Packan. Comparison of waveguide coupled and coaxial coupled ECRA magnetic nozzle thruster using a thrust balance. In *Proc. of the 36th Int. Electric Propulsion Conf. (Vienna, Austria)*, pages 2019–188, 2019.
- [54] B. Tian, M. Merino, and E. Ahedo. Two-dimensional plasma-wave interaction in an helicon plasma thruster with magnetic nozzle. *Plasma Sources Science and Technology*, 27(11):114003, 2018.
- [55] K. G. Budden. *Radio waves in the ionosphere: the mathematical theory of the reflection of radio waves from stratified ionised layers*. Cambridge University Press, 1961.
- [56] M. Merino, A. Sánchez-Villar, E. Ahedo, Paul Bonoli, Jungpyo Lee, Abhay Ram, and John Wright. Wave propagation and absorption in ECR plasma thrusters. In *35th International Electric Propulsion Conference*, number IEPC-2017-105, Atlanta, GA, 2017. Electric Rocket Propulsion Society.
- [57] A. Sánchez-Villar, J. Zhou, M. Merino, and E. Ahedo. Coupled plasma transport and electromagnetic wave simulation of an ECR thruster. *Plasma Sources Science and Technology*, 30(4):045005, 2021.
- [58] A. Sánchez-Villar and M. Merino. Advances in wave-plasma modelling in ECR thrusters. In *Space Propulsion Conference 2018*, number 00346, Seville, Spain, 2018. Association Aéronautique et Astronautique de France.
- [59] A. Sánchez-Villar, J. Zhou, M. Merino, and E. Ahedo. PIC/fluid/wave simulations of the plasma discharge in an ECR plasma thruster. In *36th International Electric Propulsion Conference*, number IEPC-2019-633, Vienna, Austria, 2019. Electric Rocket Propulsion Society.
- [60] A. Domínguez-Vázquez. *Axisymmetric simulation codes for Hall effect thrusters and plasma plumes*. PhD thesis, Universidad Carlos III de Madrid, Leganés, Spain, 2019.
- [61] A. Sánchez-Villar, M. Merino, and E. Ahedo. A numerical parametric investigation on the optimal design and operation of coaxial ECR thrusters. In *Space Propulsion Conference 2021*, number 00396, March 17-19, 2021. Association Aéronautique et Astronautique de France.
- [62] A. Sánchez-Villar, A. Domínguez-Vázquez, E. Ahedo, and M. Merino. A numerical parametric investigation on the operation and design of coaxial ECR thrusters. *Plasma Sources Science and Technology*, to be submitted for publication.
- [63] A. Sánchez-Villar, F. Boni, V. Désangles, J. Jarrige, D. Packan, E. Ahedo, and M. Merino. Comparison of a hybrid coaxial ECR thruster model to experimental measurements. *Plasma Sources Science and Technology*, to be submitted for publication.
- [64] M. A. Heald and C. B. Wharton. *Plasma diagnostics with microwaves*. Wiley, 1965.
- [65] J. A. Bittencourt. *Fundamentals of plasma physics*. Springer, Berlin, Germany, 2013.

- [66] M. Brambilla. *Kinetic theory of plasma waves: homogeneous plasmas*. Number 96. Oxford University Press, 1998.
- [67] R. Gaelzer, L. F. Ziebell, and O. J. G. Silveira. Dielectric tensor for inhomogeneous plasmas in inhomogeneous magnetic field. *Physics of Plasmas*, 6(12):4533–4541, 1999.
- [68] N. Bertelli. *A beam tracing code for the description of lower hybrid wave propagation in tokamak plasma*. PhD thesis, Universita Degli Studi Di Pavia, 2007.
- [69] J. D. Jackson. *Classical electrodynamics*. American Association of Physics Teachers, College Park, MD, 1999.
- [70] F. W. J. Olver, D. W. Lozier, R. F. Boisvert, and C. W. Clark. *NIST Handbook of Mathematical Functions*, volume 5. Cambridge Press, 2010.
- [71] E. T. Whittaker and G. N. Watson. *A course of modern analysis* 4th ed., 1927.
- [72] J. Zhou, D. Pérez-Grande, P. Fajardo, and E. Ahedo. Numerical treatment of a magnetized electron fluid within an electromagnetic plasma thruster code. *Plasma Sources Science and Technology*, 28(11):115004, 2019.
- [73] D. Pérez-Grande, J. Zhou, A. Domínguez-Vázquez, P. Fajardo, and E. Ahedo. Development updates for a two-dimensional axisymmetric hybrid code for plasma thruster discharges. In *35th International Electric Propulsion Conference*, number IEPC-2017-201, Atlanta, GA, 2017. Electric Rocket Propulsion Society.
- [74] J. C. Nédélec. Mixed finite elements in \mathbb{R}^3 . *Numerische Mathematik*, 35(3):315–341, 1980.
- [75] K. Yee. Numerical solution of initial boundary value problems involving Maxwell’s equations in isotropic media. *IEEE Transactions on antennas and propagation*, 14(3):302–307, 1966.
- [76] B. N. Jiang, J. Wu, and L. A. Povinelli. The origin of spurious solutions in computational electromagnetics. *Journal of computational physics*, 125(1):104–123, 1996.
- [77] M. Hara, T. Wada, T. Fukasawa, and F. Kikuchi. A three dimensional analysis of RF electromagnetic fields by the finite element method. *IEEE Transactions on Magnetics*, 19(6):2417–2420, 1983.
- [78] P. Monk. *Finite element methods for Maxwell’s equations*. Oxford University Press, 2003.
- [79] J. M. Jin and D. J. Riley. *Finite element analysis of antennas and arrays*. John Wiley & Sons, 2009.
- [80] MFEM: Modular finite element methods library. <http://mfem.org>.
- [81] S. Shiraiwa, J. C. Wright, P. T. Bonoli, T. Kolev, and M. Stowell. RF wave simulation for cold edge plasmas using the MFEM library. In *EPJ Web of Conferences*, volume 157, page 03048. EDP Sciences, 2017.
- [82] J. C. Nédélec. A new family of mixed finite elements in \mathbb{R}^3 . *Numerische Mathematik*, 50(1):57–81, 1986.
- [83] G. Mur. Edge elements, their advantages and their disadvantages. *IEEE transactions on magnetics*, 30(5):3552–3557, 1994.
- [84] GLVis: Opengl finite element visualization tool. glvis.org.
- [85] A. D. Greenwood and J. M. Jin. A novel efficient algorithm for scattering from a complex BOR using mixed finite elements and cylindrical PML. *IEEE transactions on antennas and propagation*, 47(4):620–629, 1999.

- [86] D. M. Pozar. *Microwave engineering*. John Wiley & Sons, 2011.
- [87] C. Geuzaine and J. F. Remacle. Gmsh: A 3-D finite element mesh generator with built-in pre- and post-processing facilities. *International journal for numerical methods in engineering*, 79(11):1309–1331, 2009.
- [88] R. Otin, W. Tierens, F. Parra, S. Aria, E. Lerche, P. Jacquet, I. Monakhov, P. Dumortie, B. Van Compernelle, and JET Contributors. Full wave simulation of RF waves in cold plasma with the stabilized open-source finite element tool ERMES. In *23rd Topical Conference on Radiofrequency Power in Plasmas*, AIP Conf. Proc. 2254, pages 05009–1,050009–4, 2019.
- [89] R. Otin. ERMES: A nodal-based finite element code for electromagnetic simulations in frequency domain. *Computer Physics Communications*, 184(11):2588–2595, 2013.
- [90] C. Hazard and M. Lenoir. On the solution of time-harmonic scattering problems for Maxwell’s equations. *SIAM Journal on Mathematical Analysis*, 27(6):1597–1630, 1996.
- [91] D. Garcia-Donoro, L. E. Garcia-Castillo, and S. W. Ting. Verification process of finite-element method code for electromagnetics: Using the method of manufactured solutions. *IEEE Antennas and Propagation Magazine*, 58(2):28–38, 2016.
- [92] C. Charles, R.W. Boswell, and M.A. Lieberman. Xenon ion beam characterization in a helicon double layer thruster. *Applied Physics Letters*, 89(26):261503, 2006.
- [93] F. Cannat, J. Jarrige, P. Q. Elias, and D. Packan. Experimental investigation of magnetic gradient influence in a coaxial ECR plasma thruster. In *Space Propulsion Conference, Cologne, Germany*, 2014.
- [94] T. Lafleur, D. Packan, F. Cannat, J. Jarrige, and P. Q. Elias. Modelling of magnetic nozzle thrusters with application to ECR and helicon thrusters. In *34th International Electric Propulsion Conference*, paper 2015-359, Kobe, Japan, July 6-10, 2015. Electric Rocket Propulsion Society, Fairview Park, OH.
- [95] S. Correyero, M. Merino, P. Q. Elias, J. Jarrige, D. Packan, and E. Ahedo. Characterization of diamagnetism inside an ECR thruster with a diamagnetic loop. *Physics of Plasmas*, 26(5):053511, 2019.
- [96] E. B. Hooper. Plasma flow resulting from electron cyclotron resonance heating on a magnetic hill. *Physics of Plasmas*, 2:4563, 1995.
- [97] A. Fruchtman, G. Makrinich, and J. Ashkenazy. Two-dimensional equilibrium of a low temperature magnetized plasma. *Plasma Sources Science and Technology*, 14:152–167, 2005.
- [98] E. Ahedo and J. Navarro-Cavallé. Helicon thruster plasma modeling: Two-dimensional fluid-dynamics and propulsive performances. *Physics of Plasmas*, 20(4):043512, 2013.
- [99] T. Lafleur. Helicon plasma thruster discharge model. *Physics of Plasmas*, 21(4):043507, 2014.
- [100] M. Magarotto, M. Manente, F. Trezzolani, and D. Pavarin. Numerical model of a helicon plasma thruster. *IEEE Transactions on Plasma Science*, 48(4):835–844, 2020.
- [101] N. Bertelli, E. F. Jaeger, J. C. Hosea, C. K. Phillips, L. Berry, S. P. Gerhardt, D. Green, B. LeBlanc, R. J. Perkins, and P. M. et al. Ryan. Full wave simulations of fast wave heating losses in the scrape-off layer of NSTX and NSTX-U. *Nuclear Fusion*, 54(8):083004, 2014.
- [102] E. H. Kim, N. Bertelli, J. Johnson, E. Valeo, and J. Hosea. 2D full-wave simulation of waves in space and tokamak plasmas. In *EPJ Web of Conferences*, volume 157, page 02005. EDP Sciences, 2017.

- [103] S. Gammino, G. Ciavola, L. G. Celona, D. Mascali, and F. Maimone. Numerical simulations of the ECR heating with waves of different frequency in electron cyclotron resonance ion sources. *IEEE Transactions on Plasma Science*, 36(4):1552–1568, 2008.
- [104] F. Jaeger, A. J. Lichtenberg, and M. A. Lieberman. Theory of electron cyclotron resonance heating. I. Short time and adiabatic effects. *Plasma Physics*, 14(12):1073, 1972.
- [105] M. A. Lieberman and A. J. Lichtenberg. Theory of electron cyclotron resonance heating. II. Long time and stochastic effects. *Plasma Physics*, 15(2):125, 1973.
- [106] A. Domínguez-Vázquez, J. Zhou, P. Fajardo, and E. Ahedo. Analysis of the plasma discharge in a Hall thruster via a hybrid 2D code. In *36th International Electric Propulsion Conference*, number IEPC-2019-579, Vienna, Austria, 2019. Electric Rocket Propulsion Society.
- [107] D. Pérez-Grande. *Fluid modeling and simulation of the electron population in Hall effect thrusters with complex magnetic topologies*. PhD thesis, Universidad Carlos III de Madrid, Leganés, Spain, 2018.
- [108] J. Zhou, P. Jiménez, M. Merino, P. Fajardo, and E. Ahedo. Numerical simulations of the plasma discharge in a helicon plasma thruster. In *36th International Electric Propulsion Conference*, number IEPC-2019-330, Vienna, Austria, 2019. Electric Rocket Propulsion Society.
- [109] F. Cichocki, A. Domínguez-Vázquez, M. Merino, and E. Ahedo. Hybrid 3D model for the interaction of plasma thruster plumes with nearby objects. *Plasma Sources Science and Technology*, 26(12):125008, 2017.
- [110] E. Ahedo, R. Santos, and F. Parra. Fulfillment of the kinetic Bohm criterion in a quasineutral particle-in-cell model. *Physics of Plasmas*, 17(7):073507, 2010.
- [111] A. Domínguez-Vázquez, F. Cichocki, M. Merino, P. Fajardo, and E. Ahedo. Axisymmetric plasma plume characterization with 2D and 3D particle codes. *Plasma Sources Science and Technology*, 27(10):104009, 2018.
- [112] J. M. Fife. *Hybrid-PIC modeling and electrostatic probe survey of Hall thrusters*. PhD thesis, Massachusetts Institute of Technology, 1998.
- [113] E. Ahedo, P. Martínez-Cerezo, and M. Martínez-Sánchez. One-dimensional model of the plasma flow in a Hall thruster. *Physics of Plasmas*, 8:3058–3068, 2001.
- [114] S. T. Hepner and B. Jorns. The role of low frequency drift waves in driving non-classical transport in magnetic nozzles. In *AIAA Propulsion and Energy 2020 Forum*, page 3644, 2020.
- [115] E. Ahedo and V. de Pablo. Combined effects of electron partial thermalization and secondary emission in Hall thruster discharges. *Physics of Plasmas*, 14:083501, 2007.
- [116] F. I. Parra, E. Ahedo, J. M. Fife, and M. Martínez-Sánchez. A two-dimensional hybrid model of the Hall thruster discharge. *Journal of Applied Physics*, 100(2):023304, 2006.
- [117] F. Taccogna, S. Longo, and M. Capitelli. Plasma sheaths in Hall discharge. *Physics of Plasmas*, 12(9):093506, 2005.
- [118] M. Martínez-Sánchez, J. Navarro-Cavallé, and E. Ahedo. Electron cooling and finite potential drop in a magnetized plasma expansion. *Physics of Plasmas*, 22(5):053501, 2015.
- [119] T. Lafleur, F. Cannat, J. Jarrige, P. Q. Elias, and D. Packan. Electron dynamics and ion acceleration in expanding-plasma thrusters. *Plasma Sources Science and Technology*, 24(6):065013, 2015.

- [120] M. Merino and E. Ahedo. Plasma detachment in a propulsive magnetic nozzle via ion demagnetization. *Plasma Sources Science and Technology*, 23(3):032001, 2014.
- [121] M. Merino and E. Ahedo. Fully magnetized plasma flow in a magnetic nozzle. *Physics of Plasmas*, 23(2):023506, 2016.
- [122] B. Wachs and B. Jorns. Background pressure effects on ion dynamics in a low-power magnetic nozzle thruster. *Plasma Sources Science and Technology*, 29(4):045002, 2020.
- [123] T. Vialis, J. Jarrige, and D. Packan. Separate measurements of magnetic and pressure thrust contributions in a magnetic nozzle electron cyclotron resonance plasma thruster. In *Space Propulsion Conference*, 499, Seville, Spain, May 2018.
- [124] A. Fruchtman. Neutral depletion in a collisionless plasma. *Plasma Science, IEEE Transactions on*, 36(2):403–413, 2008.
- [125] J. M. Little and E. Y. Choueiri. Critical condition for plasma confinement in the source of a magnetic nozzle flow. *IEEE Transactions on Plasma Science*, 43(1):277–286, 2014.
- [126] M. Usoltceva, R. Ochoukov, W. Tierens, A. Kostic, K. Crombé, S. Heuraux, and J. M. Noterdaeme. Simulation of the ion cyclotron range of frequencies slow wave and the lower hybrid resonance in 3D in RAPLICASOL. *Plasma Physics and Controlled Fusion*, 61(11):115011, 2019.
- [127] R. Moloney and et al. Experimental validation and performance measurements of an ECR thruster operating on multiple propellants. In *36th International Electric Propulsion Conference, Vienna, Austria, IEPC-2019-199*, 2019.
- [128] J. Jarrige, S. Correyero Plaza, P. Q. Elias, and D. Packan. Investigation on the ion velocity distribution in the magnetic nozzle of an ECR plasma thruster using LIF measurements. In *35th International Electric Propulsion Conference, IEPC-2017-382*, Atlanta, GA, 2017. Electric Rocket Propulsion Society, Fairview Park, OH.
- [129] J. S. Sovey, V. K. Rawlin, and M. J. Patterson. Ion propulsion development projects in US: Space electric rocket test I to deep space 1. *J. Propul. Power*, 17:517, 2001.
- [130] H. G. Kosmahl, D. B. Miller, and G. W. Bethke. Plasma acceleration with microwaves near cyclotron resonance. *J. Appl. Phys.*, 38(12):4576–4582, 1967.
- [131] B. Wachs and B. Jorns. Technique for two-frequency optimization of an ECR magnetic nozzle thruster. *Int. Electr. Propuls. Conf.*, pages 1–11, 2019.
- [132] S. Hepner, B. Wachs, and B. Jorns. Wave-driven non-classical electron transport in a low temperature magnetically expanding plasma. *Appl. Phys. Lett.*, 116(26), 2020.
- [133] E. Ahedo, J.M. Gallardo, and M. Martínez-Sánchez. Effects of the radial-plasma wall interaction on the axial Hall thruster discharge. *Physics of Plasmas*, 10(8):3397–3409, 2003.
- [134] S. Barral, K. Makowski, Z. Peradzynski, N. Gascon, and M. Dudeck. Wall material effects in stationary plasma thrusters. II. near-wall and in-wall conductivity. *Phys. Plasmas*, 10(10):4137–4152, 2003.
- [135] S. Peterschmitt. *Development of a stable and efficient electron cyclotron resonance thruster with magnetic nozzle*. PhD thesis, Institut Polytechnique de Paris, 2020.
- [136] F. Boni and J. Jarrige. The curling probe : a numerical and experimental study. Application to the electron density measurements in an ECR plasma thruster. 033507, 2021.

- [137] M. J. Druyvesteyn and F. M. Penning. The mechanism of electrical discharges in gases of low pressure. *Rev. Mod. Phys.*, 12(2):87–174, 1940.
- [138] D. L. Brown, M. L. R. Walker, J. Szabo, W. Huang, and J. E. Foster. Recommended practice for use of Faraday probes in electric propulsion testing. *J. Propuls. Power*, 33(3):582–613, 2017.
- [139] R. B. Lobbia and B. E. Beal. Recommended practice for use of Langmuir probes in electric propulsion testing. *J. Propuls. Power*, 33(3):566–581, 2017.
- [140] L. Spitzer and R. Härm. Transport phenomena in a completely ionized gas. *Physical Review*, 89(5):977, 1953.
- [141] K. Holste, P. Dietz, S. Scharmann, K. Keil, T. Henning, D. Zschätzsch, M. Reitemeyer, B. Nauschütt, F. Kiefer, F. Kunze, et al. Ion thrusters for electric propulsion: Scientific issues developing a niche technology into a game changer. *Review of Scientific Instruments*, 91(6):061101, 2020.
- [142] K. Dannenmayer, S. Mazouffre, M. Merino, and E. Ahedo. Hall effect thruster plasma plume characterization with probe measurements and self-similar fluid models. In *48th AIAA/ASME/SAE/ASEE Joint Propulsion Conference & Exhibit*, number AIAA-2012-4117, Atlanta, Georgia, July 30 - August 1, 2012. American Institute of Aeronautics and Astronautics.
- [143] F. Cichocki, M. Merino, and E. Ahedo. Modeling and simulation of EP plasma plume expansion into vacuum. In *50th AIAA/ASME/SAE/ASEE Joint Propulsion Conference & Exhibit*, number AIAA-2014-3828, Cleveland, Ohio, July 28-30, 2014. American Institute of Aeronautics and Astronautics.
- [144] E. Ahedo, Correyero. S, J. Navarro, and M. Merino. Macroscopic and parametric study of a kinetic plasma expansion in a paraxial magnetic nozzle. *Plasma Sources Science and Technology*, 29(4):045017, 2020.
- [145] J. Zhou, G. Sánchez-Arriaga, and E. Ahedo. Time-dependent expansion of a weakly-collisional plasma beam in a paraxial magnetic nozzle. *Plasma Sources Science and Technology*, 30(4):045009, 2021.
- [146] M. Merino, J. Nuez, and E. Ahedo. Fluid-kinetic model of a propulsive magnetic nozzle. *Plasma Sources Science and Technology*, submitted for publication.